X-RAY DIFFRACTION TOPOGRAPHY: METHODS AND APPLICATIONS

BODLEIAN LIBRARY OXFORD
DEPOSITED
THESIS
12·4·72

B.K. Tanner, B.A.

Robinson Senior Scholar, Oriel College

Thesis submitted for the degree of Doctor of Philosophy

in the University of Oxford

November 1971

PREFACE

This thesis contains an account of work performed in the Department of Metallurgy, Oxford University in the period October 1968 - October 1971. No part of it is substantially the same as that submitted to any other University and the thesis is a description of my own original research. Where projects have been carried out in collaboration with others and where results of other workers are described, due reference is made in the text. References are listed in alphabetical order at the end of the thesis.

The author would like to express his sincere thanks to Professor P.B. Hirsch, F.R.S., for laboratory facilities, to Dr. C.J. Humphreys, for his friendship and his unobstructive, stimulating and eminently sensible supervision, and Dr. M.J. Whelan, for so admirably deputising during the absence of Dr. Humphreys. The assistance of all three in obtaining the Elliott GX6 is gratefully acknowledged.

Thanks are due to all my colleagues for their assistance at various times and for their part in providing an atmosphere conducive to creative thought, and to several workers in the field, with whom discussion has been most stimulating. In particular, thanks must be expressed to the following:

Dr. A.A. Balchin and Mr. H.P.B. Rimmington for growing the layer compounds, the X ray study of which is described in Chapter VII,

Dr. G.R. Booker and Dr. J. Filby for providing semi-conductor specimens,

Dr. D.E. Crutchley for providing the iron single crystals and assisting the experiments of Chapter VIII,

The Director of the Oxford University Computing Laboratory for time on KDF9 and 1906A computers,

Mr. A. Guest of Mullards Ltd., for providing the channel plate and discussing its uses,

Mr. D.R. Hunter for performing the S.E.M. experiments described in Chapter V,

Mr. A. McKnight for photographic assistance,

Mr. H.R. Petit for polishing the silicon wedge used in Chapter IV,

Dr. G.D.W. Smith and Mr. T.F. Godfrey for help in preparing fluorescent screens,

Mr. C.H. Sworn for allowing the use of his computed dislocation profiles in Chapter IV,

Mr. D.W. Tansley for assistance in constructing the channel plate assembly,

Dr. J.M. Titchmarsh for helpful discussion concerning the problem of the surface relaxed dislocation,

Dr. E. Whittaker for obtaining the fluorite samples and discussing the work.

Finally, I would like to thank Mrs. Enid Browne for typing the manuscript, and especially my wife, Ruth, for her love and encouragement, for help in typing the draft, proof reading and collating references.

The work was performed while the author was in receipt of a Science Research Council Studentship, and for this,

thanks are due to the Council. The author wishes to thank the Provost and Fellows of Oriel College for the award of the Robinson Senior Scholarship, and the Master and Fellows of Balliol College for a grant to attend the Antwerp Summer School in 1969.

Material from Chapter II has been published in

J. Phys. D. (Appl. Phys.) 3 (1970) 1144

and from Chapter III in

Phys. Stat. Sol.(a) 6 (1971) 689.

Papers based on the following sections have been read at conferences:

Chapter II "Safety in X ray laboratories", I.O.P. (Nov. 1970) London,

Chapters IV and V C.V.D. Coordination meeting, (July 1971) University of Southampton,

Chapter VII British Association for Crystal Growth Conference (Sept. 1971) University of Sussex,

Chapters III and IV X ray Topography Symposium (Sept. 1971) University of Bristol.

Oriel College,

Oxford.

October 1971.

B K Tanner

B.K. Tanner.

ABSTRACT

This thesis describes the application of the well established technique of X-ray diffraction topography to a variety of problems, and includes considerations of the optimum conditions for taking rapid topographs.

Chapter I contains a brief review of the subject together with an indication of the range of applicability. Several modifications of X-ray topography exist and several are briefly described to illustrate the principles and mechanisms of image formation. Contrast is formed in one or both of two ways. Regions of crystal may be so badly misoriented from the bulk, that no beams from the source can satisfy the reflection condition formulated by Bragg. This type of contrast is known as orientation contrast. The second type of contrast arises from the point to point lattice displacements giving a different reflecting power around the defect. This second type of contrast, termed extinction contrast, is dependent on the perfect crystal diffraction. A description of the different types of extinction contrast is given in terms of the dynamical theory of diffraction in a perfect crystal and the significance of the direct, intermediate, and dynamical images stressed. The chapter concludes by sketching some of the important fields of application.

The second chapter is concerned with the relative merits of scanning and wide beam X-ray topography. A description of the technique of wide beam topography using the Kβ line is given and it is demonstrated that the resolution is as

good as that using Lang's scanning technique. A new wide beam method using the tungsten La_1 line is proposed and demonstrated. From expressions derived for the exposure times, it is seen that the important parameter to maximise is the power per unit horizontal length of the X-ray source. The speeds of the two techniques are compared for a variety of generators and the advantage of using an Elliott GX6 is made clear.

A direct imaging system is clearly preferable in principle to film recording and Chapter III is devoted to a discussion of such systems. Following a review of previously developed imaging systems, a new method of directly displaying X-ray images using a channel plate is demonstrated. The remainder of the chapter gives detailed calculations of the efficiency of a channel plate to X-rays in the wavelength region 0.5 - 2 Å. Using published data, the efficiency is calculated for several cases and compared with previous experimental work. To better than an order of magnitude, these efficiencies may be used to predict the intensity of the image produced on the image converter screen.

Chapter IV falls into two sections. The first describes an experiment to determine the minimum thickness at which dislocations are visible in crystals using normal topographic techniques. It was found that the value was dependent on the fraction of the material thickness taken up by mis-oriented material. This explanation was found to be in qualitative agreement with experiment, the minimum thickness fell from 0.4 of an extinction distance for the low order

reflections to 0.2 of an extinction distance for high order reflections. The second part consists of a comparison between experimental image profiles and those simulated on a computer. Quite reasonable agreement was found and the sources of error in the method of computing and ways to avoid them are discussed in terms of practical and basic limitations.

The remainder of this thesis describes application of X-ray topography to four different types of material. Chapter V is devoted to a study of defects in a silicon slice following device fabrication. Interest in the effect of crystallographic defects on the performance of integrated circuit devices has led to a large number of investigations over the last decade and these are reviewed and their conclusions summarised. An attempt is made to measure the stress at the junction edge, produced by the mismatch in the ionic radii between dopant and matrix. As a result of approximations in the theory and measurements, the force per unit length of junction, measured to be 2×10^4 dynes/cm, must be taken as order of magnitude only. Similarly, only an order of magnitude estimate of the stress is permissible. There follows a description of a combined Scanning Electron Microscope and X-ray topographic experiment to determine the cause of breakdown fingers, sometimes seen at the junction edges in the beam induced conductivity mode in the S.E.M. It is concluded that they are due to scratches in the oxide mask prior to diffusion. The rest of the chapter is given to a detailed description of dislocations and their contrast observed in a silicon slice heavily doped with boron. The

slip behaviour is not analysed in detail, but seems to support the conclusion that this deformation, due to thermal shock, is independent of the doping. Interactions between 'emitter edge' dislocations are described and the anomalously narrow image widths of such dislocations explained by considering the effects of overlapping strain fields. Burgers vectors of dislocations inside the diffused regions are determined, and the contrast of these dislocations at high density is interpreted as an effect due to overlapping images. Interactions between the 'inside' and 'emitter edge' dislocations are described. In regions where the dislocation density was low, the dislocations exhibited a reversal of contrast on reversal of the diffraction vector. With the diffraction vector parallel to the dislocation line, the contrast was black-white, reversing with the diffraction vector. With the diffraction vector at 60° to the line, the contrast was either black or white, reversing with the diffraction vector. This effect is interpreted in terms of surface relaxation and computations performed using the Penning-Polder theory are in qualitative agreement with the experimental results.

Chapter VI describes the application of X-ray topography to the study of defects in natural fluorite. Dislocations are identified with Burgers vectors parallel to $\langle 101 \rangle$ directions. These are nearly pure edge in character and the Burgers vector is presumed to be $\frac{1}{2}\langle 101 \rangle$. A direct correspondence is observed between bundles of dislocations and regions of birefringence contrast. A uniform birefringence

contrast in the matrix, which can not be explained in terms of dislocation stress, is also observed. This is explained in terms of impurity atoms, sited between $\{111\}$ planes during growth, distorting the crystal normal to the $\{111\}$ faces. The boundaries between regions of birefringence lie along inclined $\langle 110 \rangle$ directions and on this model, no strain is associated with these boundaries, in agreement with the X-ray topographic evidence. Extensive planar faults, lying on $\{111\}$ planes and with fault vector a non integral value of the lattice spacing, are postulated to be thin lamellae of material containing markedly different impurity concentration.

In Chapter VII, some vapour grown layer compounds are studied. Individual dislocations are resolved in $SnSe_2$, $TiSe_2$, SnS_2, TiS_2, ZrS_2 and HfS_2. The Burgers vectors of the dislocations in SnS_2 were determined and their origins discussed. Large area stacking faults bounded by $\frac{1}{3}\langle 1\bar{1}00 \rangle$ partial dislocations are also observed in these specimens. Dislocation and defect configurations in the other compounds are described and a modified divergent beam method for taking topographs of bent crystals is demonstrated.

Some preliminary experiments on pure iron are described in Chapter VIII. Contrast is observed suggestive of dislocation helices and rows of loops in these strain-anneal grown crystals. Arrays of dislocations of pure edge type and Burgers vector parallel to $[100]$ are interpreted as being contained in a low angle boundary wall, following Futagami. The tilt angle across such boundaries is measured to be a few seconds of arc.

Finally, Chapter IX suggests a few directions for further investigation.

NOMENCLATURE

Unless otherwise stated, the following convention has been adopted:

λ	X-ray wavelength
θ_B	Bragg Angle
ξ_g	Extinction distance
g	Reciprocal lattice vector
μ	Linear absorption coefficient
t	Crystal Thickness
b	Burgers vector
u	Direction of dislocation line

CONTENTS

Chapter I	X-ray Topography; Techniques, Images and Applications. A General Survey	1
Chapter II	Rapid High Resolution X-ray Topography; Fat or Thin Beams?	24
Chapter III	Direct Display Techniques	45
Chapter IV	Contrast of Images in Thin Crystals	77
Chapter V	X-ray Topographic Study of Defects in Silicon following Device Fabrication	103
Chapter VI	Study of Defects in Natural Fluorite	131
Chapter VII	Study of Vapour Grown Layer Compounds by X-ray Topography	148
Chapter VIII	Preliminary X-ray Studies of Iron Single Crystals grown by the Strain Anneal Method	167
Chapter IX	Suggestions for Further Work	174
Appendices:		
	Appendix A	178
	Appendix B	182
References	.....	184

C H A P T E R I

X-RAY TOPOGRAPHY; TECHNIQUES, IMAGES AND APPLICATIONS. A GENERAL SURVEY

1. Introduction

In the light of three recent, masterley reviews, it is perhaps almost impertinent to attempt a survey of the literature in the field of X-ray diffraction topography. Two of these papers are transcripts of the proceedings of the International Summer Course in Material Science held at the University of Antwerp, Belgium in 1969. A review of techniques and applications with a host of references was presented by Dr. A.R. Lang and a review of image contrast was presented by Professor A. Authier. Those articles may be found in the conference proceedings, (Lang, 1970; Authier, 1970(a)) and the reader is thoroughly recommended to them. An exposition of the theory of dynamical X-ray diffraction in a form relevant to X-ray topography has also been published recently and is well worth detailed study, (Authier, 1970(b)). Two other review papers, one on techniques, (Bonse, Hart and Newkirk, 1967) and the other on dynamical theory, (Batterman and Cole, 1964) are also recommended.

Inevitably, the review contained in this chapter will fail to do justice to some works, but it is hoped that it will serve to indicate the flexibility and applicability of X-ray techniques to single crystal systems. It is a pity that, despite the exhortations of Dr. Lang, X-ray topography is still not widely accepted as a routine to be used with other

FIG 1.1

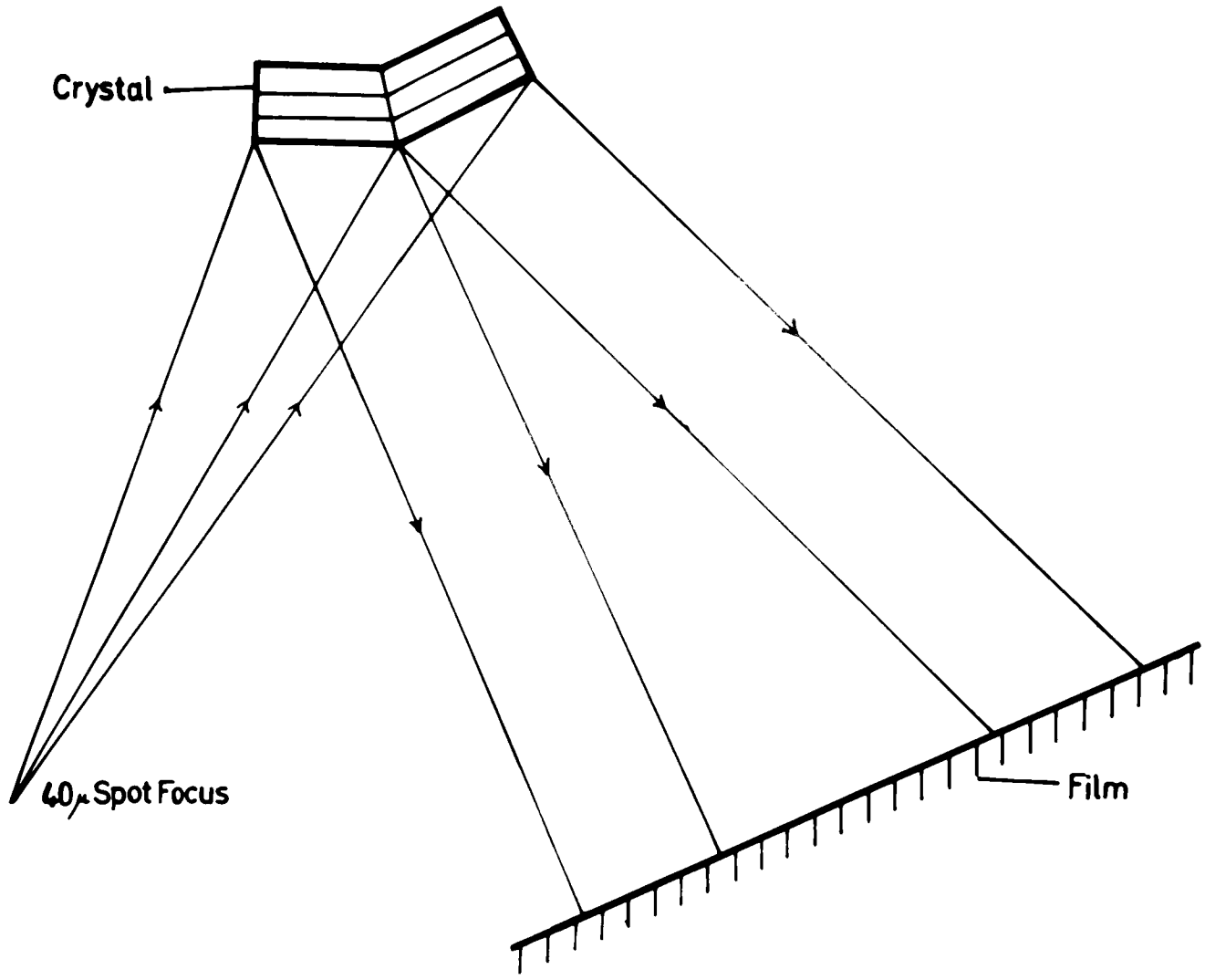
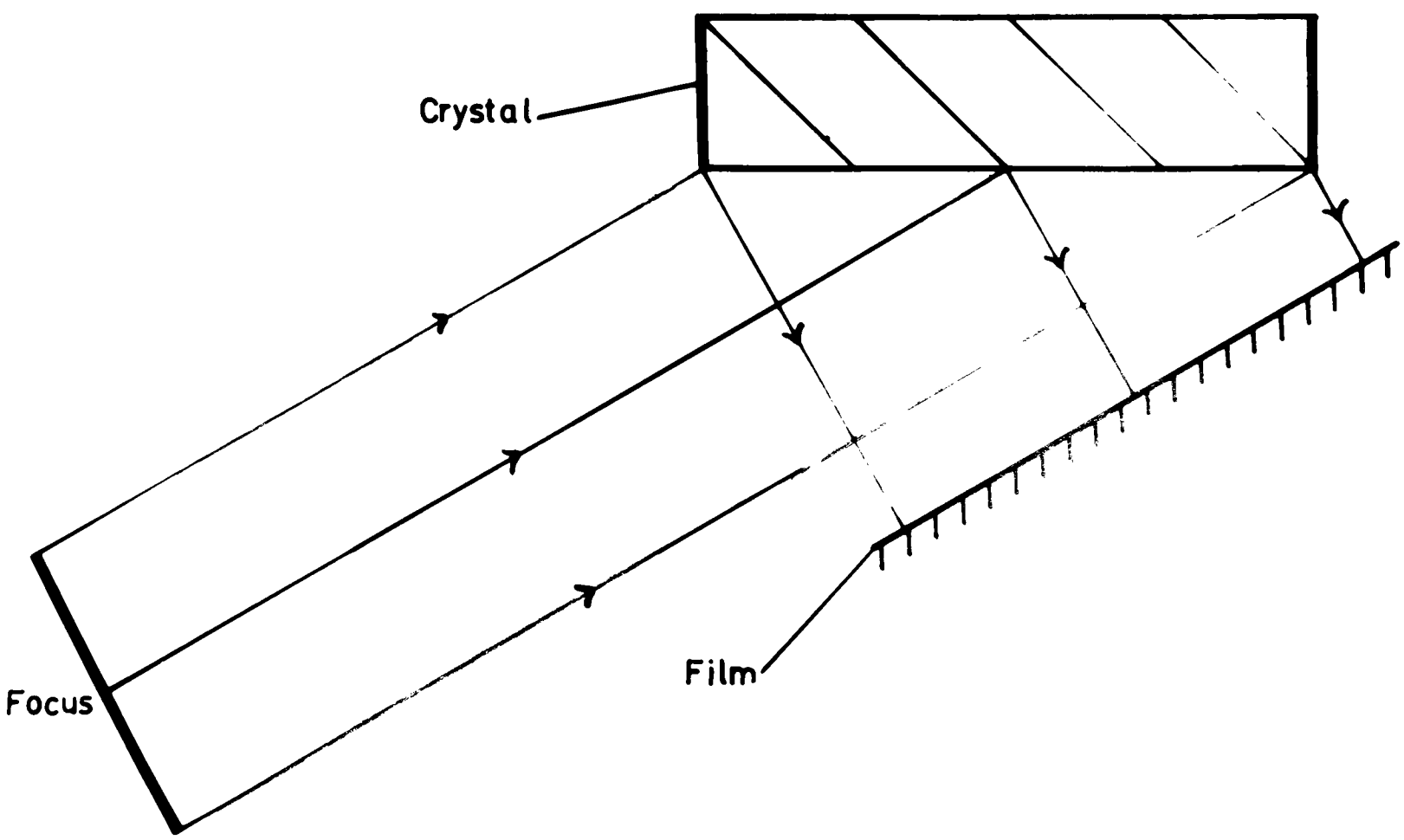


FIG 1.2



techniques as a matter of course. As is shown in Chapter V, the application of two techniques to the same specimen, each measuring different properties, can have extremely rewarding consequences. Even if conditions are such that little information is obtainable from the X-ray topographs, in conjunction with other measurements, it may have a far greater significance than when standing alone.

2. Techniques of X-ray Topography

Methods of X-ray topography, both in transmission and reflection, may conveniently be classified into two groups:

(a) Those that detect gross misorientations which are large compared with the angular divergence of the beam-termed "orientation" contrast;

(b) Those that detect point-to-point variations in lattice perfection by different scattering power-termed "extinction" contrast.

Table 1.1 lists the main features of the most common types of X-ray topography. Several techniques are discussed in detail below, to explain the geometry and illustrate the principles.

Schulz Method

This is shown schematically in Fig. 1.1. White radiation from a point focus is reflected from the surface of the specimen. While there is no significant change in intensity in the X-rays

Table 1.1

Radiation Employed in Imaging	Transmission or Reflection	Method
Continuous	R	Line focus
Continuous	R	Micro focus
Continuous	T	Micro focus
Characteristic	R	Line focus - specimen close to film
Characteristic	R	Point focus - specimen and film rocked together
Characteristic	R	Highly Collimated Beam - Specimen and film translated together
Characteristic	R	Collimated Beam - specimen and film translated
Characteristic	R	Double crystal - high sensitivity to misorientation
Characteristic	T	Double crystal - low sensitivity
Characteristic	T	Anomalous Transmission
Characteristic	T	Collimated Beam - specimen and film translated together
Characteristic	T	Line focus - Only one characteristic line reflected in Monochromator
Characteristic	T	Curved crystal Collimator Crystal and Film Oscillated
Characteristic	T	Line focus - oscillating Soller Slits

Type of Contrast	Resolution	Workers
Extinction	25 μm	Ramachandran (1944)
Orientation (and Extinction)	<25 μm	Schulz (1954)
Orientation (and Extinction)		Fujiwara (1964), Piermans (1964)
Orientation and Extinction	1 μm	Berg (1931), Barrett (1945) Newkirk (1958,1959)
Extinction	-	Wooster and Wooster (1945)
Orientation and Extinction	-	Merlini and Guinier (1957)
Orientation and Extinction	1 μm	Lang (1957(b)) Schiller (1964)
Orientation	1 μm	Bonse (1965), Hart (1968)
Extinction	1 μm	Kohra et al. (1970)
Orientation and Extinction	30 μm ~5 μm	Barth and Hoseman (1958) Gerold and Meier (1959)
Orientation and Extinction	1 μm	Lang (1957(a), 1959(a), 1959(b))
Extinction	1 μm	Hosoya (1968) Dionne (1967)
Extinction	1 μm	Kohra and Takano (1968)
Orientation and Extinction	~1 μm	Oki and Futagami (1969)

reflected from the misoriented region, there is an angular separation which causes gaps or overlaps in the image. By placing the film a large distance, up to 40 cm, from the specimen, individual dislocations in nearly perfect crystals may be detected, (Schulz, 1954).

Berg-Barrett

This arrangement is shown in Fig. 1.2. Characteristic X-rays from a line source are reflected from the surface of the crystal. Reflecting planes are usually chosen so that the diffracted beam is nearly normal to the crystal face and then the film may be placed very close to the crystal surface. This prevents loss of resolution due to separation of the $K\alpha_1\alpha_2$ doublet, as the crystal and film are so close that the images have no room to separate, (Newkirk, 1958; 1959).

Gerold and Meier - Anomalous Transmission

This arrangement is shown in Fig. 1.3. As may be seen from the dynamical theory, (von Laue, 1949), at the Bragg position X-rays propagate in a crystal in two Bloch waves, one with nodes at the atoms and one with anti-nodes at the atoms. This effect leads to the phenomenon of anomalous transmission, (Borrmann, 1941), as one Bloch wave is transmitted better than the other. In a very thick crystal only one Bloch wave will reach the exit surface, but due to this anomalous transmission effect, appreciable intensity is detected even for $\mu t = 10$. A dislocation interferes with this propagation and a shadow is cast. The loss of energy occurs in both direct and

FIG 1.3

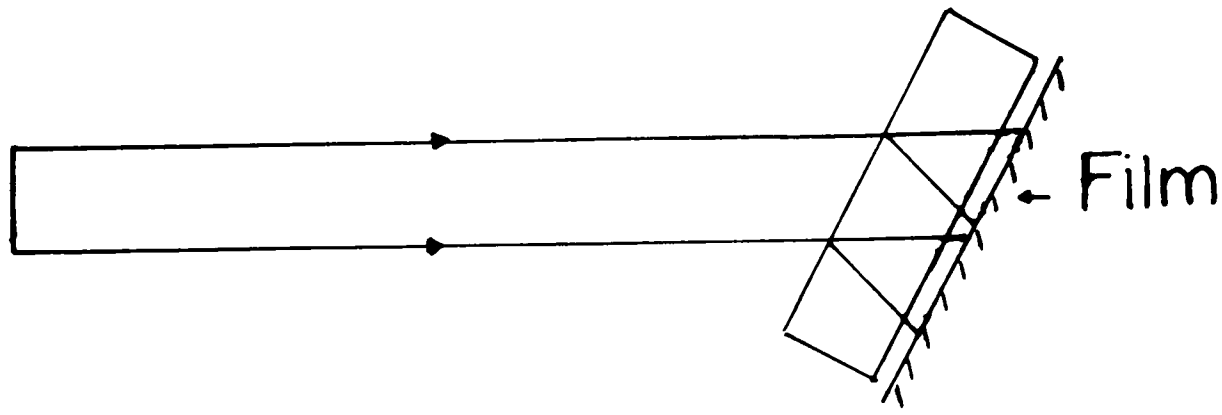


FIG 1.4

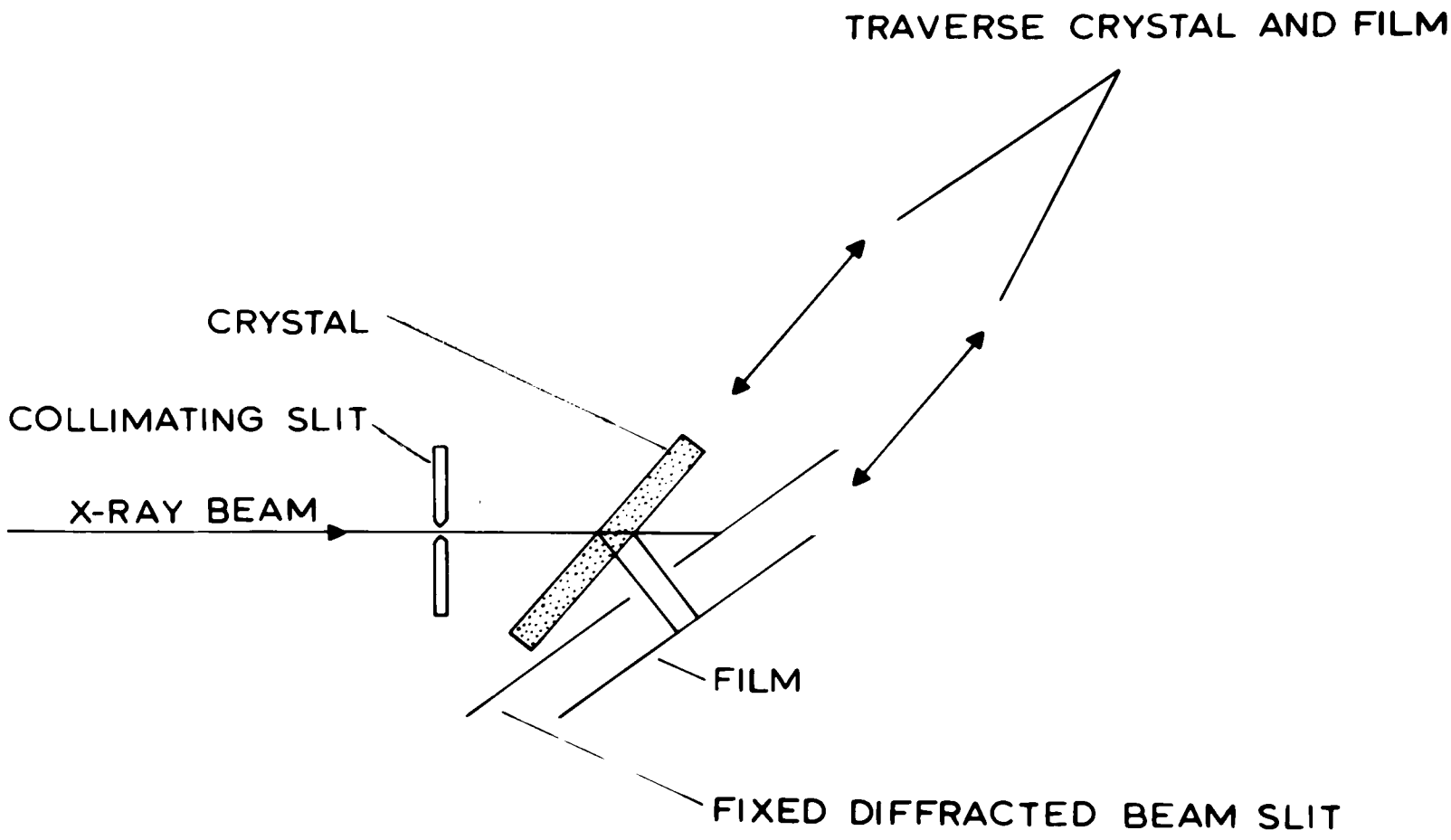
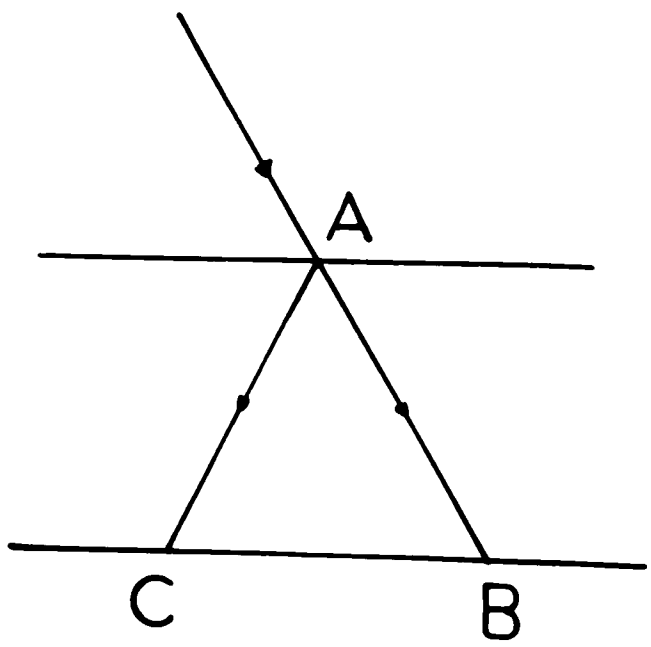


FIG 1.5



diffracted beams and if the film is placed close to the specimen exit surface, high resolution topographs may be obtained, (Gerold and Meier, 1959).

Lang Technique

Figure 1.4 shows schematically the apparatus used in Lang's technique. The X-ray beam from a point focus is highly collimated to prevent simultaneous reflection from the $K\alpha_1$ and $K\alpha_2$ lines. In order to view the entire specimen, the crystal and film are translated together across the beam, (Lang 1959(a); 1959(b)). The topographs taken with the arrangement stationary are termed "section" topographs, as opposed to the "projection" topograph described, and provided that the source width is small compared with the length of the base BC of the Borrmann triangle shown in Fig. 1.5, important information as to the direction of energy flow and the position of defects in the crystal may be obtained, (Lang, 1957(a)).

By reducing the width of the fixed diffraction slit between crystal and film to less than the width of the diffracted beam, it is possible to restrict the intensity received to only certain parts of the crystal. This method of limited projection topography has been used successfully to remove contrast due to crystal surfaces, (Lang, 1963; Caslavsky, 1970; Caslavsky and Suri, 1970).

Wide Beam Topography

This method, which combines the resolution of Lang's technique with simplicity of design, is shown in Fig. 1.6.

FIG 1.6

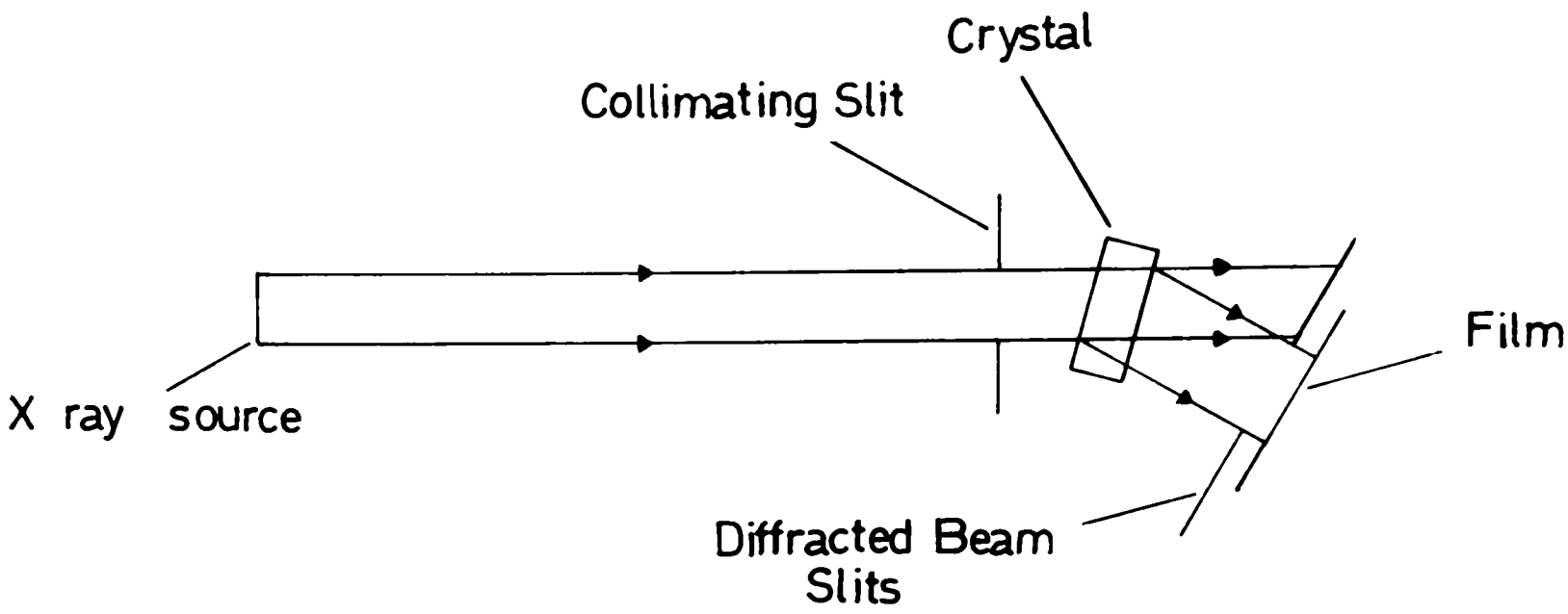
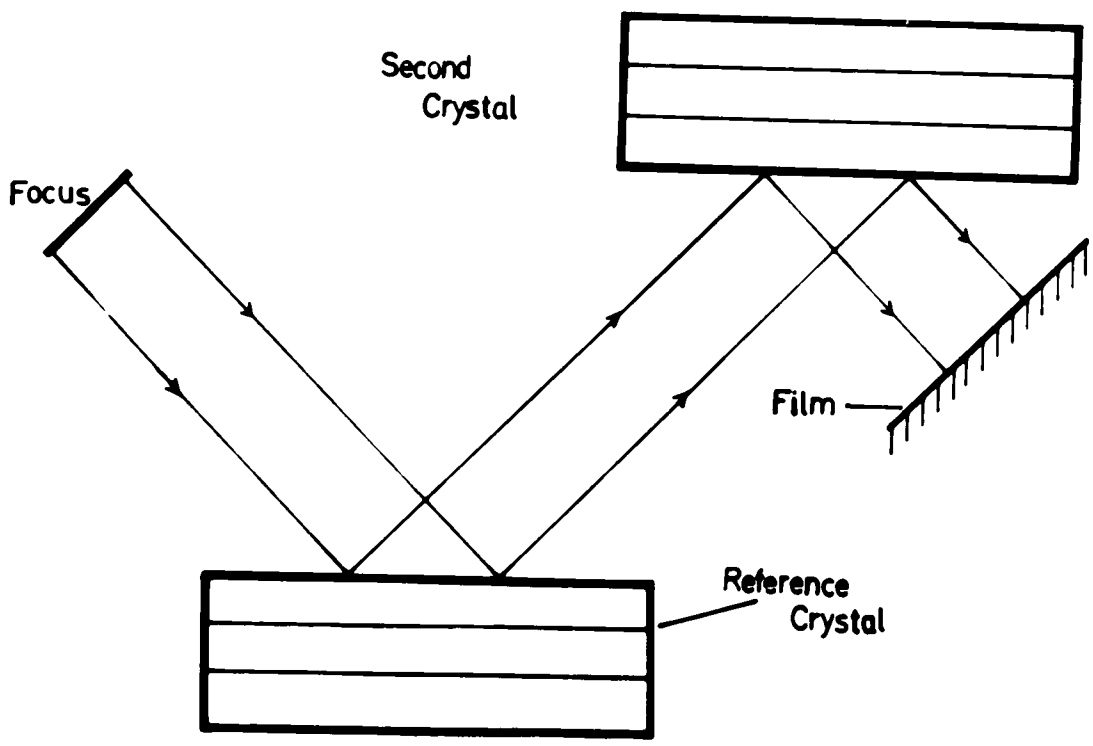

Crystal
Collimating Slit
Film
X ray source
Diffracted Beam
Slits

FIG 1.7


Second
Crystal
Focus
Film
Reference
Crystal

Radiation from a line focus is allowed to fall on the crystal and the diffracted beam is detected. It is essential that only one characteristic line be diffracted, and methods of monochromatisation include use of an Ru filter to remove the $AgK\alpha_1$ line from the AgKα doublet, (Hosoya, 1968), use of the Kβ lines, (Dionne, 1967), and use of an oscillating Soller slit to restrict the beam divergence, (Oki and Futagami, 1969).

Double Crystal Techniques

The highly sensitive double crystal technique is shown in Fig. 1.7. The reference crystal and the specimen consist of the same material cut so that the interplanar spacing of both crystals is equal. X-rays from a line source are successively reflected from the reference crystal and specimen, and recorded on film. The shape of the rocking curve is extremely narrow, dispersion is eliminated and strains of the order of 10^{-8} to 10^{-9} may be detected. This technique has been used to study the misorientation around a dislocation line, (Bonse, 1962), and to study impurity bands, (Bonse, 1965; Hart, 1968). The transmission arrangement has been demonstrated by Kohra and coworkers, (Kohra et al., 1962).

Recently Kohra, Hashizume and Yoshimura (1970) have shown that the (+,+) and non parallel (+,-) settings are not so highly sensitive to misorientation and such a double crystal technique has similar properties to Lang's technique.

Ultra-Sensitive Techniques

1. Triple Crystal Spectrometer

The sensitivity of the parallel setting is further exploited

by reflection from three crystals successively. This highly sensitive technique has been used to measure the normal and anomalous absorption coefficients of silicon, (Lefeld-Sosnowska, 1964).

2. X-ray Moiré Topography

Analogously to the optical case, if X-rays pass through successive lattices of reciprocal lattice vectors g_1 and g_2, a Moiré pattern of spacing, D, such that

$$\frac{1}{D} = \underline{G} = \underline{g}_1 - \underline{g}_2 \qquad (1.1)$$

is observed. As one can measure very large values of D from the X-ray topographs, the method is sensitive to relative differences in lattice spacing of the order of 10^{-7} to 10^{-8} and to angular rotations of 10^{-7} to 10^{-8} radians. Two methods have been developed. In the X-ray interferometer, (Bonse and Hart, 1965), a single block of single crystal silicon is cut so as to split and then recombine the diffracted beams. The transmission is dependent on the positions of the nodes and anti-nodes of the stationary wave pattern with respect to the lattice of the combining crystal and any phase change in one of the separated diffracted beams may be detected. Applications for this elegant and sensitive device have been discussed by the inventors, (Bonse and Hart, 1965(a),(b); 1966(a),(b); 1968).

The second method of Bràdler and Lang, (1968), is to superimpose two separate crystal plates. Lang has devised a method of orientating specimens to within a second of arc and

the application of this technique to the study of quartz has been demonstrated, (Lang, 1968).

X-ray Moiré fringes may also be observed in the superposition of nearly parallel platelets of vapour grown CdS, (Chi kawa, 1965(a); 1967).

3. Experimental and Photographic Procedures

The factors influencing the resolution and quality of X-ray topographs have been elucidated by Lang (1970) and as his experimental routine has been followed, only a brief tabulation is included. This may be found in Appendix B; for a more detailed discussion, see section 4 of the above reference.

4. Contrast of Images in X-ray Topography

As has been previously stated, two types of contrast may be described, namely the orientation contrast, due to gross misorientations and extinction contrast, which arises from point to point variations in the lattice perfection. The former needs little further discussion, as it is clear that a gross misorientation will reflect in a different direction to the matrix. Lattice imperfections show contrast due to differing reflecting power, and it is of importance to study the causes in depth.

Types of images observed in X-ray topographs may be broadly classified into three main types :-

(a) Direct images - intensity greater than background;

(b) Dynamical images - intensity usually less than background;

(c) Intermediary images - often oscillating contrast.

It is convenient in this context to split the dynamical images into two sub-sections :-

1) Tie point jumping images - found in highly distorted regions;

2) Tie point migration images - found in lightly distorted regions.

Usually, in the formation of dynamical images, both effects are important. Before discussing these various kinds of image, it is important that the propagation of the X-rays in a perfect crystal should be studied. The thickness of the crystals used is usually such that to explain the observed contrast, it is essential to use a dynamical theory in which the constant interchange of energy between direct and diffracted beams is considered. The situation where the crystal is so thin that kinematical conditions are relevant is studied in Chapter 4.

(a) Dynamical Theory in a Perfect Crystal

As X-rays are electromagnetic waves, their propagation is described by Maxwell's Equations. In a periodic medium, these may be expressed in the form, (Zachariasen, 1945),

$$\nabla_{\wedge} \left[\nabla_{\wedge} (1 - \chi) \underline{D} \right] = - \frac{1}{c^2} \frac{\partial^2}{\partial t^2} \underline{D} \qquad (1.2)$$

where $\underline{D}$ is the electric displacement vector,

c is the velocity of light,

and χ is the dielectric susceptibility.

As the medium is periodic, χ will also have the periodicity of the crystal lattice, and may be written in a Fourier expansion

$$\chi = \sum_{H} \chi_{H} e^{-2\pi i \underline{H}\cdot\underline{r}} \qquad (1.3)$$

χ_H may also be expressed in terms of the structure factor F_H :

$$\chi_{H} = \frac{r_o \lambda^2 F_H}{\pi V_L} \qquad (1.4)$$

where r_o is the classical electron radius,

λ is the wavelength,

and V_L is the volume of the unit cell.

We require solutions which are also periodic, thus we look for solutions $\underline{D}_H$ where :

$$\underline{D} = \sum_{H} \underline{D}_{H} e^{-2\pi i.\underline{K}_H\cdot\underline{r}} \qquad (1.5)$$

where

$$\underline{K}_H = \underline{K}_o + \underline{H} \qquad (1.6)$$

and $\underline{K}_o$ is the wave vector inside the crystal

and $\underline{H}$ a reciprocal lattice vector.

The vacuum wave vector is $\underline{K}$.

Substitution of equations (1.5) and (1.4) into (1.2) yields:

$$\sum_{L} \left\{ \chi_{H-L} \, (\underline{K}_H \cdot \underline{D}_L) \, \underline{K}_H - \chi_{H-L} \, \underline{K}_H^2 \, \underline{D}_L \right\} = (K^2 - K_H^2) \, \underline{D}_H \qquad (1.7)$$

These are the fundamental equations of the dynamical theory in a perfect crystal. In the X-ray case, it is usually satisfactory to consider only one reciprocal lattice point.

Then, these equations reduce to :-

$$\chi_H (\underline{K}_H \cdot \underline{D}_o) \underline{K}_H - \chi_H (K_H)^2 \, D_o = [\, |K|^2 - |K_H|^2 (1 - \chi_o)\,] \, \underline{D}_H$$

$$\chi_{\bar{H}} (\underline{K}_o \cdot \underline{D}_H) \underline{K}_o - \chi_{\bar{H}} \, |K_o|^2 \, \underline{D}_H = [\, |K|^2 - |K_o|^2 (1 - \chi_o)\,] \, \underline{D}_o \qquad (1.8)$$

Taking the scalar product of the first equation with $\underline{D}_H$ and the second with $\underline{D}_o$ leads to :-

$$\begin{aligned} (2\,\delta_o - \chi_o)\, D_o - \chi_{\bar{H}}\, P \cdot D_H &= 0 \\ -\,\chi_H\, P \cdot D_o + (2\,\delta_H - \chi_o)\, D_H &= 0 \end{aligned} \qquad (1.9)$$

where $$P = \frac{\underline{D}_o \cdot \underline{D}_H}{|D_o| \, |D_H|}$$

and $(1 + \delta_H)$ and $(1 + \delta_o)$ are the refractive indices of the two waves D_o and D_H.

For a non trivial solution the determinant of equations (1.9) must vanish.

This yields :-

$$(2\delta_o - \chi_o)(2\delta_H - \chi_o) = \chi_H \chi_{\bar{H}} P^2 \qquad (1.10)$$

or $$\zeta_o \zeta_H = \tfrac{1}{4} K^2 \chi_H \chi_{\bar{H}} P^2$$

where $$\zeta_o = K_o - K(1 + \tfrac{1}{2} \chi_o)$$

and $$\zeta_H = K_H - K(1 + \tfrac{1}{2} \chi_o).$$

If only one wave exists, i.e., $D_H = 0$, then the locus of the wave vector $\underline{K}_o$ is a sphere centred at O in reciprocal space, of radius $K(1 + \frac{1}{2} \chi_o)$. If the two waves are excited, the locus is determined by equation (1.10) and is called the dispersion surface. The point defined by the vectors $\underline{K}_o$ and $\underline{K}_H$ on this surface is called the tie point. The dispersion surface is a hyperboloid and its intersection with the plane containing O and H is a hyperbola, whose asymptotes are tangents to the circles about O and H with radius $K(1 + \frac{1}{2} \chi_o)$, Fig. 1.8.

It is seen that the dispersion surface has two branches for each direction of polarisation, making four in all, for the case considered here. In the symmetrical case, the minimum separation of the dispersion surface branches is given by the reciprocal of the extinction distance; and is equal to $\sec\theta\, |K|\, (\chi_H \chi_{\bar{H}})^{\frac{1}{2}} P$. It should also be noted that the diameter of the dispersion surfaces is about 10^{-6} times that of the spheres, and it is usual to replace the spheres by their tangents. The pair of tie points excited by a plane wave may be determined by geometrical construction. A necessary requirement is that the wave vector tangential to the crystal

FIG 1.8

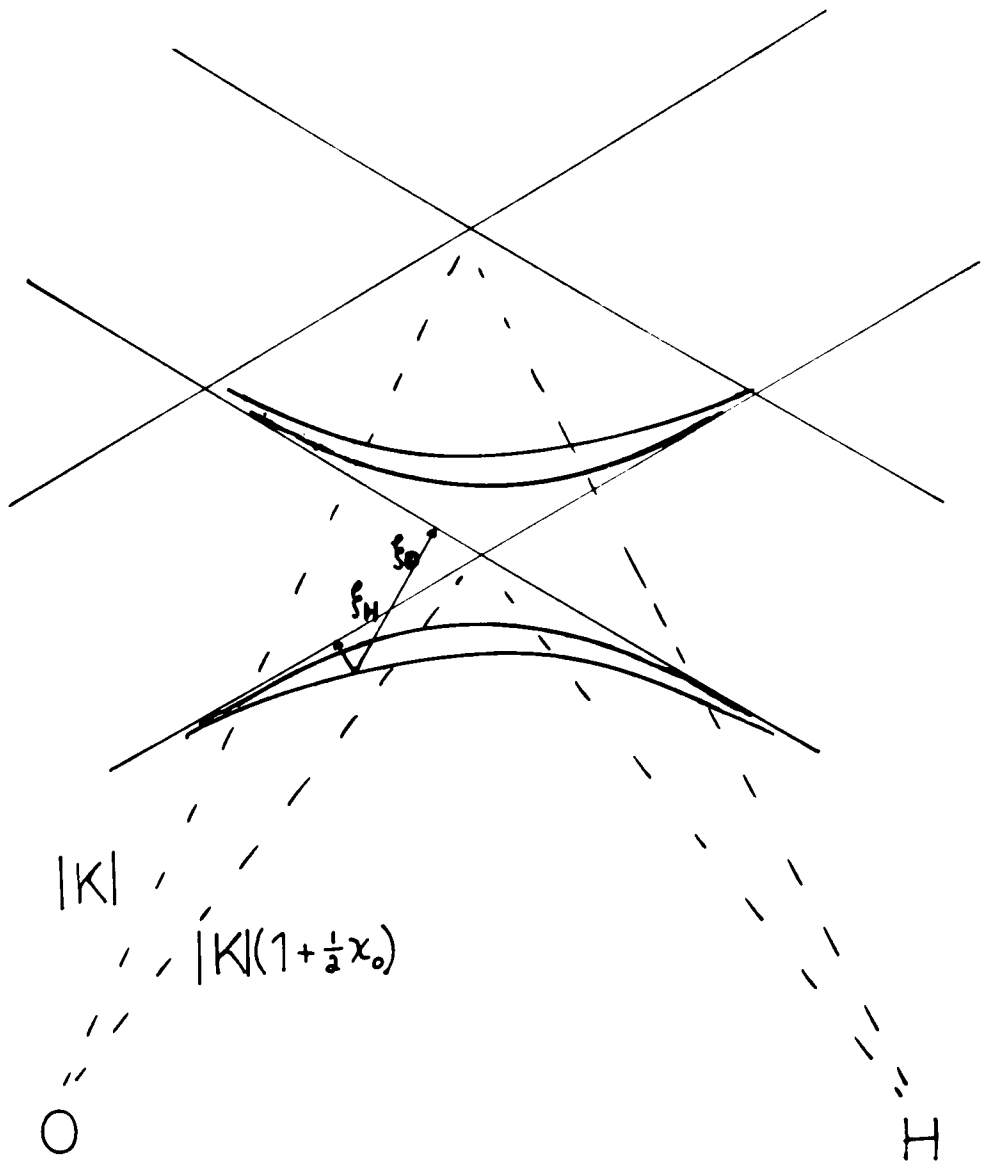
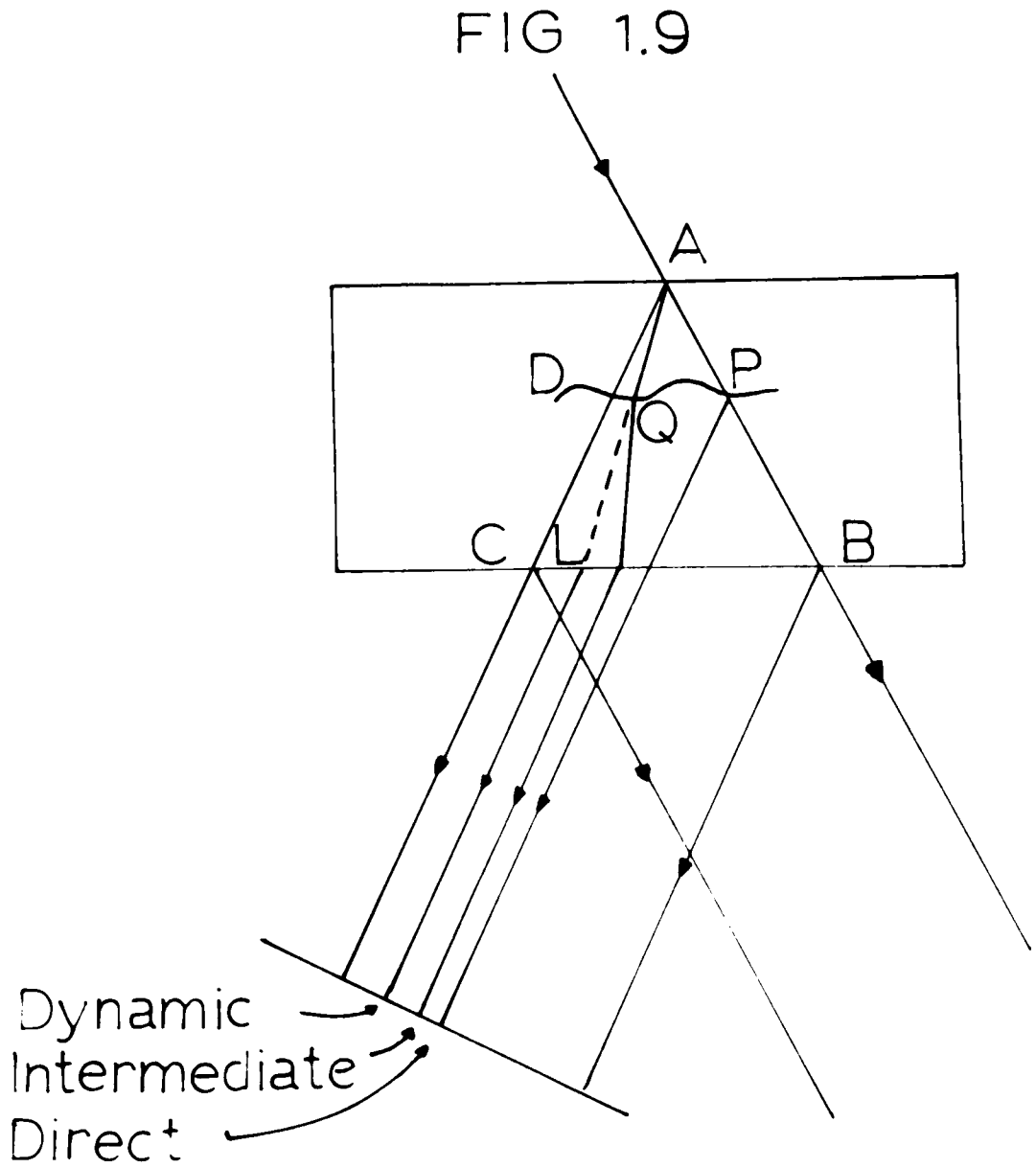


FIG 1.9



surface is continuous, and this is satisfied if the ends of the crystal wave vectors and the incident wave vector lie on the normal to the crystal surface.

The Bloch wave field associated with each tie point propagates in a direction normal to the dispersion surface. When absorption is included by making both wave vectors and susceptibility complex, it is usually found that wave fields associated with Branch 1, the upper branch, have a much lower absorption coefficient than those on Branch 2. This leads to the phenomenon of anomalous transmission, [Borrmann, 1941; 1950]. For Branch 1, the nodes of the electric field lie on the reflecting plane and absorption is very small. For Branch 2, the antinodes lie on the reflecting plane and absorption is very high. The directions of propagation of the two wave fields are in general different. Authier, Balibar and Epelboin (1970) have shown that under incident plane wave conditions, where the Branch 1 and Branch 2 wave fields are separated in space, a defect which interfered directly with the propagation of one wave field only, caused no disturbance in the other wave field. The wave fields thus propagate independently.

In general, the incident wave front must be considered to be spherical in shape, and while this may be considered as a sum of plane waves, the relative phases between components must be retained. In section topographs with a highly divergent beam, all tie points across the dispersion surface are excited. For each polarisation, two wave fields, associated with both branches of the dispersion surface, will propagate in any direction. The interference of these two wave fields leads

to the spherical wave fringes observed in section topographs. In a wedge-shaped crystal, hyperbolic fringes are observed, (Kato and Lang, 1959). These, and related phenomena, in perfect crystals are well understood in terms of the spherical wave theory of Kato, (1960; 1961(a),(b); 1963(a),(b)). Considerable work has also been done on the behaviour of these Pendellosung fringes in slightly distorted crystals in terms of an extension of Kato's spherical wave theory, (Kato and Ando, 1966a,b; Kato, 1963c,d; 1964(a),(b); Kato and Patel, 1968; Patel and Kato, 1968).

Contrast from planar defects arises in a similar manner to that in the electron case. On crossing the fault, each wave field creates two new wave fields. These two wave fields interfere with one another and result in interference fringes being observed. The contrast of faults in section topographs has been extensively treated by Authier and co-workers, (Authier, 1968; Zarka, 1969; Authier and Sauvage, 1966), and by Kato, Usami and Katagawa, (1967). The extension to projection topographs is relatively straightforward.

(b) Dynamical Diffraction in a Highly Distorted Crystal

The origin of the three types of image mentioned previously may be seen by reference to Fig. 1.9, due to Authier, (1967). A narrow pencil of X-rays is incident on the crystal at A. Consider the effect of a large distortion, e.g., a dislocation, on the propagation of X-rays within the "Borrmann fan" ABC. The dislocation cuts the direct beam at P. Around the dislocation, the lattice planes are bent and rays not exactly satisfying

the Bragg condition in the perfect crystal are reflected. These rays are not near enough to the Bragg condition in the perfect crystal to set up wave fields propagating in the Borrmann fan, and thus simply undergo normal attenuation. As is shown in Chapter 4, this leads to a net increase in intensity around the defect, thus forming the "direct image" by "extinction contrast".

Where the dislocation cuts the Borrmann fan, dynamical and intermediate images are formed. Consider the dislocation at Q, cutting a wave-field propagating in the direction AQ. In distorted regions, the wave fields cannot propagate unchanged. In the lightly deformed region, the tie points remain on the same branch of the dispersion surface but migrate along it in a direction dependent on the sense of the deformation. However, in highly distorted regions interbranch scattering occurs, that is, each wave field excites another wave field on the opposite branch of the dispersion surface, Fig. 1.10. The new wave fields propagate along directions such as QM, and interfere with the original wave fields propagating in this direction. These interference fringes give rise to the intermediary image.

As may be seen in Fig. 1.10, the creation of the new wave fields results in a loss of energy from the original wave fields. This loss causes the dynamical image and the dislocation effectively casts a shadow. There are two circumstances in which dynamical images are readily observable in traverse topographs :

1. $\mu t \gg 1$ where the direct image ceases to be visible due

FIG 1.10

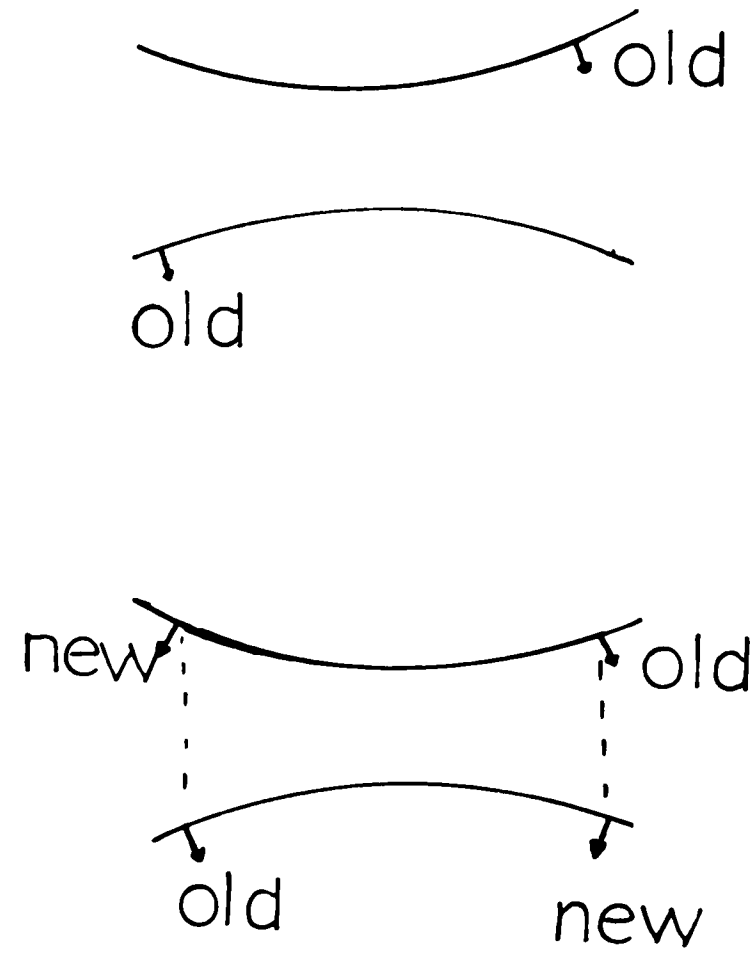
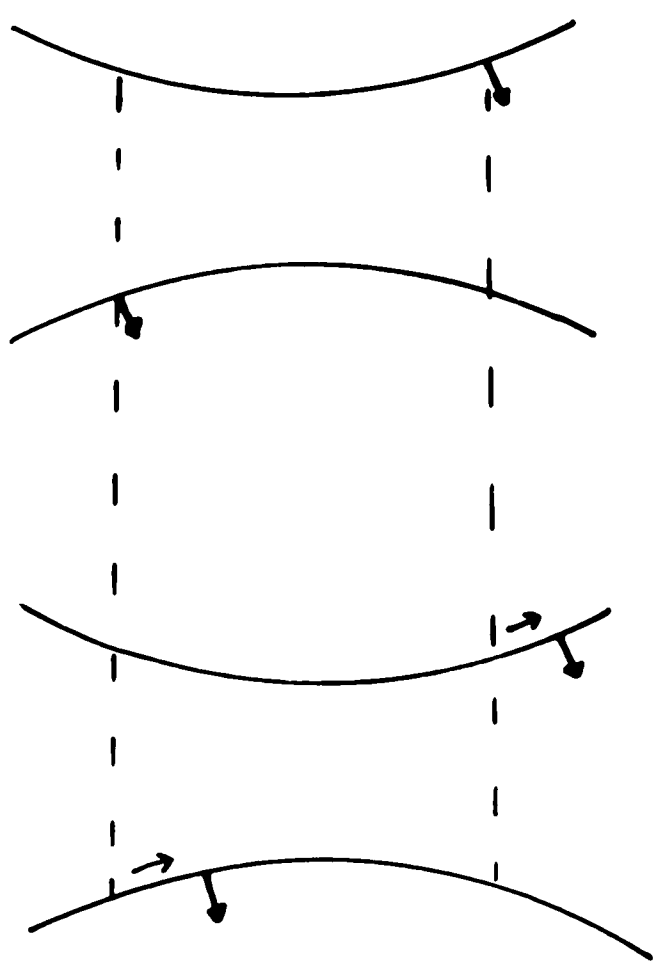


FIG 1.11



to absorption. Due to the effect of anomalous transmission mentioned earlier, one finds that Branch 1 wave fields exist even for very thick crystals and dynamical images may be formed from these, (Borrmann Topography).

2. $\mu t \ll 1$. Due to the margin enhancement, which arises due to the greater density of wave fields close to the extremities of the Borrmann fan than in the centre, the dynamical image becomes narrow and if the dislocation lies at right angles to the crystal surface and also the g vector, dynamical images are visible. This latter case is demonstrated in Chapter IV.

The last type of image, the tie point migration image, is often classified as a dynamical image, but due to the interest in this type of image in Chapter V, it is felt that in this context, a separate comment on it's formation is justified. In slightly distorted material, the tie points migrate along the respective branches of the dispersion surface, Fig. 1.11, but do not jump to another branch. This modifies the direction of energy flow, and also alters the amplitudes of the plane waves excited by each wave field on emergence from the crystal. Theories treating tie point migration have been developed by Penning and Polder, (1961) and Kato, and show that the X-rays effectively propagate along curved paths. The theory is only applicable for lightly distorted crystals, and is not applicable near the dislocation core. Hart (1963) has, however, shown that in particular circumstances, the broad tie point migration images may be

observed in regions up to 100 μm from the dislocation core.

In analysis of defects by X-ray topography it is thus important to consider the mechanism of image formation which may be quite complex.

5. Applications of X-ray Topography

The major application of X-ray topography is the exploitation of the strain gradient sensitivity in studying dislocation configurations. In general this is performed under conditions of low absorption, though several workers have used very thick crystals and exploited the Borrmann effect. The Burgers vector may be determined, in the same way as in electron microscopy, by studying the image in several reflections. When the projected strain field is zero, the dislocation is invisible. The conditions for this to occur are:

$$\underline{g} \cdot \underline{b} = 0 \qquad \text{and} \qquad \underline{g} \cdot \underline{b} \wedge \underline{u} = 0 \, .$$

From this, the direction of the Burgers vector may be determined, though not the sense nor magnitude. Several techniques, relying on the asymmetry of the image in special circumstances, have been devised to measure the sense of the Burgers vector, (Lang, 1965; Chi kawa 1964(a),(b); Hart and Lang, 1963; Hart, 1963; Bonse, 1962).

Five broad headings will be given as a guide to the fields of application of X-ray topography :-

a) Studies of metals,

b) Studies of semi-conductors,

c) Studies of minerals,

d) Magnetic studies,

e) Miscellaneous applications!

a) **Metals**

Little work has been done until fairly recently on deformation of metals, simply due to the problems of growing low enough dislocation density material. Owing to the sensitivity to lattice deformation of X-ray topography, the upper limit on dislocation density is about 10^5 lines/cm^2, if individual dislocations are to be resolved. Young and his co-workers have produced some fine studies of *in situ* deformation of copper grown by the Bridgman method, (Young and Sherrill, 1971). Nøst and co-workers have deformed aluminium *in situ*, (Nøst and Nes, 1969; Rustad and Lohne, 1971), but apart from these studies, no step by step deformation work on metals has been done. As crystal growth techniques improve, this deficiency should be rectified. These workers have, however, produced some very fine studies of the grown-in dislocations, the effect of annealing and light deformation, (Young, Savage, 1964; Young, 1965; Bertocci, Bertocci and Young, 1969; Young and Sherrill, 1967a,b; Nøst, 1965; Nøst and Sorensen, 1966; Nes and Nøst, 1966; Nost, Sørensen and Nes, 1967).

Becker and Pegel (1969) deformed molybdenum and observed how helices collapsed on deformation but most topography papers have simply reported the in-grown dislocation arrangements in, for example, γ brass, (Michell *et al.*, 1971; cadmium, (Badrick and Puttick, 1971), aluminium, (Authier, Rodgers and Lang, 1965),

copper, (Clareborough, Michell and Smith, 1967) and iron silicon, (Lang and Polcarova, 1965). An interesting experiment by Fremiot, Baudelet and Champier, (1968), on the effect of the oxide layer on aluminium crystals and the work of Michell and co-workers, (Michell and Ogilvie, 1966; Michell and Smith, 1968), on the effect of the atmosphere on vapour grown cadmium and magnesium, indicates that X-ray topography may have considerable value in this field.

Nittono and co-workers have made some studies on copper whiskers, (Nittono and Nagakura, 1969), and the effects of alloying, (Nittono, Onodera and Nagakura, 1970). The experiments on the deformation of copper whiskers, (Nittono, 1971) are of considerable interest.

b) Semi-conductors

The bulk of the work using X-ray topography has been performed on semi-conducting materials. This stems largely from the fact that, because of their technological importance, considerable effort has been put into the production of perfect single crystals. A further advantage is that silicon and germanium are not plastic at room temperature, making handling easy.

Since the early studies of dislocations in semi-conductors, e.g., (Jenkinson and Lang, 1962), little attention has been paid to the distribution of defects in the as-grown material. Certainly in silicon, enough is known about the crystal growth to regularly produce zero dislocation density material. Interest has been two-fold: firstly in studies of basic phenomena utilising the perfect material and secondly, to

study the effect of diffusion associated with integrated circuit manufacture.

Semi-conducting material was used to study dislocation mobility under stress, (Suzuki et al., 1966; Patel and Freeland, 1970; Kannan and Washburn, 1970). Silicon has been used to study the behaviour of Frank-Read type dislocation sources, (Authier and Lang, 1964; Miltat and Bowen, 1970; Foct, 1968). Germanium was used in the indentation studies of Wagatsuma et al., (1971).

The work on the effect of integrated circuit manufacture on crystal properties, a large amount of which has been performed by Schwuttke and his co-workers, is of great interest and will be referred to in detail in Chapter V. A useful review of the X-ray topographic applications has been published by Meieran (1970). This also reviews the studies of the stress produced by oxide and metal films, another effect of technological importance which has proved amenable to the X-ray method.

Further applications have been to study the buried layer produced by high energy ion implantation, (Bonse and Hart, 1969; Bonse, Hart and Schwuttke, 1969) and the stress produced by local melting in an electron beam, (Carron, 1966; Carron and Walford, 1967; 1968(a,b)).

c) Minerals

Study of dislocations in minerals by electron microscopy is often hampered by the considerable difficulty of thinning these materials. However, the low dislocation densities often

encountered, and the ability to study relatively thick specimens, has meant that X-ray topography has been used quite extensively in studies of natural crystals.

Calcite has been extensively studied and the partial dislocations and their interactions analysed in detail, (Sauvage and Authier, 1965; Authier and Sauvage, 1966; Sauvage, 1968). The phenomenon of elastic twinning has also been studied in these crystals, (Jourdan and Sauvage, 1970).

Magnesite and dolomite have been studied and the defects observed identified, (Zarka, 1969). The dislocations in barite have been studied by X-ray topography and Burgers vectors identified, (Phakey and Aly, 1970). Similarly, natural apatite has shown very low dislocation density and some interesting fault surfaces, (Phakey and Leonard, 1970).

Quartz is undoubtedly the most intensely studied mineral and using X-ray topography, fault surfaces, (Yoshimatsu, 1965), both Brazil and Dauphine twins, (Phakey, 1969; Lang, 1967) and dislocation configurations have been observed. Important, too, are the comparative studies of synthetic quartz, which not only have technological importance in the manufacture of quartz oscillators, but may shed light on the growth mechanisms of natural quartz, (Lang and Muiscov, 1967). Moiré fringes at cracks in quartz plates were observed by Lang and Muiscov (1965).

Quite extensive studies have been performed by Lang and co-workers on the perfection of diamond, (Lawn, Kamiya and Lang, 1965; Lang, 1964). Studies of abraded diamonds, (Frank, Lawn, Lang and Wilks, 1967) led to the development of the theory

used in Chapter V to study strain contrast in diffused windows. Finally, dislocations in muscovite mica have been studied and Burgers vectors determined for both perfect and partial dislocations, (Caslavsky and Vedam, 1970).

d) Magnetic studies

An important application has been in the study of magnetic domains. These may be made visible either by orientation contrast, (Kranjc, 1969a,b), where the domain rotation is large, or by extinction contrast due to the strain associated with the domain wall, (Polcarova and Gemperlova, 1969); when the domain rotation is small. Domains in iron-silicon have been observed using this latter effect by Polcarova and Lang,(1962, 1968) and Wu and Roessler,(1971), in yttrium iron garnet, (Patel, Jackson and Dillon, 1968), iron whiskers, (Nagakura and Chikaura, 1971).

Antifero-magnetic domains in chromium have recently been observed by Hosoya and Ando (1971).

e) Miscellaneous Applications

Probably the most ingenious is the experiment of Itagaki, (1970), to determine if dislocations in ice, previously observed by Webb and Hayes,(1967), were charged. An a.c. electric field caused blurring of the dislocation images in the X-ray topographs, thus implying that the dislocations were indeed charged.

Dislocation studies have been made on almost all materials for which crystals have been obtained with a low density of

dislocations. Examples include beryllium oxide, (Chikawa and Austerman, 1968(a),(b)), magnesium oxide, (Lang and Muiscov, 1964; Lang and Miles, 1965), lithium fluoride, (Lang, 1964), and α-Oxalic Acid Dihydrate, (Michell, Smith and Sabine, 1969). This list is unending, for as crystal growth improves, so more materials become available suitable for X-ray topographic study.

In Chapters VI and VII the present author adds several more compounds to the list of materials in which dislocations have been identified by X-ray topography.

C H A P T E R II

RAPID HIGH RESOLUTION X-RAY TOPOGRAPHY:- FAT OR THIN BEAMS?

1. Introduction

While the technique of X-ray transmission topography due to Lang produces excellent resolution images of crystal defects (Lang,1958, 1959, 1963), it suffers from three major disadvantages:

a) The need for a high precision traversing system.
b) Its extreme sensitivity to small strains in the crystal.
c) Long exposure times.

The first two troubles may often lead to poor quality, or even total loss of picture, while the third is simply tiresome and leaves dynamic or step-by-step experiments wishful thinking.

Several scanning systems have been devised, for example, the micrometer drive method of Lang, or the spring drive of Authier, (Authier and Rimski, 1963; Miltat, 1971). All these various systems, provided they are carefully made, will produce good quality topographs provided that the scanning speed is slow. If this is too large, the large force required to reverse the direction of scan can often result in sufficient jarring of the table to move the crystal off the Bragg reflecting position. As the force is proportional to the rate of change of momentum, it is essential to have a slow

scan, of say 4 inches/hour.

Vibrations may be reduced by mounting the electric motor away from the table and connecting the output to a Selsyn transmitter. This converts the torque to an electrical signal and use of a pair enables re-conversion to a torque at the camera table. These devices, which exhibit much less vibration than a standard synchronous motor, allow various speeds of traverse, as a gear box may be mounted on the electric motor, and generally produce quite an improvement in picture quality, (Humphreys, 1967).

The extreme sensitivity of Lang's technique to small strains arises from the conditions imposed on the angular divergence of the beam in order to prevent simultaneous reflection from the Ka_1 and Ka_2 lines. The beam divergence required is typically 5×10^{-4} radians and if the crystal is bent beyond this amount, Bragg reflections will not occur. Unless care is taken in mounting specimens, due to elastic strain, only part of the crystal will give appreciable diffracted intensity. Inspection of wafers containing integrated circuits is often troubled in this way by the bending caused by the oxide layer used as a diffusion mask, (Schwuttke, 1965).

Several techniques have been devised to circumvent this. Schwuttke and co-workers originally oscillated the crystal through a small angle as it was traversed across the beam, in a technique known as the Scanning Oscillator Technique, (Schwuttke, 1965, 1966). More recently they have developed an electronic feed-back system which will keep the crystal

set exactly at the position of maximum intensity, (van Mellaert and Schwuttke, 1970).

Kohra and Takano used a curved crystal monochromator to focus the X-ray beam. By placing a slit at the focus, only one of the $K\alpha_1$-$K\alpha_2$ doublet lines was selected, (Kohra and Takano, 1970). The beam striking the specimen was able to have a considerable divergence and by rotating crystal and film about a common eccentric axis, good quality micrographs of distorted crystals were obtained.

These two methods rely, however, on a point focus. The obvious way to dispense with the scanning mechanism and to use a beam of larger divergence is to use a line focus. Unless a resolution of no better than about 30 μm is required, some way has to be found to avoid the double reflection of the $K\alpha_1$ $K\alpha_2$ doublet.

Two successful wide beam methods have been developed which may give an improvement of all three deficiencies of Lang's method without loss of resolution. In one, the $K\alpha_1$ line from a silver target is removed by use of a Ruthenium filter, (Hosoya, 1968; Ando and Hosoya, 1971). The absorption edge of Ruthenium falls conveniently between the $K\alpha_1$ and $K\alpha_2$ lines of AgKα radiation and using a filter prepared from the Ru metal powder bonded together with a water solution of polyvinyl alcohol, Hosoya obtained high resolution topographs without recourse to a scanning system. The method is only applicable to AgKα radiation, no other absorption edge falls conveniently between $K\alpha_1$ and $K\alpha_2$ lines of a common element.

The second method, that of Dionne, uses the Kβ radiation and has the advantage that it can be used with a variety of wavelengths, (Dionne, 1967). As will be shown below, high resolution topographs of deformed crystals may be taken with exposure times comparable with those of the Lang technique.

One more line focus technique is worth mentioning here. Improvements on an earlier technique, (Carlson and Wegener, 1961; Anderson, 1965, 1968), have enabled high resolution topographs to be taken using an oscillating Soller slit assembly to restrict the beam divergence but yet allow uniform intensity on the topograph, (Oki and Futagami, 1969; Shetty, Taylor and Calvert, 1969). While this technique leads to a decrease in exposure time, it still suffers from a high strain sensitivity and any non-uniformity in the Soller slit oscillation mechanism leads to 'striping' of the image.

In the following sections, the criteria for maximum efficiency in taking rapid topographs will be discussed and the usefulness of the wide beam method as a complementary technique to that of Lang will be demonstrated.

2. Exposure times in X-ray Topography

In order to determine the parameters effecting exposure times, let us consider the intensity from a perfect crystal in the diffracting geometry shown in Fig. 2.1. As the response of the Nuclear Emulsions is very nearly linear, the exposure time will be inversely proportional to the intensity reaching the film.

The intensity reaching the crystal due to a small area

FIG 2.1

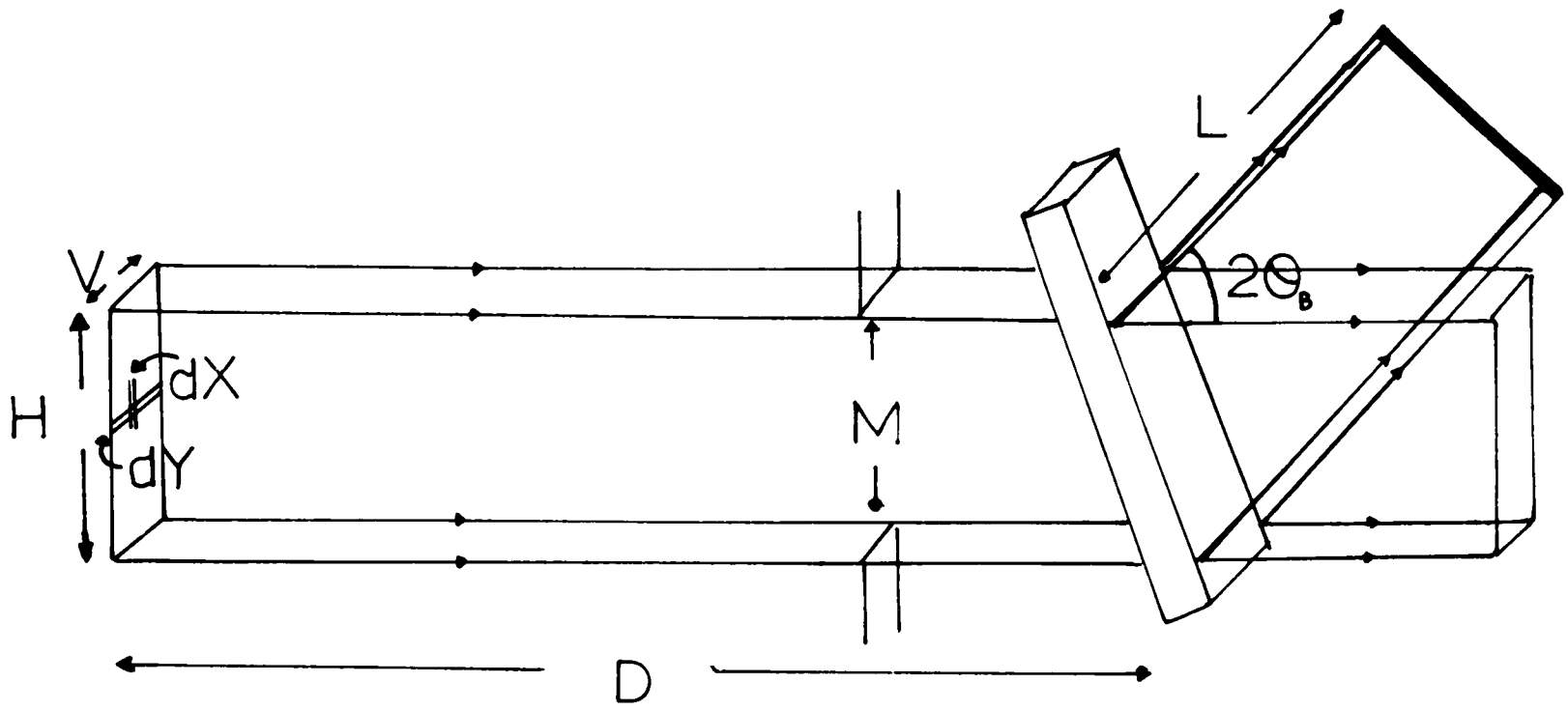
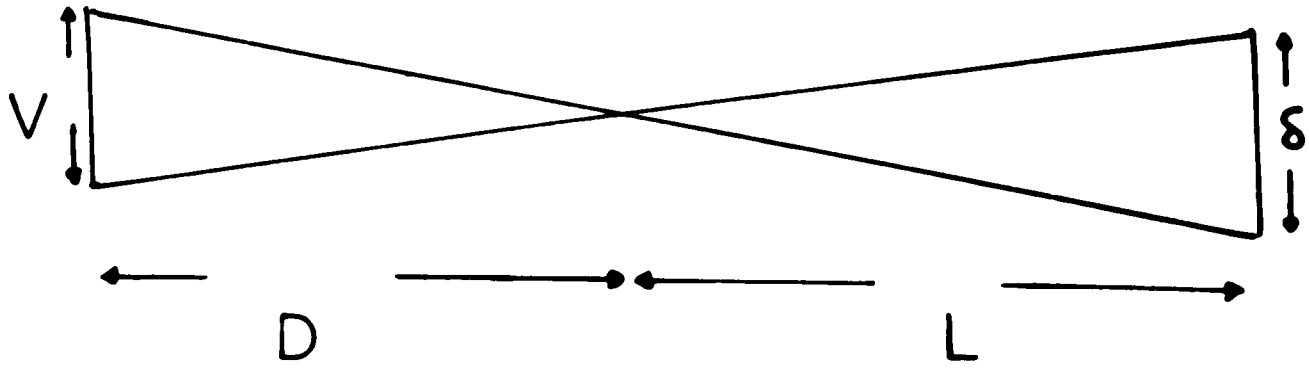


FIG 2.2



of the target of area dY·dX will be :-

$$dI = \frac{P \cdot dX\, dY}{H.V.D} \qquad (2.1)$$

where P is the total power of the X-ray tube. In the vertical direction, the whole divergence of the beam is utilised but in the horizontal direction, only a fraction of the beam divergence $\Delta\theta_B$ is utilised, where $\Delta\theta_B$ is the width of the intrinsic rocking curve of the crystal.

Thus only a fraction of the source of length $D\,\Delta\theta_B$ is used.

The diffracted intensity then becomes

$$I_{diff.} \propto \frac{P}{H.V.} \int_0^V dX \int_0^{D\Delta\theta_B} \frac{dY}{D^2} \qquad (2.2)$$

The exposure time t for a stationary topograph is given by :-

$$\frac{1}{t} = K\,\Delta\theta_B \cdot \frac{P}{H.D.} \qquad (2.3)$$

(This result may also be proved in a slightly different manner using the intensity diffracted by a perfect crystal given by the dynamical theory of diffraction, (Whelan, 1969).)

The result given in equation (2.3) may also be extended to a crystal containing defects. Direct images in X-ray topography arise from kinematic diffraction by the misoriented lattice planes around a defect of X-rays which are incident

on the crystal at angles away from the Bragg position. These X-rays do not undergo primary extinction in the perfect material and hence emerge with an intensity above that of the background. As was pointed out by Authier, if the angular divergence of the beam is less than the perfect crystal rocking curve, direct images are not formed, (Authier, 1967).

Due to any point in the misoriented region one then finds the intensity

$$I_{defect} = K_{defect} \frac{P}{H.D.} \cdot \Delta\theta_{deformed} \qquad (2.4)$$

where (K_{defect}) takes into account the increase in intensity due to no primary extinction and ($\Delta\theta_{deformed}$) is the angular reflecting range at that point in the deformed material.

Dynamical images arise from disturbance of the wavefields propagating in the perfect crystal and the intensity of these will be proportional to the expression in equation (2.3).

For a traverse topograph, the exposure time, T, will be given by :-

$$\frac{1}{T} = K \cdot \frac{P}{H} \cdot \frac{\Delta\theta_B}{D} \frac{M}{R \cos\theta_B} \qquad (2.5)$$

where M is the width of the collimating slit, R is the length of traverse and θ_B is the Bragg angle.

If M is chosen such that all the source is utilised, then only one characteristic X-ray line is to be diffracted :-

$$\frac{M}{D} \leqslant \Delta\theta_{\lambda_1\lambda_2} \qquad (2.6)$$

where $\Delta\theta_{\lambda_1\lambda_2}$ is the angular separation between the line being used and its nearest neighbour. This gives for the minimum exposure time for a stationary topograph, (with M = H) :-

$$\frac{1}{t_m} = K\,\Delta\theta_B \cdot \frac{P}{H^2}\,\Delta\theta_{\lambda_1\lambda_2} \qquad (2.7a)$$

and for a traverse topograph :-

$$\frac{1}{t_m} = K\,\Delta\theta_B \cdot \frac{P}{H} \cdot \frac{\Delta\theta_{\lambda_1\lambda_2}}{R\,\cos\theta_B} \qquad (2.7b)$$

While equation (2.5) is equivalent to the expression given by Dionne, the form in which the equations are written here enables the important parameters to be more easily identified.

The other major constraint for high resolution topographs is the vertical resolution. In the vertical direction, the resolution, δ, is not controlled by the diffraction conditions but, as is seen in Fig. 2.2, is given by the expression :-

$$\delta = \frac{V}{D} \cdot L \qquad (2.8)$$

where L is the separation of plate and specimen.
In order to separate the diffracted and direct beams

$$L \gg \frac{M}{\sin 2\theta_B} \qquad (2.9)$$

Combining equations (2.6), (2.8) and (2.9) gives :-

$$\delta = \frac{V\ \Delta\theta_{\lambda_1\lambda_2}}{\sin 2\theta_B} \qquad (2.10)$$

One is now equipped to compare the merits of wide-beam and Lang topography.

The method of Dionne, using Kβ radiation will be treated in detail, but the same considerations will apply to the technique of Hosoya, as it is not possible to completely filter out all of the AgKβ radiation. The present author attempted to reproduce the technique of Hosoya, using, as did Lang, (1970), a RuO_2 filter bonded with paraffin wax. Due to a very high background scatter, satisfactory topographs were only obtained for the 224 reflections. In the reflections with smaller Bragg angles, though the images were sharp, they appeared extremely weak above a high background intensity.

3. Wide Beam X-ray Topography

a) Method

Radiation from a line source is allowed to fall on a nearly perfect single crystal mounted on a goniometer on a turntable, as shown schematically in Fig. 2.3. As the only differences in this technique and that of Lang are that the line focus is used, the collimating slits are wider and no scanning is required, it is often convenient, though not by any means essential, to perform wide beam experiments using the same camera. Construction of a wide beam camera, is, however, extremely simple. Provision is required to turn the crystal and counter about the same axis, but owing to the fact that the angular widths of the diffracted beam peaks are extremely wide, about a degree of arc, the crystal may be set easily at the Bragg position by manual adjustment of

FIG 2.3

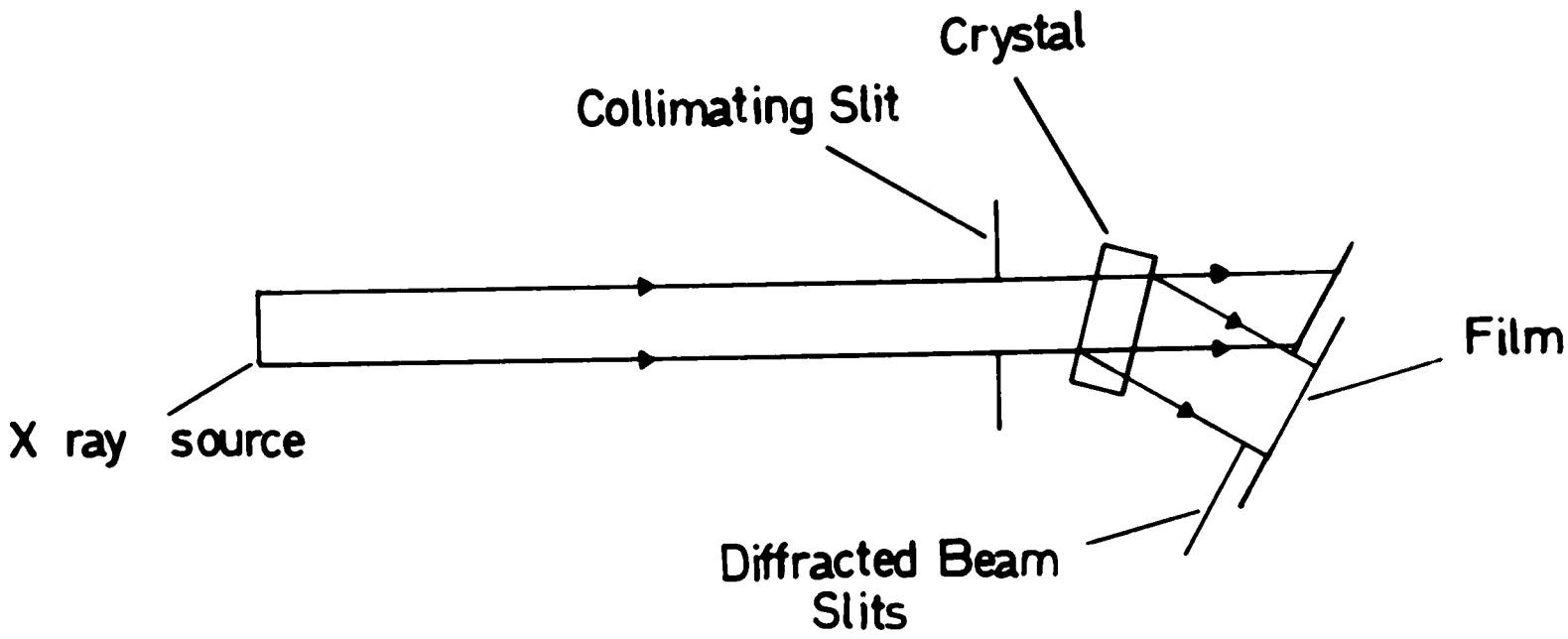
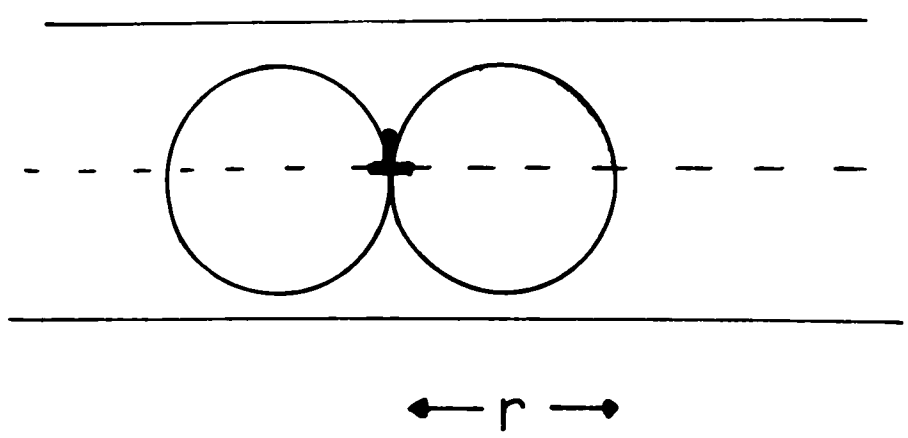

Crystal
Collimating Slit
Film
X ray source
Diffracted Beam
Slits

FIG 2.4


r

a lever, about six inches long, attached to the goniometer. Collimating slits are best manufactured from tantalum. It is essential, however, that there are two degrees of freedom in the goniometer drive, as it is usually necessary to adjust the position of the specimen to ensure that the required area is in the beam. In this respect, use of a Lang camera for this technique enables the position of the specimen to be adjusted by remote control using the scanning mechanism. It also enables very large areas of crystal to be studied as the crystal can be traversed across the beam in a manner analogous to the Lang technique. The larger beam divergence does not impose the same tolerance requirements on the traverse as does the highly collimated beam, and loss of image due to drift off from the Bragg position is eliminated.

Old diffraction cameras often lend themselves to conversion into a divergent beam camera. An old camera, consisting essentially of two turntables about a concentric axis, has been satisfactorily modified for wide beam topography by the author.

b) Resolution and Image Quality

Images are recorded on Nuclear Emulsions and processed according to the recipe of Lang. One might expect that the two techniques should produce identical images of defects, as the wide beam method is equivalent to an integration in space whereas the Lang method is an integration in time. This is subject to three conditions, namely :

i) That it is possible to ignore the contribution to

the intensity of X-rays which are at such large angles to the exact Bragg position as to be present only when the source is longer than that used in the Lang technique.

ii) The wide beam technique uses truly monochromatic radiation.

iii) The background scatter from the slits and collimator are the same in the two techniques.

i) Direct images are formed from kinematic reflection by X-rays not exactly satisfying the Bragg condition and are hence integrated images. One considers image formation to occur when the effective misorientation around the defect is greater than about the width of the rocking curve, (Authier, 1967). The total intensity is then proportional to the volume of material enclosed in a contour of equal misorientation surrounding a defect. It is important to determine what effects there would be on the intensity of the defects due to increasing the beam divergence for 5×10^{-4} radians, (Lang method), to 2.5×10^{-2} radians, (wide beam method). Let us consider the simple case of a dislocation lying parallel to the crystal surface and make the approximation that the diffracted beam is perpendicular to the crystal face.

The effective misorientation around the defect across a section parallel to the crystal face and through the dislocation line is given by, (Appendix A);

$$\delta(\Delta\theta) \simeq \frac{k}{r} \qquad (2.11)$$

where r is the distance from the dislocation line and k is a constant.

Now referring to Fig. 2.4, for a rough approximation, the shape of the contours of equal misorientation may be taken as cylinders of circular cross-section.

The intensity diffracted by the defect, $I(\Delta\theta)$ is given by :-

$$I(\Delta\theta) = Cr^2 \qquad (2.12)$$

where C is a constant.

Then :

$$I(\Delta\theta) \propto |\delta(\Delta\theta)|^{-2} . \qquad (2.13)$$

Table 2.1 shows the relative intensities if only beams with deviation greater than $\Delta\theta$ are considered in the image.

Table 2.1

Intensity from misorientations greater than $\Delta\theta$

$\Delta\theta$ (radians)	$I(\Delta\theta)$
3×10^{-5}	10^9
6×10^{-5}	2.5×10^8
5×10^{-4}	4×10^6
2×10^{-2}	2.5×10^3

The full width at half height of the 220 reflection in silicon with CuKα radiation is 5.5 secs (3×10^{-5} radians). Thus, by ignoring beams with deviations greater than 5×10^{-4}, the angular width of the source in the Lang technique, one only introduces an error of about ½% in the intensity of

the image. One therefore expects that wide beam topographs, (with an angular source width of 2×10^{-2} radians), should produce direct images about ½% more intense than in the Lang techniques provided the intensity reflected by the perfect crystal is equal. To all intents and purposes, therefore, the direct images will be as intense in both techniques.

As the angular width of the beams in both techniques is usually much wider than the rocking curve width, the image widths in both techniques will be governed by the angular width of the rocking curve and the nature of the defect only.

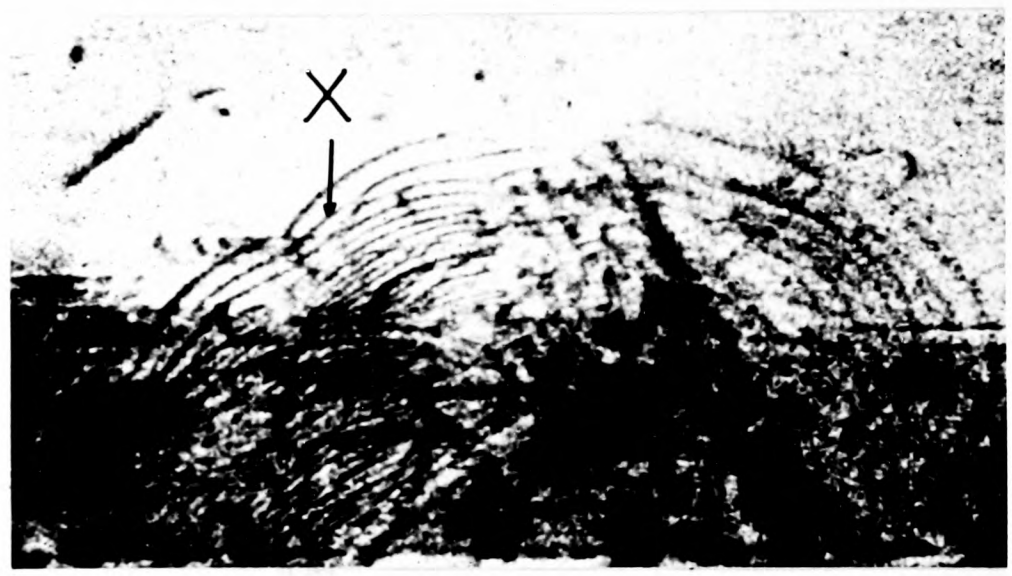
Figure 2.5 shows a topograph of "emitter edge" dislocations in silicon imaged in the Lang technique using $CuK\alpha_1$ radiation, the wide beam technique using $CuK\beta$ radiation and the wide beam technique using $WL\alpha_1$ radiation respectively. The agreement in dislocation widths is seen in the composite in Fig. 2.6, in which sections of the $CuK\beta$ topograph of Fig. 2.5 are superimposed on the Lang topograph. As all three radiations have approximately the same rocking curve half width, one expects that the images of the same dislocation should be identical in width. Figure 2.7 shows a micro-densitometer trace of the dislocation marked X, taken from the topographs of Fig. 2.5, and the agreement in image widths is seen to be quite good.

ii) The above argument is clearly only applicable if in the divergent beam method only one characteristic X-ray line contributes to the image. However, the Dionne method uses $K\beta$ radiation and hence a loss of resolution can occur, in principle, due to the β_1, β_2 and β_3 lines giving multiple

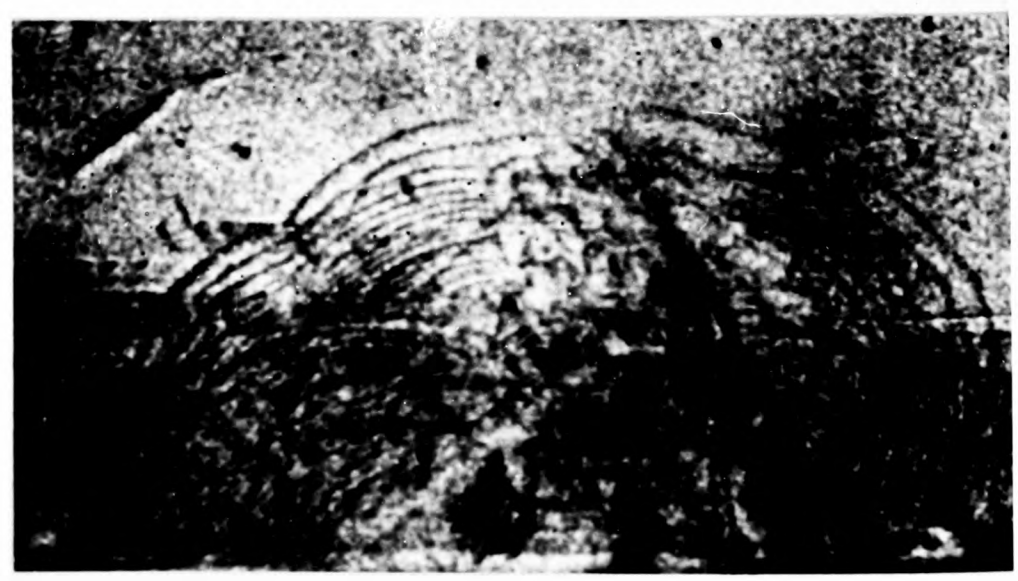
FIG 2.5



(a)

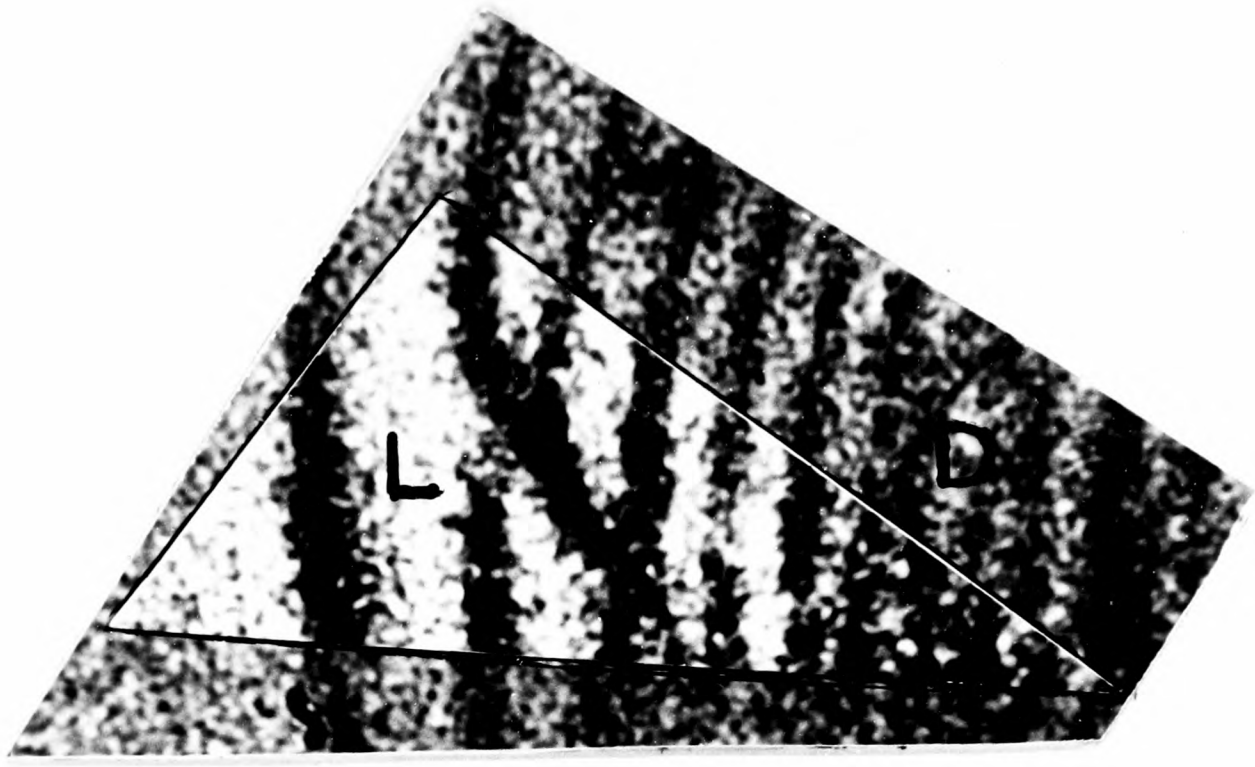


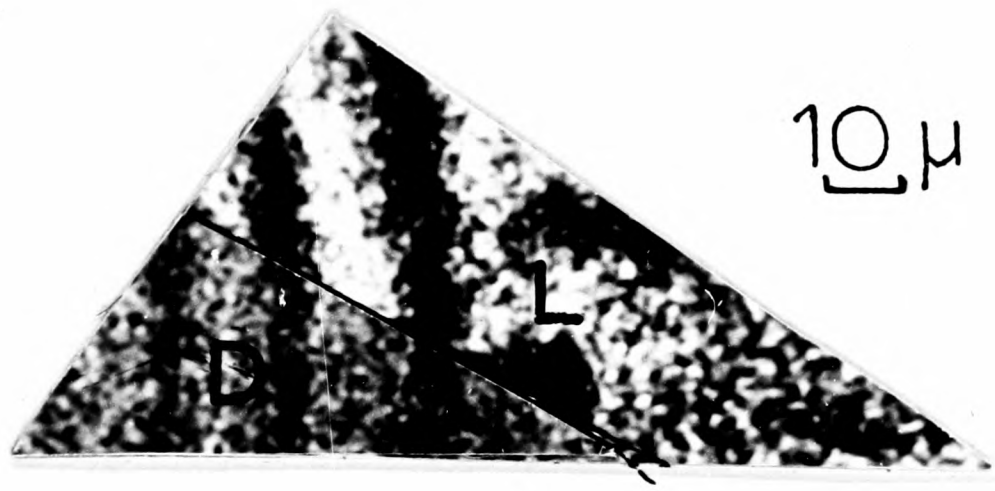
(b)



(c)

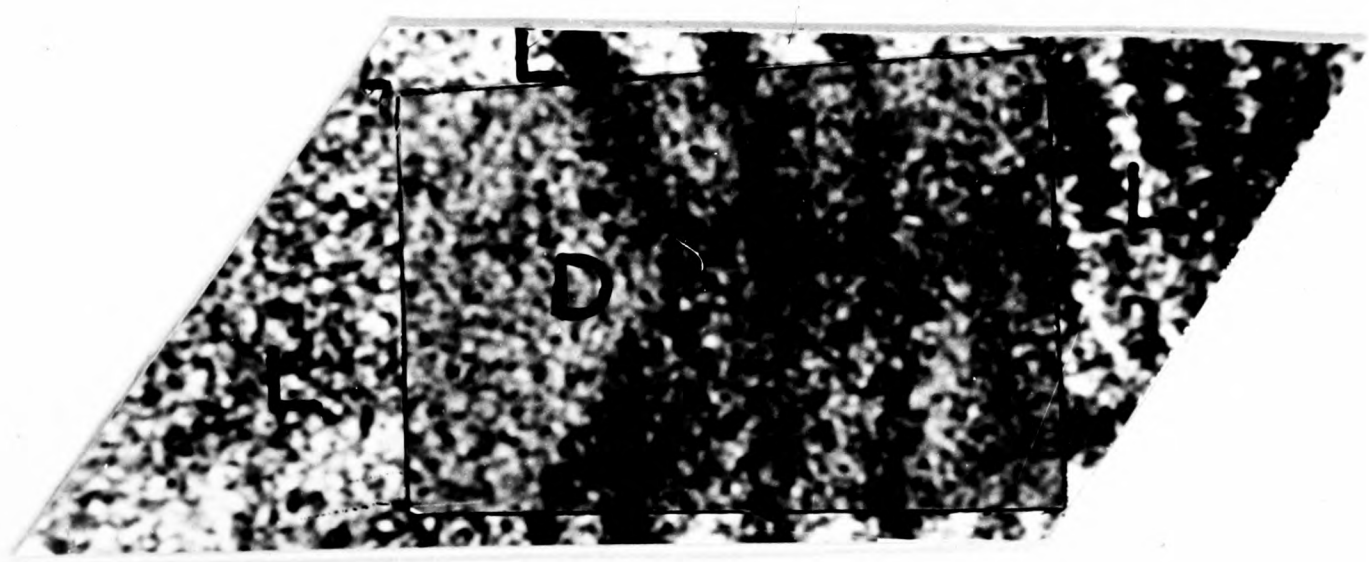
FIG 2.6





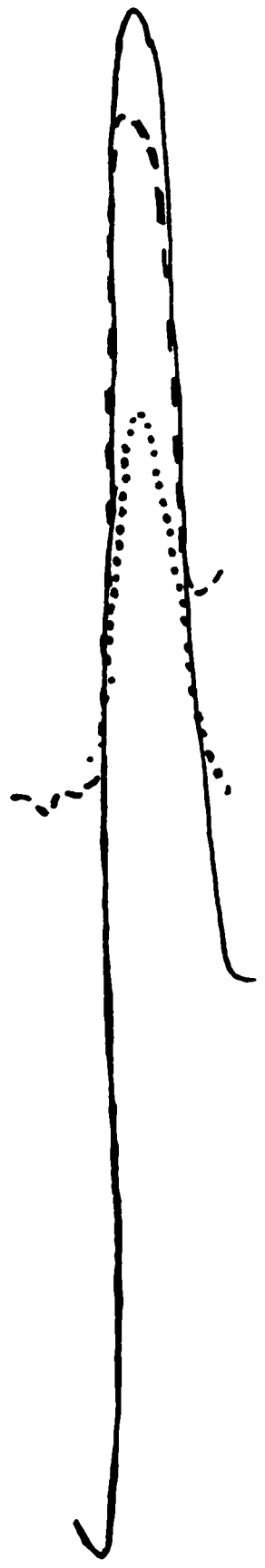
10 μ

Cu Kα,
Cu Kβ



L = Lang
D = Dionne
} Techniques

FIG 2.7



—— Lang CuKα

– – – W-B CuKβ

····· W-B W Lα

images. The magnitude of this effect may be seen from Tables 2.2 and 2.3. It is clear, however, that the β_2 line

Table 2.2

X-ray line wavelengths (A). Compton and Allison (1935)

Element	$K\alpha_2$	$K\alpha_1$	$K\beta_3$	$K\beta_1$	$K\beta_2$
24 Cr	2.28891	2.28503	-	1.90620	-
29 Cu	1.541232	1.537395	-	1.38935	1.37824
42 Mo	0.712105	0.707831	0.631543	0.630978	0.619698
47 Ag	0.56267	0.55828	0.49665	0.49601	0.48603
	$L\alpha_2$	$L\alpha_1$	$L\beta_3$	$L\beta_1$	$L\beta_2$
74 W	1.48762	1.47695	1.28126	1.24458	1.20285

Table 2.3

Relative intensities. Compton and Allison (1935)

Element	$K\alpha_2$	$K\alpha_1$	$K\beta_3$	$K\beta_1$	$K\beta_2$
24 Cr	50.6 (51.5)	100	-	21 (17.9)	0.66
29 Cu	46.0 (49.7)	100	-	15.8 (20.0)	0.15
42 Mo	50.6 (49.9)	100	12.0	23.3 (27.9)	0.348 (0.517)
47 Ag	51.7 (49.9)	100	?	24.0 (29.0)	0.422 (0.617)
	$L\alpha_2$	$L\alpha_1$	$L\beta_3$	$L\beta_1$	$L\beta_2$
74 W	12.0	100	8.0	52.0	20.0

has typically only one hundredth of the intensity of the β_1 line, and β_2 images will therefore not be detectable. For targets of high atomic number (e.g., Mo or Ag), Table 2.2 shows that the $K\beta_3$ line and $K\beta_1$ line are separated, the $K\beta_3$ intensity being about 50% that of the $K\beta_1$ line. The separation of these two lines is very small and the resolution loss due to the double image will normally be less than the

image widths. For example, with molybdenum radiation incident on silicon at the 220 Bragg position, the double images due to β_1 and β_3 have an angular separation of about 1.5×10^{-4} radians. Hence, for a specimen to plate distance of 1 cm, the image will be broadened by about 1.5 μm. As the photo-electron track-lengths for molybdenum radiation are about 2 μm, double images will not be seen. Thus, images using hard Kβ radiation will be rather wider than those of the Lang technique, but only by a small amount.

iii) As is immediately apparent in Fig. 2.6, the background intensity is much higher in the wide beam technique than in the Lang technique. This scatter originates mainly from the slit and collimator and, as shown in Fig. 2.8, is only marginally effected by the specimen. Even at large angles the scatter is extremely high. Introduction of a double slit reduces the scatter, Fig. 2.9, and by using a shorter source length with correspondingly narrow double slits (2mm) considerable improvement can be made. The background scatter is not only a nuisance from the point of view of the topograph, but it is also a major health hazard. Extreme care should be taken when setting up wide beam topographs to ensure that the body is not exposed and it is essential to place lead shielding around the apparatus. In the Lang technique a pair of collimating slits are used which are so narrow that only radiation scattered from the first slit making a very small angle with the incident beam direction is allowed to escape. As this may be effectively described as the direct beam, provided one does not venture into the direct beam, there

FIG 2.8

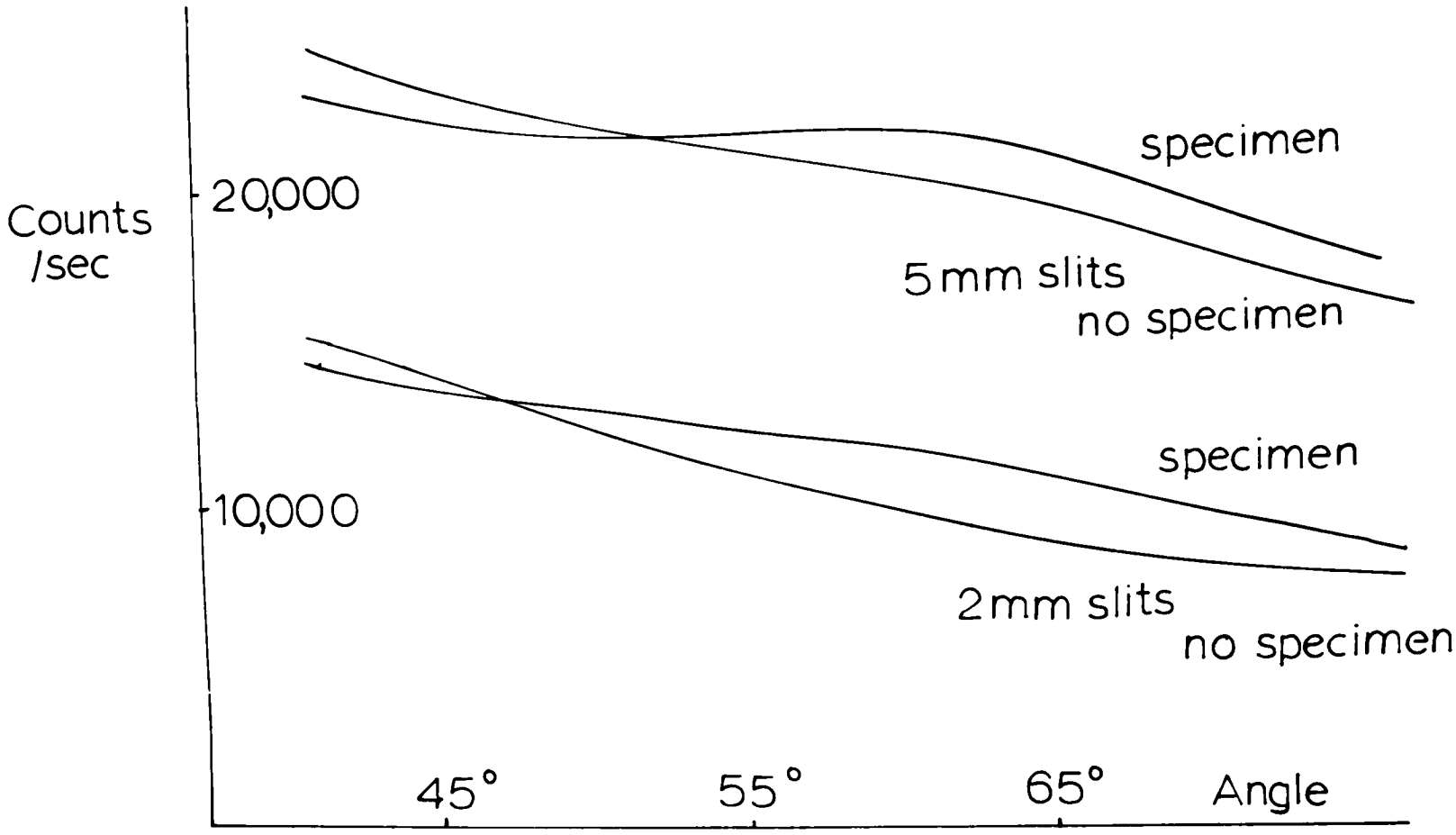
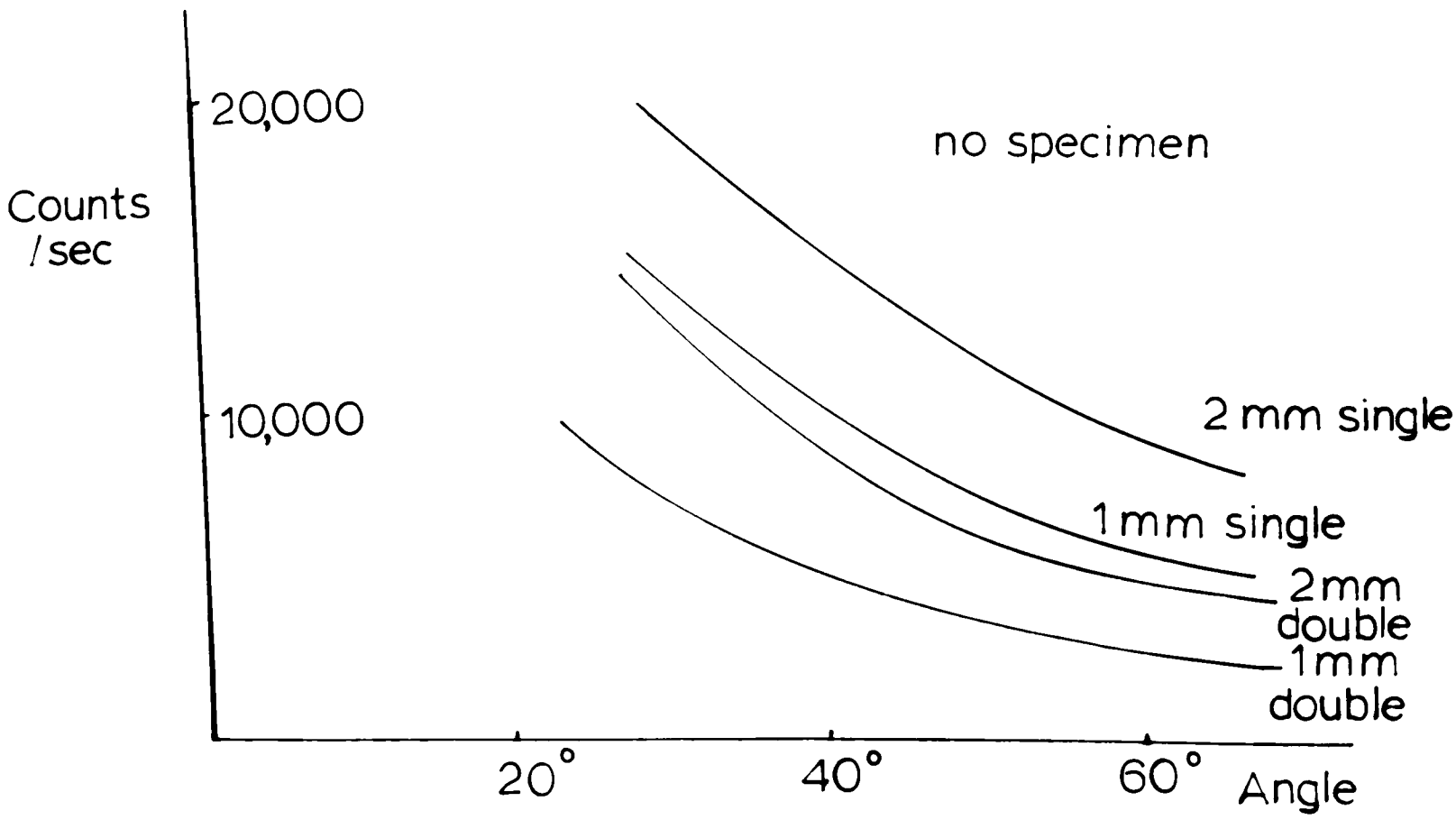

Counts
/sec
20,000
10,000
specimen
5mm slits
no specimen
specimen
2mm slits
no specimen
45°
55°
65°
Angle

FIG 2.9


Counts
/sec
20,000
10,000
no specimen
2 mm single
1mm single
2mm
double
1mm
double
20°
40°
60°
Angle

is little danger.

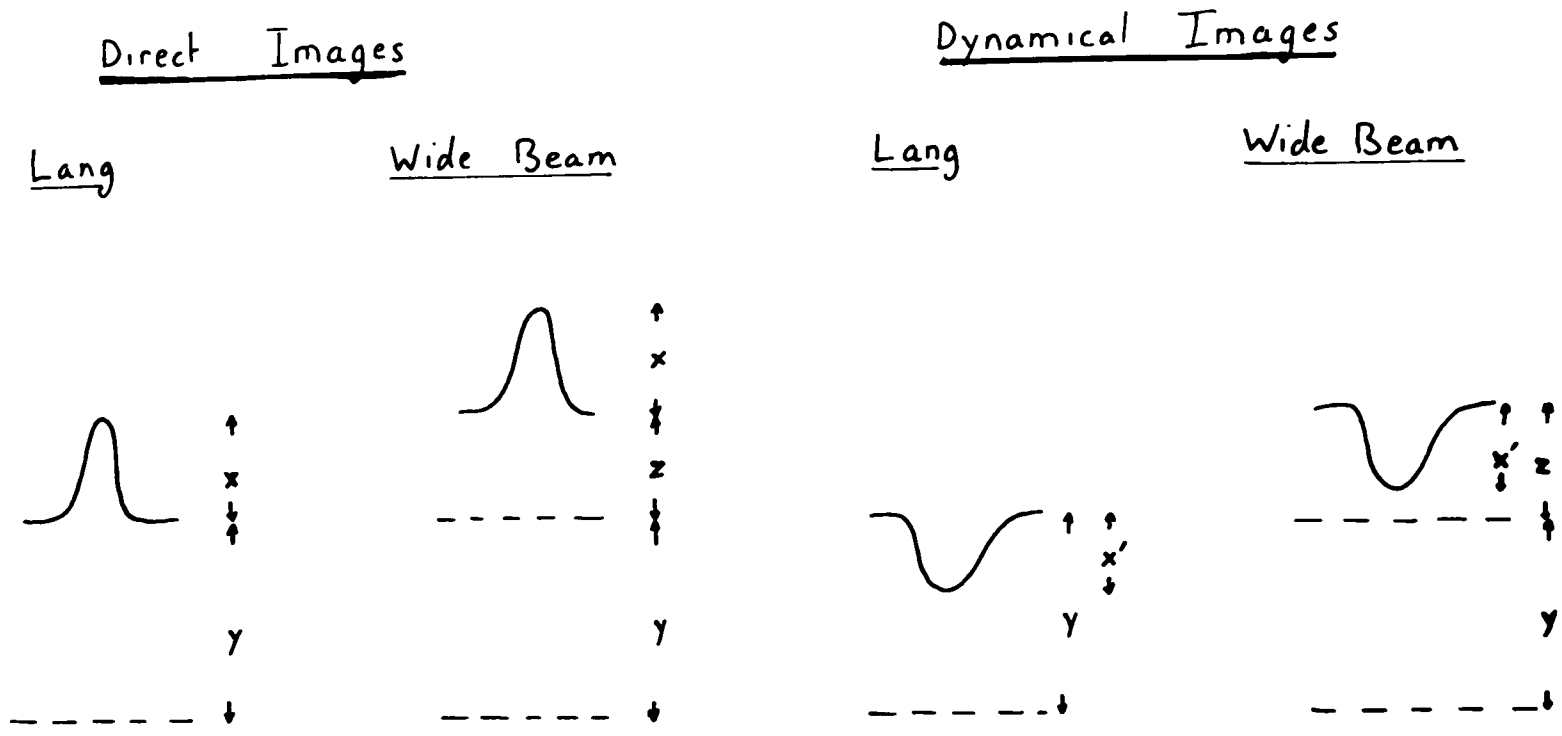
It is seen in Fig. 2.5 that the white dynamical images appear much less intense relative to the background in the wide beam method than in the Lang technique. An explanation may be sought on the lines shown in Fig. 2.10. Shown there is the visibility, defined in the normal way as $\frac{I\ max - I\ min}{I\ max + I\ min}$, for the direct and dynamical images in the case of the Lang and wide beam techniques. Inspection of the visibility ratios, R_{direct} and $R_{dynamic}$, shows immediately that for any value of x and x', R_{direct} is always less than $R_{dynamic}$. In other words, any increase in background scatter leads to a greater loss of visibility in the dynamical image than in the direct image. The dynamic image will then appear weaker with respect to the direct image, which is exactly what is observed in practice.

The loss of visibility in the dynamical image is thus a direct consequence of the increased background scatter.

c) Application to study of bent specimens

Figure 2.11 shows a Lang topograph of a silicon disc which has been jet-thinned for transmission electron microscopy. Such specimens seem to contain large amounts of elastic strain and as in this case, only two narrow regions of the crystal where the $K\alpha_1$ and $K\alpha_2$ lines come into the reflecting position give appreciable intensity in the diffracted beam. Measurements of the angular peak position as a function of the position of the beam on the crystal show, and may be confirmed from the micrograph, that the radius of curvature

FIG 2.10



x, x' = Image
y = Dynamical Background
z = Scatter

Visibility

$$V_L = \frac{x}{2y + x}$$

$$V_w = \frac{x}{2z + 2y + x}$$

Visibility

$$V_L = \frac{x'}{2y - x'}$$

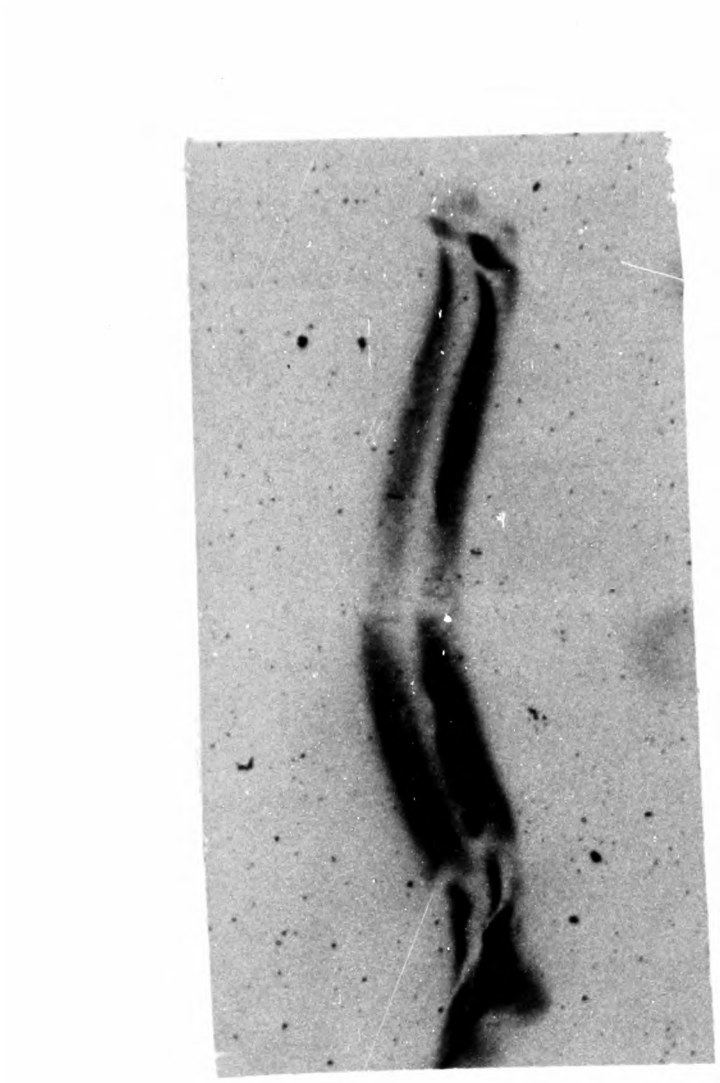
$$V_w = \frac{x'}{2z + 2y - x'}$$

Ratio of Visibility of Lang Technique to Wide Beam Technique

$$R_{Direct} = \frac{V_L}{V_w} = 1 + \frac{2z}{2y + x}$$

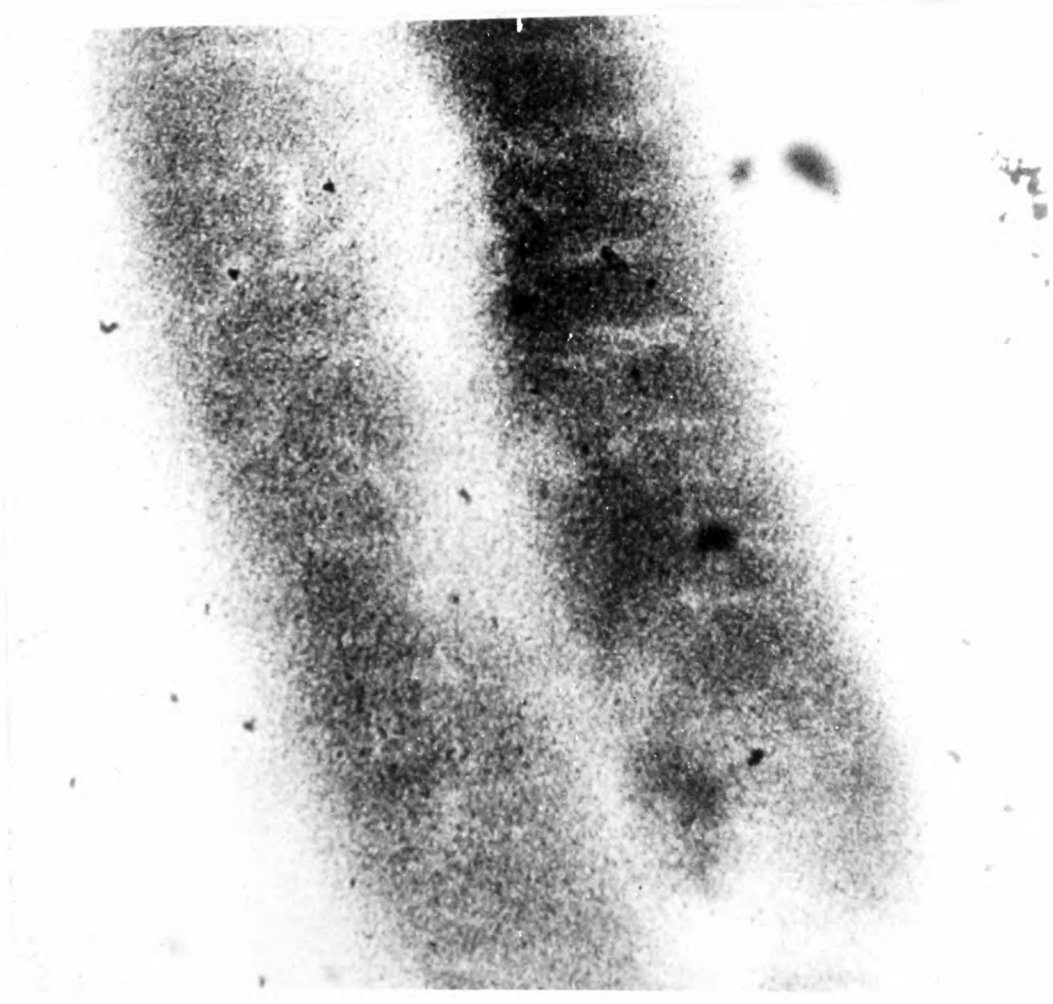
$$R_{Dynamic} = \frac{V_L}{V_w} = 1 + \frac{2z}{2y - x'}$$

FIG 2.11



1mm

Cu Kα



100μ

is about 20 cm. Using the wide beam technique X-ray topographs of T.E.M. specimens have been taken with good resolution, as shown in Fig. 2.12. If high voltage electron microscopy and X-ray topography are to be done on the same specimen, whether thinned overall or jet thinned as here, it may be essential to use the wide beam technique in order to avoid loss of image due to small elastic strains in the very thin specimens.

A modification of the method is described in Chapter 7, where it is used to study HfS_2.

4. Comparative speeds of wide beam and Lang topography

The wide beam technique has been proved to circumvent the first two deficiencies of the Lang technique without sacrifice of resolution, but it has yet to be demonstrated that it is any quicker.

Table 2.4 shows values of the parameters P and H defined in equations (2.7), together with expected vertical resolution, δ, for the two techniques. In the Lang technique, the vertical resolution is not usually limited in practice by the equation (2.10), but by not being able to place the photographic plate nearer than 1 cm from the crystal.

Table 2.5 shows relative exposure times using the techniques of Dionne and Lang for several generators. The widths of topograph taken are all the same (12 mm) and the intensities have been corrected for the lower intensity of the CuKβ line as given by Table 2.3. Where the source length is less than 12 mm, one assumes that in the wide beam method, some form of scanning is employed.

FIG 2.12



Table 2.4

X-ray set parameters

Lang topography

Set	Source Size $(mm)^2$	Projected Width (mm)	Power (watts)	$\frac{P}{H}$ w/mm	δ (with L=1 cm)	Cost (1969)
Hilger-Watts Microfocus	0.1x1.4	0.14	140	1,000	3 µm	£2,250
Philips AMR Microfocus	0.1 x 1	0.1	200	2,000		£4,000
ENRAF Philips Sealed Tubes	0.4 x 8	0.4	800	2,000	8 µm	£1,500
Elliott GX6	0.2 x 2	0.2	2,000	10,000	4 µm	£8,000
Rigaku-Denki	1 x 10	1	60,000	60,000	3 µm	£38,000
Norelco	12 x 0.1	0.5	$\frac{750}{24}=31$	62	<1 µm	?

Divergent beam

Set	Source Size $(mm)^2$	Width (mm)	Power (watts)	$\frac{P}{H}$	$\frac{P}{H^2}$	δ	Cost
Hilger-Watts	6 x 0.1	6	450	80	12.5 w/mm^2	0.6 µ	£2,250
ENRAF Philips Tubes	0.4 x 8	8	800	100	12.5 w/mm^2	2.4 µ	£1,500
Elliott GX6	2 x 0.2	2	2,000	1,000	500	1 µ	£8,000
Rigaku-Denki	1 x 10	10	60,000	6,000	600	6 µ	£38,000
Norelco	12 x 0.1	12	750	62	2.5	<1 µm	-

Table 2.5

Relative exposure times for 12 mm topograph

Take off angle 6°

Set	Lang			Wide beam, (Dionne)		
	$\frac{P}{H.R.}\ \Delta\theta_{a_1a_2}$	T	δ µm	$\frac{1}{5}\frac{P}{H}.\frac{\Delta\theta_{a\beta}}{R}$	t	δ µm
Hilger-Watts	2	0.5	3	1.25	0.8	0.6
ENRAF	4	0.25	8	1.25	0.8	2.4
Elliott GX6	21	0.05	4	16.6	0.06	1
Rigaku-Denki	125	0.008	3	10.0	0.01	6
Norelco	0.125	8	0.1	0.5	2	0.6

(Taking 0.5 mm
of 12 mm line)

In all cases where the spot focus of the tube may be used for Lang topography (i.e., except the Norelco tube where a projected height of 1.2 mm would give a resolution of about 12 µm with D = 100 cm), the Dionne technique will not have an advantage over Lang's technique.

It is clear from the above analysis that the Hilger-Watts microfocus generator never functioned correctly ever since installation. Compared with the Norelco generator, exposure times should be approximately 1/16th, whereas in practice exposures were only about 1/3rd as fast. It must be assumed that difficulties in saturating the bias led to the focal spot never reaching 1.4 mm or else that drift of the focal

spot occurred during experiments. Malfunction of the generator must be invoked to account for the fact that wide beam topography was 3 to 4 times as fast as Lang topography using this set.

However, the vertical resolution of the Lang technique in the geometry described here is often rather poor. In many cases, an instrumental resolution of 1 μm in the vertical direction is necessary for high resolution work. The resolution may be improved by taking the focal spot off at 3°, but in many cases smaller take-off angles are impossible. In order to reach the required vertical resolution, the specimen to source distance must be lengthened.

Table 2.6 shows the exposure times of Table 2.5 corrected for 1 μm resolution in the vertical direction.

Table 2.6

Exposure times for 12 mm topograph with vertical resolution 1 μm, take off 3°

Set	Lang	Wide Beam	
		Dionne, Kβ	Hosoya, ($AgK\alpha_2$)
Hilger	0.75	0.8	0.32
ENRAF	1	0.8	0.32
Elliott	0.1	0.06	0.024
Rigaku-Denki	0.012	0.01	0.004
Norelco	8	2	0.8

In this case one sees that the wide beam techniques will

in most cases be quicker than the Lang technique. Hosoya's technique using the AgKα_2 line may be expected to be better than the technique of Dionne using the Kβ line, as the ratio of the intensity of the α_2 to α_1 lines is about one half. Some loss in intensity in the Kα_2 line will inevitably occur in the Ru filter, and, though this has not been included, will certainly not be worse than a factor of 2.

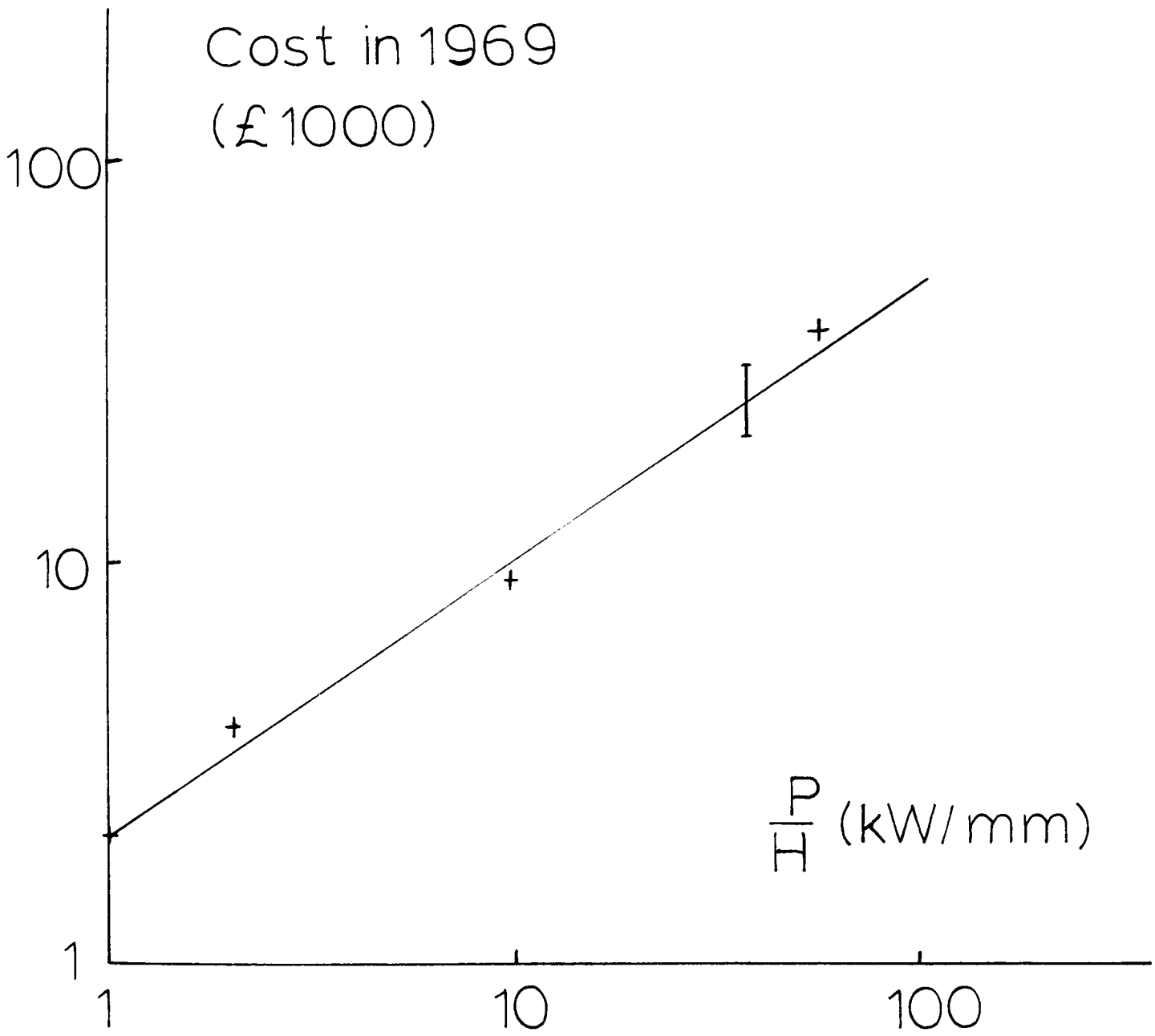
Use of the tungsten Lα_1 line as an alternative to CuKβ_1 radiation was found to increase the speed of the wide beam technique by about a factor of 2. While the WL lines are relatively weaker than the CuK lines, there is still a considerable gain by their use. As can be seen from Tables 2.2 and 2.3, the Lα_2 line of tungsten is about 1/8th of the intensity of the Lα_1 line, and due to the response of the film, double images do not occur. Figure 2.5(c) shows a high resolution topograph using WLα_1 radiation and the microdensitometer traces of Fig. 2.7 confirm that the images are no wider than when using the CuKβ line. The background scatter was, however, greater than when using CuKβ radiation.

5. Conclusions

To sum up, then, one cannot make general rules as to whether wide beam topography is advantageous to Lang topography as far as speed is concerned, contrary to the impression given by some authors. The conclusions reached may well be different depending on the dimensions of the source available.

What is clear, however, is that it is profitable to have as high a power per unit length of line as possible.

FIG 2.13



Examination of Fig. 2.13 shows immediately where the constraints will lie. A case was made successfully by the author, however, (via Dr. M.J. Whelan) for an Elliott GX6 generator. This has reduced exposure times to values of the order of 2 min/mm for a Lang projection topograph using $CuK\alpha_1$ radiation of silicon recorded on Ilford G5 nuclear emulsion. Exposure times are thus now comparable with the time required to set up the experiment.

Summary

Techniques for avoiding the disadvantages of the Lang technique without loss of resolution were discussed. Expressions for the exposure times of X-ray topographs were obtained from first principles.

The method of wide beam topography of Dionne was described and a detailed discussion given of the resolution and image contrast in comparison to Lang's technique. A new wide beam technique using the tungsten $L\alpha_1$ line was demonstrated and it was shown that the wide beam method has a great advantage over Lang's technique in the examination of the same specimen by transmission electron microscopy and X-ray topography.

Using the expressions derived earlier for the exposure times, the speeds of the two techniques were compared and it was shown that the conclusion reached was dependant on the dimensions of the X-ray source. The reasons behind the purchase of an Elliott GX6 generator were explained.

C H A P T E R III

DIRECT DISPLAY OF X-RAY IMAGES

1. Introduction

In the previous chapter, means of reducing the prohibitively long exposure times of X-ray topographs without loss of resolution or information were discussed and demonstrated. One is, however, still working under a large disadvantage in that it is not actually possible to see the image one is recording. In principle, a system where the X-ray image is displayed directly to the experimenter would not only enable dynamic experiments to be performed, but also remove the frustration caused by such technical details as taking an excellent topograph of the wrong grain in a specimen containing several sub-grains. Also, if X-ray topography is ever to become accepted as a useful "on-line" inspection technique, it is highly desirable to remove the requirement of film processing before the next operation in the production stage can be carried out. One example will be given to illustrate this point. In the manufacture of quartz oscillators, it is essential that the sections are not cut containing a growth-boundary. As these boundaries show up on the X-ray topographs as regions of enhanced contrast of 100-200 micrometers wide, provided the images may be displayed quickly and easily, this is an excellent application of X-ray topography to an industrial process. No analysis of the topographs is required except in determining the position of

the boundaries before the sample is cut. Consequently, over the last few years the idea of devising a detection system to provide direct viewing has gained momentum, and several systems have been described and demonstrated.

Due to the low intensity of the X-ray fluxes used, image intensification is essential at some stage in the detector. Devices may be broadly classified under two headings :-

a) Devices converting X-rays to light with subsequent intensification of the optical image;

b) Devices converting X-rays to electrical signals with subsequent amplification of the electrical signal.

These will now be discussed separately in more detail.

a) Optical Intensification Devices

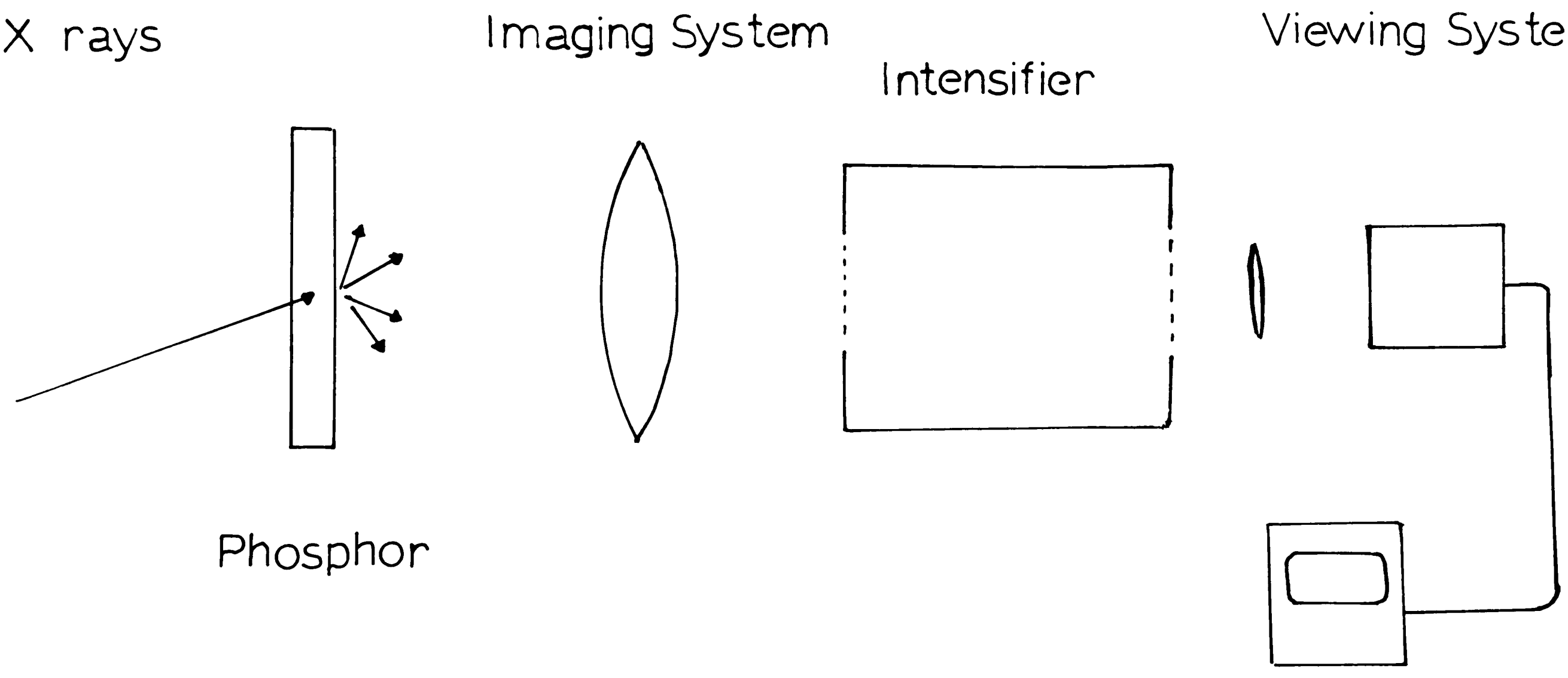
The principle behind all devices so far constructed is the same, and is illustrated in Fig. 3.1. X-rays are converted to light in a phosphor screen and the image is formed on the input of an optical image intensification system. The intensified image may be viewed either directly, or for convenience, using a vidicon closed-circuit television camera and monitor.

The resolution of such a system will be limited by two factors :-

1) That of the intensifier;
2) That of the phosphor.

Provided that enough illumination is available to overcome

FIG 3.1


X rays
Imaging System
Intensifier
Viewing System
Phosphor

the dark-current in the intensifier, the first problem may be overcome by forming a magnified image of the phosphor onto the intensifier input. The only drawbacks are the need for an expensive lens system and facility for small adjustment of the lenses to provide an in-focus image on the intensifier input window.

In practice, the limiting factor at present is the compromise between a thick phosphor screen, giving low resolution and high conversion efficiency, and a thin screen giving high resolution but low conversion efficiency.

The conversion efficiency, E, of a thin phosphor screen is given by :-

$$E = F\mu t \qquad (3.1)$$

provided $\mu t \ll 1$, and where μ is the X-ray absorption coefficient, t is the screen thickness, and F is the factor, dependent on the chemical structure of the phosphor, determining the fraction of absorbed energy re-emitted as light. Ideally then, one requires a very thin screen with small grain-size phosphor, or preferably, a thin single crystal phosphor to give good spatial resolution. One requires a high absorption coefficient and high efficiency for re-emission.

Table 3.1 shows the absorption coefficients and grain-sizes for several common phosphors.

From this it would appear that CsI (Th) should be the most suitable X-ray phosphor for this device. Unfortunately, CsI (Th) would seem to have a much lower re-emission factor (F), than ZnS (Ag) polycrystalline powder, (Lang and Reifsnider,

1969) and also the minimum thickness that a CsI (Th) crystal was obtainable was 100 μm, (Nuclear Enterprises 1968).

Table 3.1

Absorption Coefficients of Phosphors

Phosphor	μ cm^{-1}			Grain Size
	Cr Kα	Cu Kα	Mo Kα	
ZnS (Ag)	950	320	100	8 μm
Zn_2SiO_4 (Mn)	510	180	130	1 μm
NaI (Th)	2,600	1,000	120	Single Crystal
CsI (Th)	3,700	1,500	185	Single Crystal

As the resolution is increased, one needs a thinner screen, producing a lower intensity optical image. It is then that the intensifier characteristics become important and one needs an intensifier of low dark-current, high gain and high resolution. Table 3.2 shows some characteristics of image intensifiers on the market in 1969. Provided that the X-ray input is sufficiently intense, one can obtain adequate direct topographs from the high dark current, low gain devices, which tend to be less expensive than those with high gain and low dark-current. An image isocon has recently been used successfully to record images produced on a phosphor screen, (Hashizume et al.,1971). With a much lower intensity, it was necessary to use a much thicker screen, and while an X-ray

topographic image was definitely observed by the author using a Marconi Image Isocon, (Mouser et al., 1967), as can be seen in Fig. 3.2, a resolution of a mm is barely justifiable.

Table 3.2

Image Intensifier Characteristics

Tube	Type	Resolution μm	Diameter mm	Background μ lux	Gain	Cost*
EMI 9694	4 stage Magnetic	17	48	0.01	10^6	£2,600
Siemens (Westing-house)	1 stage electro-static + S.E.C.tube	80	40	0.01	?	£4,000
Mullard XX1060	3 stage electro-static	22	25	0.2	$3x10^4$	£1,500
Standard Telecommu-nications Ltd.	3 stage electro-static	36	18	30	$\sim 3x10^4$	
Marconi	1 stage intensifier + Image Isocon	120	75	1		
Marconi	Image Isocon	100	75	50		

* Prices in 1969.

The Mullard XX 1060 was used to display X-ray topographic images with a resolution approaching 200 μm using a 111 surface

FIG 3.2

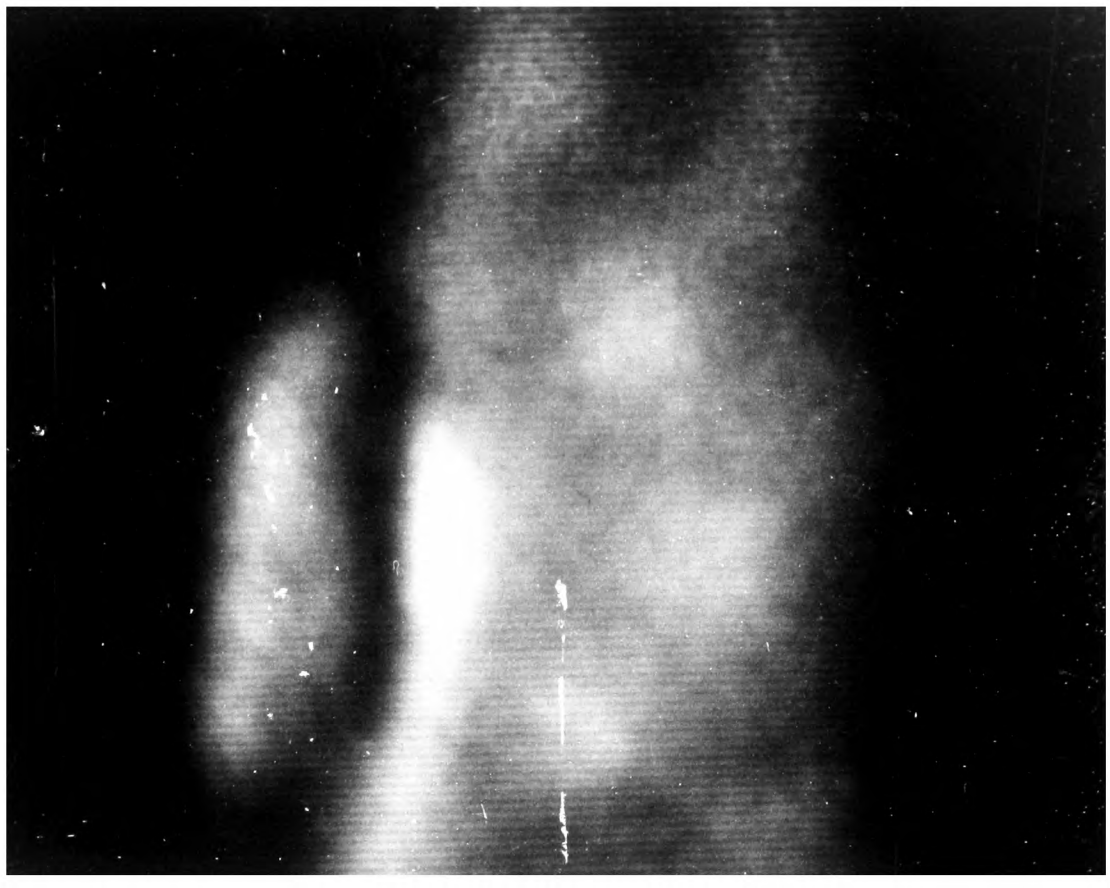
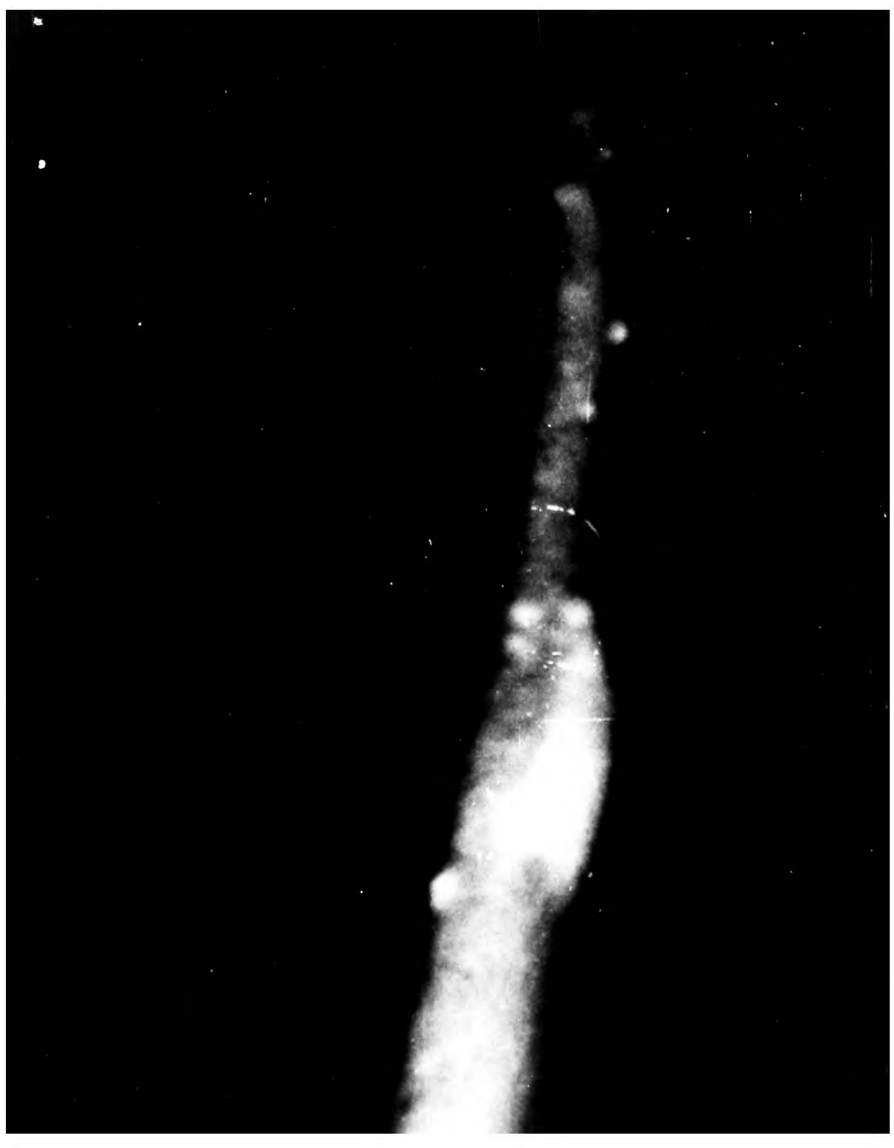


FIG 3.3



reflection from silicon (Fig. 3.3). The contrast arises from defects generated in the areas which have been heavily doped with boron. A ZnS (Ag) phosphor of thickness 200 μm was deposited directly on the fibre optic plate of the XX 1060 and an ENRAF generator with a copper target was operated at 40 kV 15 mA using the 0.4 mm spot focus at a distance of 40 cm. In transmission, the illumination was insufficient to overcome the dark-noise in the intensifier tube.

Two satisfactory systems for low fluxes have so far been devised, (Lang and Reifsnider, 1969; Meieran et al., 1969). Lang and Reifsnider used an EMI 9694, (Randall 1966), with a CsI (Th) single crystal phosphor (or Zn (Ag) powder) and produced excellent topographs from low intensity beams in which individual dislocations could be observed. Meieran et al. used an intensifier which was coupled to an extremely sensitive S.E.C. (secondary electron conduction) tube. The resolution of this system, using a magnifying lens giving a 2.4 X enlargement between screen and intensifier, is about 30 μm.

While these last two systems give excellent direct display topographs, the intensifier is bulky, fragile and expensive. In general, the systems which rely on conversion of the X-rays to electrical signals are more robust and cheaper.

b) Electronic Amplification Devices

Three systems have been described in which the absorption of X-rays with the subsequent photo-emission of electrons is utilised, (Chickawa and Fujimoto, 1968; Rozgonyi et al., 1970; Parpia and Tanner, 1971). Chickawa and Fujimoto absorbed the

X-rays in the PbO photocathode of a vidicon tube fitted with a Beryllium window. The thickness of the photo-conductive target layer was the limiting factor in the resolution achieved. The sensitivity is dependent on the fraction of X-rays absorbed in the target layer, which decreases as the resolution increases. For a resolution of 30 μm a rotating anode generator was required to provide the necessary high flux.

The system of Rozgonyi et al. using a silicon diode array to absorb the X-rays, gave a resolution of 15 μm. However, this requires the array to be thin and unless a rotating anode generator is used, only with soft radiation is the absorption enough to produce a signal above the dark current.

A cheaper and more sensitive system has been constructed using a channel multiplier array, more often known as a channel plate, (Parpia and Tanner, 1971).

2. Direct Display using a Channel Plate

a) Principles of operation

The channel electron multiplier, (Adams, 1966; Adams and Manley, 1965, 1966, 1967), consists of a lead glass tube coated with a semi-insulating layer, with a length to diameter ratio of about fifty. The resistance between the ends is between 10^8 and 10^{14} ohms. In vacuum, and with a potential of the order of 1 kV applied across the ends, any electron entering the low potential end will be accelerated by the axial electric field. A collision with the wall causes secondary electrons to be emitted which are in turn accelerated and generate an electron cascade. At 1 kV, the gain is typically 10^3, while at

3 kV the gain may be up to 10^8. As the gain is dependent only on the length to diameter ratio, the multiplier may be scaled down and honeycombed arrays of multipliers, channel plates constructed, (Guest, Holmshaw and Manley, 1969).

The techniques for manufacture are similar to those used for fibre optics and the glass tubing is drawn down to the required diameter, stacked together, sliced and polished to obtain the required dimensions. The semi-insulating layer is produced by reduction of the glass, producing a layer a few tens of Ångstroms thick. Electrical contact between the tubes is made by an evaporated nicrome film so that a potential may be applied to the array by a ring electrode.

For use as an X-ray detector, the incident X-rays are absorbed in the channel plate matrix and any ejected photo-electrons which find their way into the channel are accelerated and multiplied, (Fig. 3.4). Electrons emerging from the rear of the channel plate are post accelerated through about 8 kV onto a fluorescent screen. The probability of detection of a photo-electron is discussed in the last section of this chapter.

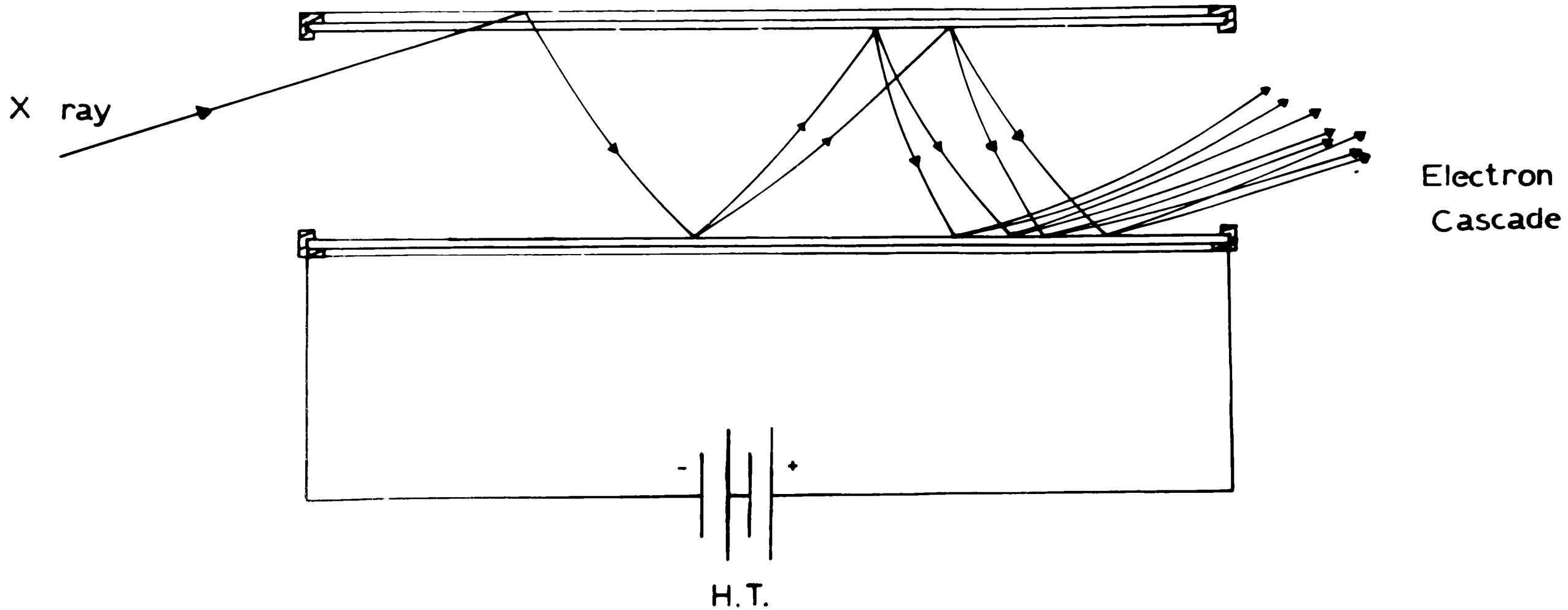
b) Instrumental

In the instrument constructed by the author, proximity focussing of the electrons emerging from the channel plate was employed. A similar system using one loop electromagnetic focussing, (Turner et al., 1969) has been constructed by Parpia in Cambridge, (Parpia and Tanner, 1971).

The channel plate used was the Mullard G40-20 S plate

FIG 3.4

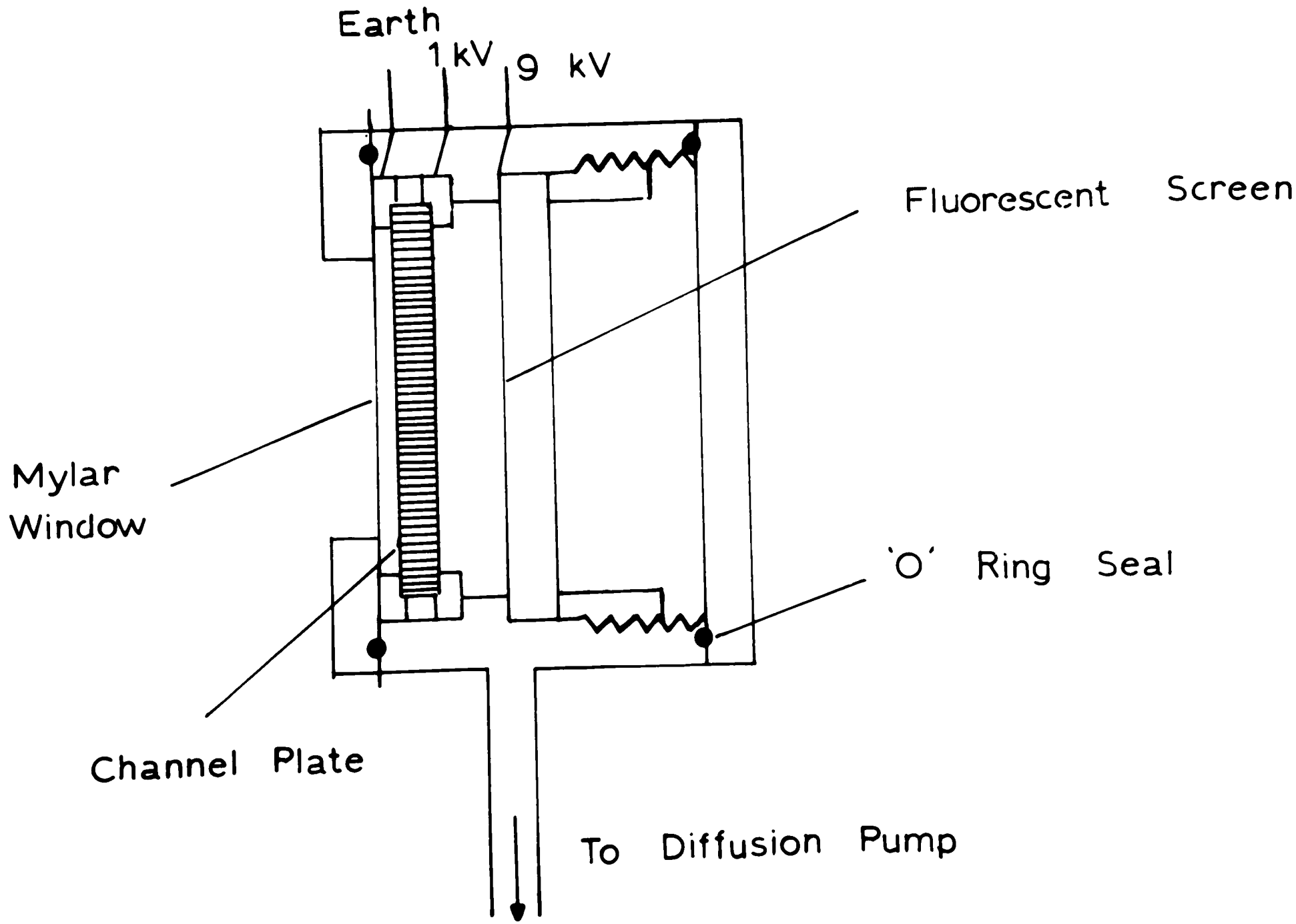
Channel Electron Multiplier
as an X ray Detector



with channel diameter 40 μm, and pitch 50 μm inclined at an angle of 13° to the plate normal. Figure 3.5 is a schematic diagram of the device. The channel plate is held securely in its ring holder by the pressure of the atmosphere on the Mylar window which bows inwards against the channel plate. The fluorescent screen is pressed against H.T. contacts by a large hollow screw and the whole assembly is machined out of perspex for the sake both of transparency and insulation. To obtain proximity focussing the gap between plate and screen was about 1.5 mm, with an applied potential of 8 kV. In order to prevent the phosphor flaking off under the high field gradient, a technique of screen preparation due to Mr. T.F. Godfrey was employed. The glass disc was coated with tin oxide to produce a conducting layer and the P1 phosphor (Mn: Zn_2 SiO_4) was deposited through acetone. A few drops of ortho-phosphoric acid, however, added to the solution produced a great improvement in the bonding of the phosphor to the disc. Electrical contact was made by pressure against fine wires which were brazed onto brass stubs on the outside of the holder. Vacuum sealing of the stubs was provided by small 'O' ring seals. The power supplies used were a 30 kV Brandenburg Unit Type No. 800 and a 5 kV ex-Harwell Unit Type No. 1359A. To safeguard against overload of the channel plate, a 130 Mohm limiting resistor was included in the channel plate - screen circuit. In the event of a short circuit between the channel plate and screen, this would prevent excessive currents being drawn, thus avoiding burning out the channel plate.

The front and back plates were each secured by six 2 B.A.

FIG 3.5


Earth
1 kV
9 kV
Fluorescent Screen
Mylar Window
'O' Ring Seal
Channel Plate
To Diffusion Pump

screws with an 'O' ring seal. This arrangement facilitated the removal of components. As the Mylar had an aluminium coating, it proved possible to dispense with the front ring and make the earth contact to the Mylar itself.

An idea of the size of the holder may be obtained from Fig. 3.6, and the actual layout from the drawing in Fig. 3.7. The only bulky part of the apparatus was the pumps which enabled pressures of about 5×10^{-5} torr to be maintained.

c) Experimental

Using the wide beam technique of X-ray topography, topographs were taken of a silicon wafer which had undergone a heavy boron diffusion in selected areas 1 mm square. Strains in the diffused region due to the mis-match of ionic radii, (Prussin, 1961), generated dislocations which produced enhanced contrast in the diffracted X-ray beam. Figure 3.8(a) shows the 111 reflection topograph recorded on the screen of the channel plate intensifier and Fig. 3.8(b) shows the same image recorded on Ilford L4 Nuclear Emulsion. The image on the intensifier was photographed on 100 ASA film at f 5.6 with an exposure of 30 seconds (with a magnification of unity). The nuclear emulsion exposure took 5 minutes. The Elliott GX 6 generator was operated at 50 kV 10 mA on the 2mm line focus, using a copper target, with a source of specimen distance of 40 cm. This corresponds to a value for $\frac{P}{H.D.}$ of 6.25 watts/mm/cm. No photomultiplier was needed to set up the topograph.

Satisfactory topographs were obtained in transmission at slightly higher power, but due to the limited width of the

FIG 3.6

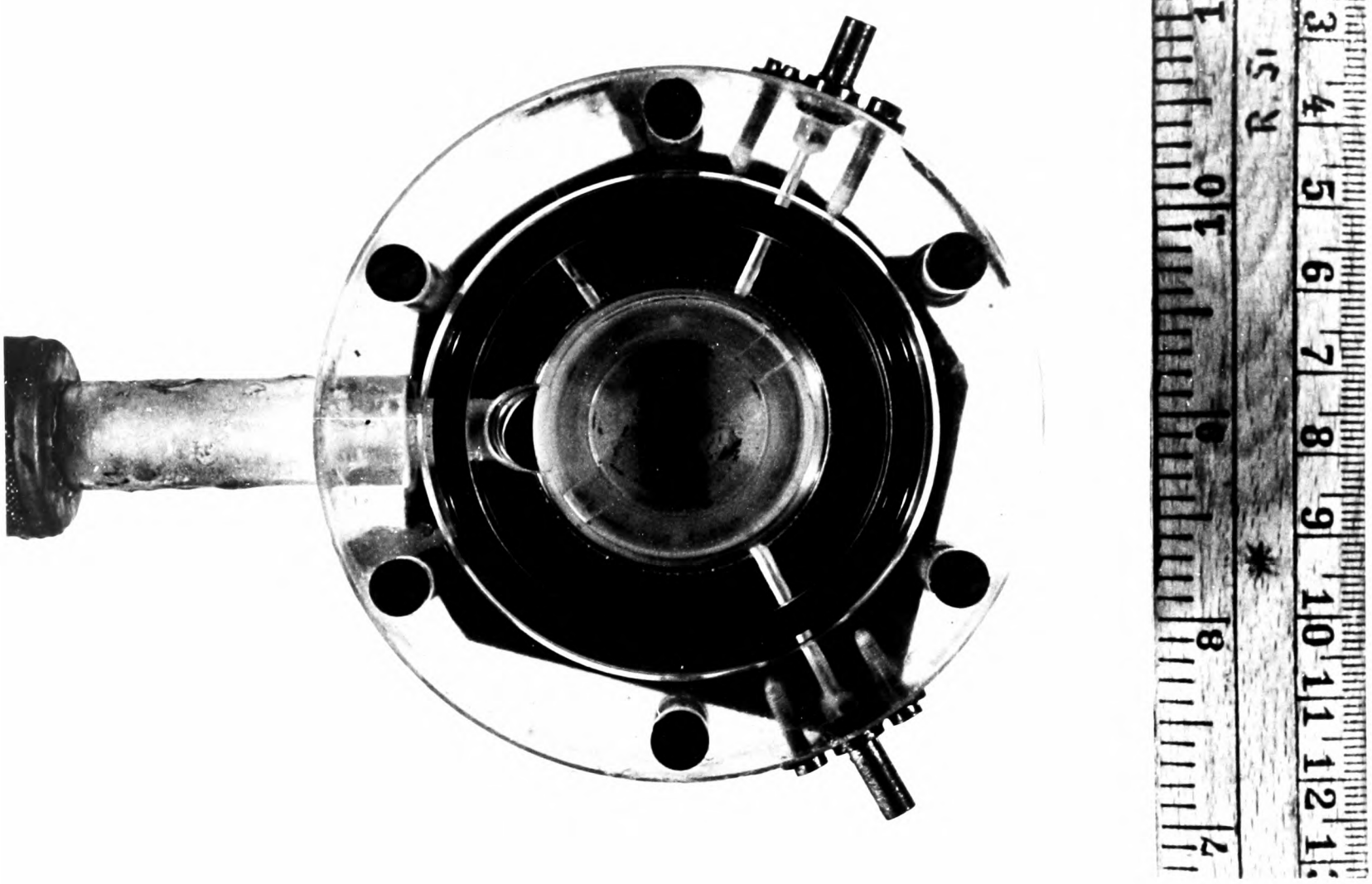


FIG 3.7

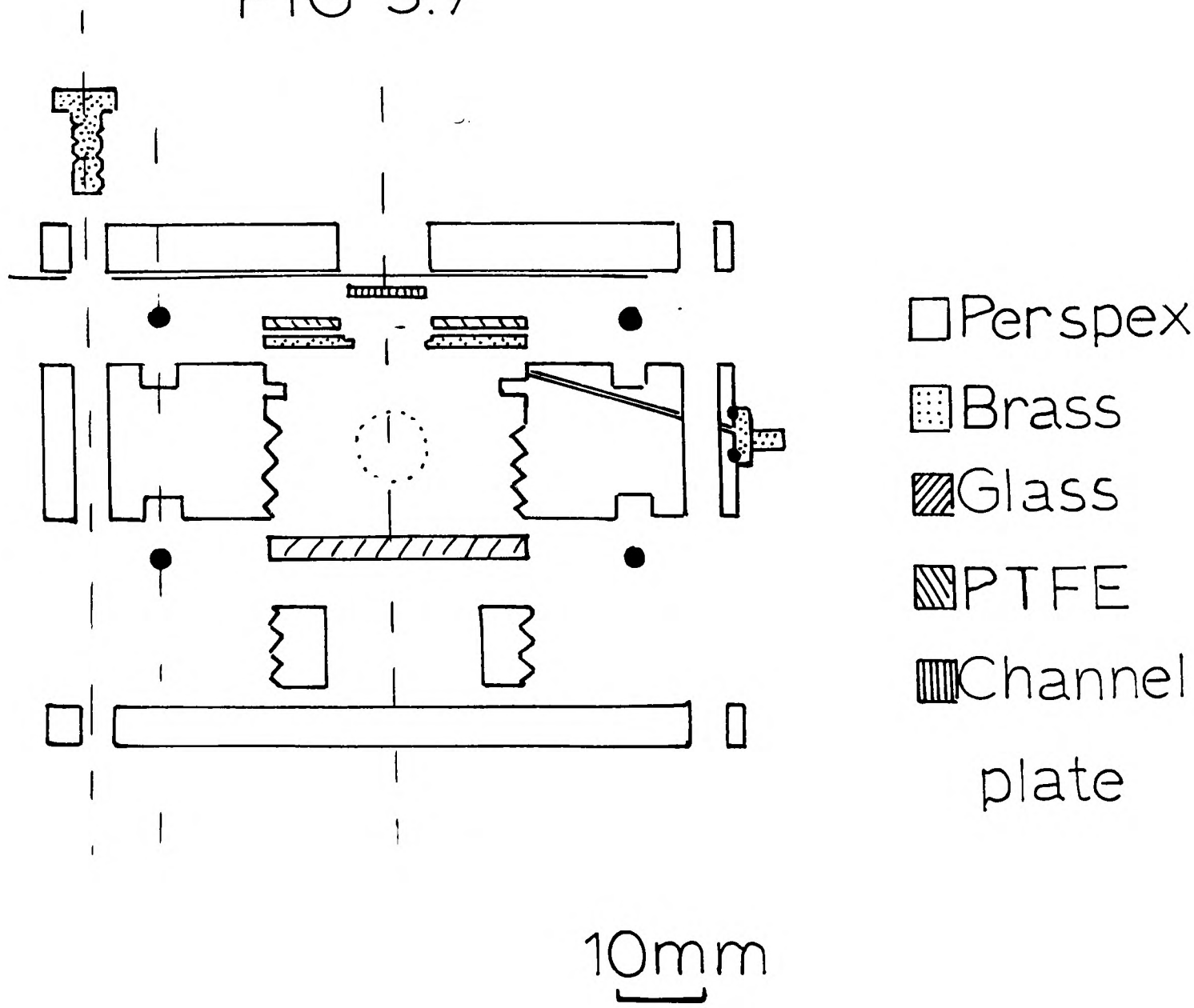


FIG 3.8



1m.m.



(a)

(b)

X-ray beam were less spectacular. No attempt was made to adapt the device for scanning in the Lang technique, but this is quite feasible in principle using an edge-welded bellows on the vacuum line.

From the topograph, the minimum distance measurable at the corner of the diffused region is about 100 microns. As a result of the inevitable divergence of the imaging electrons in the proximity focussing mode, this resolution is what may be expected of the device. Parpia, using the single loop electromagnetic focussing mode, has achieved a resolution of 50 μm, the limit set by the pitch of the channels. This improved focussing tends also to improve contrast. The major advantage of the electromagnetic focussing is, however, the fact that the increased distance between plate and screen reduces the electric field gradient and consequently the problem of the phosphor flaking off was not encountered. In both devices care was necessary to avoid sharp points on the electrodes which gave rise to field emission. This was overcome by polishing the electrodes.

The major advantage in proximity focussing is that the device is less bulky, simpler to construct and cheaper than using electromagnetic focussing. It is possible to construct a robust and efficient direct display device for X-ray topographic images for a few hundred pounds. As laboratories may often have vacuum pumps and H.T. units removed from obsolete equipment, the net outlay may well by only that of the channel plate itself.

3. Efficiency of Channel Plates to X-rays of Wavelengths 0.5 - 2 Å

a) Considerations of method

No experimental work has yet been concerned with the detection efficiency of Channel multipliers and plates to X-rays of crystallographic wavelength (0.5 - 2 Å). The studies on soft X-rays, (Smith and Pounds, 1968; Parkes et al., 1970), showed that the efficiency of the channel plate varied quite sharply with the angle of incidence of the X-ray to the channel wall giving a peak efficiency at about 6°, this angle being nearly independent of wavelengths from 68 to 2 Å. The peak detection efficiency varied from 3.5% at 2.1 Å to 16% at 68 Å, falling off to nearly zero by the time the angle of incidence reached 30°, (Parkes et al., 1970). Both the experimental evidence and theoretical calculations showed that the peak detection efficiency fell with decreasing wavelengths.

Calculations and measurements of the detection efficiency of channel plates to hard X-rays, i.e., upwards of 80 keV, indicated that the efficiency fell with increasing wavelengths, (Adams, 1965). The crystallographic region appeared to lie in the trough.

In the hard and soft wavelength regions, rather different models for the absorption and subsequent detection of a photo-electron were employed, and at first sight it was not obvious which mechanism would dominate in the crystallographic region. Adams considered the X-rays to enter the channel plate matrix

parallel to the channel and on absorption to eject a photo-electron with a given range. From geometrical considerations and assuming there is a constant probability that an electron will have any range up to a value known as the effective range, the detection efficiency is derived. Further assumptions are that only one mono-energetic electron is ejected for each X-ray absorbed, no 'cascade' processes occur, and also that the distribution of ejected electrons is isotropic. In the crystallographic region, the effective electron range is only a few hundreds of Angstroms and only a thin cylinder surrounding the channel contributes to the detection on this model. Efficiencies thus calculated give values of the order of a few tenths of a percent in the region 0.5 - 2 Å.

Smith and Pounds consider the X-rays to enter the channel wall at an angle. Using the photo-electron yield, derived on the assumption that the photo-electron flux falls off exponentially with depth, (Rumsh et al., 1960), the efficiency for a cylindrical photocathode was calculated.

As electron absorption coefficients in the range 5 - 20 keV were not readily available the present author has used a method similar to Smith and Pounds, but based on the effective range, for which data is available, (Coslett and Thomas, 1964). The method is then a hybrid between that of Smith and Pounds and that of Adams. It will be seen that to first order, the efficiency distribution as a function of angle is identical with that of Smith and Pounds. Indeed, it is shown that the distribution is identical to first order for any function for the decay of the electron flux, provided that the emission of electrons is isotropic.

b) Photo-electron Yield

Consider the X-rays to make an angle α with the channel wall, (Fig. 3.9), and let the intensity at a point (X,Y) inside the wall be I.

Intensity absorbed in dx dy = $I \mu \sec\alpha \, dy$ (3.2)

The fraction of mono-energetic photo-electrons ejected with ranges between R and R + dR which escape into the channel is that fraction contained in the hemi-spherical cap of radius R, assuming no electrons cross channels and that the distribution is isotropic.

Thus, provided R is much less than the thickness of the wall and the diameter of the channel :

Fraction of electrons escaping = $\frac{1}{2}(1 - \frac{X}{R})$ (3.3)

Now $I = I_o \, e^{-\mu \sec\alpha \, y}$ (3.4)

where I_o is the incident intensity.

Also, $y = x \cot \alpha$ (3.5)

Then the fraction detected

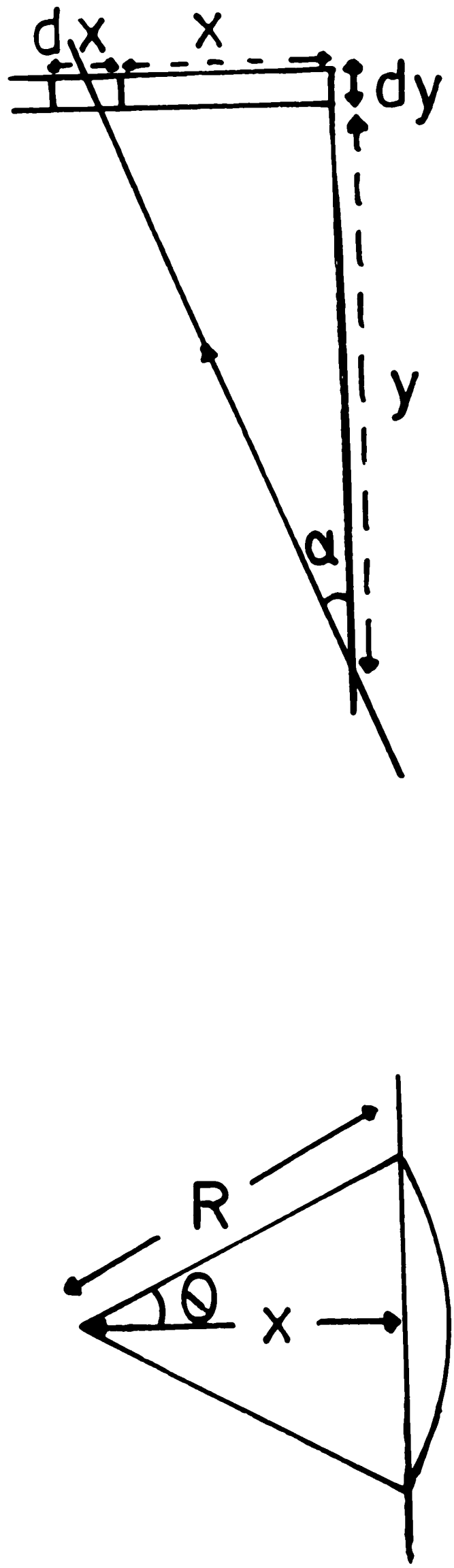
$$= \frac{\mu}{2}(1 - \frac{x}{R}) \operatorname{cosec} \alpha \, e^{-\mu \operatorname{cosec} \alpha \, x} \, dx \qquad (3.6)$$

Total fraction entering the wall that are detected is the

$$\int_o^R \frac{\mu}{2} (1 - \frac{x}{R}) \operatorname{cosec}\alpha \, e^{-\mu x \operatorname{cosec}\alpha} \, dx$$

$$= \frac{1}{2} \left[1 - \frac{\sin \alpha}{\mu R} (1 - e^{-\mu R \operatorname{cosec}\alpha}) \right] \qquad (3.7)$$

FIG 3.9



If the range distribution is taken such that the number of electrons with range between R and R + dR,

$$dN = \frac{N}{R_p} dR \qquad (3.8)$$

where N is the total number of electrons and R_p is the effective range, one then obtains for the fraction of X-rays entering the wall at angle α which are detected :-

$$\chi_\alpha = \frac{1}{2}\int_0^{R_p} \frac{1}{R_p}\left(1 - \frac{\sin\alpha}{\mu R}\left(1 - e^{-\mu R \operatorname{cosec}\alpha}\right)\right) dR \qquad (3.9a)$$

$$= \frac{\mu R_p}{8} \operatorname{Cosec}\alpha - \frac{\mu^2 R_p^2}{36} \operatorname{Cosec}^2\alpha + \left(\cdots \right. \qquad (3.9b)$$

Equation 3.9 should be compared with the photo-electron yield, χ_α, calculated by Rumsh et al. :

$$\chi_\alpha = A\left(\frac{\mu}{a'} \operatorname{Cosec}\alpha - \frac{\mu^2}{a'^2} \operatorname{Cosec}^2\alpha + \left(\cdots \right.\right.$$

where A is a constant, μ is the X-ray absorption coefficient, again, and a' is the electron absorption coefficient.

To first order, one then has an identical distribution and it will be seen that only when α becomes less than about 10° is the second term important and the distributions diverge. It may be shown that provided the emission is isotropic, the distribution is independent of the function used to describe the decay of the electron flux.

Suppose only some fraction of the photo-electrons f(x) reach the surface. That f(x) is solely a function of x implies

Then photo-electron yield will be

$$\chi_a = \int_{x_1}^{x_2} \frac{\mu}{2} \text{ Cosec } a \; e^{-\mu \text{ cosec } a \; x} \; f(x) \; dx \qquad (3.10)$$

Provided we can make the approximation :

$$e^{-\mu \text{ cosec } a \; x} = 1$$

i.e., we do not consider small angles

$$\chi_a = \frac{\mu}{2} \text{ cosec } a \int_{x_1}^{x_2} f(x) \; dx \qquad (3.11)$$

where x_1 and x_2 are the chosen limits of integration.

This gives

$$\chi_c = \mu \; G \; \text{Cosec} a \qquad (3.12)$$

where G is a factor determining the total fraction of electrons which escape.

Thus provided that it is possible to define an absorption coefficient for the incident radiation, one always finds a cosec$a$ distribution for the photo-electron yield. When the cross-section for absorption becomes so high that the probability of the photon being absorbed by the surface atoms becomes almost unity, one expects a photo-electric yield which is independent of angle of incidence. This is confirmed by the experimental data in the region 300 - 1200 A, (Heroux et al., 1965), provided that this is corrected for the refraction

at the vacuum-matrix interface, (Stanford et al., 1966).

c) Efficiency of an infinitely long cylindrical channel

For a cylindrical photocathode, the angle of incidence varies from 0 to θ, where θ is the angle the X-ray beam makes with the channel axis, (Fig. 3.10). Then, following the mathematics of Smith and Pounds, considering the wall to be made up of strips of which the area absorbing X-rays is given by :-

$$r \, d\psi \quad 2r \cos\psi \quad \cot\theta \tag{3.13}$$

Then count rate from strip is :

$$dn = N \quad 2r^2 \cos\psi \cot\theta \sin\alpha \quad \chi_\alpha \, d\psi$$

where N is the X-ray flux and χ_α is the yield at angle α

Now

$$\cos\psi = \sin\alpha \; / \; \sin\theta \tag{3.14}$$

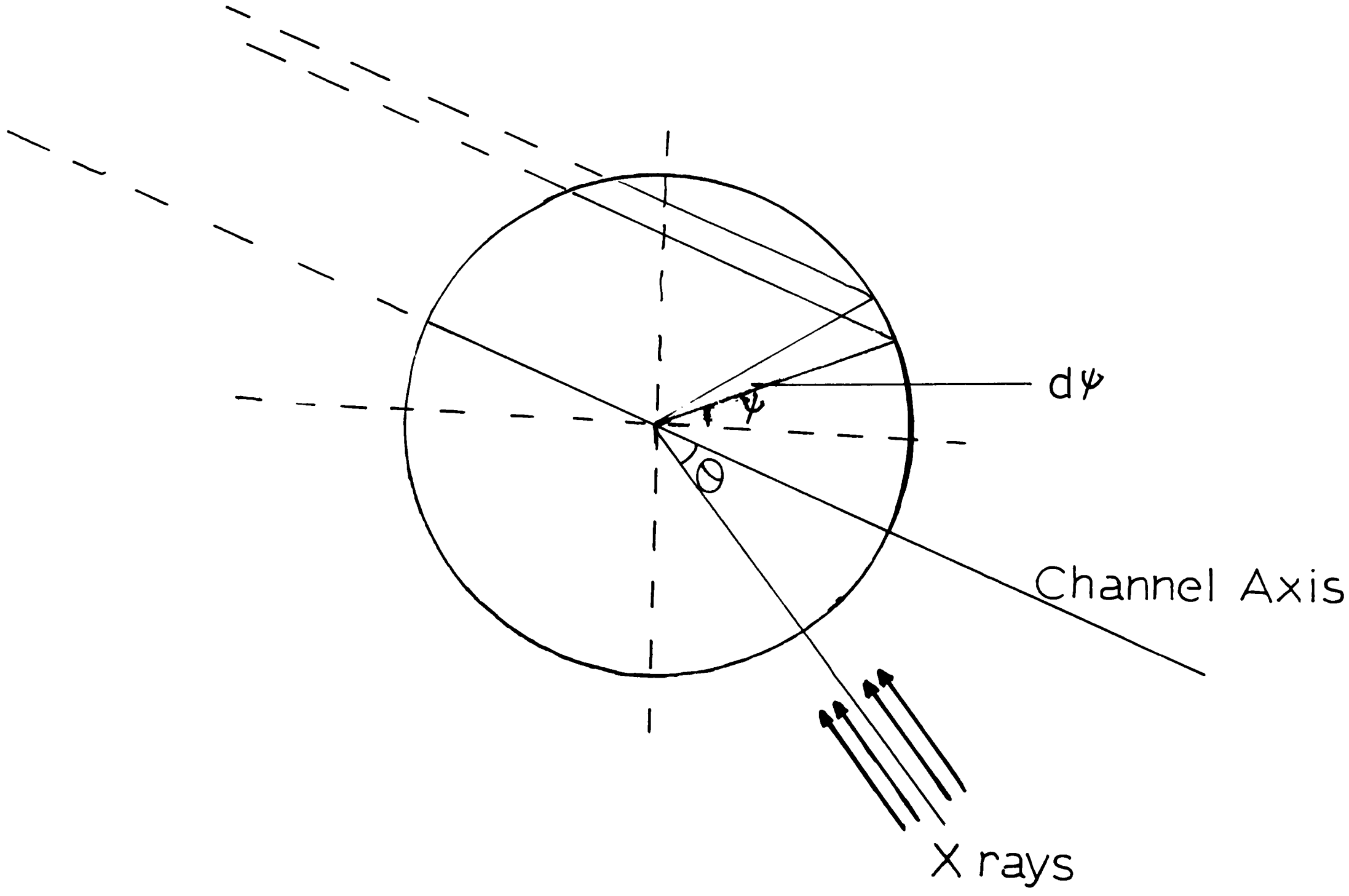
and the total count rate is found by integration over ψ up to a maximum value at which losses begin to occur due to total external reflection. If this happens at a value of $\alpha = \alpha_c$, one then obtains for the photon detection efficiency :-

$$\text{p.d.e.} = \frac{1}{N \pi r^2} \int_{-\psi_{max}}^{\psi_{max}} dn$$

$$= \frac{4r^2}{N \pi r^2} \cot\theta \; N \int_0^{\psi_{max}} \sin\alpha \quad \chi_\alpha \cos\psi \, d\psi$$

$$= \frac{4}{\pi} \quad \frac{\cot\theta}{\sin\theta} \int_{\alpha_c}^{0} \frac{\chi_\alpha \sin^2\alpha \cos\alpha \, d\alpha}{(\sin^2\theta - \sin^2\alpha)^{\frac{1}{2}}} \tag{3.15}$$

FIG 3.10



If the open channel takes up only a fraction (I - F) of the entire face-plate, one obtains by substitution of equation (3.9), and integration :-

$$\text{p.d.e.} = \frac{1-F}{2\pi}\ \mu R_p\ \text{Cot}\theta\ \left(1 - \frac{\sin^2\alpha_c}{\sin^2\theta}\right)^{\frac{1}{2}}$$

$$- (1-F)\ \frac{\mu^2 R_p^2}{18}\ \text{Cot}\theta\ \text{Cosec}\theta$$

$$+ (1-F)\ \frac{\mu^2 R_p^2}{9\pi}\ \text{Cot}\theta\ \text{Cosec}\theta\ \left\{\sin^{-1}\left(\frac{\sin\alpha_c}{\sin\theta}\right)\right\} + (\ \cdots\cdot \qquad (3.16)$$

Provided $\alpha_c \ll \theta$

$$\text{p.d.e.} = \frac{1-F}{2\pi}\ \mu R_p\ \text{Cot}\theta - \frac{1-F}{18}\ \mu^2 R_p^2\ \text{Cot}\theta\ \text{Cosec}\theta \qquad (3.17)$$

A plot of μR_p as a function of wavelengths is shown in Fig. 3.11. Values of ρR_p (where ρ is the density of the matrix) are independent of the material, (Coslett and Thomas, 1964), and taken from that paper. Values of $\frac{\mu}{\rho}$ are taken from the Handbook of Chemistry and Physics (1961) for a glass of composition shown in Table 3.3, (Guest, 1970).

Using the above data, the photon detection efficiency of the 40 μm diameter channel plate as a function of angle of incidence is given for CuK and CrK radiations in Fig. 3.12. [Here, I-F = 0.62, (Guest et al., 1969).]

FIG 3.11

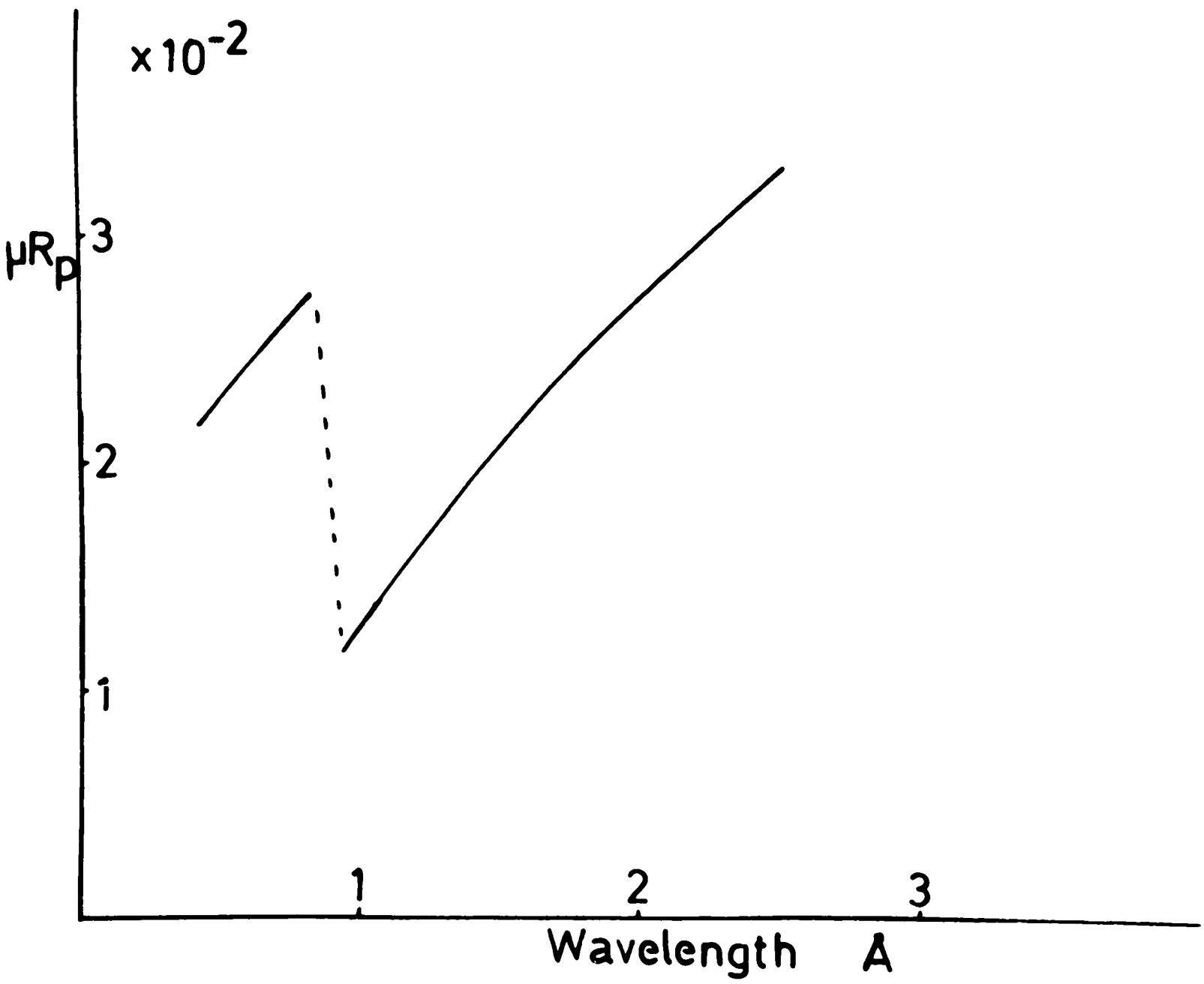


FIG 3.12

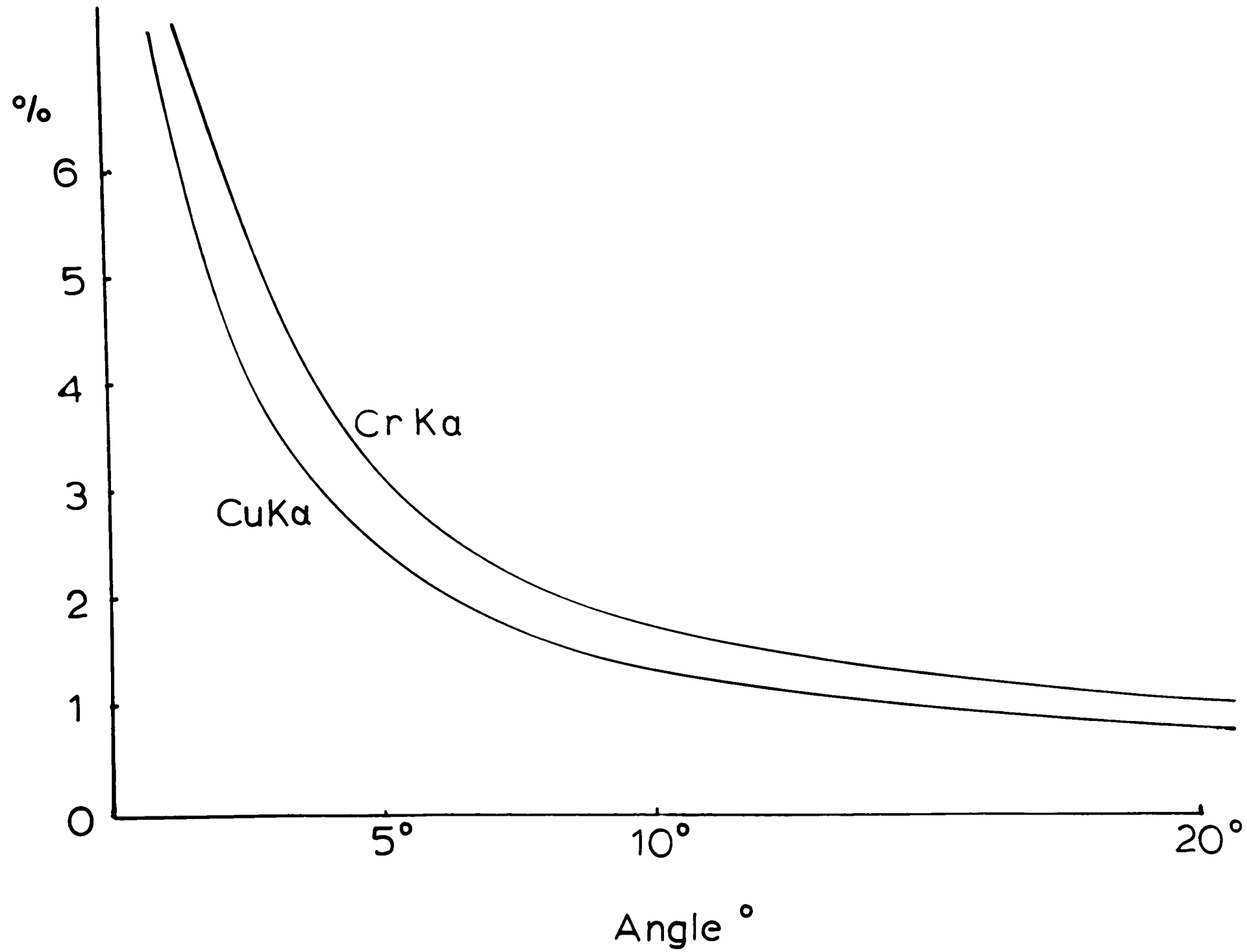


Table 3.3

Approximate composition of Channel Plate Matrix

Substance	Mole %
SiO_2	72
Pb	11
Na	5
K	5

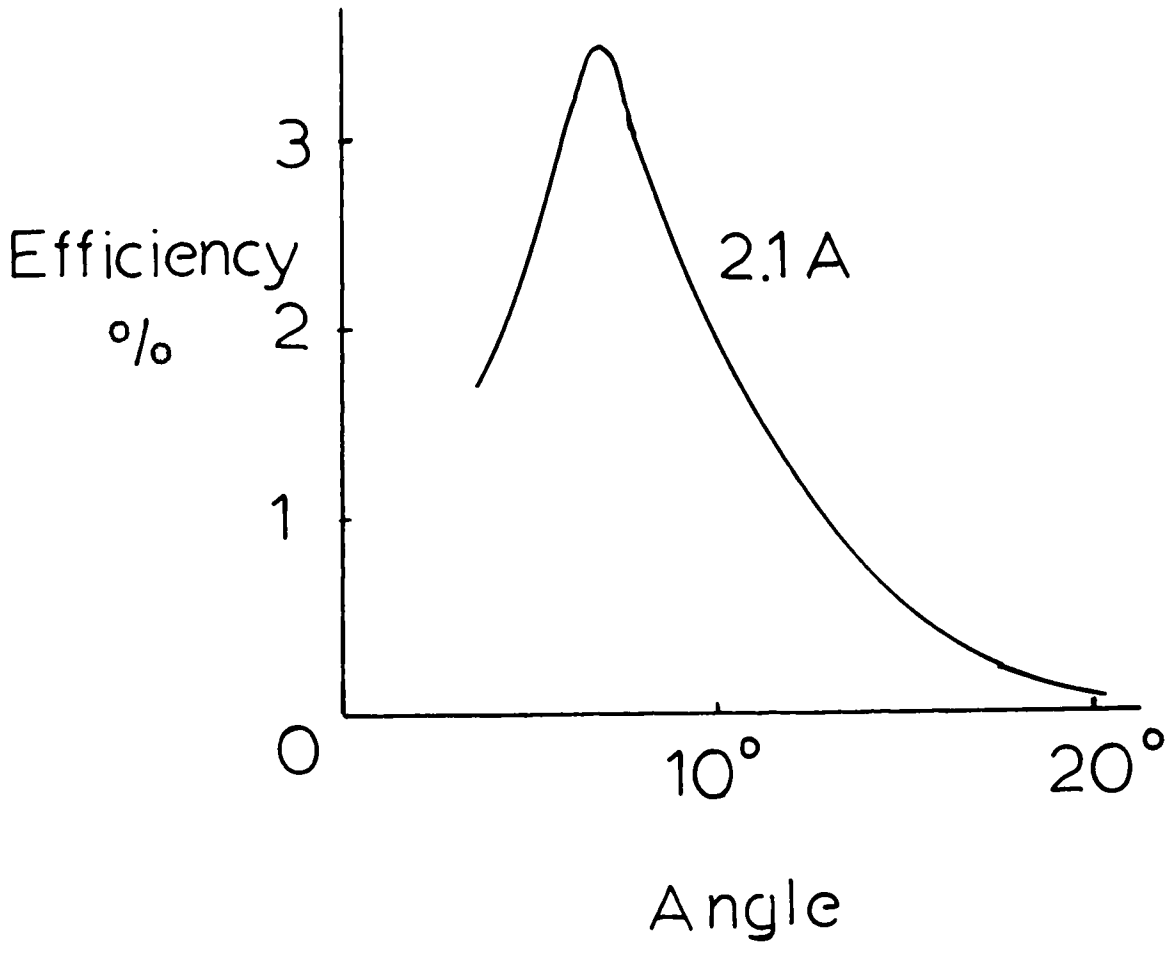
(Remainder of composition classified by Mullard Ltd.)

d) Photon Detection efficiency as a function of angle - comparison with experiment

The experimentally determined efficiency, as a function of angle at 2.1 Å, taken from the paper of Parkes et al. is reproduced in Fig. 3.13. At first sight, the comparison with Fig. 3.12 is not striking. The Cotθ variation fits the experimental curve of Smith and Pounds on a single channel multiplier much better than the results of Parkes et al. on a channel plate.

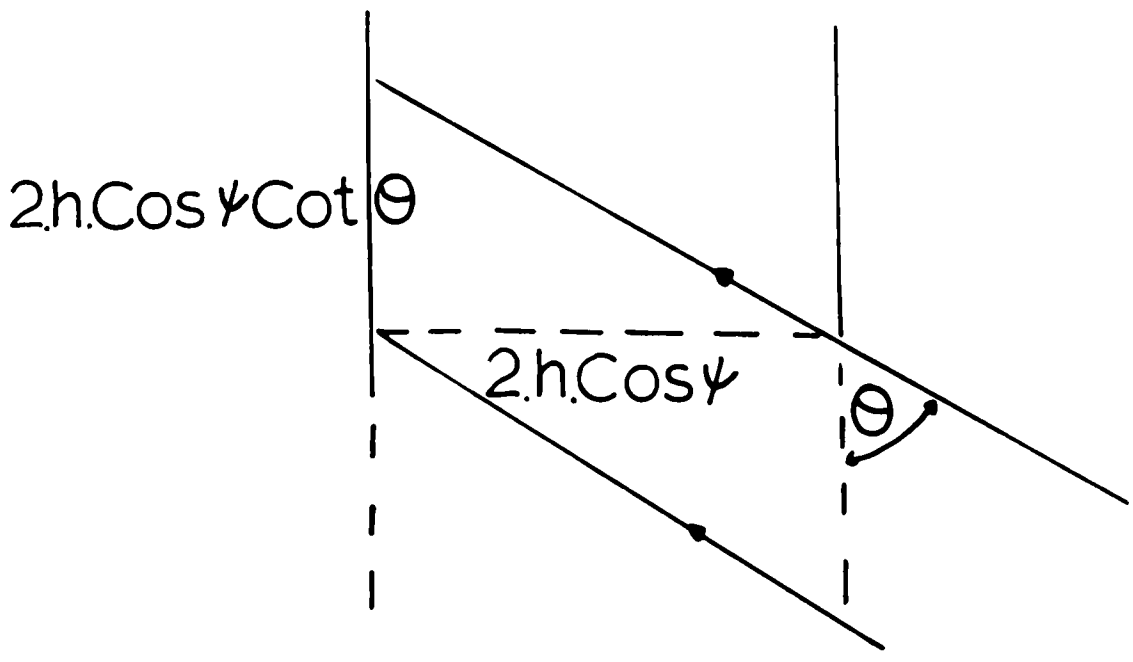
In the low angle region, the discrepancy would appear to be connected with the fact that the calculations were done for an infinitely long channel. In the experiments at Leicester, only pulses emerging from the channel plate with a charge above a certain value were selected. This may well mean that X-rays entering the channel wall quite far down the channel were not detected. At large angles this would be

FIG 3.13



(Due to Parkes et al)

FIG 3.14



a negligible fraction, but would become significant at low angles. Hence the efficiency might be expected to fall in the low angle region, and it will be shown later that this is indeed the case.

To account for the peak detection efficiency lying at about 6^{o} and being nearly independent of angle over a large wavelength range, it appears that this correction for a finite channel length is the only plausible one. Smith and Pounds gave α_c as the critical angle of the radiation concerned. While this was a plausible explanation for the drop in efficiency at low angles at 67 Å, reflection losses will not begin to occur in the wavelength region 0.5 - 2 Å before about 0.1^{o}. In the following section, the theory is modified to take into account only those X-rays which are absorbed within a distance δ from the entrance of the channel. Only electrons entering the channel such that they are accelerated through nearly the whole potential across the plate are considered to give large enough cascade pulses to be detected.

e) <u>Small angle correction</u>

As small angles may require higher order terms in χ_{α} to be considered, it is important that the region in which a given number of terms will give a good approximation be investigated.

From equation (3.9a) :-

$$\chi_a = \frac{1}{2}\left\{\frac{\mu R_p}{2.2!}\,\mathrm{Cosec}\,a - \frac{\mu^2 R_p^2}{3.3!}\,\mathrm{Cosec}^2 a + \frac{\mu^3 R_p^3}{4.4!}\,\mathrm{Cosec}^3 a + \cdots\cdots \cdots\cdots \frac{(-1)^{n+1}\,(\mu R_p)^n\,\mathrm{Cosec}^n a}{(n+1)\,(n+1)!}\right\} + \cdots\cdots \qquad (3.18)$$

Table 3.4 shows these terms evaluated for CuKα radiation ($\mu R_p = 2 \times 10^{-2}$). From it, one can see that provided the region less than about 1^o is not considered, taking two terms is sufficient.

Table 3.4

Photo electron yield

a^o	T_1	T_2	T_3
5	2.9×10^{-2}	1.1×10^{-3}	
4	3.5×10^{-2}	2.2×10^{-3}	
3	4.8×10^{-2}	3.6×10^{-3}	3×10^{-5}
2	7×10^{-2}	8.8×10^{-3}	8×10^{-4}
1	1.4×10^{-1}	3.4×10^{-2}	8×10^{-3}
0.5	2.9×10^{-1}	1.4×10^{-1}	5×10^{-2}
0.2	7.3×10^{-1}	9×10^{-1}	8×10^{-1}
0.1	1.45	4	8
0.01	14.5	400	8000

Consider, as in Fig. 3.14, a section across a channel such that the projected diameter is $2h\mathrm{Cos}\,\psi$, where 2h is the channel diameter. The length of channel down which X-rays is absorbed

is $2h\text{Cos}\,\phi\,\text{Cot}\theta$.

If only those absorbed in a length δ are detected, then if $2h\text{Cot}\theta\,\text{Cos}\,\phi > \delta$ we get a loss in detection efficiency.

As $\text{Cos}\,\phi = \sin\alpha/\sin\theta$, this happens at a critical grazing angle of incidence α_L such that

$$\sin\alpha_L = \frac{\delta}{2h}\sin\theta\tan\theta \qquad (3.19)$$

No losses occur at all for values of θ above θ_L where

$$\text{Cot}\theta_L = \frac{\delta}{2h} \qquad (3.20)$$

When losses occur, for values of α from 0 to α_L, the detection is complete and for values of α from α_L to θ only a fraction, $\frac{\delta}{2h\text{Cot}\theta\,\text{Cos}\,\phi}$ is the beam is detected.

One then obtains for the photon detection efficiency :-

$$\text{p.d.e} = \frac{4}{\pi}\frac{\text{Cot}\theta}{\text{Sin}\theta}\int_0^{\alpha_L}\frac{\chi_\alpha \sin^2\alpha\cos\alpha}{(\sin^2\theta-\sin^2\alpha)^{\frac{1}{2}}}\,d\alpha$$

$$+\frac{4}{\pi}\frac{\text{Cot}\theta}{\text{Sin}\theta}\int_{\alpha_L}^{\theta}\frac{\chi_\alpha \sin^2\alpha\cos\alpha}{(\sin^2\theta-\sin^2\alpha)^{\frac{1}{2}}}\cdot\frac{\delta}{2h\sin\alpha}\cdot\frac{\sin\theta}{\cot\theta}\,d\alpha \qquad (3.21)$$

$$=\frac{4}{\pi}\frac{\text{Cot}\theta}{\text{Sin}\theta}\int_0^{\alpha_L}\frac{\chi_\alpha \sin^2\alpha\,d(\sin\alpha)}{(\sin^2\theta-\sin^2\alpha)^{\frac{1}{2}}}+\frac{2\delta}{h\pi}\int_{\alpha_L}^{\theta}\frac{\chi_\alpha \sin\alpha\,d(\sin\alpha)}{(\sin^2\theta-\sin^2\alpha)^{\frac{1}{2}}} \qquad (3.22)$$

Substitution for χ_α and integration gives :-

$$\text{p.d.e.} = \frac{4}{\pi}\ \text{Cot}\theta\ \frac{\mu R_p}{8}(1-F)\left(1-\left(1-\frac{\sin^2\alpha_L}{\sin^2\theta}\right)^{\frac{1}{2}}\right)$$

$$+\ \frac{4}{\pi}\cdot\frac{\delta}{2h}\cdot\frac{\pi}{2}\cdot\frac{\mu R_p}{8}(1-F)-\frac{4}{\pi}\cdot\frac{\mu R_p}{8}(1-F)\ \frac{\delta}{2h}\sin^{-1}\left(\frac{\sin\alpha_L}{\sin\theta}\right)$$

$$-\ \frac{4}{\pi}\text{Cot}\theta\ \text{Cosec}\theta\ \frac{\mu^2 R_p^{\,2}}{36}(1-F)\sin^{-1}\left(\frac{\sin\alpha_L}{\sin\theta}\right)$$

$$-\ \frac{4}{\pi}\cdot\frac{\delta}{2h}\cdot\frac{\mu^2 R_p^{\,2}}{36}(1-F)\ \text{Cosec}\theta\ \log_e\left(\frac{\sin\theta}{\sin\alpha_L}+\sqrt{\frac{\sin^2\theta-\sin^2\alpha_L}{\sin\alpha_L}}\right)$$

(3.23)

where the first three terms are due to the coseca term in χ and the last two terms are due to the $\text{cosec}^2\alpha$ term.

As $\dfrac{\sin\theta}{\sin\alpha_L} = \dfrac{2h}{\delta}\ \text{Cot}\theta$

the expression becomes :

$$\text{p.d.e.} = \frac{\mu R_p}{2\pi}(1-F)\left(1-\left(1-\left(\frac{\delta}{2h}\tan\theta\right)^2\right)^{\frac{1}{2}}\right)$$

$$+\ \frac{\mu R_p}{4}\cdot\frac{\delta}{2h}(1-F)-\frac{\mu R_p}{2\pi}(1-F)\cdot\frac{\delta}{2h}\cdot\sin^{-1}\left(\frac{\delta}{2h}\tan\theta\right)$$

$$-\ \frac{\mu^2 R_p^{\,2}}{9\pi}(1-F)\ \text{Cot}\theta\ \text{Cosec}\theta\cdot\sin^{-1}\left(\frac{\delta}{2h}\tan\theta\right)$$

$$-\ \frac{\mu^2 R_p^{\,2}}{9\pi}(1-F)\cdot\frac{\delta}{2h}\cdot\text{Cosec}\theta\ \log_e\left(\frac{2h\ \text{Cot}\theta}{\delta}+\sqrt{\left(\frac{2h\ \text{Cot}\theta}{\delta}\right)^2-1}\right)$$

(3.24)

This is plotted for radiation of wavelength 1.5 Å and 4 Å

in Fig. 3.15, taking $\theta_L \simeq 5.5^o$ so that $\frac{\delta}{2h} = 10$. It is seen that a maximum occurs at about 4^o and the efficiency drops towards zero as the angle of incidence drops to zero. As θ tends towards θ_L, the expression tends to expression (3.17), being equal to the expression for no end correction at θ_L. The absolute magnitude of the peak efficiency is in reasonable, though by no means good, agreement with experiment, being between 20 and 30% too low. It may be that this discrepancy will disappear if cascade processes, in which the excited atom decays emitting a fluorescent X-ray which is subsequently re-absorbed, are taken into account. The peak may be shifted to a larger angle if a larger value of θ_L were chosen, but the magnitude of the peak would then drop. The theory offers no explanation for the rapid drop to zero of the experimental efficiencies by 20^o. However, as the efficiency measured by Smith and Pounds on a single channel multiplier, which has a much larger diameter, fell off much more slowly, only reaching zero at 75^o, it may be that the nicrome film used in making electrical contact between channels in the channel plate is responsible. This film extends a short distance into the channel, and in this region the presence of a negatively charged metal film is likely to repel any photo-electron created in the matrix which would otherwise have escaped into the channel. This, added to the fact that the detection efficiency for nicrome, which is proportional to $\frac{\mu}{\rho}$, is about half that of lead glass, could be the explanation for this loss of detection efficiency.

FIG 3.15

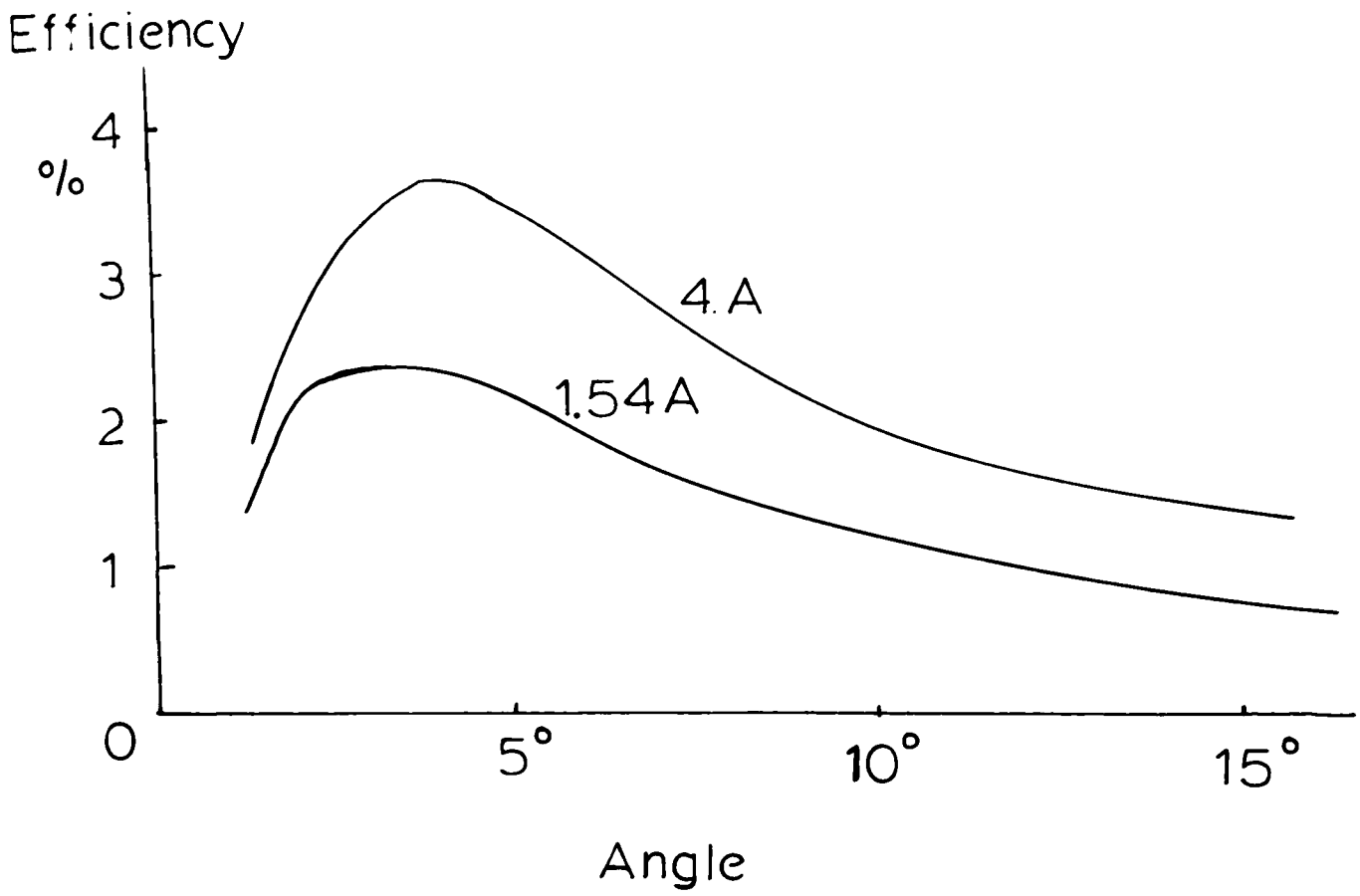
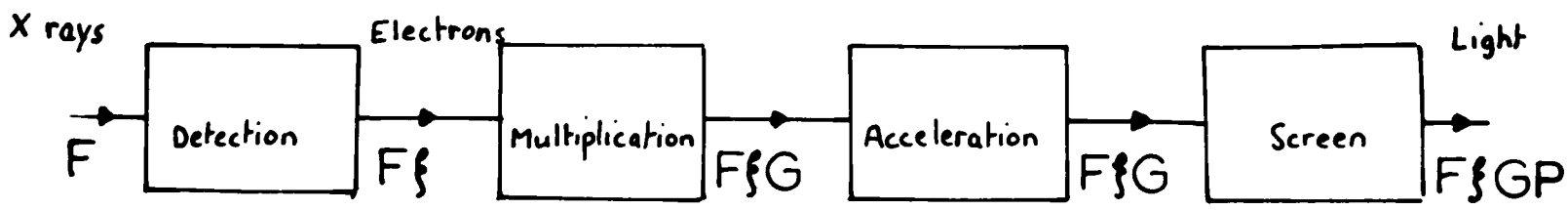


FIG 3.16



where

F is X ray flux in counts / sec / m^2

ʃ is Detection Efficiency

G is Grain in channel plate

P is no. of green light photons liberated per 8 kv electron

f) Cascade processes and discussion of possible refinements of model

In this section, the effect of re-absorption of the fluorescent X-rays, which are emitted when the excited atom from which a photo-electron has been ejected to its ground state, is considered.

Consider, as before, X-rays entering matrix at angle α, with μ the absorption coefficient for the incident X-rays and μ' the absorption coefficient of the fluorescent X-rays.

Fraction of incident intensity absorbed at depth x in layer of thickness dx is :

$$\mu \operatorname{Cosec}\alpha \; e^{-\mu x \operatorname{cosec}\alpha} \; dx \; .$$

The flux of fluorescent X-rays will fall off exponentially with depth and let us consider those fluorescent X-rays reaching a layer of thickness R' from the channel (where R' is the range of that fraction of electrons with range between R' and R'+ dR' which are ejected on the subsequent absorption of the fluorescent radiation).

The total fraction reaching R' is given by :

$$dF = \int_0^\infty \mu \operatorname{cosec}\alpha \; e^{-(\mu x \operatorname{cosec}\alpha + \mu'(x-R')} \; dx \qquad (3.25)$$

This gives :

$$F = \frac{\mu \operatorname{cosec}\alpha \; e^{\mu' R'}}{\mu \operatorname{cosec}\alpha + \mu'} = \frac{\mu}{\mu'} e^{\mu' R'} \operatorname{cosec}\alpha \left(1 + \frac{\mu}{\mu'} \operatorname{cosec}\alpha\right)^{-1} \qquad (3.26)$$

If R' is small compared with $\frac{1}{\mu'}$, then fraction absorbed in layer thickness dx', x' from the channel is given by :-

$$dF' = \frac{\mu}{\mu'} \text{ Coseca } e^{\mu'R'} (1 + \frac{\mu}{\mu'} \text{ Coseca})^{-1} \mu' dx' \qquad (3.27)$$

Fraction reaching surface from dx' is then :

$$\frac{1}{2} (1 - \frac{x'}{R'}) \mu \text{ Coseca } e^{\mu'R'} (1 + \frac{\mu}{\mu'} \text{ Coseca})^{-1} dx' \qquad (3.28)$$

For the total fraction of electrons with ranges between R' and R' + dR' detected one obtains :-

$$\int_0^{R'} \frac{1}{2} (1 - \frac{x'}{R'}) \mu \text{ Coseca } e^{\mu'R'} (1 + \frac{\mu}{\mu'} \text{ Coseca})^{-1} dx'$$

$$= \mu \frac{\text{Coseca}}{4} e^{\mu'R'} (1 + \frac{\mu}{\mu'} \text{ Coseca})^{-1} \qquad (3.29)$$

If the range distribution is again taken such that :

$$\frac{dN}{dR'} = \frac{N}{R_p'}$$

one obtains for the fluorescent yield, χ_a' ,

$$\chi_a' = \frac{\mu \text{ Coseca}}{4} (1 + \frac{\mu}{\mu'} \text{ Coseca})^{-1} \int_0^{R_p'} \frac{R'}{R_p'} e^{\mu'R'} dR' \qquad (3.30)$$

Now if $\mu'R' \ll 1$,

one obtains :-

$$a' = \frac{\mu R_p' \operatorname{Cosec}\alpha}{8} \left(1 + \frac{\mu}{\mu'} \operatorname{Cosec}\alpha\right)^{-1}$$

$$= \frac{\mu R_p' \operatorname{Cosec}\alpha}{8} - \frac{\mu R_p'}{8} \frac{\mu}{\mu'} \operatorname{Cosec}^2\alpha + (\cdots\cdots) \quad (3.31)$$

Comparison with equation (3.9b) shows that only to second order is the absorption coefficient of the fluorescent X-rays of importance. To first order, the effective range of the primary ejected electron is simply replaced by the effective range of the secondary electron and the angular variation is identical.

Quantum mechanical calculations, (Burcham, 1963), show that the distribution of photo-electrons is not isotropic. The distribution for nearly zero velocity, is roughly a cosine distribution in a plane normal to the polarisation vector and containing the direction of motion of the incident photon. No attempt has been made to take this term into account. As a low-energy electron is likely to be scattered through a large angle in any interaction with atoms of the matrix, this may account for the observed agreement between the calculated and observed distributions, assuming isotropy. An isotropic distribution is, however, a perfectly correct physical picture for the cascade process.

4. Efficiency of γ-ray converter

In this section, the efficiency of the X-ray converter assembly is calculated on the basis of the results of the

previous section, and compared with the experiment.

Figure 3.16 shows a block diagram of the stages involved in conversion of X-rays to light using the channel plate converter.

The number of visible light photons/m^2/sec, M, emitted by the screen is given by :-

$$M = F \xi G P \qquad (3.32)$$

where F is the X-ray flux

ξ is the conversion coefficient of the channel plate

G is the electron gain in the plate

and P is the number of visible light photons created by an 8 keV electron striking the screen.

With $P = 10^3$ and there being approximately 10^6 photons of visible light per lumen, we obtain for the intensity on the screen :

$$I = F \xi G \times 10^{-13} \text{ lumen/m}^2. \qquad (3.33)$$

The Mullard G40-20S channel plates have channels making 13° to the plate normal. It can be seen from Fig. 3.15 that in this region the efficiency is slowly varying, and indeed, experimentally, no appreciable change in intensity with small change in angle was detected. For CuKα radiation $\xi \simeq 1\%$. The gain, G, at 1.4 kV is 10^4, (Guest et al., 1969). One than obtains $I = 10^{-11} F$ lux, for the expected intensity under the experimental conditions described in section 3.2. In the experiments described the X-ray flux was about 7×10^{10} counts/sec/m^2.

Substitution yields an expected intensity of 0.75 lux on the screen.

The intensity reaching the film of the recording camera is given by :

$$I' = \frac{I\, r^2\, a^2}{x^2} \qquad (3.34)$$

where r is the radius of the aperture of the lens

a is the angle subtended by the object at the lens

x is the height of the side of the image.

At unit magnification, x is also height of the object, and the object distance is such that :

$$u = 2L$$

where L is the focal length.

Now aperture number, f, is given by :-

$$f = \frac{L}{2r}$$

and

$$a = \frac{x}{u} \quad .$$

One then obtains,

$$I' = \frac{I\ \ r^2\ \ x^2}{4f^2\ 4r^2\ x^2} = \frac{I}{16f^2} \quad . \qquad (3.35)$$

At f number of 5.6

$$I' = \frac{I}{500} \quad .$$

In the experiments performed one then has :

$$I' = 1.5 \times 10^{-3} \text{ lux}$$

$$\simeq 1.5 \times 10^{-4} \text{ ft. candle.}$$

For a photographic film, the correct exposure time, t, in seconds is given by :

$$t = \frac{0.8}{\text{A.S.A. number} \times I'} \qquad (3.36)$$

where I' is in foot candles.

On film of speed A.S.A. 100,

$$t = 50 \text{ seconds.}$$

This is in quite good agreement with the exposure times of between 20 and 60 seconds required to produce a satisfactory image on the film. (Figure 3.8(a) is for exposure time 30 seconds.)

Conclusions and Suggestions

Use of a channel plate as an X-ray imaging device has been shown to be a simple and cheap method of direct display. With the advent of channel plates of smaller diameter and pitch, the resolution of the system could be greatly improved. For higher resolution work, electromagnetic focussing will be essential as it has already been demonstrated that this mode is superior to proximity focussing. The device is as efficient for AgKα X-rays as for CuKα and slightly more efficient for MoKα, (see Fig. 3.11). This gives an advantage over fluorescent screen detectors, which decrease in efficiency

with decreasing wavelength.

The expected intensity on the screen of the device has been calculated and found to be in reasonable agreement with experiment. Use of the intensity formula, (Equation (3.32)), will enable potential uses to be evaluated, provided the X-ray flux is known.

Improvement of intensity may be achieved by increasing the plate to screen voltage (and increasing P in equation (3.32)), though electromagnetic focussing is again necessary to avoid flake-off of the screen.

A further improvement in efficiency may be possible if a gold foil of about 1000 $\mathring{A}$ thickness is placed in front of the channel plate.

Then for 1.5 $\mathring{A}$ X-rays, $\frac{\mu}{\rho}$ = 214 cm/gm and ρR_p = 218 $\mu g/cm^2$.

As ρ = 19.32 gm/cc, R = 1,100 $\mathring{A}$.

One may thus expect that half the electrons ejected by X-rays absorbed in the gold will escape, i.e., a quarter will enter the channel plate. As the fraction of X-rays absorbed is about 4%, one may expect a further increase in detection efficiency of the channel plate of 1%, that is, a doubling of the efficiency at an angle of incidence of 13^{o}.

It is predicted that within the next few years, the channel plate will become a common device for X-ray applications. Its size, cost and low noise are very favourable, the main limitations at present being moderate resolution and relatively low gain.

Summary

The merits of the various techniques of electronic imaging

of X-ray images have been discussed with particular emphasis on the use of a cascade image intensifier to intensify the optical image produced by the interaction of X-rays with a thin phosphor screen. A new method of directly displaying X-ray topographic images using a channel plate was described.

The remainder of the chapter was devoted to detailed calculations of the predicted efficiency of a channel plate to X-rays of wavelengths in the region 0.5 - 2 Å. An explanation was given for the experimental observation that the photo-electron yield obeys a Cosec law right into the U.V. range. Using published data, the efficiency was calculated for several cases and comparison with previous experimental work made. It was shown that, to an order of magnitude, this data could be used to predict the intensity produced by the image converter previously described.

C H A P T E R IV

CONTRAST OF IMAGES IN THIN CRYSTALS

1. Introduction

As has been emphasised many times before, one of the major disadvantages of X-ray topography is that, as a result of the large image widths, only in specimens with dislocation density less than about 10^5 lines/sq. cm are individual dislocations discernable. The application of X-ray topography to the study of the initial stages of deformation of metals has to a large extent been hampered by the difficulty of growing low dislocation density metal crystals. In recent years, as crystal growth techniques have improved, several authors have reported growth of large dislocation free copper crystals, (Young and Sherrill, 1967; Fehmer and Uelhoff, 1969; Sworn, 1971), and low dislocation densities in other metals, for example, aluminium, (Authier, Rodgers and Lang, 1965; Nøst and Sorensen, 1966, Nøst and Nes, 1969; Fremiot et al., 1968), molybdenum, (Pegel and Becker, 1969), tin, (Brummer and Alex, 1970), and cadmium, (Badrick and Puttick, 1971). However, in most cases, as deformation starts, the dislocation density rises extremely rapidly and one again has trouble in resolving individual dislocations. To make a meaningful study of the early deformation stages, it would appear necessary to use X-ray topography in conjunction with high voltage electron microscopy. As it would be advantageous to study the same specimen in both instruments, it is essential that the contrast of defects in X-ray topographs of very thin

crystals be examined in detail.

It was argued by Penning and Goemans, that in crystals thinner than about 1/3rd to 1/6th of an extinction distance, dislocations should cease to be visible by extinction contrast, (Penning and Goemans, 1968). The experimental evidence was a little unsatisfactory, for although they demonstrated that dislocations did indeed disappear in a very thin specimen, no figure was given for the thickness at which they ceased to be visible. Attempts to feather down the edges of MgO and iron-silicon alloy crystals chemically by Lang gave only a rough figure of about 1/3rd of an extinction distance, the upper limit set by Penning and Goemans, (Lang, 1970).

In the first part of this chapter, the thickness at which dislocation invisibility sets in is measured to an accuracy of 1 μm for several reflections using different radiations. The last part is devoted to a comparison of dislocation images observed in the thin crystal with computed dislocation profiles.

2. Extinction Contrast in Very Thin Crystals

a) Theory

The intensity reaching the film in the diffracted beam of a traverse topograph has been shown to be equal to the integrated intensity and independent of the shape of the wave front provided that the integration is carried out across the whole of the rocking curve, (Takagi, 1969; Authier, 1970(b)). This holds for both perfect and deformed crystals. For a thin perfect crystal, in which absorption may be neglected, the intensity on the film will be proportional to the integrated

reflecting power calculated in the plane wave case. This has been shown, (Zachariesen, 1945), to be given by the expression :-

$$R_g = \left|\frac{\gamma_g}{\gamma_o}\right| \frac{I_g}{I_o} = \frac{\pi}{2} \int_0^{2A} J_o(\rho)\, d\rho \qquad (4.1)$$

where I_o is the intensity in the direct beam, I_g the intensity in the diffracted beam corresponding to reciprocal lattice vector g and J_o is the zero order Bessel function.

The limit A is defined as

$$A = \frac{\pi t}{\xi_g} \qquad (4.2)$$

where t is the crystal thickness and ξ_g is the extinction distance. The extinction distance itself is defined as :-

$$\xi_g = \frac{\pi V_c \sqrt{\gamma_o \gamma_g}}{C\, r_o \lambda \sqrt{F_g F_{\bar{g}}}} \qquad (4.3)$$

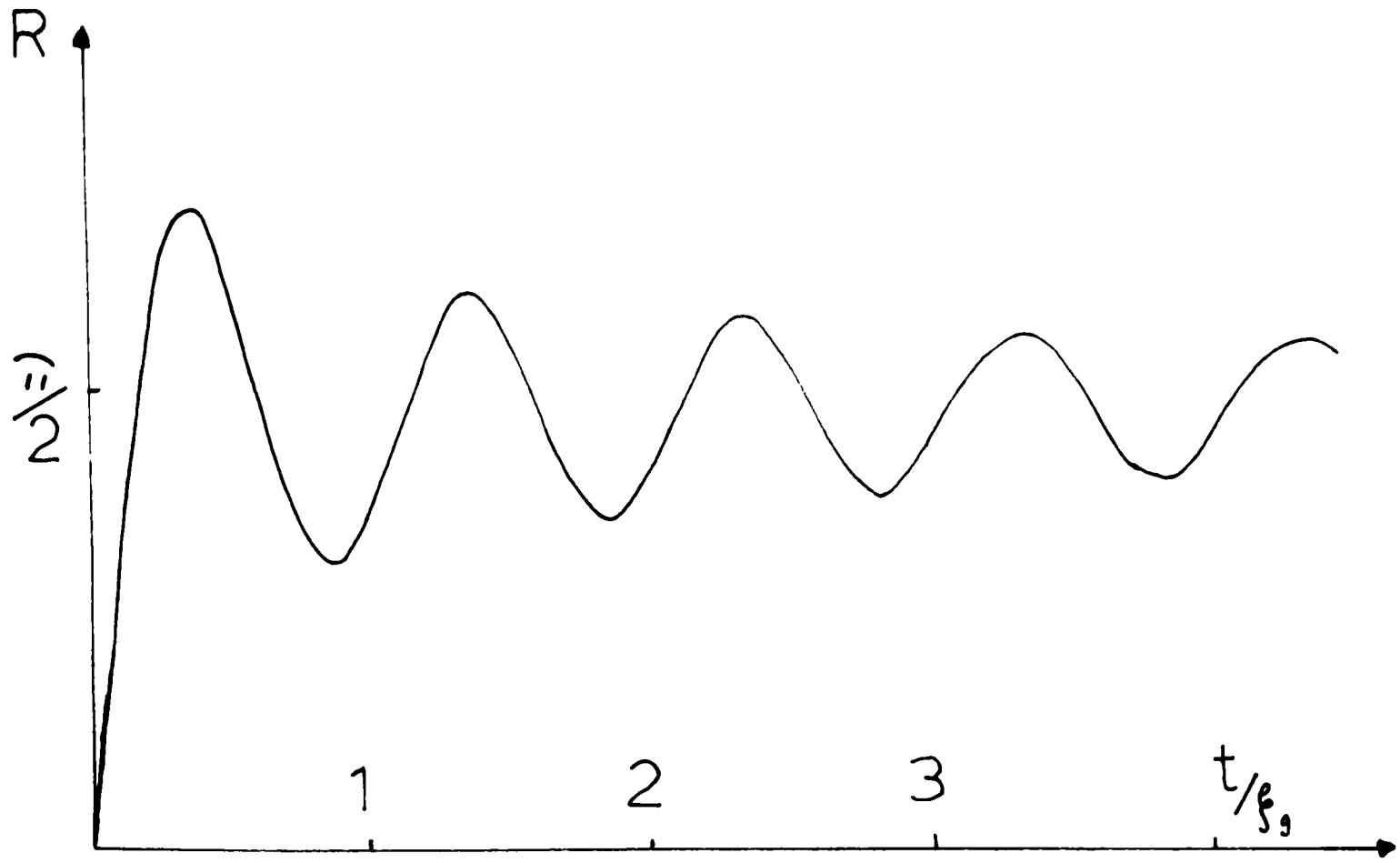
where V_c is the volume of the unit cell, r_o the classical electron radius, λ is the X-ray wavelength, γ_o and γ_g are the cosines between the crystal normal and the direct and diffracted beams respectively, F_g is the structure factor,

and $C = 1$ for the σ polarisation

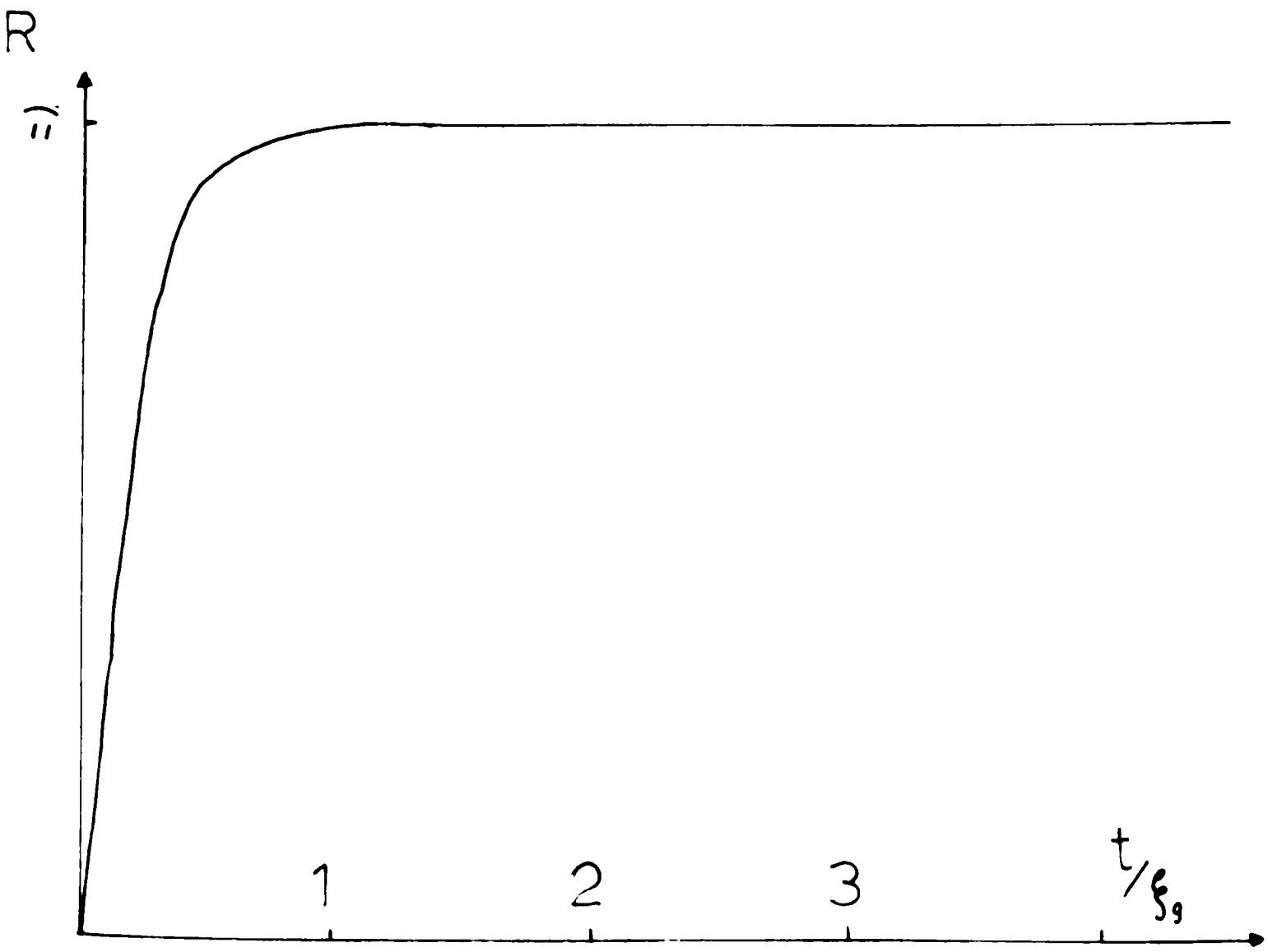
$= \cos 2\theta_B$ for the π polarisation.

Figure 4.1(a) shows the plot of R_g as a function of crystal

FIG 4.1



(a)



(b)

thickness for plane polarised X-rays in the Laue case with zero absorption. Figure 4.1(b) shows a similar plot for the Bragg case. The intensity is proportional to the thickness, for crystal thicknesses less than about $\frac{\xi_g}{8}$.

The direct image in X-ray topographs is considered to occur when the lattice planes around a defect are misoriented by about the width of the rocking curve in the perfect material. Here, X-rays from parts of the source not exactly satisfying the Bragg condition for the perfect crystal are reflected.

Suppose this region of "bad" material is of thickness, Δ . In general, $\frac{\Delta}{\xi_g}$ will be considerably less than unity and, as the X-rays diffracted by the "bad" material are not diffracted by the perfect crystal, the "bad" material diffracts kinematically. The intensity from the defect will thus be proportional to $\frac{\Delta}{\xi_g}$.

Two cases will now be considered :

(i) Crystal is thick, i.e., $t \gg \xi_g$;

(ii) Crystal is thin, i.e., $t \ll \xi_g$.

(i) Thick crystal - Zero absorption

Inspection of Fig. 4.1(a) shows that for a thick crystal in the Laue case the intensity oscillates about a mean value as the thickness increases. (When absorption effects are taken into account this mean value decreases, as does the amplitude of the oscillation.) These oscillations give rise to the well-known Pendellosung or thickness fringes observed in X-ray traverse topographs. Apart from these oscillations, the reflecting power has a mean value of $\frac{\pi}{2}$, independent of

crystal thickness.

In the Bragg case for a thick crystal, no oscillations are observed, and the reflecting power is equal to π, independent of thickness. In this latter case, the intensity reflected from a perfect crystal of thickness, t, will be equal to the intensity reflected from a crystal of thickness, $t - \Delta$. In other words, the perfect material above and below the layer of "bad" material will reflect the same intensity as the surroundings. Thus one observes enhanced intensity due to the kinematical scattering of the "bad" layer of thickness, Δ .

Similarly, in the Laue case, the gradient of the intensity-thickness curve at any point is always less than the gradient at zero thickness. The reflected intensity from a small region of "bad" material will thus always be greater than that lost from reducing the crystal thickness from t to $t - \Delta$. (In fact, at crystal thickness such that the intensity is at a minimum on the intensity-thickness curve, one gains intensity by reducing the crystal thickness from t to $t - \Delta$.) In the Laue case also, direct images are thus always more intense than the background.

(ii) Thin crystal - Zero absorption

For crystal thickness less than about $\frac{\xi_g}{\pi}$, the intensity reflected is proportional to the thickness of crystal. The net effect of a "bad" layer of thickness, Δ , and a perfect crystal of thickness, $t - \Delta$, is to produce the same intensity as that from the perfect crystal of thickness, t. In very thin crystals, in both Laue and Bragg cases, dislocations

should cease to be visible.

b) Experimental

A polished slice of float-grown silicon of orientation (111) and initially about 200 μm thick was used for this experiment. As is seen from Fig. 4.2, the dislocation density of the material was of the order of 5×10^3 lines/cm^2. The slice was mounted at a low angle on a glass slide and mechanically polished until the thin end of the wedge gave appreciable transmission of white light. A topograph taken at this stage revealed a large amount of strain in the thin region and also considerable surface damage. To remove this, the specimen was further thinned in hydrogen fluoride and nitric acid. This produced a wedge free from elastic strain varying from a thickness of about 5 μm to about 120 μm. The specimen was mounted carefully with "Tackiwax" at the thick end. (The author is extremely grateful to Mr. H.R. Petit for his skill in thinning this specimen.)

(i) Laue case

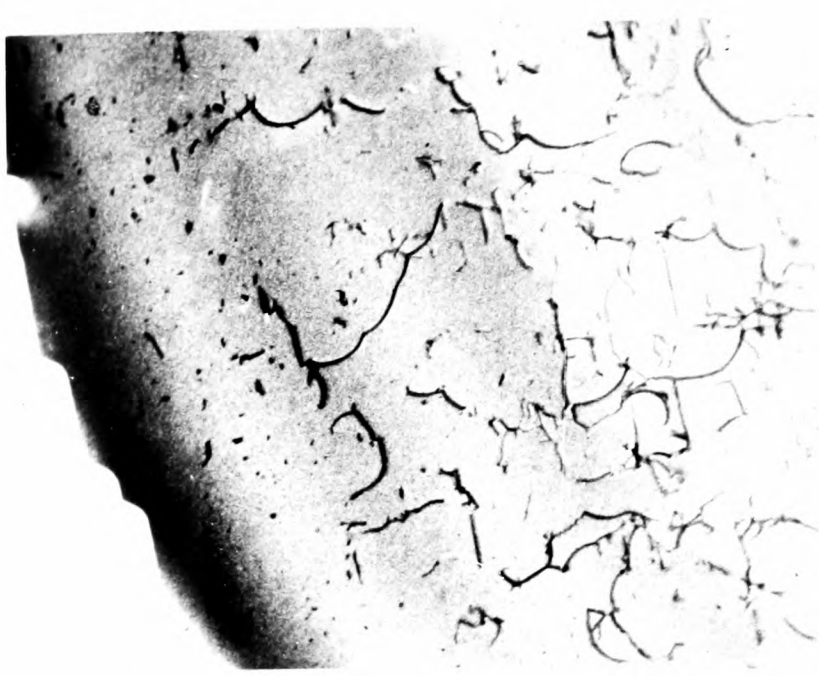
Figure 4.3(a) and (b) show a repeat of Penning and Goemans' experiment, except that a wedge-shaped specimen is used rather than a flat one. It is immediately obvious that defects appearing using CuKα radiation, (ξ_g = 15 μm), are invisible with AgKα radiation, (ξ_g = 45 μm), both topographs being taken with the same 220 reflection.

By utilising the thickness fringes in the CuKα topograph, it is possible to measure, quite accurately, the thickness at

FIG 4.2

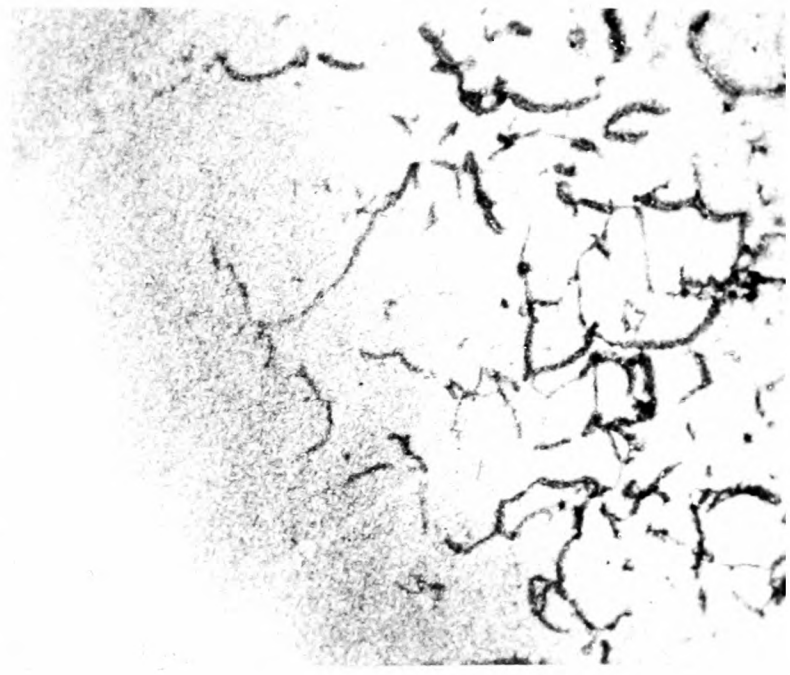


FIG 4.3



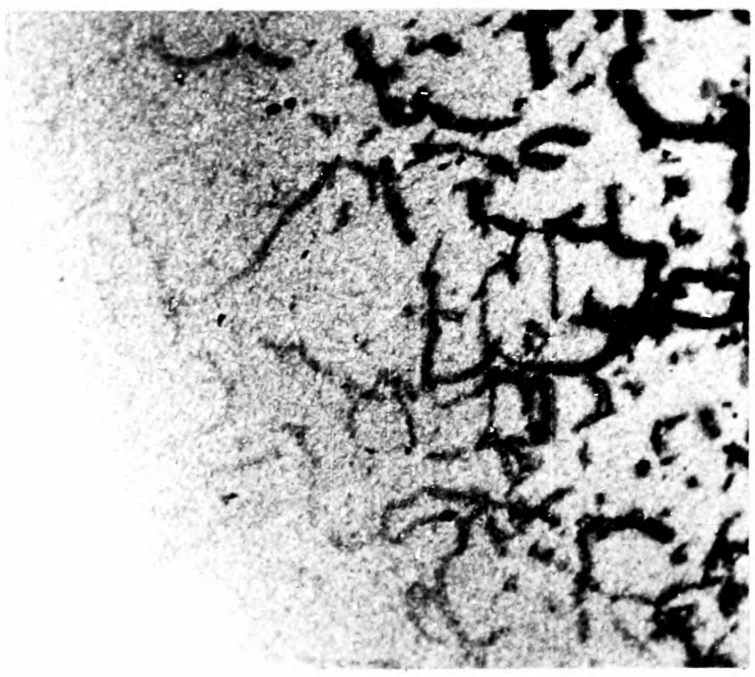
(a)

CuKα 220



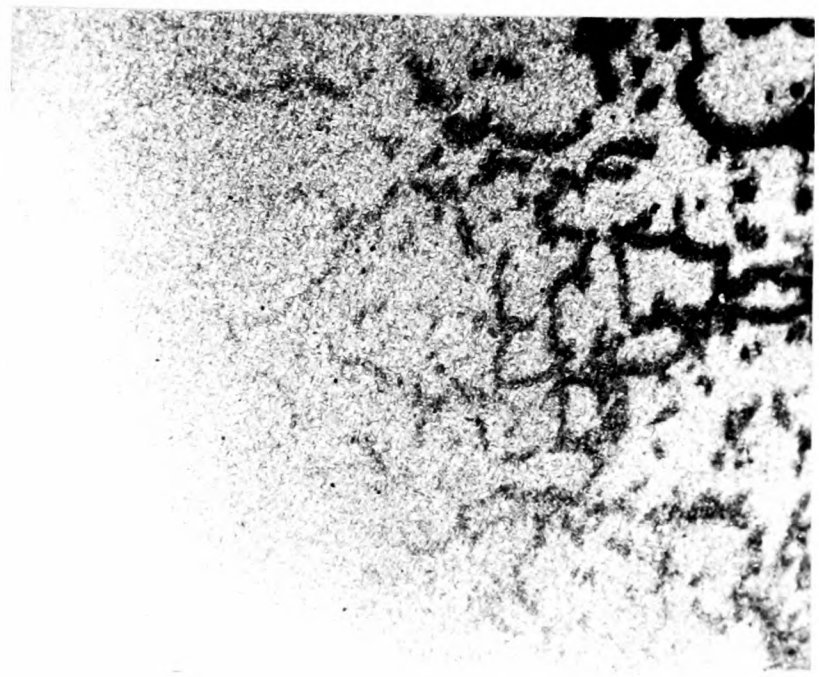
(b)

AgKα 220



(c)

AgKα 440



(d)

MoKα 555

500μm

FIG 4.4

which visibility ceases. However, to do this, polarisation must be taken into account. Table 4.1 shows some extinction distances in silicon for various reflections and radiations used. It should be noted that the extinction distance for the π polarisation is always longer than the σ polarisation.

Table 4.1

Extinction Distances in Si (μm)

Reflection	CuKα		MoKα		AgKα	
	σ	π	σ	π	σ	π
220	15.5	22.5	36.47	38	46.79	48.5
111	19.8	22	41.31	42	52.70	53
224	16.0	77.0	48.03	58	62.68	72
311	22	39	55.92	61	71.61	74
440	-	-	54.08	73	70.9	84
555	-	-	128.4	330	178.0	250

Figure 4.4 shows the intensity as a function of the thickness for 220 reflections with CuKα radiation in the unpolarised case. One can then determine the thickness at any point in the specimen, simply from the position with respect to the thickness fringes. It is important to ensure one is actually starting at the first fringe, and this may be checked with reference to longer extinction distance topographs. Figure 4.5(a) shows the 311 reflection with CuKα and Fig. 4.5(b)

FIG 4.4

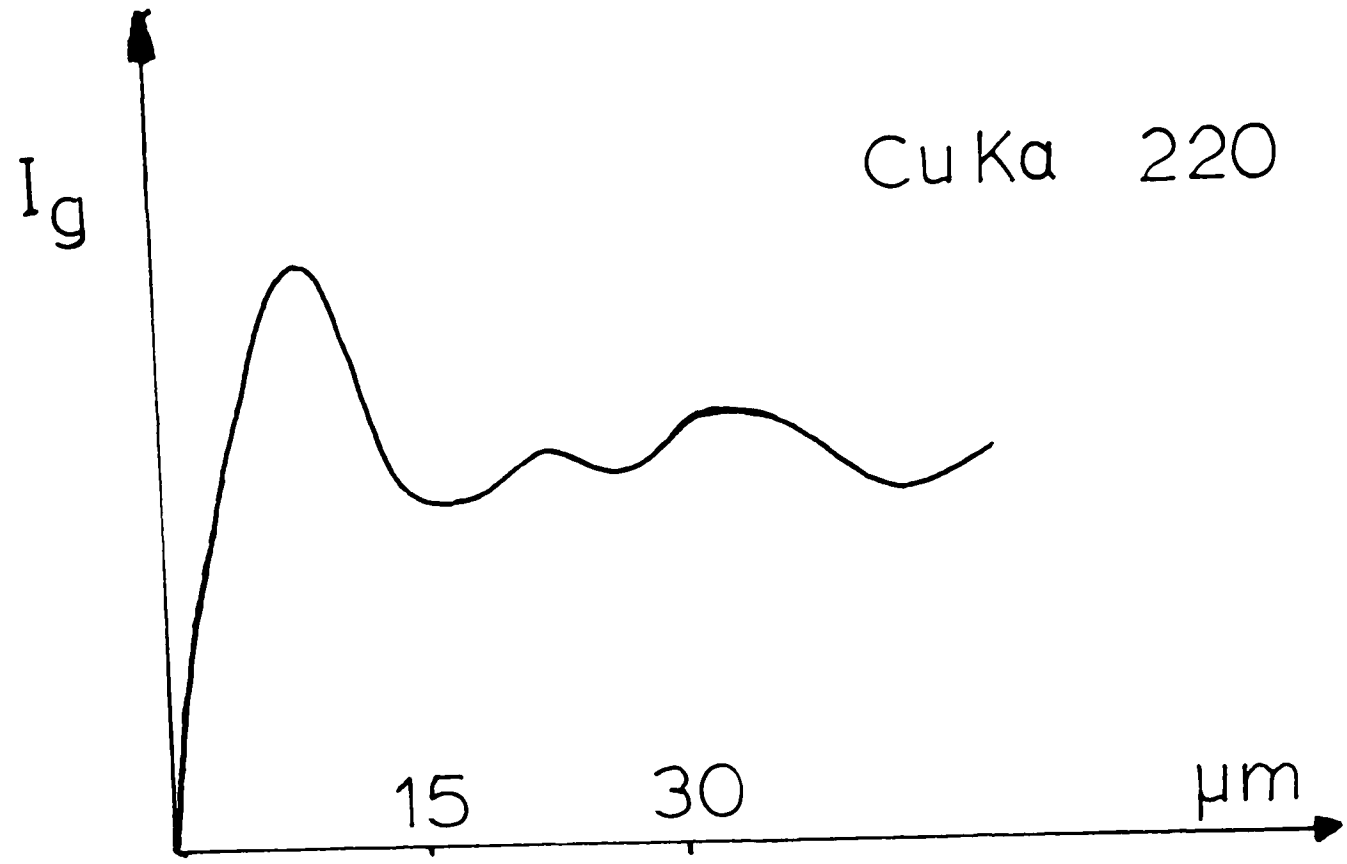

I_g
Cu Ka 220
15
30
μm

FIG 4.6

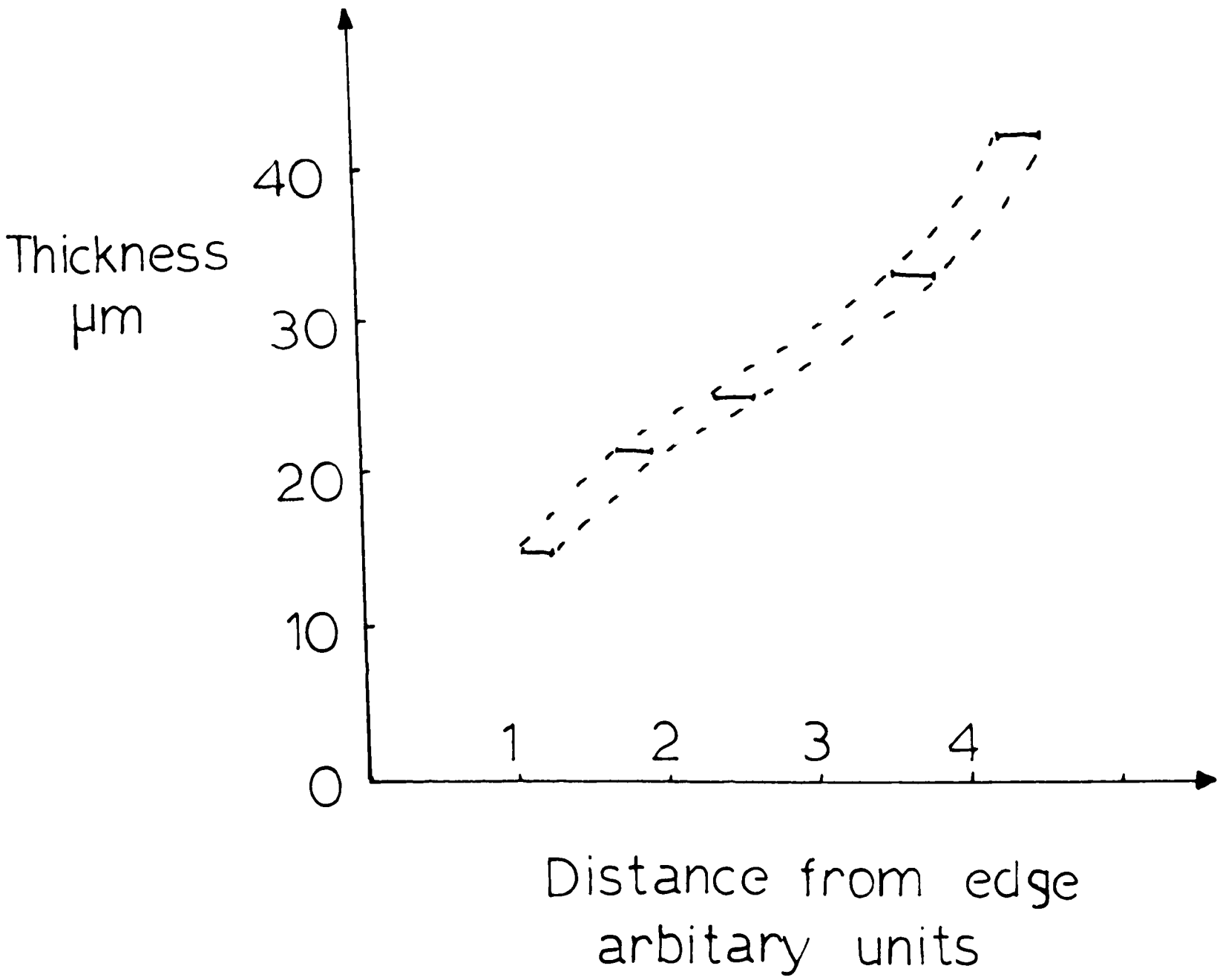
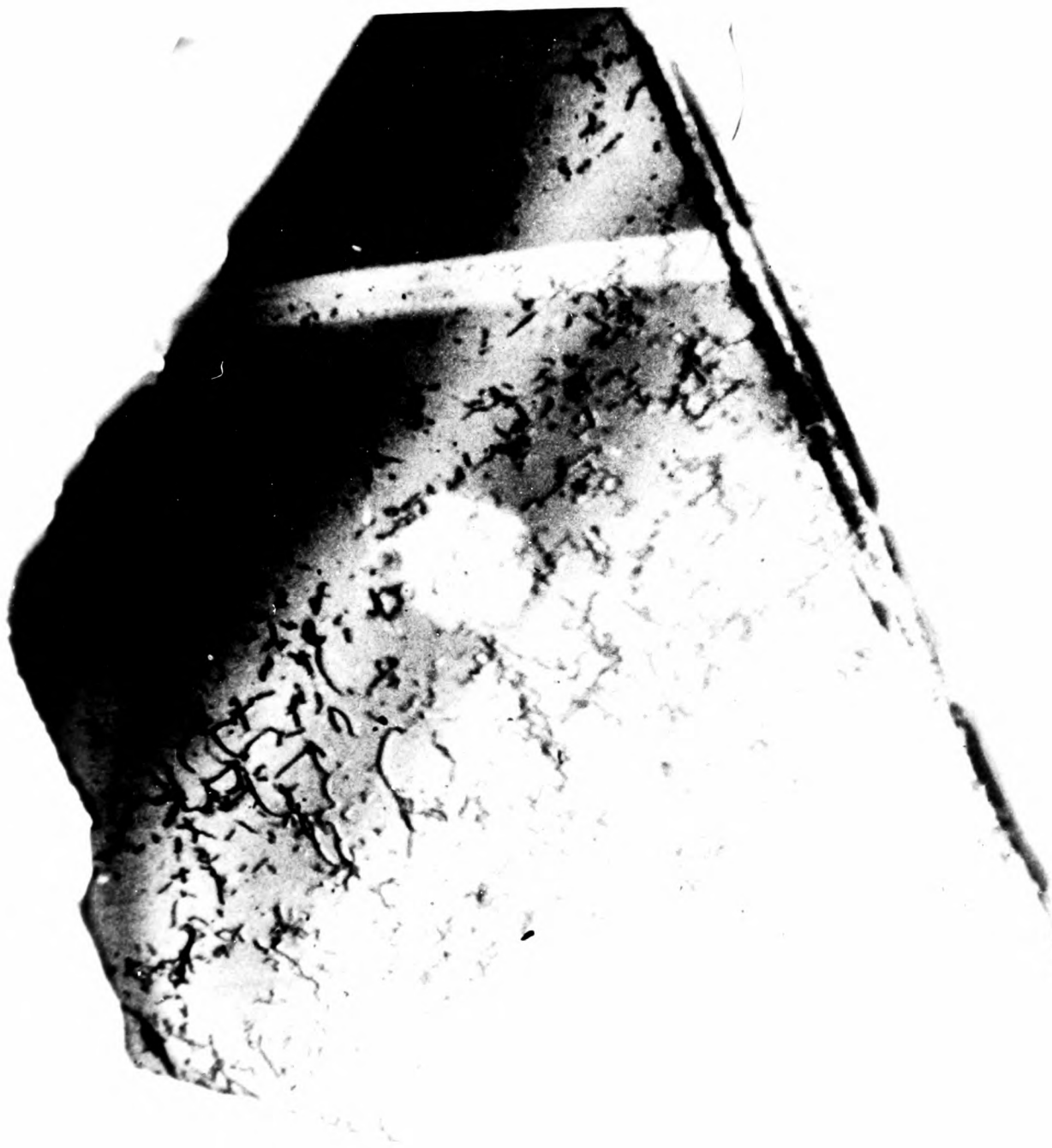
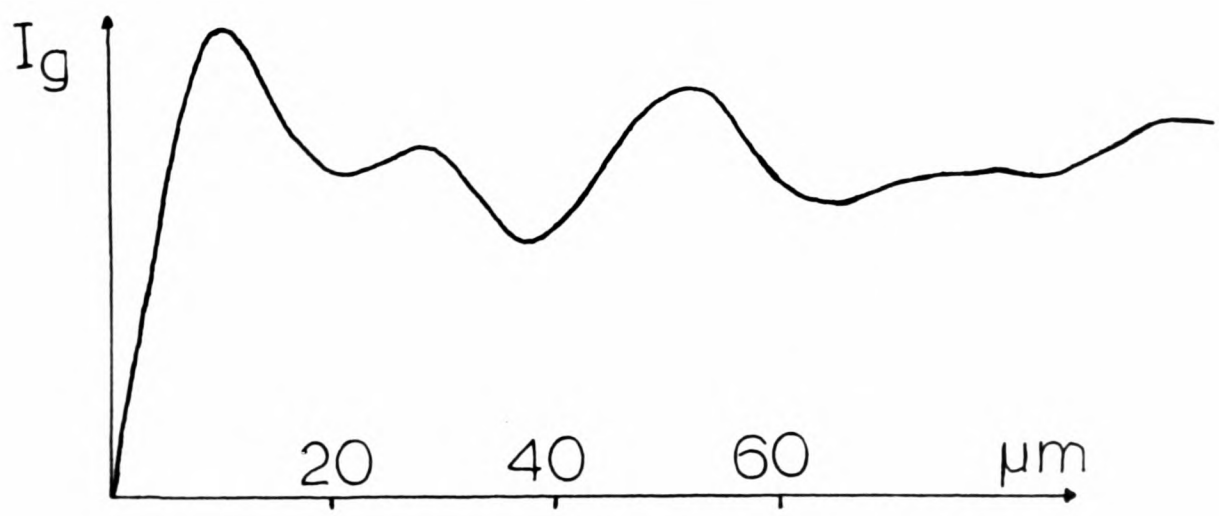

Thickness μm
40
30
20
10
0
1
2
3
4
Distance from edge
arbitary units

FIG 4.5



(a)



(b)

the corresponding profile. The loss of contrast at the fourth maximum is visible as are also the relatively high intensities of the first maximum and first minimum.

Utilising this method of measurement, Table 4.2 shows the fraction of the σ polarisation extinction distance at which visibility ceases for several reflections. An estimate of the

Table 4.2

	Position of Invisibility	Laue Case	
Radiation	Reflection	Thickness for Image Loss	t/ξ_g^{σ}
AgKα	$\bar{2}\bar{2}0$	19 microns	0.41
	$20\bar{2}$	17 microns	0.37
	$\bar{1}11$	17 microns	0.32
	$\bar{1}\bar{1}1$	18 microns	0.34
	111	20 microns	0.38
	$\bar{3}\bar{3}3$	20 microns	0.35
	$\bar{4}\bar{4}0$	18 microns	0.25
MoKα	$\bar{2}\bar{2}0$	15 microns	0.42
	$\bar{2}\bar{4}2$	18.5 microns	0.39
	$\bar{3}\bar{1}1$	21 microns	0.38
	$\bar{5}\bar{5}5$	19 microns	0.15

accuracy of this measurement is made as follows. Figure 4.6 shows a plot of the thickness as estimated from the maxima and minima of the thickness fringes, against the distance from the specimen edge, measured from the CuKα topograph of Fig. 4.3.

The error bars are an indication of the accuracy to be expected in estimating the positions of the maxima and minima on the topograph. From these, one finds that including errors due to non-uniformity in the wedge, the measured accuracy will be better than ± 1 μm.

(ii) Bragg Case

The loss of image contrast can also be observed in the Bragg case. Figure 4.7 shows a 555 surface reflection topograph with AgKα radiation. The thin end of the wedge is at the top of the photograph and it can be seen that loss of image does indeed occur in the thin region.

c) Discussion

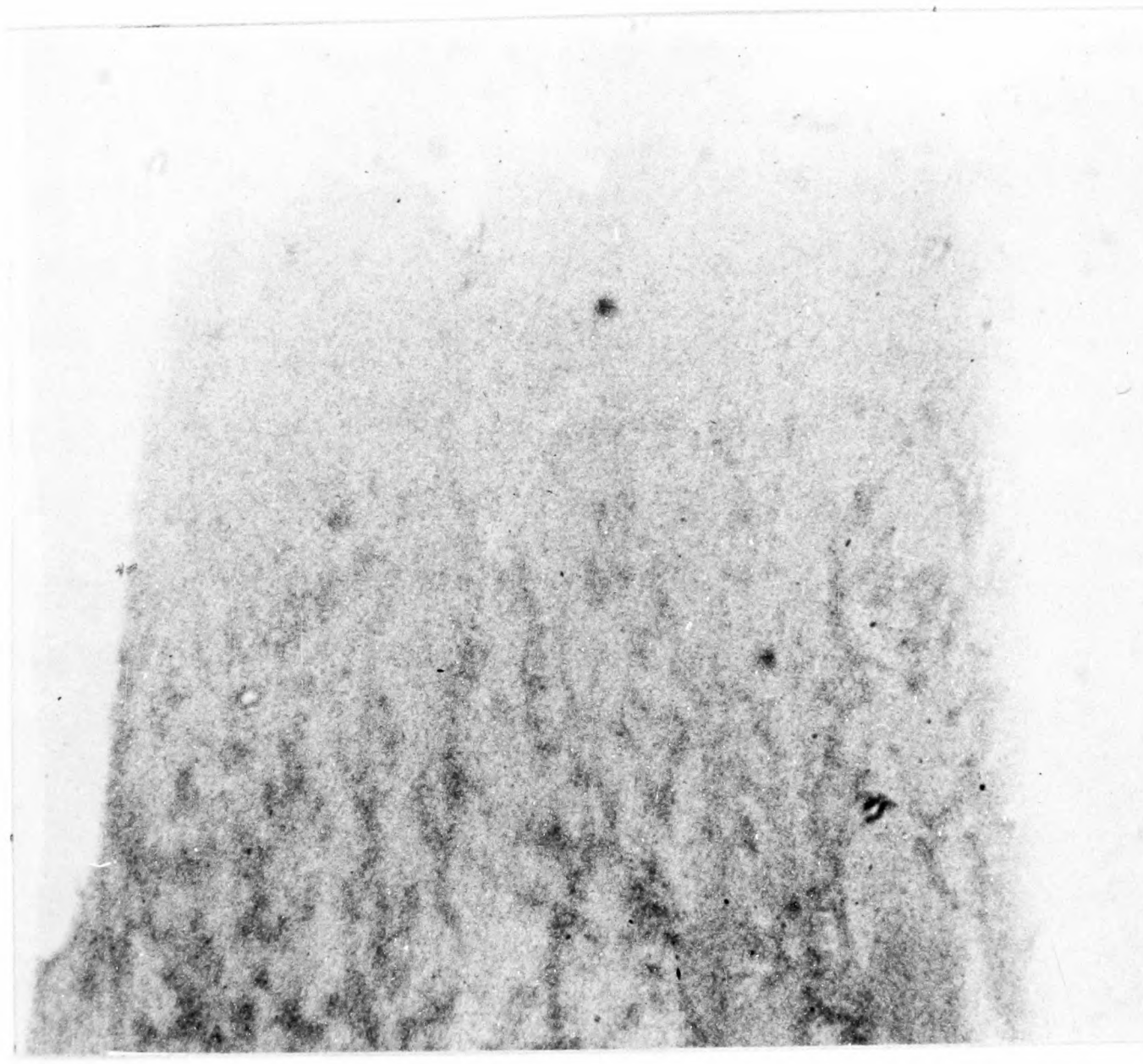
It is clear from Fig. 4.3 and Table 4.2 that one cannot give a general figure for the fraction of the extinction distance at which image loss occurs. A definite decrease is observed as one goes to higher order reflections, which cannot be explained either by experimental error or from polarisation effects. Inclusion of intensity due to the π component would tend to increase, rather than decrease, the thickness at which image loss occurs. However, an explanation may be sought in the following way.

Consider the effect of increasing the thickness of misoriented material, Δ , for a constant thickness of crystal, t, where the intensity is no longer a linear function of t.

The visibility is defined as :

$$V = \frac{I_\Delta + I_{t-\Delta} - I_t}{I_\Delta + I_{t-\Delta} + I_t} \qquad (4.4)$$

FIG 4.7



AgKα $\bar{5}5\bar{5}$

500μ

Then if $\frac{\Delta}{t} \ll 1$

$$I_{t-\Delta} + I_{\Delta} < \emptyset_t \qquad (4.5)$$

where $\emptyset$ is a constant.

If $\frac{\Delta}{t} \simeq 1$, the perfect material of thickness $t - \Delta$ diffracts kinematically:

$$I_{t-\Delta} + I_{\Delta} = \emptyset_t \qquad (4.6)$$

Thus, the visibility is greater for $\frac{\Delta}{t} \simeq 1$ than for $\frac{\Delta}{t} \ll 1$. One may then expect defects to remain visible in thinner material in the case of $\frac{\Delta}{t} \simeq 1$ than where $\frac{\Delta}{t} \ll 1$.

The thickness of misoriented material contributing to the image will be dependent on the width of the rocking curve. For the moment, the thickness will be considered inversely proportional to the rocking curve width.

Then,

$$\Delta \propto g \xi_g \qquad (4.7)$$

Expressing the crystal thickness as a fraction, K_t, of ξ_g:

$$\frac{\Delta}{t} \propto \frac{g}{K_t} \qquad (4.8)$$

Thus, as g increases, $\frac{\Delta}{t}$ increases and the visibility at a given value of K_t increases.

Figure 4.8 shows a plot of t/ξ_g against g for all the measured reflections, where t is the thickness for image loss.

FIG 4.8

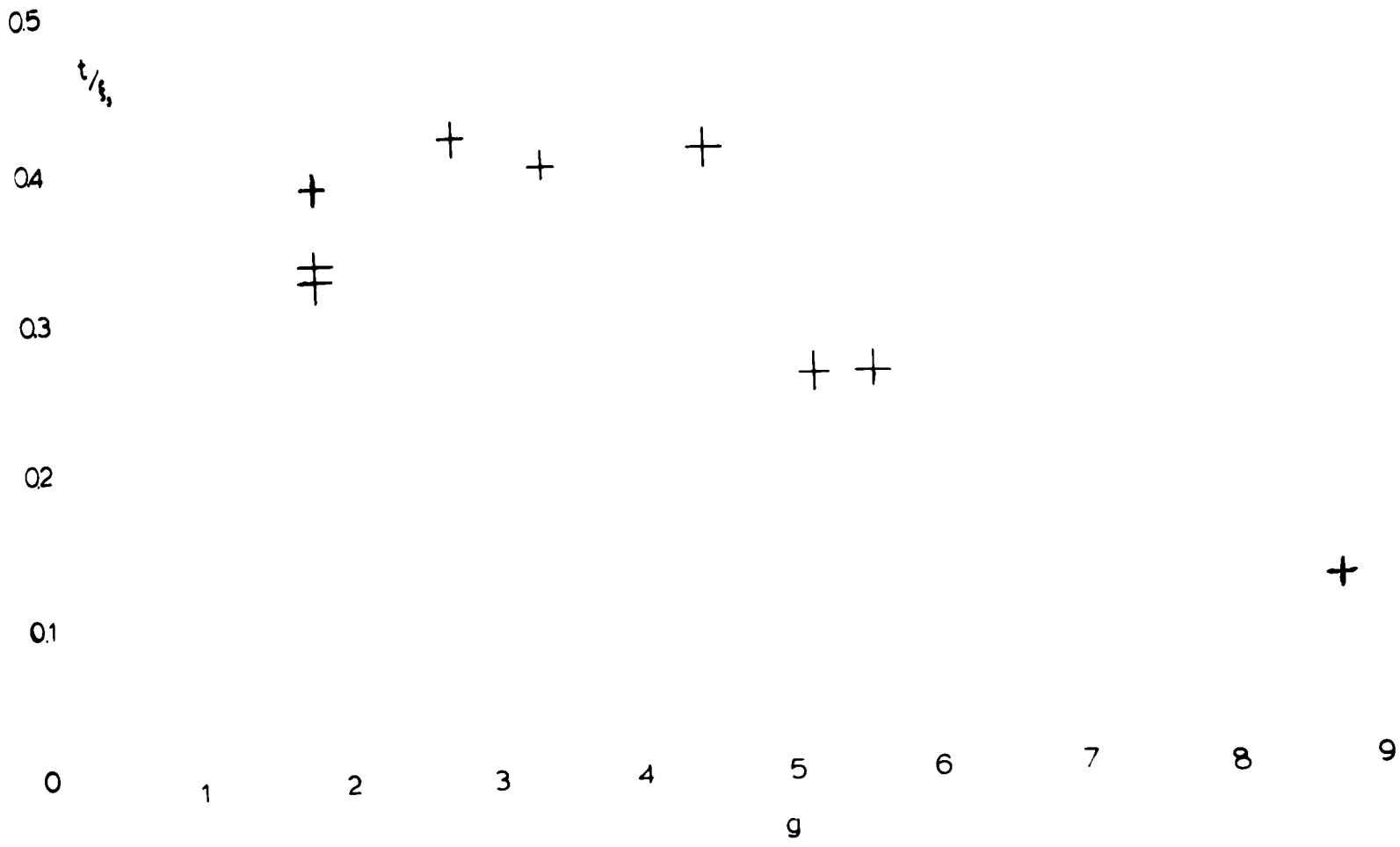
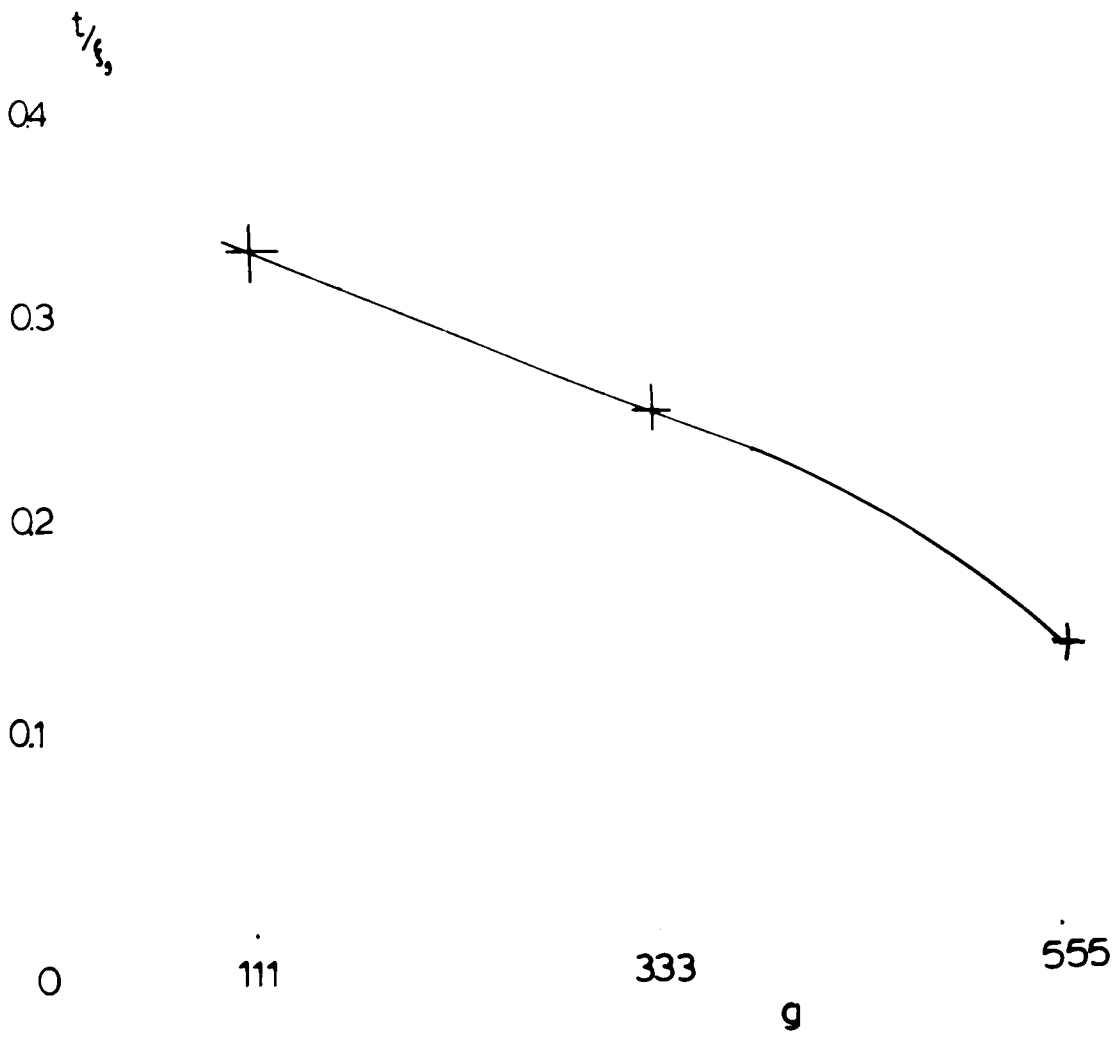


FIG 4.9



The general trend is observable, though there is considerable scatter which is not altogether unexpected. The thickness of misoriented crystal will be dependent upon the projection which the dislocation strain field makes in the X-ray incidence plane. As this varies with reflection, quite large differences occur, even between different reflections of equal magnitude g vector.

Figure 4.9 shows a similar plot to Fig. 4.8 but this time restricting to the n(111) reflections. These will have a similar effective projection of misoriented material, and one finds a monotonic decrease in t/ξ_g with increasing g. (As g continues to increase, it is assumed that the curve will flatten off.)

d) Conclusion

The thickness at which loss of visibility of dislocation image occurs in thin crystals has been measured in both Laue and Bragg cases. It is not possible to generalise much further than to revise the original statement of Penning and Goemans to ".....the lower limit is about 0.4 to 1/6 of the Pendellosung length; Usually, the value falls as higher order reflections are taken".

When using low order reflections, it is necessary to take the upper of the two limits, and for work with the H.V.E.M., one must use specimens of thickness at least 0.4 ξ_{220} to get good image contrast.

3. Images of Dislocations less than 1/3rd to 1/6th of an extinction distance from the surface of a thick crystal

It has been stated, (Badrick and Puttick, 1971), that

defects less than 1/3rd to 1/6th of an extinction distance from the entrance surface do not produce contrast in X-ray topographs. This has caused concern that X-ray topography will not be a useful tool for the study of shallow diffused semiconductor devices, (Filby, 1971). Two experiments are described below, which show no evidence to support such an effect.

Consider the dislocation marked X in Fig. 4.10. The crystal thickness at this point may be measured to be 48 μm. The position of the dislocation in the crystal may be fixed by reference to the relative positions of the direct and dynamical images, (Gerward, 1970). The intensity profile in a section topograph has been calculated previously, (Kato, 1960). For the case of low absorption ($\mu t \ll 1$), the bulk of the intensity is found in the extrema of the Borrmann fan, θA and θB, (see Fig. 4.11). One then finds from the geometrical construction, that the dynamical and direct images of a dislocation line perpendicular to the g vector and lying in the plane of the crystal, should be separated by a distance $2d \sin \theta_B$, where d is the distance of the defect from the exit surface in the symmetric condition. The direct image lies in the +g direction from the dynamical image.

Using this, one finds dislocation X lies 40 μm from the exit surface, i.e., 8 μm from the entrance. Figure 4.3(d) shows this dislocation visible in the $\bar{5}55$ MoKα reflection. Here, the dislocation is less than 1/13th of an extinction distance from the entrance surface.

The second experiment uses a slice of silicon which has

FIG 4.10

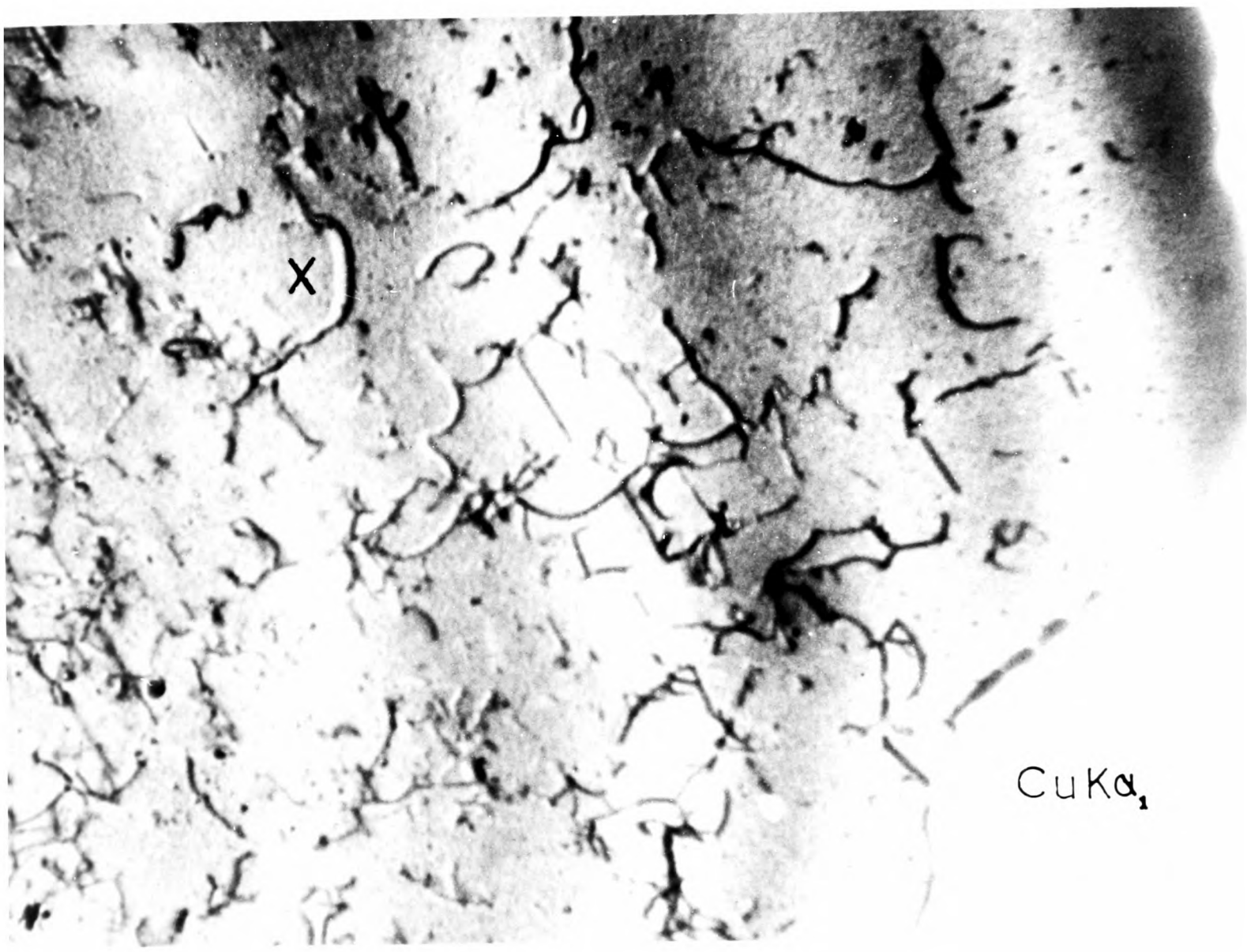
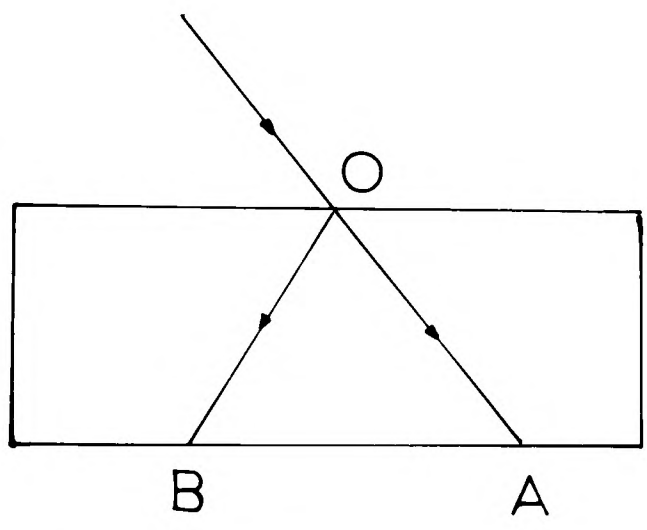


FIG 4.11



had a boron diffusion in selected areas. Figure 4.12 shows a topograph of a diffused area using MoKα radiation, 220 reflection. The diffused side is on the X-ray entrance surface. As the defects show up in the 111 surface reflection topograph using CuKα radiation, Fig. 4.13, they must lie within 4.8 μm of the surface, (ξ_{111} = 19.8 μm, $\theta_{111} = 14^{o}$). Thus, in Fig. 4.12, defects less than 1/7th of an extinction distance from the entrance surface are visible in the diffused region.

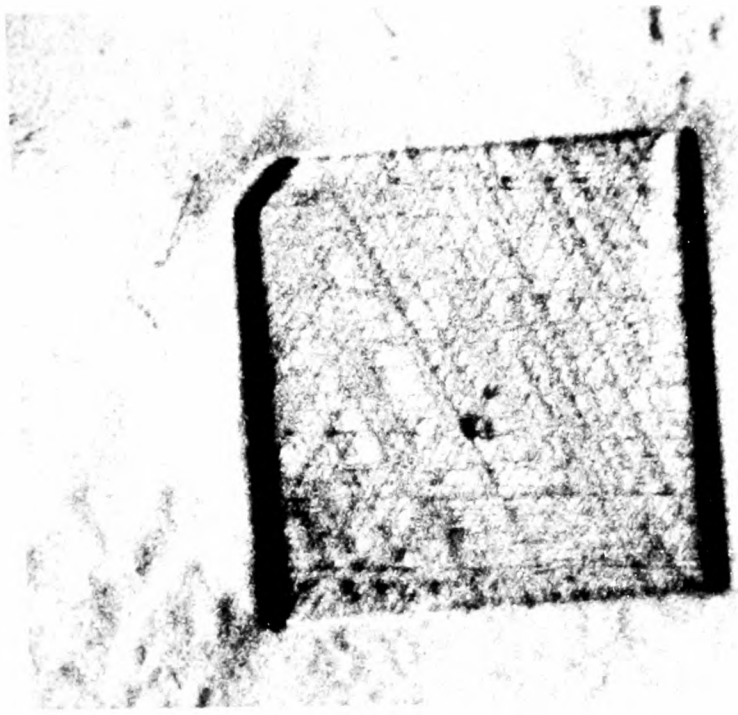
While surface relaxation effects are, most certainly, of importance in X-ray topographs, these are elastic, not diffraction effects and no support for the statement that defects less than 1/3rd of an extinction distance from the entrance surface do not produce X-ray topographic contrast has been found.

4. Comparison of theoretical and experimental image profiles in thin crystals

a) Review of theories

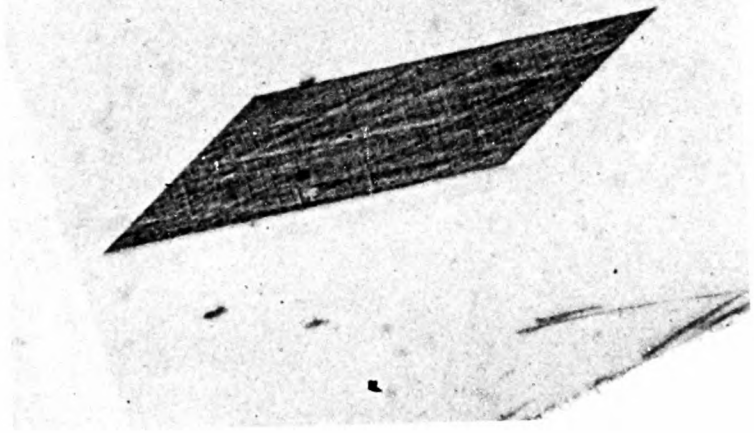
One of the factors that had made electron microscopy such a powerful and widely used metallurgical technique is the ability to simulate on a computer the contrast produced by a defect in any given diffracting conditions. The usual formulation of the dynamical theory of electron diffraction in a distorted crystal using the method of Darwin,(1914), may be found in an excellent review article by Whelan, (1970), and also in Hirsch, Howie, Pashley, Nicholson and Whelan, (1965). The extension to a situation where many beams are excited using a more basic theory, derived by solution of Schodringer's Equation in a periodic medium is found in the same references, (Howie, 1970). The

FIG 4.12



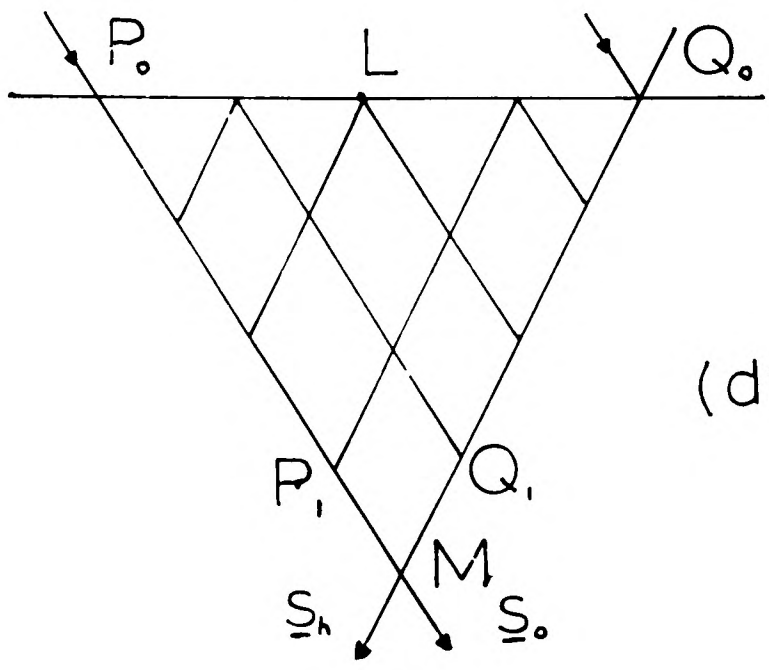
MoKα
220

FIG 4.13



CuKa
$\bar{1}1\bar{1}$

FIG 4.14



(due to Authier)

relative simplicity of computing defect profiles in the electron case relies on two important approximations. Firstly, that the electron wave incident on the crystal may be accurately approximated as a plane wave, and secondly, that due to the small Bragg angles, the fanning out of the electron beam through the crystal may be ignored. This latter "column approximation" has the important implication that one can neglect lateral components of the strain field and the contrast at any point is entirely dependent on the variation of crystal displacement as a function of depth. These approximations may be exploited still further by utilising the fact that, providing surface relaxation is neglected, and with the assumption that there is only one strong diffracted beam, one finds that there are two independent solutions to the dynamical theory equations. Any particular solution is a linear combination of these two, dependent on the boundary conditions. Using this, Head and Humble have developed an extremely rapid method of computing defect profiles, (Humble, 1970). By making several profiles at different positions along the dislocation line, an image may be built up, either by overprinting, (Humble, 1970) or by display on a cathode-ray tube, (Bullough, Maher and Perrin, 1969).

While the theory developed in the electron case is satisfactory for perfect crystals, neither approximation mentioned above is valid for X-ray diffraction in distorted crystals. The approximation to a plane wave will only be valid if the beam divergence is considerably less than the perfect crystal rocking curve. Table 4.3 shows typical values in the electron and X-ray cases and it is clear that while a plane wave is a

good approximation in the electron case, one must always consider the X-ray beam as a spherical wave in Lang's technique.

Table 4.3

Electron Microscopy		Lang's X-Ray Technique	
Beam Divergence	Reflecting Curve Width	Beam Divergence	Reflecting Curve Width
10^{-3} c	10^{-2} c	5×10^{-4} c	10^{-5} c

The column approximation is found to be a good approximation in electron microscopy except where the image is formed quite close to the dislocation core, (Howie and Sworn, 1970) as observed using the weak beam technique of electron microscopy, (Cockayne, Ray and Whelan, 1969). However, in the X-ray case, due to the large Bragg angles, the lateral strain components must be considered and some form of solution not using a column approximation must be sought.

A theory of X-ray diffraction in slightly distorted crystals has been developed by Penning and Polder, (1961). It has been shown, (Kato, 1963a,b), that this theory is only applicable if regions not closer than 10 μm from a dislocation core are considered. This theory is not, therefore, applicable to the general case of a dislocation image.

Two theories have been developed which enable the contrast of dislocations to be simulated. Both are applicable to a general wave propagating in a crystal and may be used both for electron and X-ray diffraction. The modified Bloch wave

formulation of Takagi arrives at a pair of coupled differential equations, looking very similar to the dynamical theory equations of Howie and Whelan, except that the differentiation is taken down the direct and diffracted beam directions, (Takagi, 1962; 1969).

Similarly, Howie and Basinski solve the propagation equation for electrons in the distorted crystal by looking for Bloch wave solutions, the amplitude of which vary with position in the crystal, (Howie and Basinski, 1968). They arrived at a second order set of coupled differential equations, which reverted to the column approximation equations if the lateral components of the wave vector of the incident wave could be neglected.

While the theory of Howie and Basinski might be expected to be applicable to greater distortions than Takagi's theory, due to the inclusion of a second order differential term, both theories require that the variation of the crystal potential be small over the range of the unit cell.

b) Methods of Solution

The fundamental equations for the wave amplitudes, $D_o(r)$ and $D_h(r)$ of Takagi's theory are given by :-

$$\underline{S}_o \cdot \text{grad}\ \underline{D}_o = \frac{\partial}{\partial S_o} D_o = -i\pi K C \chi_{\bar{h}} D_h \qquad (4.9a)$$

$$\underline{S}_h \cdot \text{grad}\ \underline{D}_h = \frac{\partial}{\partial S_h} D_h = -i\pi K[C \chi_h D_o - 2\beta_h D_h] \qquad (4.9b)$$

where $\underline{S}_o$ and $\underline{S}_h$ are the unit vectors in the incident and

reflected directions, C = 1 or $\cos 2\theta$ for σ and π polarisations, K is the wave vector in vacuum and $\beta_h = \dfrac{|K_h|^2 - |K_o|^2}{2K^2}$.

It may be shown, (Authier, Malgrange and Tournarie, 1968) that, by using a first order Taylor expansion, these may be reduced to :-

$$D_o(M) = D_o(P_1) + p(-i\pi K C \chi_{\bar{h}}) D_h(P_1) \qquad (4.10a)$$

$$D_h(M) = D_h(Q_1) + q(-i\pi K C \chi_h) D_o(Q_1) + q(2\pi i K \beta_h) D_h(Q_1) \qquad (4.10b)$$

with $p = P_1M$, $q = Q_1M$ and P,Q and M defined in Fig. 4.14. The wave amplitudes at M are thus completely defined by their amplitudes at P_1 and Q_1. By means of a step-by-step calculation, the wave amplitude at any point in a distorted crystal may thus be determined.

All computed profiles shown here were evaluated using a Runge-Kutta integration of the fundamental equations on a grid between the Borrmann fan extremities, (Sworn, 1971). The program was written and run by Mr. C.H. Sworn of the Cavendish Laboratory, Cambridge. The method is similar to, but faster than that of Taupin, (1967), (Jouffrey and Taupin, 1967). A check on its validity was made by comparing the result for a plane wave of unlimited extent with a similar run using Howie and Basinski's theory. Their method of numerical integration with respect to crystal depth involves a modified Runge-Kutta integration considering 20 to 200 columns simultaneously. At each stage the lateral derivatives were evaluated and the

correction for the 'non-column' approximations made to the resultant amplitude. There was good agreement between the two solutions, (Sworn, 1971).

c) Shape of Wavefront in Traverse Topographs

As was demonstrated previously, the wavefront in X-ray topography cannot be approximated to a plane wave. In fact, the wavefront will be composed of a series of spherical waves originating from different parts of the source. However, the intensity reaching the film of a traverse topograph is dependent only on the intensity reaching the crystal integrated over the Borrmann triangle. It is not dependent on the detailed shape of the wavefront, (Takagi, 1969; Authier, 1970(b)).

Then, provided that one considers the angular divergence of the beam large enough to cover the rocking curve in both perfect and distorted crystals, the intensity may be calculated from the integrated plane wave. This may be approximated by a finite number of plane waves at different deviation parameters.

d) Comparison of Theoretical Dislocation Profiles with Experiment

In this section, microdensitometer traces of dislocation profiles are compared with profiles computed for dislocations of the same direction, Burgers vector and depth in the crystal. Considerable care was taken to ensure that the diffracted beam was parallel to the photographic plate, and it is estimated that this error was always much less than 2 μm.

Dynamical Images in Thin Crystals

Figure 4.15 shows computed and experimental profiles of a dislocation, lying about 10 μm from the X-ray entrance surface of the 60 μm thick crystal, imaged in the AgKα, $\bar{2}\bar{2}0$ reflection. The direction of the dislocation is roughly $[\bar{1}12]$ and from Fig. 4.16 the dislocation, marked A, is determined to be invisible in the $\bar{1}11$ reflection, giving the Burgers vector as $\frac{1}{2}[110]$. This dislocation is then edge in character. The foil thickness was, in all cases described here, measured from the thickness fringes. The microdensitometer traces were taken at right angles to the dislocation line in all cases, and, as the computed profiles are all parallel to the g vector, where necessary, the appropriate correction factors have been included. Also, as the computed profile is taken at the exit surface of the crystal, parallel to the crystal surface, a $\mathrm{Cos}\theta_B$ factor has been included to project the image into the plane of the film.

In order to make these high resolution profile measurements, it was necessary to magnify the images from the original topograph onto a photographic plate using the Reichert optical microscope. Care was taken to ensure that the plates were neither under - nor over-exposed - so as to give reasonable contrast in both direct and dynamical images. It is unfortunate that this procedure was necessary, but the maximum magnification of the Joyce-Loebel microdensitometer was 50x, too small for accurate comparative work.

The position of the image in the foil was again determined by the geometrical method. It is an interesting check on the

FIG 4.15

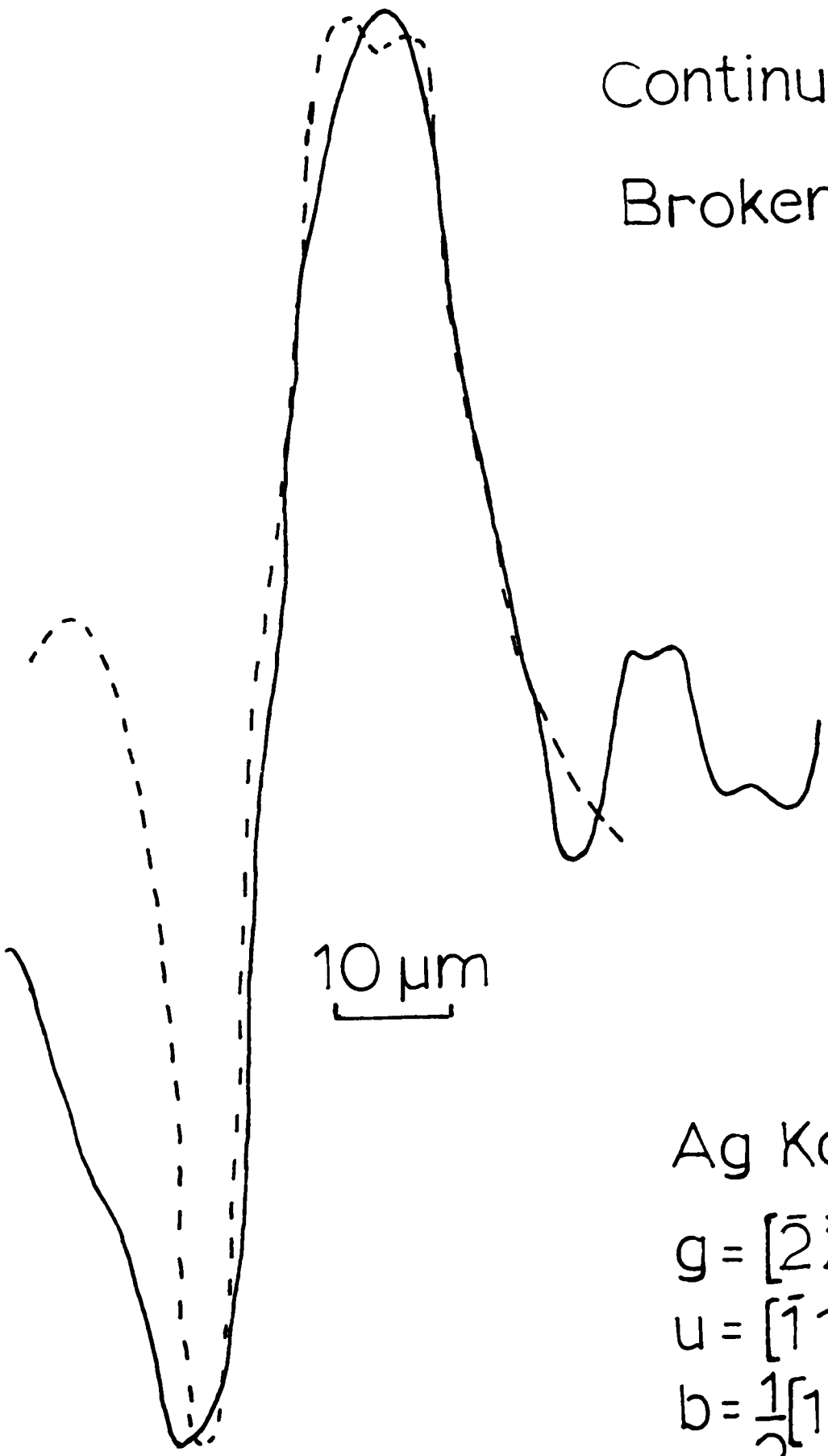
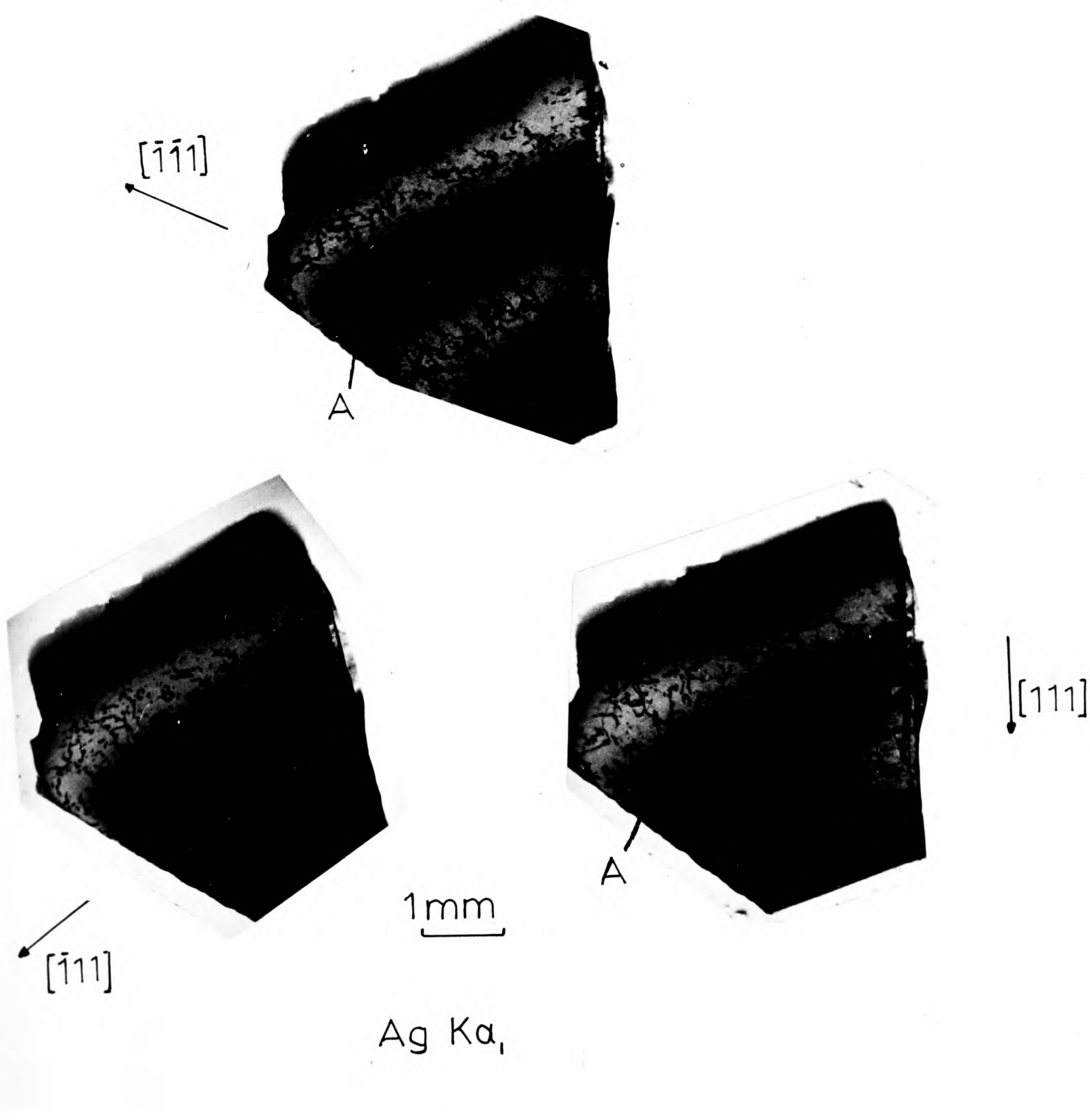

Continuous Line- Expt.
Broken Line - Theory
10 μm
Ag Kα
g = [$\bar{2}\bar{2}$0]
u = [$\bar{1}$12]
b = $\frac{1}{2}$[110]
μt = 0.055

FIG 4.16



validity of this method, that the dynamical image lies about 15 μm from the direct image in the computed profile of the dislocation 10 μm from the entrance surface. With a crystal of thickness 60 μm in the $\bar{2}\bar{2}0$ reflection with AgKα, this is in agreement with the value derived from geometry.

The agreement between experimental and theoretical profiles is quite good in this case. The relative height of dynamic and direct images are in good agreement, though the detailed shape of the dynamical image differs. In this case, the shape of the direct images is very similar, the widths being very nearly equal.

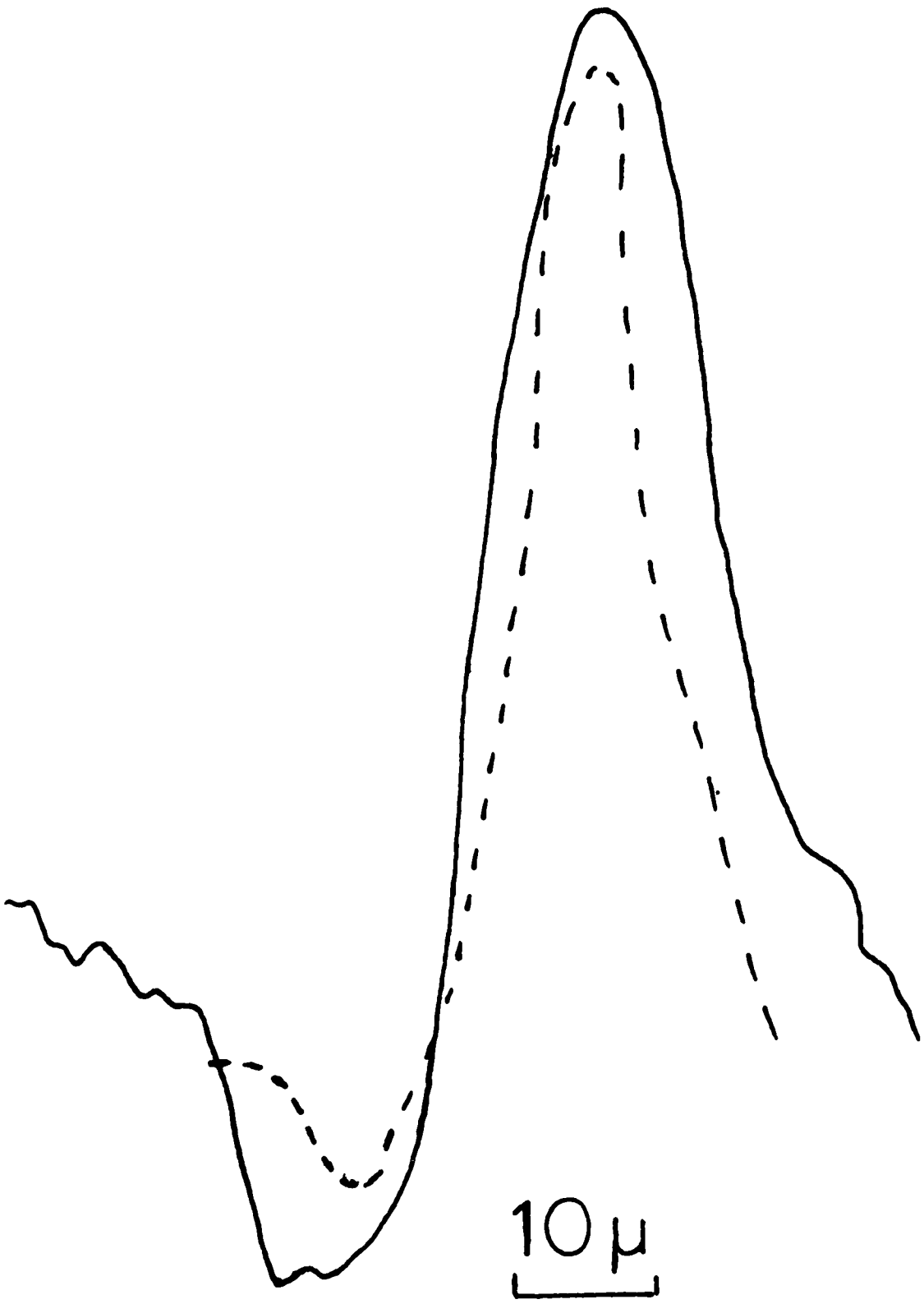
[It should be noted that altering the position of the dislocation between 5 and 10 μm from the top of the crystal, made virtually no difference to the profile. The profile was, however, markedly different for a dislocation 30 μm from the surface.]

Figure 4.17 shows another dynamical image in a thin crystal, this time of a 60° type dislocation. The foil here is 27 μm thick and a $\frac{1}{2}[110]$ dislocation lying along $[10\bar{1}]$ is imaged in the CuKα $\bar{2}\bar{2}0$ reflection. Again, the positions of the dynamic and direct images agree, and also agree with the positions predicted by the geometrical method. However, the relative heights of the dynamical and direct images are not the same, and the experimental images are both considerably wider than the theoretical ones.

Direct Images in Thin Crystals

The agreement of detailed image shape between theory and

FIG 4.17



experiment does not seem to be so good in the case where no appreciable dynamic image is observed.

Figure 4.18(a) shows the image of the dislocation shown in Fig. 4.17 images with MoKα_1 radiation in the $\bar{2}\bar{2}0$ reflection. The overall width of the images is in good agreement but, while the experimental image definitely consists of two peaks, the peaks are much closer together than in the computed profile. Similarly a dislocation lying along [011], with the same Burgers vector in the same reflecting conditions, exhibits similar characteristics, (Fig. 4.18(b)).

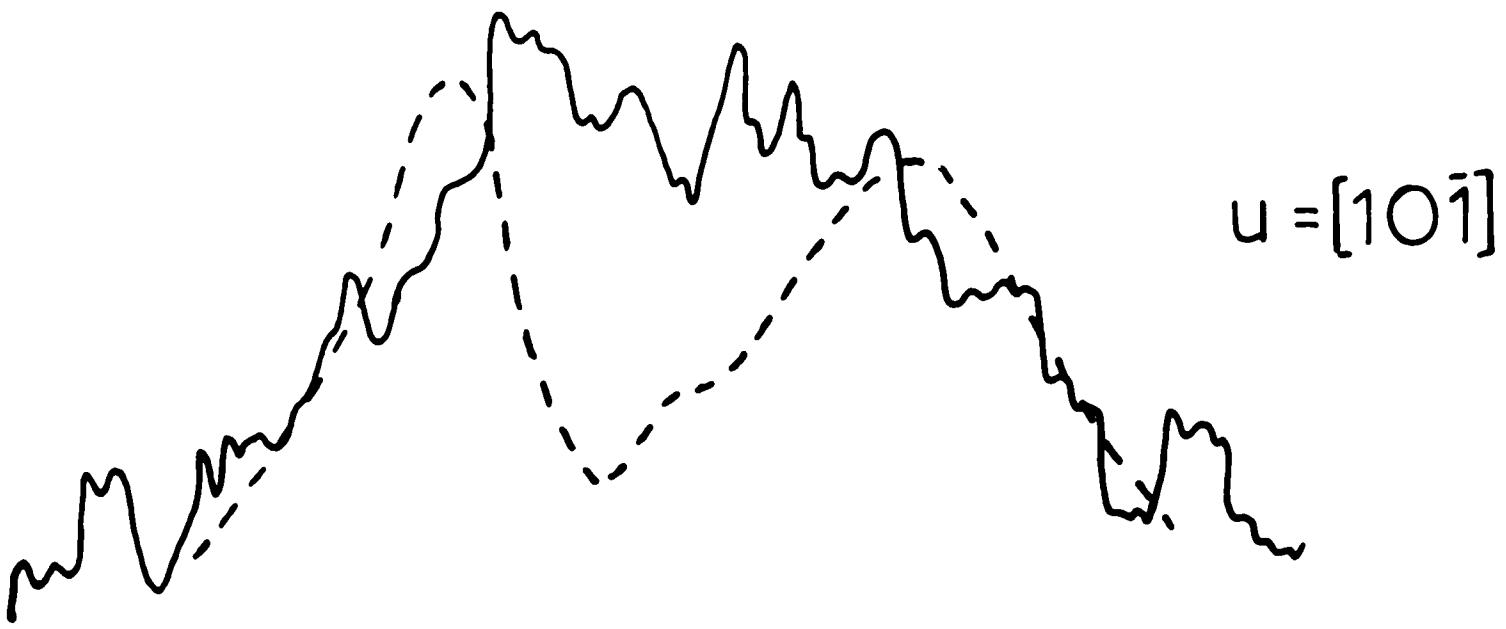
Figure 4.19 shows the dislocation along [10$\bar{1}$] imaged with MoKα $\bar{2}\bar{4}\bar{2}$ reflection. Once again, there is good agreement in the overall image width, but the detailed shape is not reproduced.

e) Discussion

The major impression gained from the studies of the last section is that the widths of the images may be quite accurately predicted on the computer, but that one cannot obtain the detailed image shape. It is then to be questioned whether the method has any value for studying images in thin crystals. After all, one can determine the separation of the dynamical and direct images by the geometrical method, and by computing the contours of equal misorientation around a defect, make quite a reasonable prediction of the image shape, (Authier, 1967).

One advantage over simply computing equal misorientation contours is certain. As pointed out by Authier, it is not clear whether in determining the volume of defect contributing to the

FIG 4.18



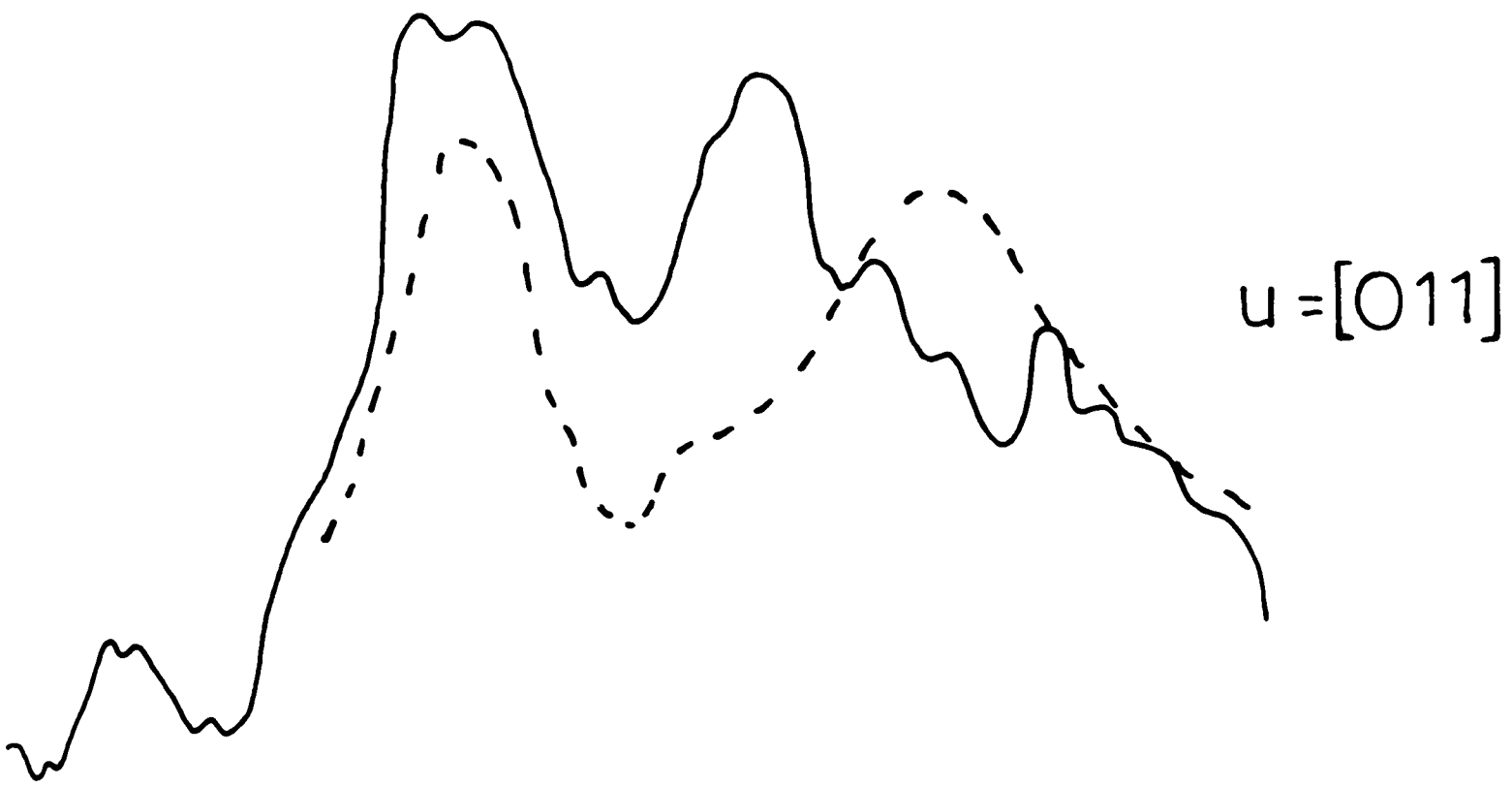
(a)

Mo Kα

g = [$\bar{2}\bar{2}$0]

10μ

b = $\frac{1}{2}$[110]



(b)

FIG 4.19

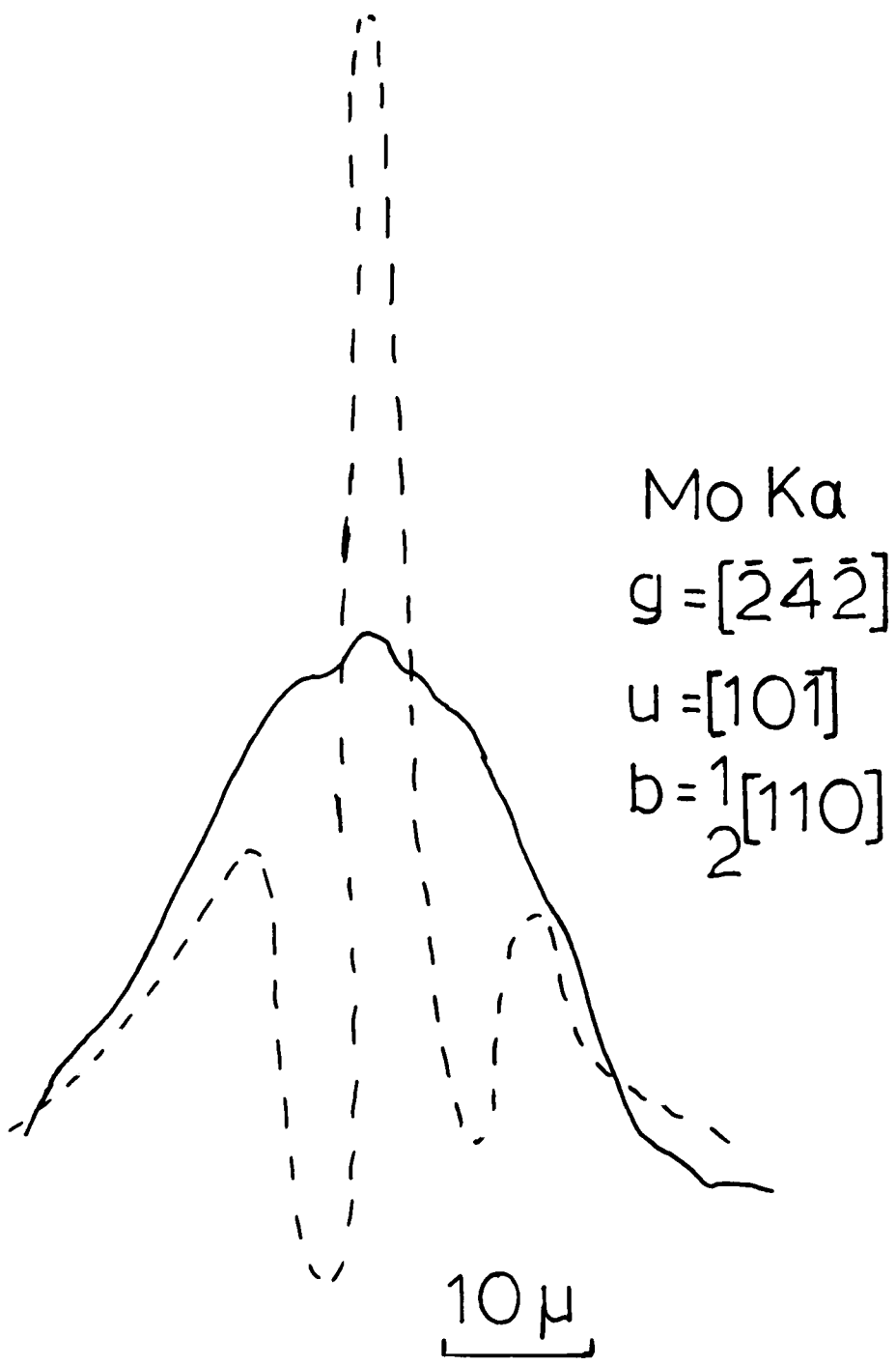
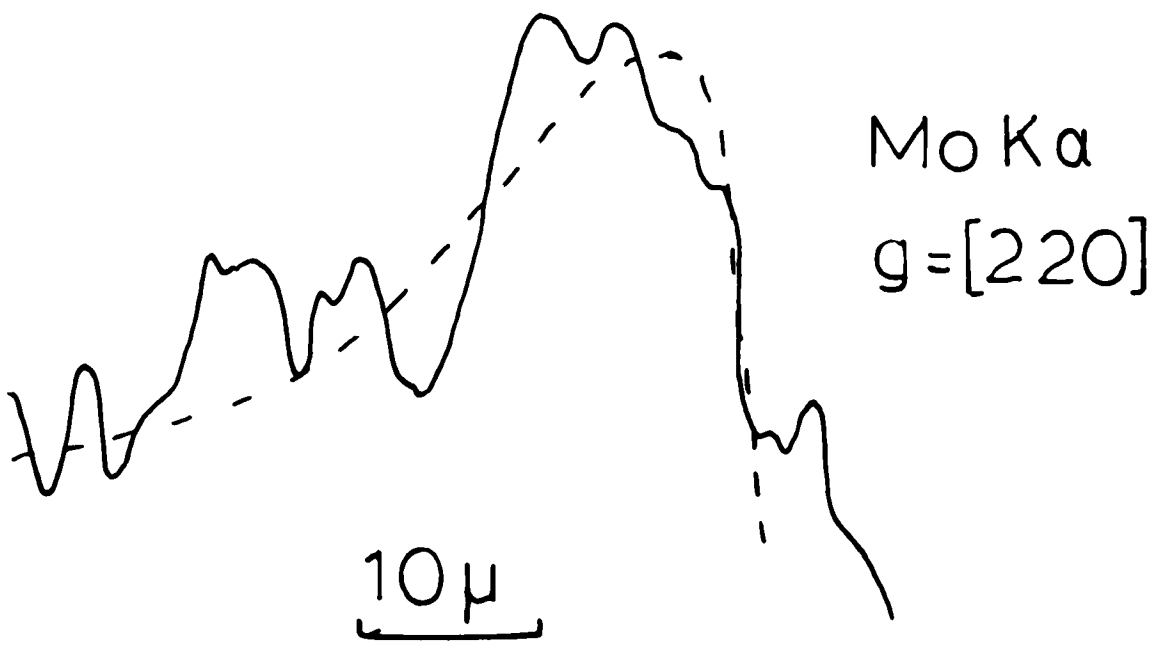


FIG 4.20



direct image, one should consider material with misorientation greater than once or twice the rocking curve width. A detailed study shows that one cannot make a general rule, (Miltat, 1971), and depending on the reflection, values between one and two times the rocking curve width are appropriate. This approach is, of course, rather rough as it neglects any formation of dynamical or intermediary images which, as has been seen, may be appreciable even in thin crystals. However, the dynamical theory computation does take these effects into account and one would thus expect that the point at which image formation occurs should be predicted quite accurately. Although the experimental evidence is somewhat limited, it does seem that this is borne out in practice.

The inability to predict the image detail is a major problem. At the centre of the image, the part of the defect contributing will be misoriented by quite a large amount. Thus, the X-rays reflected from this region will be those making large angles with the exact Bragg position, i.e., having relatively large deviation parameters. In order to compute the images accurately, one must ensure that :-

i) The angular divergence of the beam is large enough;

ii) Enough plane waves are taken.

In the present work only six beams were taken with different deviation parameters. It may be that this was not enough to smooth out the image shape. More important is that the angular divergence of the beam was taken to be $\pm$ 2 x 10^{-5} radians. Rocking curve half widths for the reflections used are shown

in Table 4.4.

Table 4.4

Rocking Curve Half Widths

Radiation	Reflection	$\Delta\theta_B$ secs	$\Delta\theta_B$ radians
AgKα	220	0.87	4.2×10^{-6}
MoKα	220	1.1	5.5×10^{-6}
	224	0.87	4.2×10^{-6}
CuKα	220	0.7	1.3×10^{-5}

One can roughly say that the misorientation around a defect, (Appendix A), is given by :-

$$\delta(\Delta\theta) \quad \alpha \quad \frac{1}{r} \tag{4.11}$$

and that the intensity due to the enclosed material :-

$$I(\Delta\theta) \quad \alpha \quad \frac{1}{|\delta(\Delta\theta)|^2} \tag{4.12}$$

Then the accuracies expected from neglect of waves with a larger divergence than that taken, may be estimated for the various reflections and are shown in Table 4.5.

The discrepancy between experimental and computed profiles for copper radiation, (Fig. 4.17), may be due to not taking a large enough beam divergence. In Fig. 4.19, the discrepancy is probably due to not taking enough beams.

Table 4.5

Estimated Accuracy in Intensity

Radiation	Reflection	Accuracy
AgKα	220	± 4 %
MoKα	220	± 6 %
	224	± 4 %
CuKα	220	± 40 %

[It should be noted that the absolute magnitude of the experimental and theoretical profiles are of no significance, and are adjusted in each case.]

These errors may be reduced by taking a large divergence, but this increases computing times for two reasons. Firstly, and obviously, having to run the program more times, and secondly, that as the deviation increases, the step length in the integration must be decreased. A requirement of Takagi's theory is that D_g and $|\underline{g} \cdot \underline{u}|$ must remain constant over a length, ℓ, where ℓ is given by :-

$$\ell = \frac{1}{\sqrt{\lambda \xi_g}} \qquad (4.13)$$

For the 220 reflection $\ell = 0.055$ μm independent of wavelength. If the step length, i.e., length over which D_g changes appreciably becomes less than this value, the theory obviously breaks down. As may be seen in Appendix A, the distance from a dislocation where the condition on $|\underline{g} \cdot \underline{u}|$ breaks down is about 0.03 μm

to 0.05 μm from the core. The error in the intensity due to neglect of this, is considerably less than 1/3% even if the defect image is only 1 μm wide. Inaccuracies due to $\nabla^2 |\underline{g} \cdot \underline{u}|$ varying over 0.05 μm may be comfortably neglected. No estimate can be made by hand of the distance from the dislocation core at which the condition on D_g breaks down, but this is something which needs study. It should be fairly simple to extract the information from a computer.

f) Conclusion

Reasonable agreement has been found between computed and experimental dislocation images. Increase of beam divergence and consideration of more beams in the theoretical case should lead to improved correlation. In the one case studied in a thick crystal, 225 μm of silicon, the agreement is quite good. Figure 4.20 shows the image of a dislocation 5 μm from the exit surface imaged with MoKα radiation in the 220 reflection. The asymmetry in the profile is observed in both cases. Further work in the thick crystals is hampered by the length of time taken to obtain a single profile.

Much work needs to be done in this field before it will be possible to use this method for image identification. This must include a study of the effects of the crystal surfaces on the image.

Summary

The thickness at which loss of visibility in dislocation images occurs was measured in the Laue and Bragg cases. It was

found that the value depended on the fraction of the material thickness taken up by misoriented material. This explanation was found to be in qualitative agreement with experiment, the fraction of the extinction distance at which loss occurred fell as higher order reflections were taken. The values given by Penning and Goemans were revised to 1/6th and 0.4 of an extinction distance. No evidence was found to support the idea that defects closer than 1/3rd to 1/6th of an extinction distance from a crystal surface give no topographic contrast.

The second part consisted of a comparison of theoretical and experimental image profiles. The sources of error in the method and ways of rectifying them were discussed in terms of practical and basic limitations.

Note:

Following the suggestions in the latter part of this chapter, Sworn, (1971), has shown that inclusion of more plane waves and increase of the beam divergence does indeed lead to much better agreement between theory and experiment in the CuKα 220 reflection.

C H A P T E R V

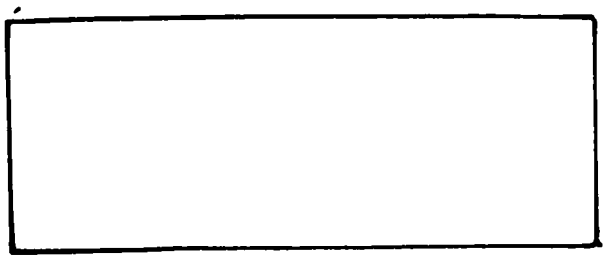
X-RAY TOPOGRAPHIC STUDY OF DEFECTS IN SILICON FOLLOWING DEVICE FABRICATION

1. Introduction

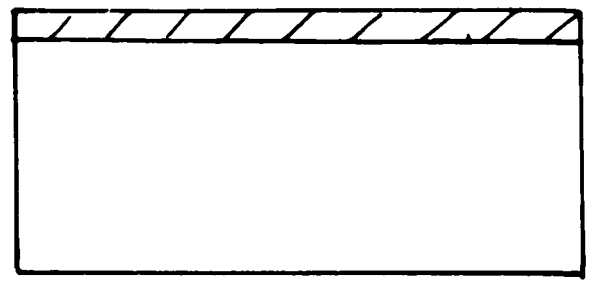
As zero dislocation density silicon crystals became readily available about the time that X-ray topography became an established technique, relatively few studies have been made of the as-grown material, (Yoshimatsu et al., 1962; Yoshimatsu, 1963; Kohra and Yoshimatsu, 1962; Yoshimatsu, 1964; Meieran and Blech, 1967; Yukimoto et al., 1967; Yukimoto, 1968; Jenkinson and Lang, 1962). Though there is considerable interest in the study of defects in web-dendrite, (Tucker and Schwuttke, 1966; Schuttke, 1967; O'Hara and Schwuttke, 1965; Meieran, 1970), the bulk of the X-ray topographic work undertaken at present is in the study of silicon which has been diffused with impurity in the process of device manufacture.

The principles of integrated circuit device manufacture are shown schematically in Fig. 5.1. A slice of silicon, 100 to 200 μm thick, which has been lapped and chemically polished is steam oxidised at about 700° C. Components are etched out of the oxide film at room temperature, using a photo-resist mask. Tri- or penta-valent impurity is diffused in at high temperature (∿ 1000° C), usually in a two step process. A small amount of solid is absorbed on the specimen

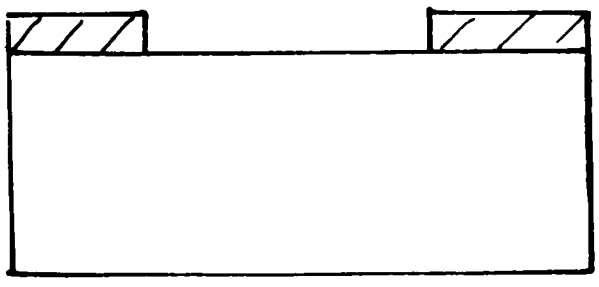
FIG 5.1



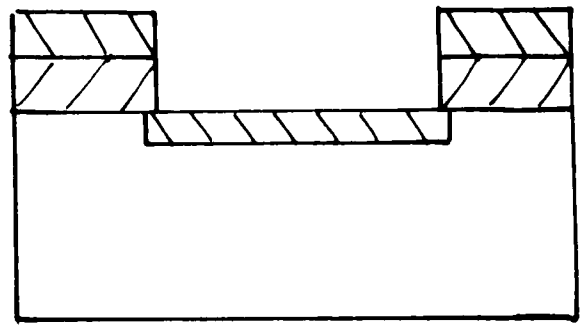
Polished slice



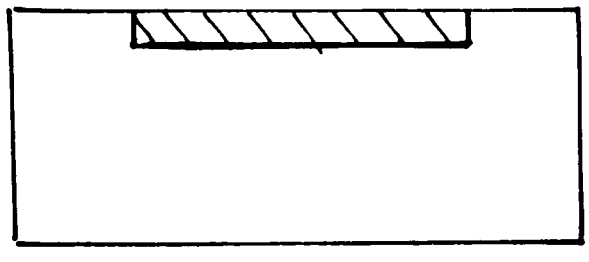
Steam oxidation



Windows cut
(Room temp.)



Diffusion



Oxide removed

surface in the short pre-diffusion and then re-distributed in a second diffusion. Connections are made between components by evaporated metal films, and a complete circuit containing a score or so transistors may be accommodated in a square millimetre, Fig. 5.2(a). The strain gradients associated with the edges of components and the presence of any crystallographic defects may be detected by X-ray topography, Fig. 5.2(b). As yields are rarely above 70% in integrated circuit manufacture, considerable effort has been made in attempts to identify the causes of device failure. Two of these are fairly well established, masking faults and crystal lattice defects.

(a) Masking Faults

In complex components, involving several diffusions, misalignment of the photo-resist mask can cause short-circuits. Similarly, scratches made in the oxide mask before diffusion can lead to short circuiting of part of the device. These faults, which are common, are believed to be responsible for a large proportion of device failures.

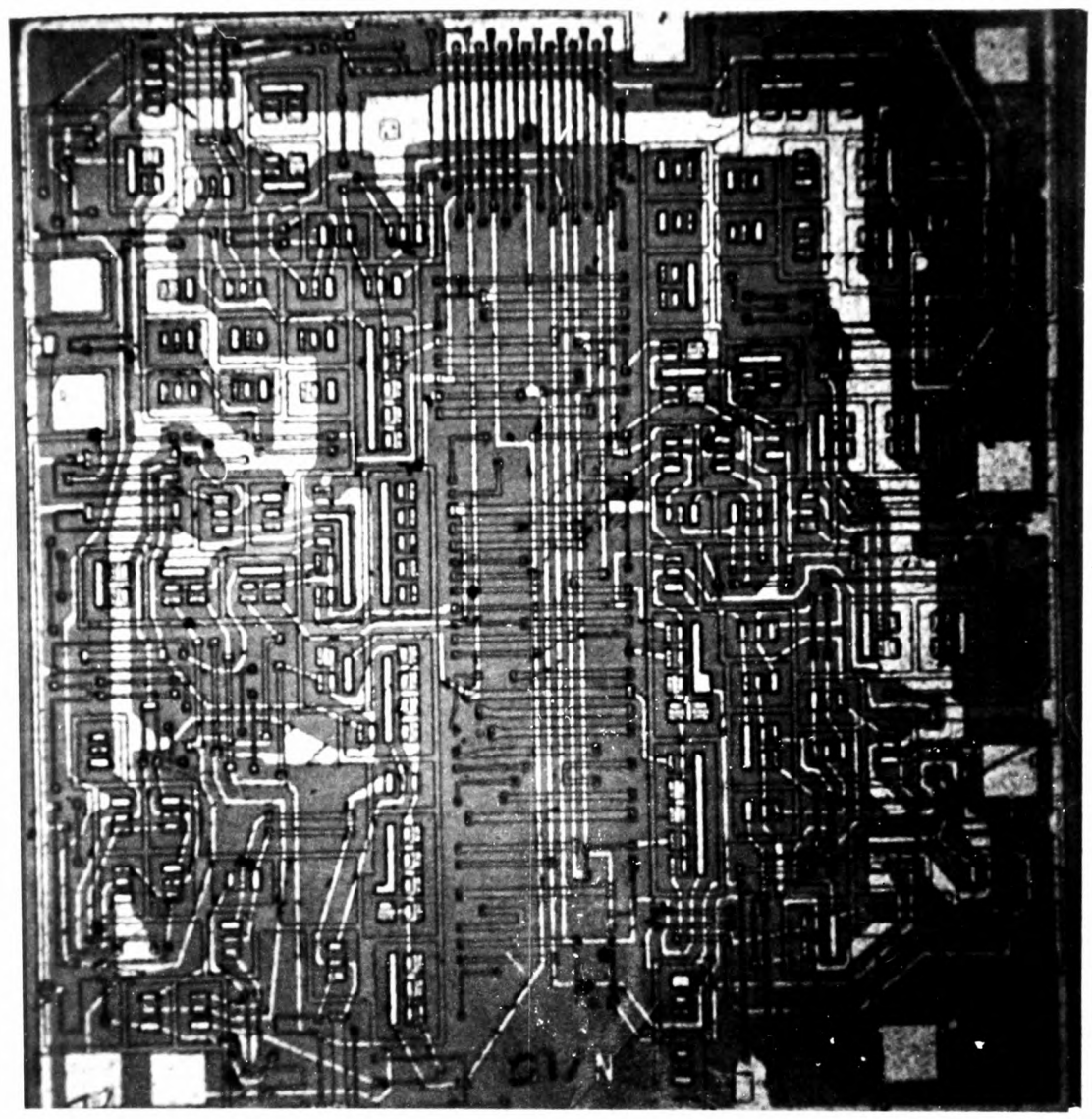
(b) Lattice Defects

Three types of dislocation are observed as a result of device processing :-

(i) Diffusion induced dislocations contained inside the diffused regions.

(ii) Diffusion induced dislocations created at the edge

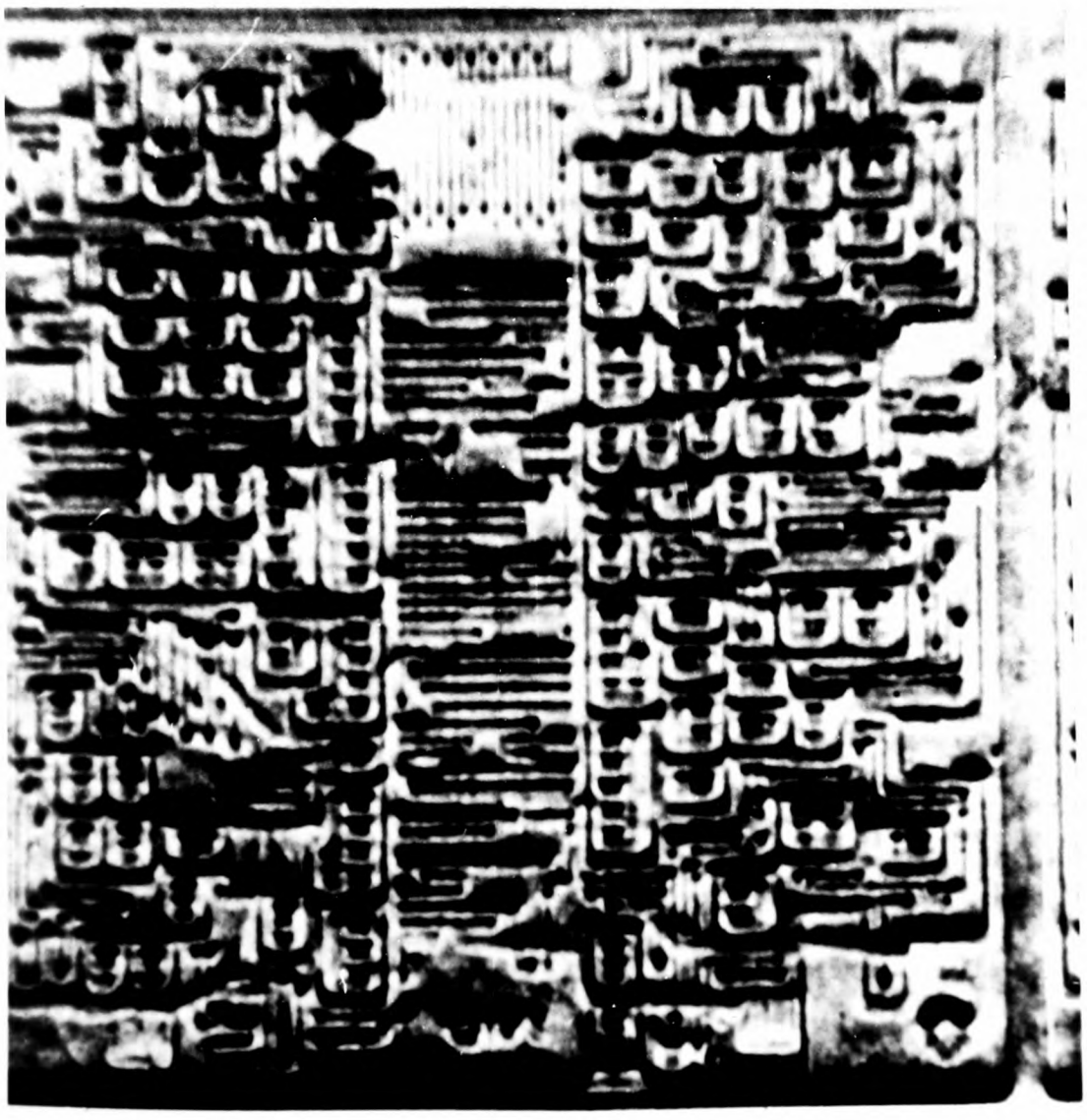
FIG 5.2



Optical

200 μ

(a)



X ray

(b)

of the diffused regions and extending inside and outside of the diffused regions.

(iii) Bulk slip caused by thermal shock, stresses associated with scratches or handling.

Dislocations 'grown in' the substrate do not effect device performance, (Schwuttke, 1970; Lawrence, 1968). Glaenzer and Jordan, (1968), have shown that dislocations produced by bending silicon at about 800°C are electrically active, while dislocations produced at about 1100° C, when they can easily become contaminated, are neutral. As the 'grown in' dislocations are subjected to high temperature heat treatments during device fabrication, these two observations are consistent. No positive correlation has yet been made between the presence of diffusion induced dislocations inside the diffused region and any electrical failure, and it is probable that these dislocations are contaminated and electrically inactive.

'Emitter edge' dislocations, generated at the junction and extending across it do cause reduction in transistor gain, (Schwuttke, 1967). Further, a monotonic relation has been found between diode leakage current and the number of slip dislocations penetrating a component, (Dale and Hamilton, 1971). Neither type of dislocation is expected to be contaminated. Large precipitates may cause short circuiting on diffusion, but small precipitates appear to have no effect on the junction characteristics, (Titchmarsh, 1971). The mechanism whereby the defects causing 'swirl' etch patterns

effect diode characteristics is, as yet, unclear.

In the first part of this chapter, X-ray topography is used to attempt a quantitative measurement of the stress at the edge of the diffused region, using the method developed by Lawn, (1968), and a combined X-ray topographic and Scanning Electron Microscope study of breakdown fingers, observed in the Beam Induced Conductivity mode, is described. The second part presents some studies of dislocations produced as a result of the diffusion. Interactions between emitter edge dislocations are observed and the anomalously narrow images explained. Burgers vectors of the inside dislocations are determined for boron diffused silicon, and interactions with emitter edge dislocations described. The unique contrast properties of the inside dislocations in low dislocation density regions are explained in terms of surface relaxation effects using the Penning-Polder theory.

2. X-ray Stress Topography at Diffusion Junctions

X-ray diffraction from discontinuous surface films has been studied both experimentally, (Meieran and Blech, 1965, 1968; Blech and Meieran, 1966; Schwuttke and Howard, 1968; Segmuller, 1968), and theoretically, (Patel and Kato, 1968; Kato and Patel, 1968; Blech and Meieran, 1967; Lawn, 1968; Frank *et al.*, 1967). Quantitative measurements have so far only been applied to oxide or metal films evaporated on the substrate. In this section, the method of analysis used by Lawn, (1968), is applied to the edge of the diffused region.

The ionic radii of boron and phosphorus are both less than that of silicon and on diffusion, a contraction occurs, straining the surrounding lattice, Fig. 5.3. With the assumption of isotropic elasticity, uniform deformation and small thickness of deformed layer, δ, compared with the width of the contrast band, Lawn has derived expressions for the atomic displacements in terms of the force per unit length of line, F. When σ is the stress in the deformed layer,

$$\underline{F} = \delta \sigma \underline{n} \qquad (5.1)$$

Consider the case of a thick crystal, where only wave fields belonging to one branch of the dispersion surface are present. In the lightly distorted region, well below the surface, the tie points migrate along the dispersion surface, (Penning and Polder, 1961). Near the surface, however, the lattice planes bend sharply, and the tie points cannot migrate back. Energy which has been transferred from one beam to the other in the lightly distorted region stays there. As the direction of tie point migration is dependent on the sense of curvature, this gives a depletion of energy in the diffracted beam on one side of the junction, and enhancement on the other. Provided small dilation terms are neglected, the condition for this breakdown to occur is that the curvature of the lattice planes becomes such that there is a rotation of the g vector by the half width of the rocking curve within the space of an extinction distance, (Lawn, 1968; Penning 1966).

FIG 5.3

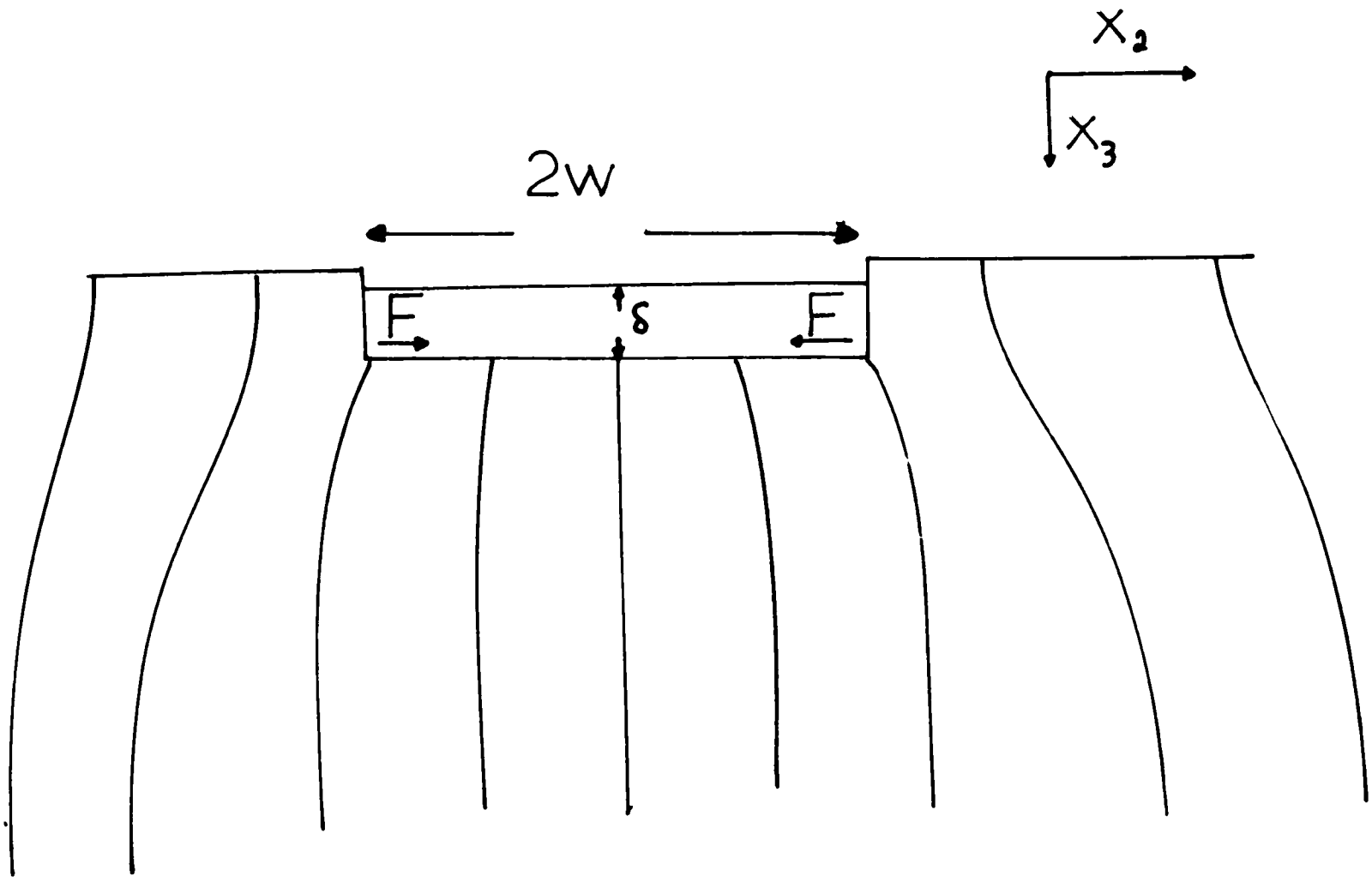
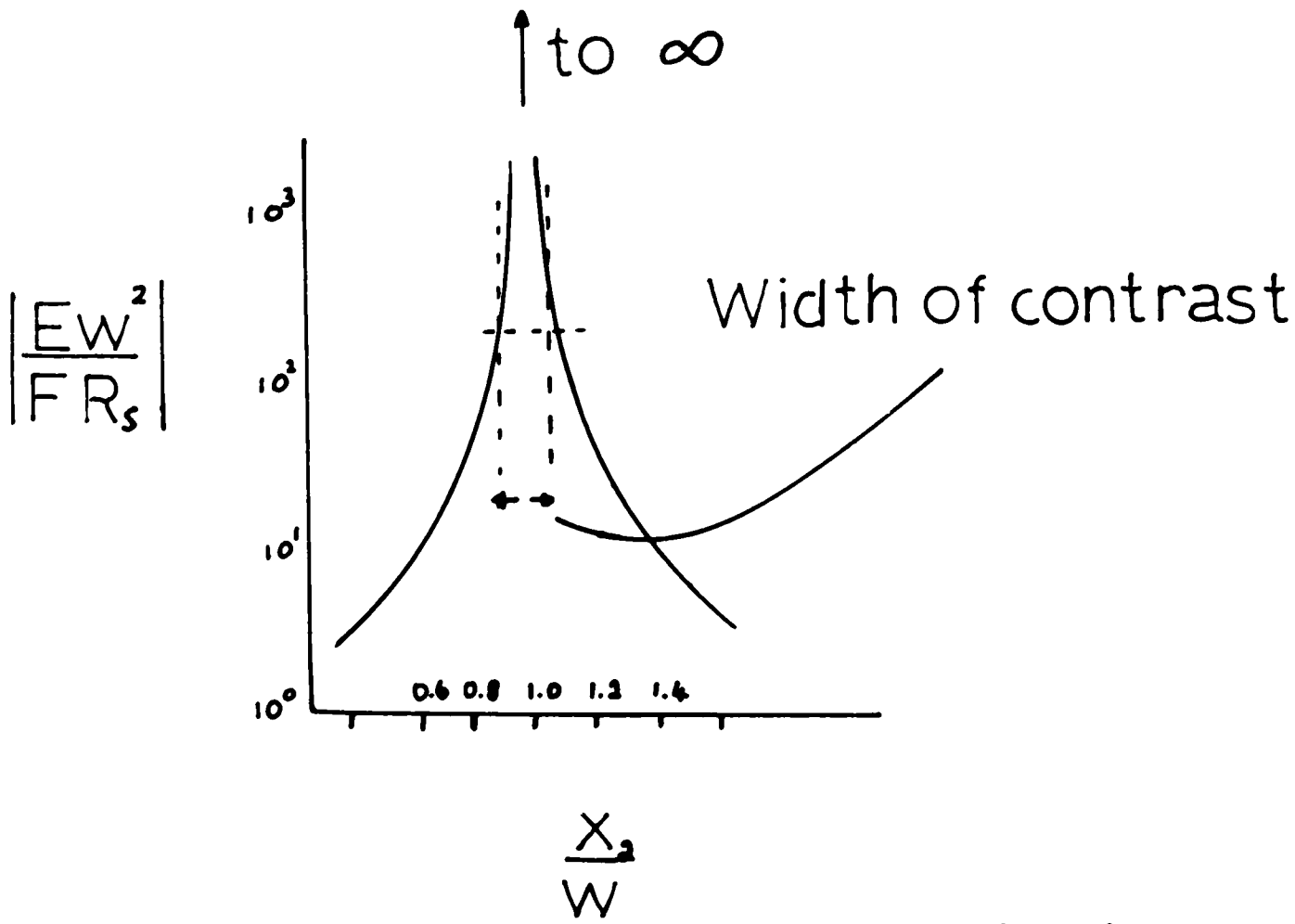

X_2
X_3
2w
F
δ
F

FIG 5.4


to ∞
$\left|\frac{EW^2}{FR_s}\right|$
10^3
10^2
10^1
10^0
0.6 0.8 1.0 1.2 1.4
Width of contrast
$\frac{X_2}{W}$
(due to Lawn)

In the thin crystal, tie point migration effects exactly cancel, as both branches are active. Extinction contrast occurs when "off Bragg angle" X-rays are reflected by the distorted region, in a manner analogous to "direct" image formation for dislocations. This occurs when the misorientation is greater than the rocking curve half width, and provided the lattice planes rotate rapidly, i.e., the distortion occurs within an extinction distance of the surface, the thick crystal criterion still holds, (Frank et al., 1967). The width of the contrast band, from a bad layer on the exit surface, is independent of crystal thickness, (Lawn, 1968).

For small Bragg angles, a general relation may be found between the width of the contrast band and the force per unit length, F. Numerical computations are necessary, and the relation given graphically by Lawn is reproduced here for convenience as Fig. 5.4. An important prediction of Lawn's theory, which has not been emphasised, is that for constant F, the width of the contrast band is independent of the width of the bad layer, 2ω, over quite a large range. Table 5.1 shows values of the fractional width of the contrast band, $\frac{x_2}{\omega}$, against curvature parameters $\frac{E\omega^2}{FR_c}$, taken from Lawn's graph.

This explains the constancy of the width of the contrast bands around the triangular windows of Schwuttke and Howard, (1968). In Fig. 3 of the above reference, the width of the contrast does not vary, although the width of the window varies from zero to a millimetre.

Table 5.1

$$\frac{E_\omega^2}{FR_c} \cdot \frac{x_2}{\omega}$$

$\frac{x_2}{\omega}$		$\frac{E_\omega^2}{FR_c}$		$\frac{x_2}{\omega}$		$\frac{E_\omega^2}{FR_c}$	
1	n	250	y	23	n.10	10^1	$y/10^2$
2	2n	70	$y/2^2$	7	$n.\sqrt{10}$	10^2	$y/10^1$
4	4n	14	$y/2^4$	2.5	n	10^3	y

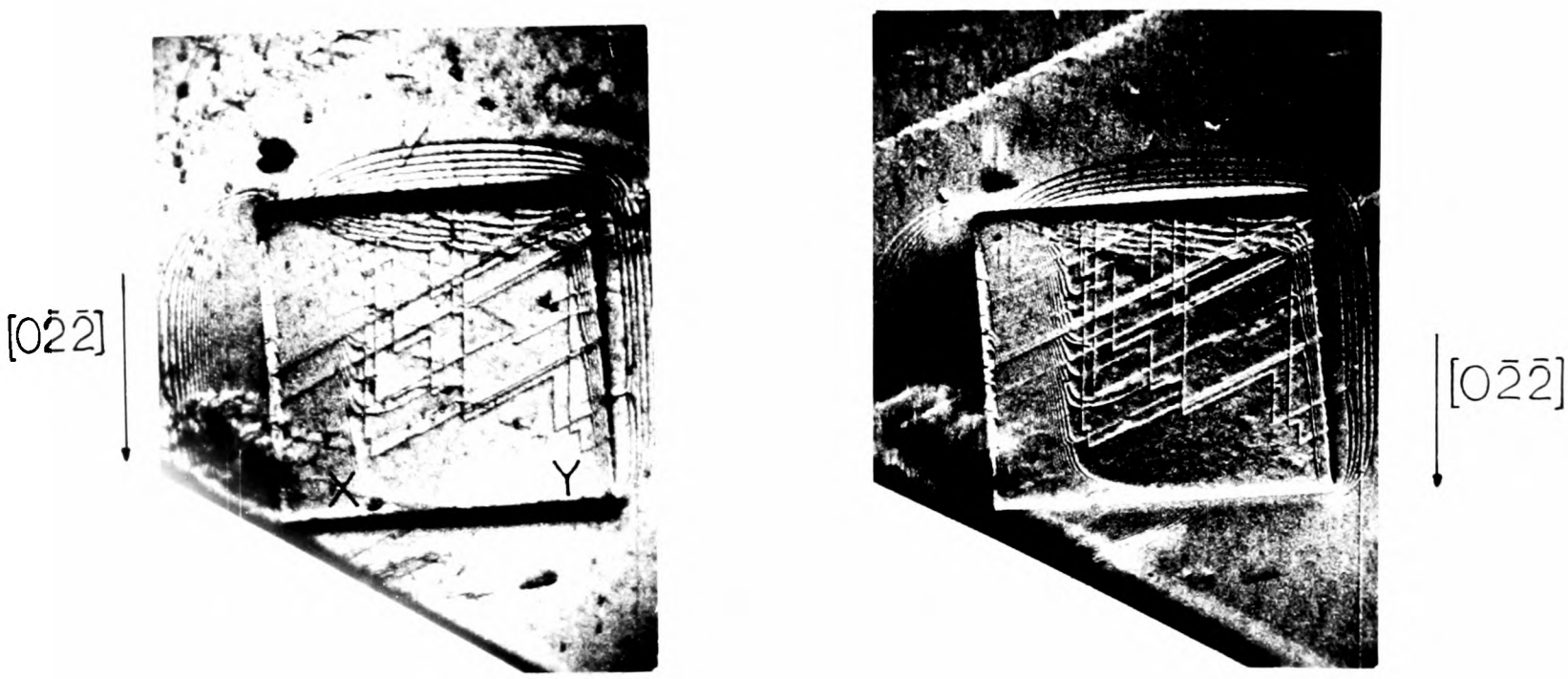
This type of analysis has been applied to the edges of the diffused regions of the specimen, part of which is shown in Fig. 5.5. The specimen, henceforth known as specimen A, is of N type 0.01 Ω cm substrate. Oxidation was performed at 900°C and a boron diffusion of surface concentration 2.5×10^{20} atoms/cc performed in 1 mm square regions at 1250°C. The oxide was removed with HF. Three things may be determined by inspection:

(a) Using the CuKα topograph, the sign of the stress is found to be tensile, as expected.

(b) In the MoKα 224 topograph, the widths of the contrast regions differ by 60%, the stress being lower at the edge with the large number of dislocations.

(c) In the MoKα 220 topograph, more stress exists in the region Y, than at X, where dislocations have formed

FIG 5.5



around the junction. The emitter edge dislocations do seem to produce a measurable decrease in the junction stress.

Table 5.2 shows values of the force per unit length of junction, as measured from the MoKα 220, 224 and CuKα 220 topographs.

Table 5.2

Force in junction due to diffusion

Radiation	Reflection	$\frac{x_2}{\omega}$	F dyne/cm
MoKα	220	0.12	1.5×10^4
MoKα	224	0.14 - 0.22	$0.7 - 2 \times 10^4$
CuKα	220	0.1	2.5×10^4

The mean value is around 2×10^4 dynes/cm, which must be taken as order of magnitude only, partly due to approximations inherent in the theory, and partly to the inaccuracy in measurement with a grid from Lawn's graph. An estimate of the stress will thus be to order of magnitude only. In any case, this will be an average stress, as the actual stress varies with junction depth. Taking the junction depth to be about 4 μm, yields a value of 5×10^7 dynes/cm^2 for the stress. This presumably corresponds to the minimum stress required to move a dislocation at 1250°C, as when this value is reached, further relaxation by dislocation motion is prevented. As expected, this is lower than the measured

minimum resolved shear stress, (Chaudhuri et al., 1962; Suzuki et al., 1966), and correlates with the value of 4.3 x 10^7 dynes/cm^2 for the stress required to move a dislocation in heavily doped silicon, measured by Moiré fringes, (Humphreys, 1967).

The maximum stress developed in the slice as a result of the diffusion is given by, (Prussin, 1961; Timoshenko, 1964).

$$\sigma_{max.} = \frac{\beta C^s E}{1 - \nu} \qquad (5.2)$$

where C^s is the surface concentration

β is the solute contraction coefficient.

This has been measured for boron, (Horn, 1954), to be 5.6 x 10^{-24} cm^3. With E = 1.3 x 10^{12} dynes/cm^2 and ν = 0.22, one obtains:

$$\sigma_{max.} = 2.4 \times 10^9 \text{ dynes/cm} .$$

Even allowing for the order of magnitude nature of the measured stress, it is apparent that significant lattice relaxation has occurred in the nucleation of the dislocations.

The method would seem to be applicable only to order of magnitude measurements. A major assumption of the model, is of a discontinuity between bad region and matrix. While this is a reasonable approximation for evaporated films, it is not so for diffused regions. It will be shown in the next section, that for low concentrations of impurity, no contrast is seen from the junction in a Lang topograph.

3. Topographic and S.E.M. investigations into the origin of "breakdown fingers"

When the Scanning Electron Microscope, (S.E.M), is used in the Beam Induced Conductivity Mode, (B.I.C), the electron beam scans a biased diode in synchonism with the cathode-ray display which detects the current in the diode, Fig. 5.6. Electron-hole pairs generated by the beam normally recombine, but in the region of the junction the strong electric fields sweep then apart. One then observes an enhanced signal from the junction. Dislocations near to a junction presumably act as recombination centres, and have been observed in this mode, (Lander et al., 1963; Czaja and Wheatley, 1964; Czaja and Patel, 1965).

Studies of p n junctions using the B.I.C. technique have sometimes revealed regions of enhanced intensity extending from the junction, (Davies et al., 1966). The work described here is a study of these 'fingers' using both S.E.M. and X-ray topography. All scanning electron micrographs are due to D.H. Hunter.

Two specimens were selected for examination, one having had a phosphorus diffusion and the other a boron diffusion. The oxide mask had been removed from both specimens.

Figure 5.7(a) shows a B.I.C. micrograph of the phosphorus doped specimen, and Fig. 5.7(b), the related optical micrograph. No surface defects corresponding to the B.I.C. fingers could be found. Analysis of X-ray topographs taken of the specimen showed that although dislocations were present in

FIG 5.6

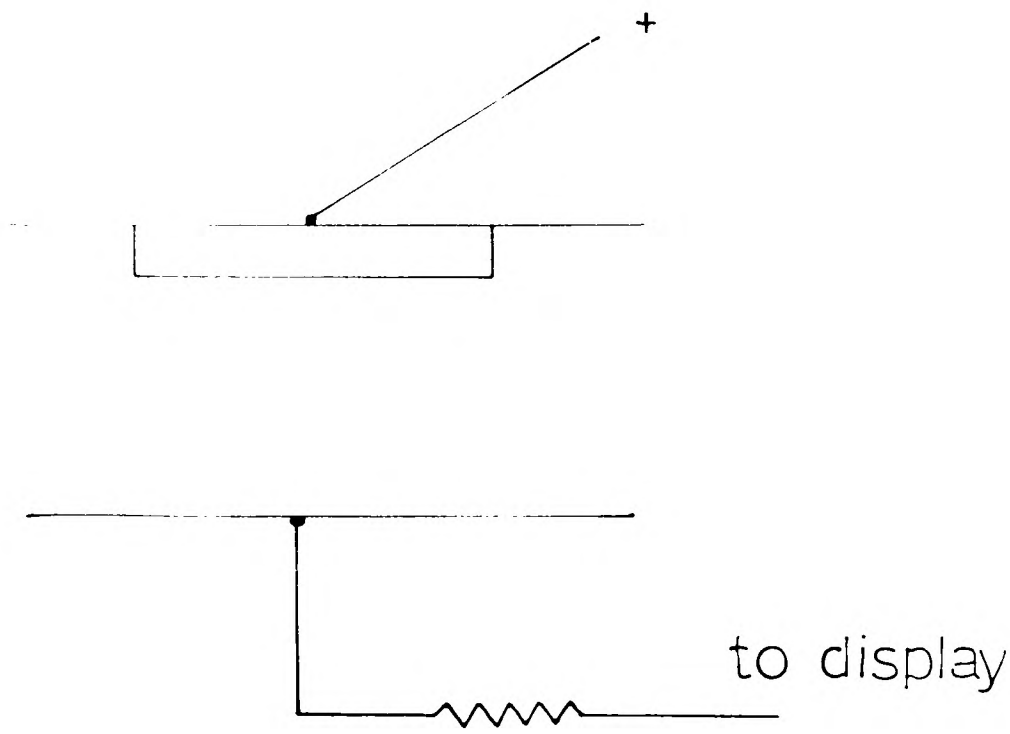
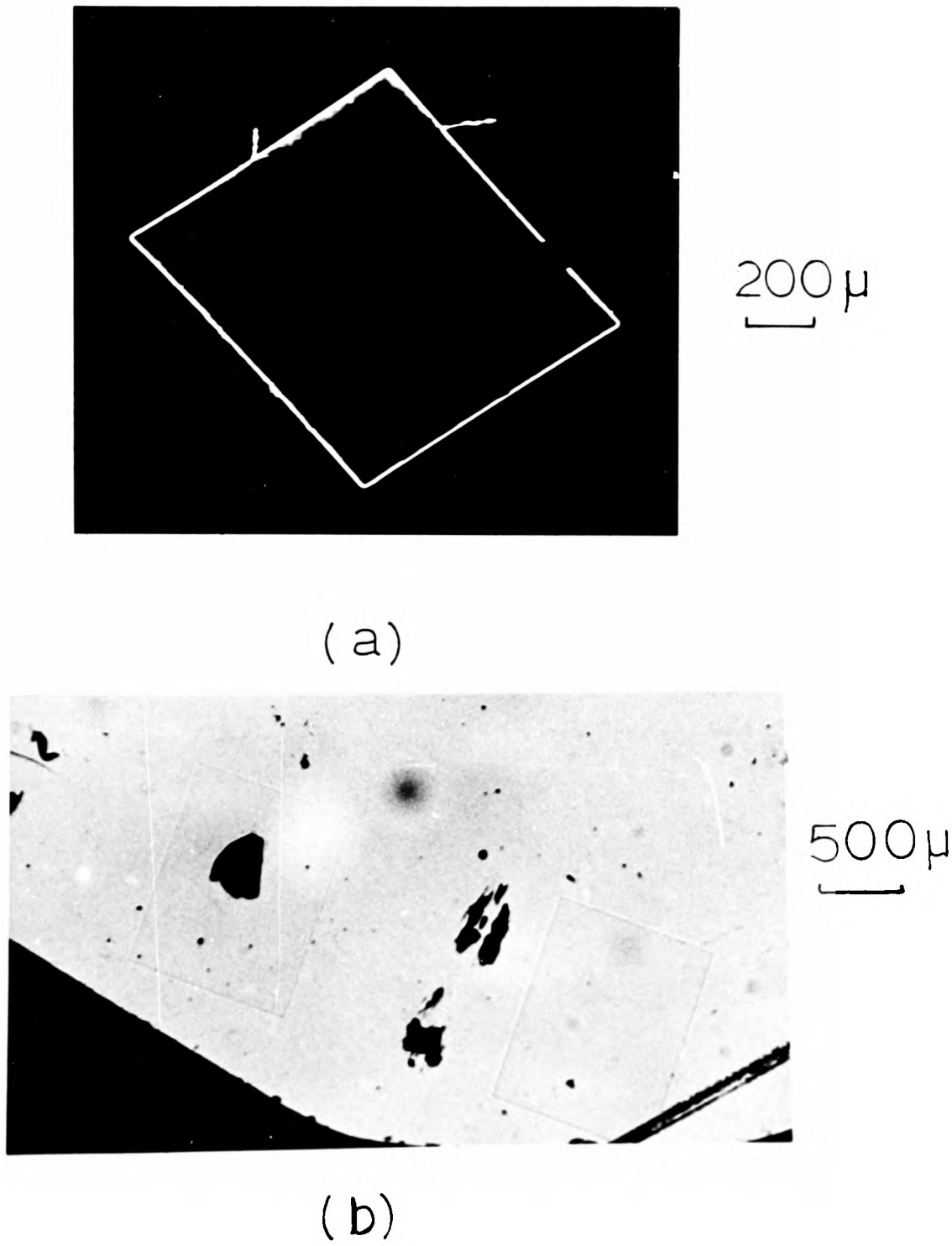


FIG 5.7

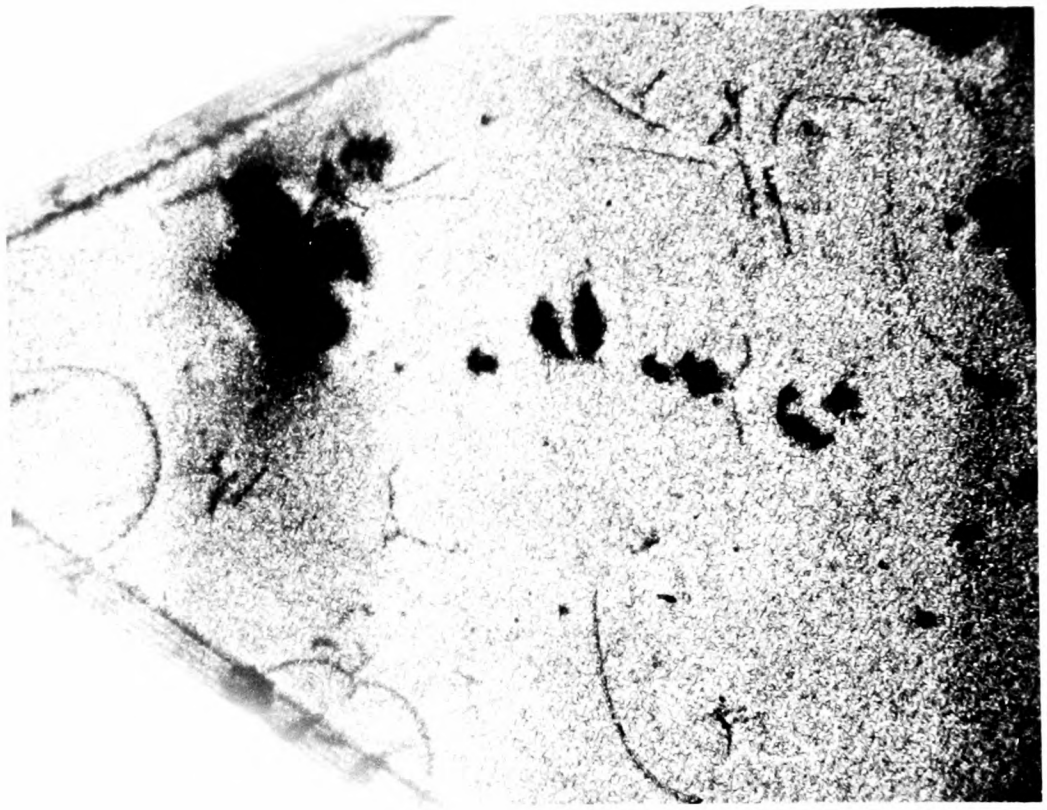


the specimen, no dislocation had either the position or direction to account for the fingers, Fig. 5.8. Careful optical enlargment, correcting for the distortion in the topograph, and superposition of the X-ray and S.E.M. micrographs confirmed this. It is thus safe to say that these fingers are not caused by dislocations crossing the junction.

Figure 5.9(a) shows regions of B.I.C. breakdown in the boron doped specimen and, again, no correspondence could be found with scratches on the surface, Fig. 5.9(b). In the X-ray topographs, Fig. 5.9(c) and 5.9(d), in addition to the scratches, the junction contrast was visible and seen to be distorted at positions corresponding to the B.I.C. breakdown fingers.

Using the method of the previous section, an estimate of the width of the contrast band may be made. In the boron doped specimen ($C_s \sim 10^{18}$ atoms/cc), this is predicted to be about 25 μm, which is in good order of magnitude agreement with the observed width of 30 μm. For the phosphorus doped specimen ($C_s \sim 10^{17}$ atoms/cc), a contrast band 10 μm wide is predicted, but not observed. It seems here that the approximation of the junction edge to a discontinuity is invalid and at no place is the distortion severe enough to cause image formation. One then infers that the strain gradients associated with the fingers are of the same order as those in the junction. That is, when the junction is visible, direct correspondence is found between fingers and X-ray contrast; when invisible, no corresponding contrast is observed. The fingers would thus seem to be extensions

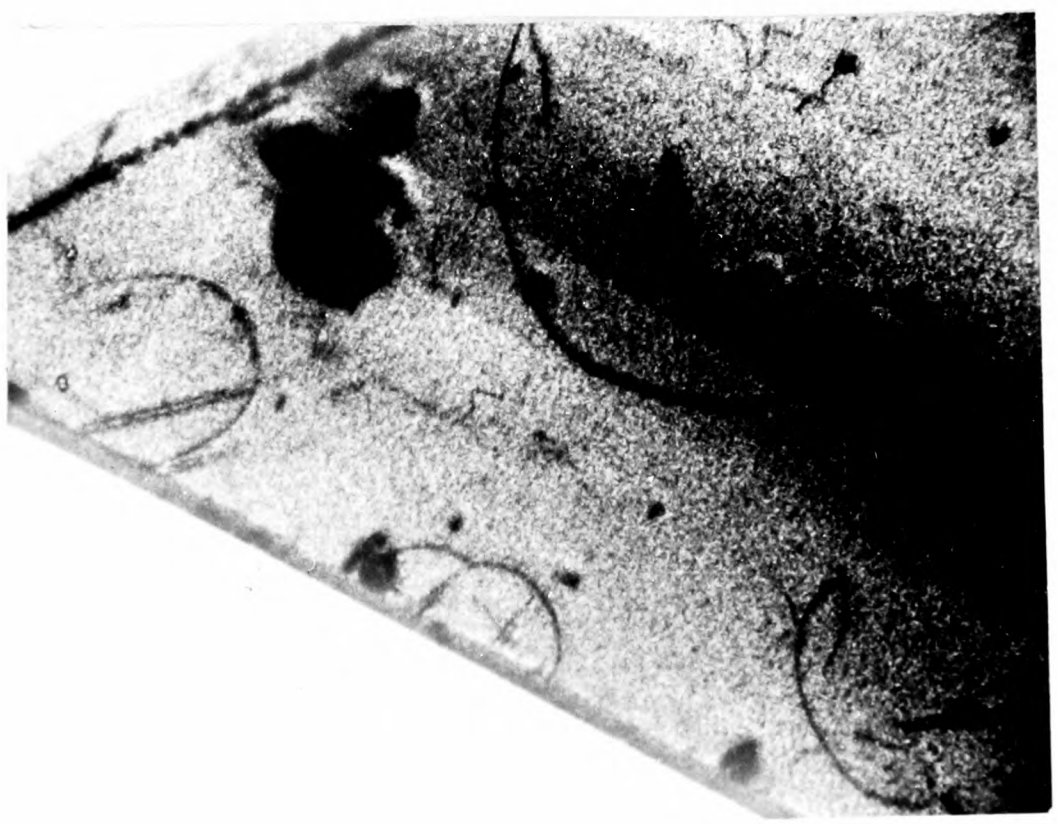
FIG 5.8



g



g



g

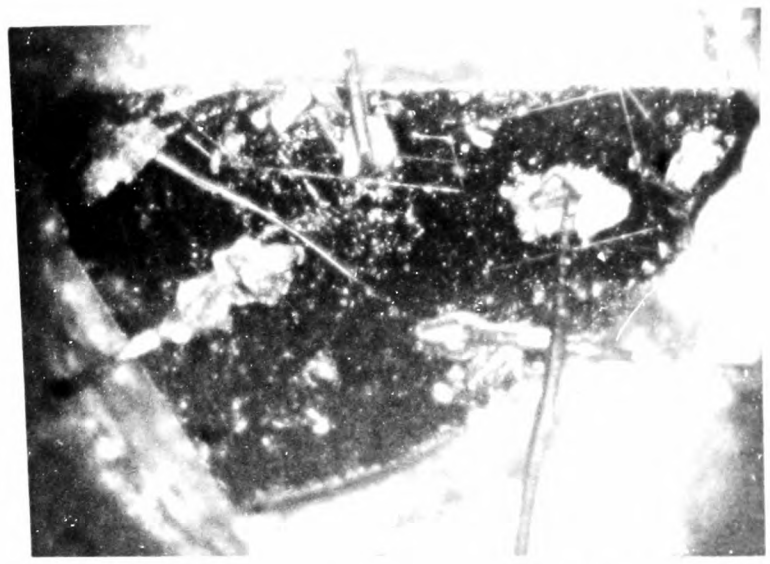
111 reflections

FIG 5.9



(a) 250μ

B.I.C.

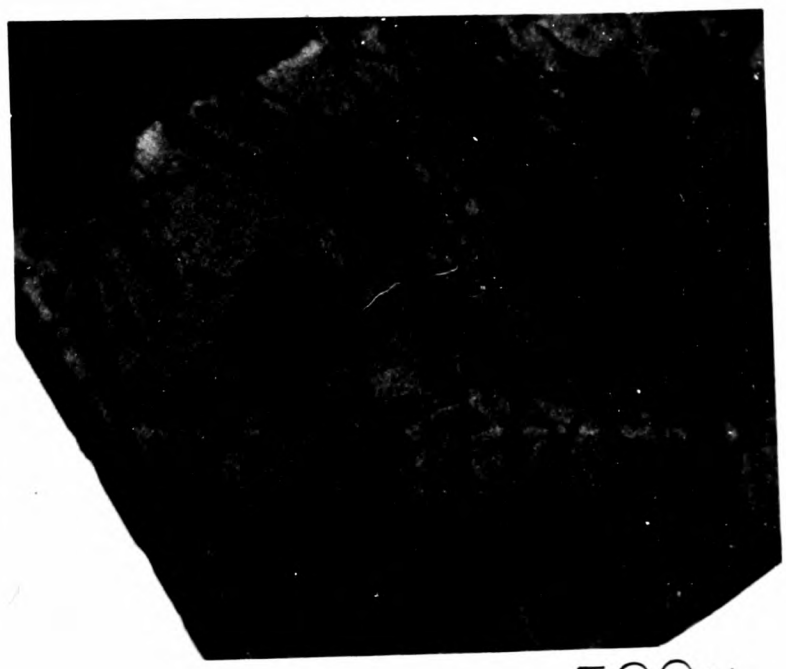


(b) 500μ

Optical



CuKα



500μ

(c)
(d)

MoKα

X ray

of the junction.

If this explanation is correct, the fingers should be visible in the voltage contrast mode in the S.E.M., (Oatley and Everhart, 1957; Joy and Titchmarsh, 1970). It is shown in Fig. 5.10 that good voltage contrast may be obtained between the fingers and substrate, indicating a definite difference in work function between the two areas. A simple explanation for the existence of these defects would be that prior to the diffussion process, the oxide mask was scratched. During the diffusion process, dopant penetrated the region of the substrate thus uncovered and on removal of the mask, no scratches visible in the optical micrograph were left. The contrast of these defects in both the S.E.M. micrographs and X-ray topographs is perfectly consistent with such oxide mask scratches.

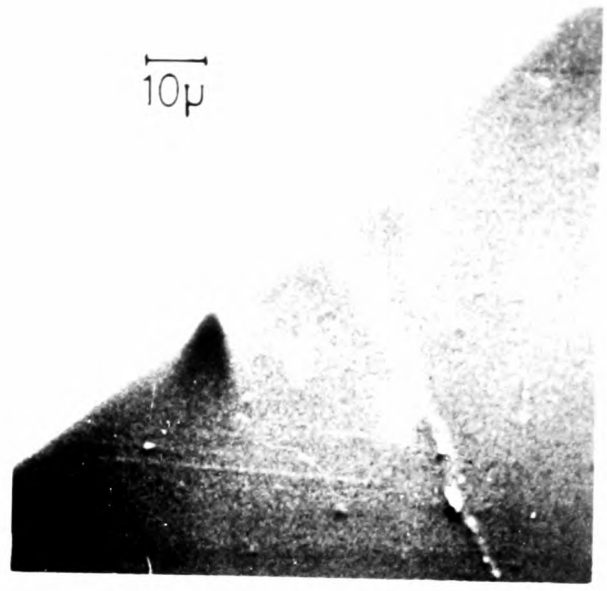
4. Contrast of Dislocations in Specimen A

(a) Slip Dislocations

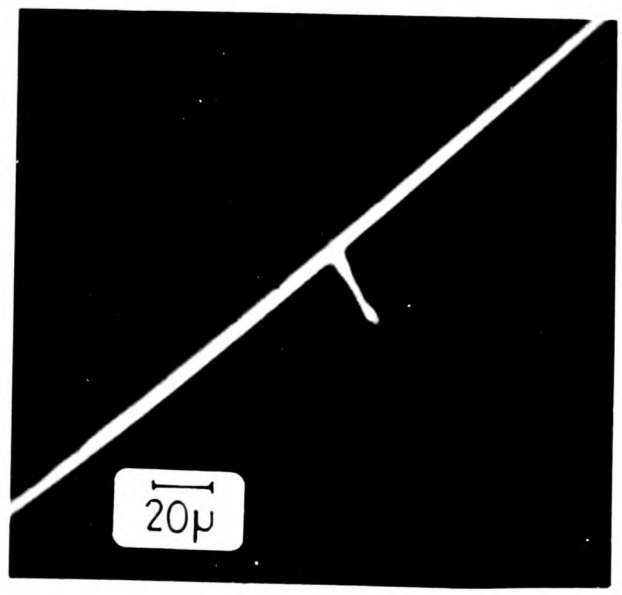
A detailed analysis of the slip dislocations in this boron diffused slice was not undertaken in view of the recent work of Miltat, (1971). However, as this specimen had a different diffusion treatment to the phosphorus diffused specimen studied by Miltat, a few general remarks supporting this authors conclusions are given here.

In specimen A, a large number of dislocation sources were observed, Fig. 5.11. The density of sources was higher near the edge of the specimen than in the centre and slip on all three systems was observed. All sources seen were

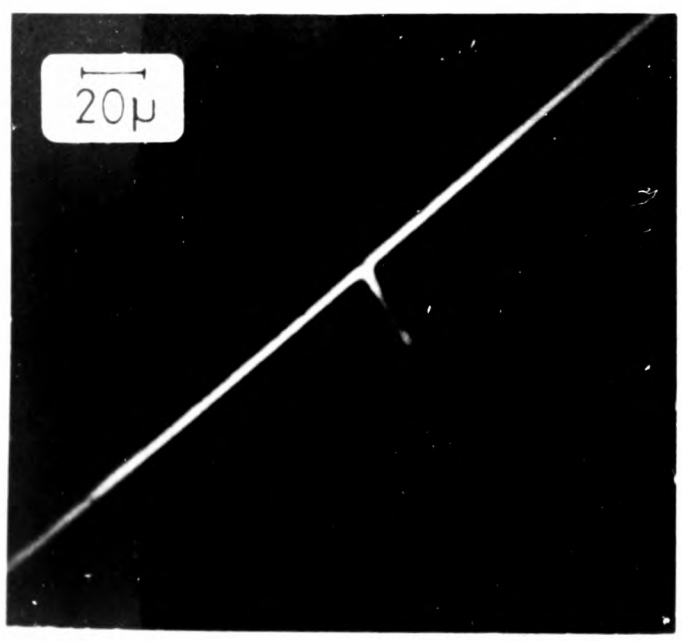
FIG 5.10



(1) Voltage Contrast

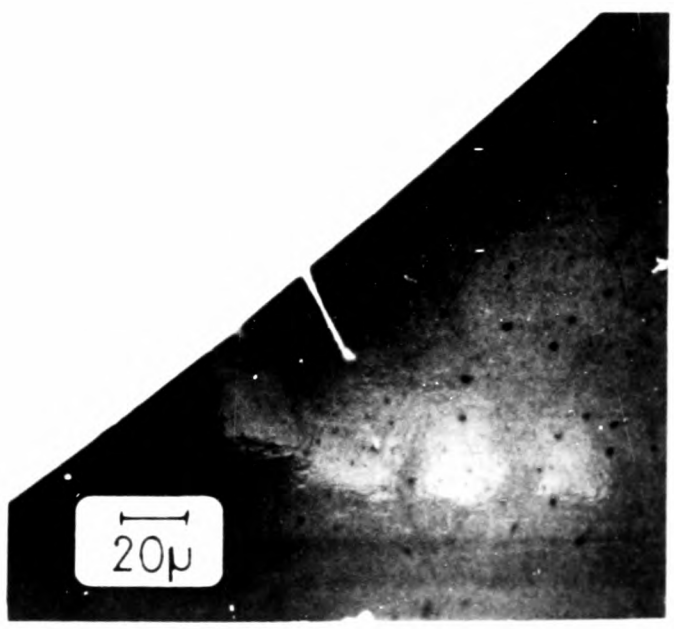


(2) Beam-induced-conductivity



(1)

Beam-induced-conductivity



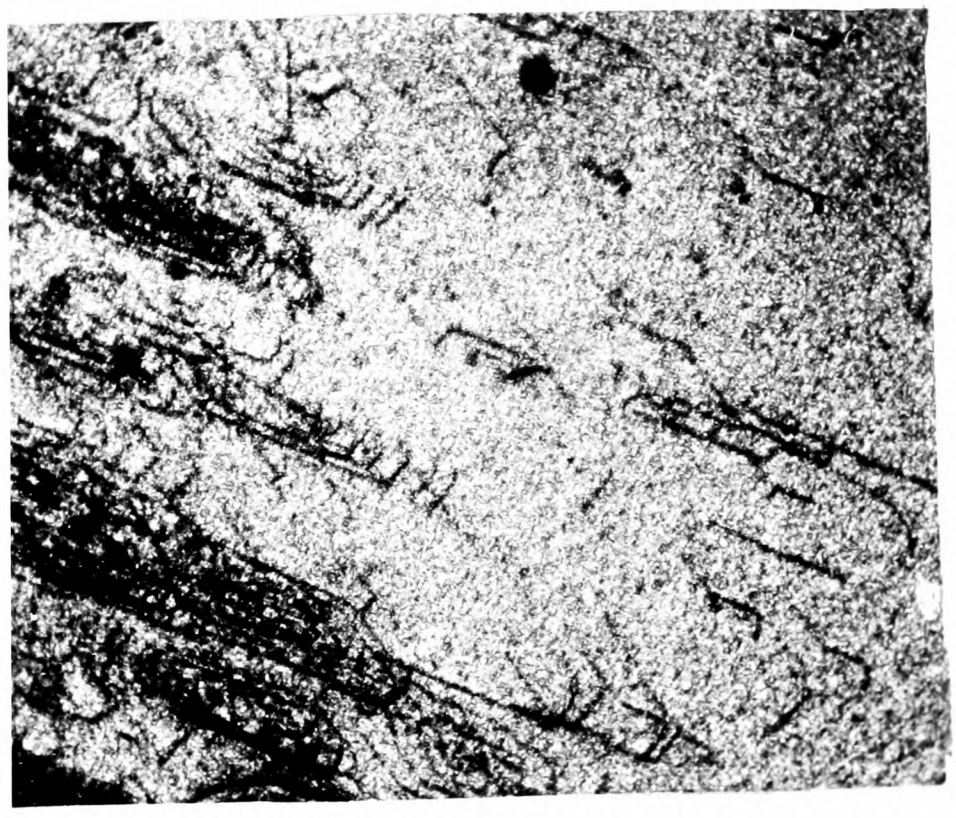
(2)

Voltage Contrast

FIG 5.11

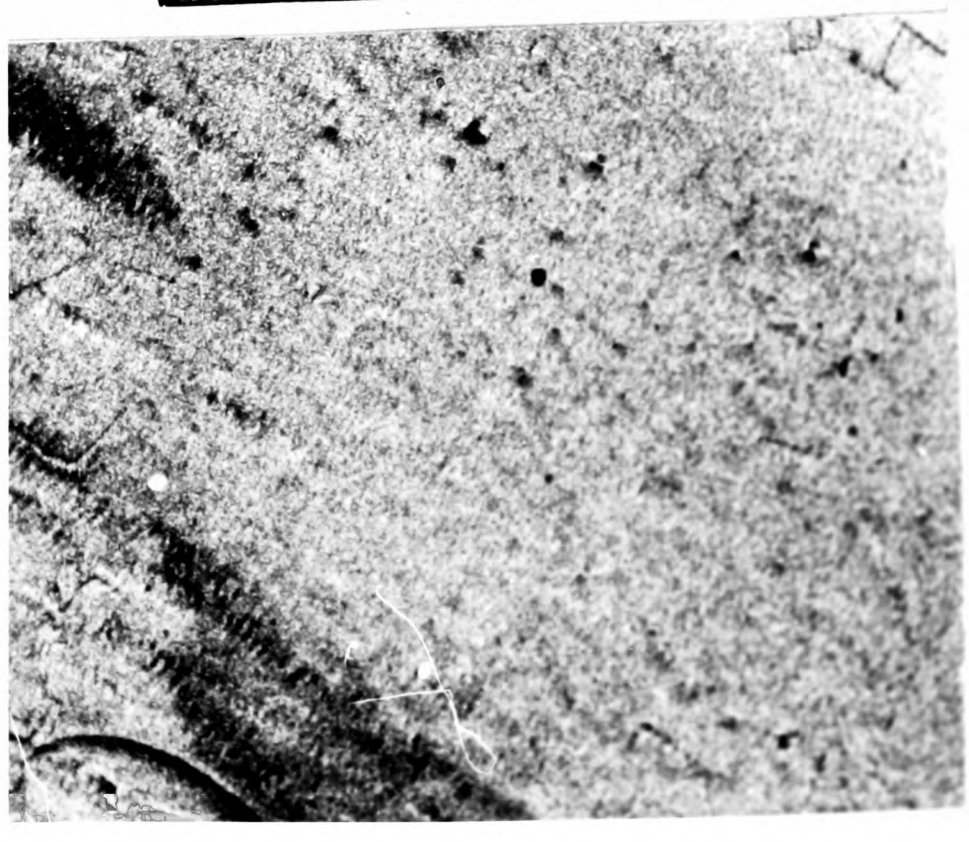


[111]



[1$\bar{1}\bar{1}$]

1 mm



[$\bar{1}$11]

of the Frank-Read type, lying on inclined {111} planes with Burgers vectors parallel to the ⟨110⟩ intersection of the planes containing the specimen and source. Each source contained two 60° segments and one or two screw segments. Interactions between sources on different slip systems were less common than in the specimen studied by Miltat, and were not investigated. While some sources were seen to be directly associated with the edge of the diffused regions, many sources acted in the bulk of the specimen from unidentifiable pinning points.

The slip behaviour in this boron doped 0.01 Ω cm n type specimen seems to be very similar to that of a phosphorus doped 1 Ω cm p type slice. The above observations lend weight to the assignment of the origin of such sources to thermal shock deformation, (Miltat and Bowen, 1970).

(b) "Emitter Edge" Dislocations

(i) Introduction

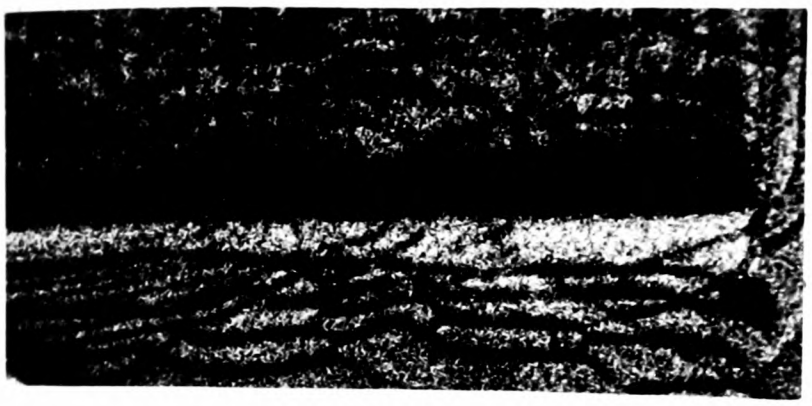
Dislocations nucleated at the junction edge and extending into the undiffused regions have been reported by several authors, (Blech, Meieran and Sello, 1965; Schwuttke and Fairfield, 1966; Lawrence, 1966; Nimura et al., 1968). In boron diffused material they are only produced in deep junctions at high dopant concentrations, and their nucleation is attributed to inhomogeneous strains at the junction interface. The presence of such "emitter edge" dislocations in shallower junctions with much lower concentrations of

phosphorus has been ascribed to the presence of an anomalous stress effect called 'stress jumping', (Fairfield and Schwuttke, 1968). However, the absence of any explanation for such an effect on the atomic scale, and several inconsistencies in the experimental evidence, (Schwuttke and Howard, 1968; Segmuller and Light, 1969), makes this phenomenon rather obscure. Further work on the occurrence of compressive strains within phosphorus diffused regions is clearly essential.

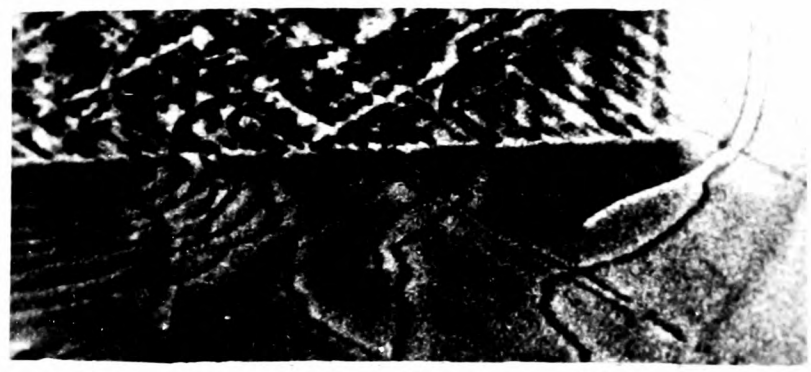
(ii) Interactions between emitter edge dislocations

Several fine examples of interactions between parallel arrays of emitter edge dislocations may be found in the literature, (Schwuttke and Howard, 1968; Nimura et al., 1968) and an analysis of these reactions was given by Sauvage and Simon, (1969). Figure 5.12 shows a set of topographs of a complex set of emitter edge dislocations. Burgers vectors along all three $\langle 110 \rangle$ directions in the foil plane are present, each family disappearing in one of the 111 reflections. At A_1 and A_2 may be seen the first stages of the interaction, at A the interaction has occurred. Dislocations of Burgers vectors $\frac{1}{2}[011]$ and $\frac{1}{2}[110]$ gliding on parallel slip planes cross. The short segments in pure screw orientation may cross slip and they interact along the line of intersection of the cross slip planes. The Burgers vector of the new dislocation is $\frac{1}{2}[10\bar{1}]$ and is pure edge in character. It is sessile and cannot easily glide. Similar interactions may be seen at B and C, in each case the short segment lies

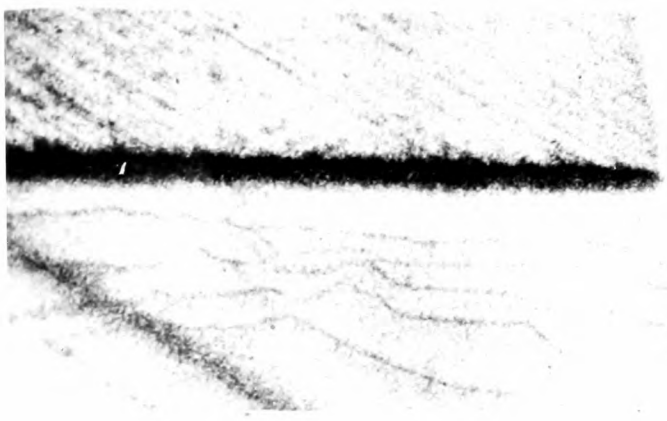
FIG 5.12



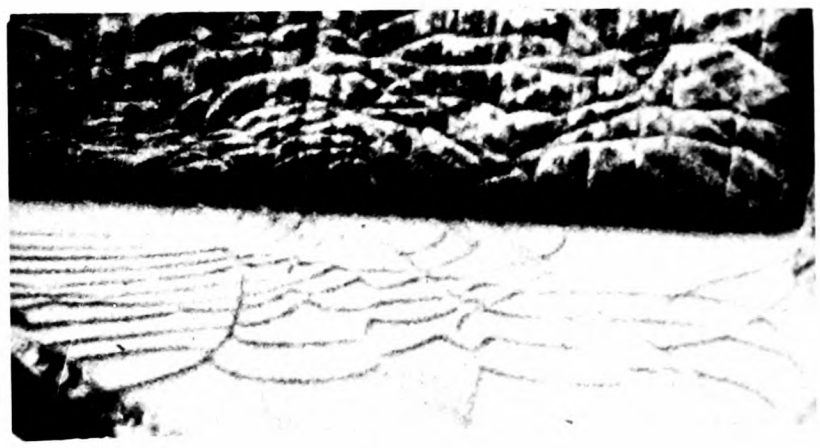
022



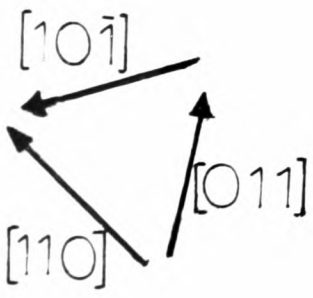
$\bar{1}\bar{1}1$

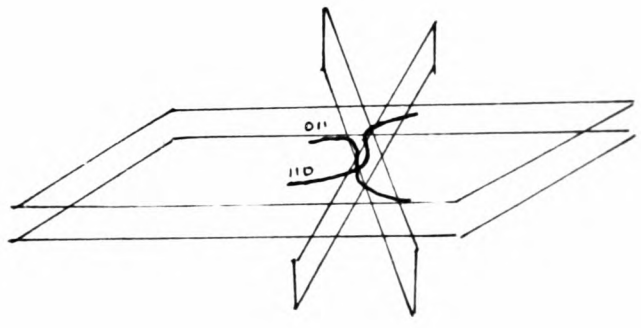


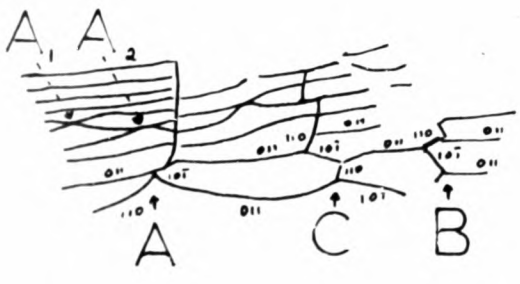
$1\bar{1}\bar{1}$

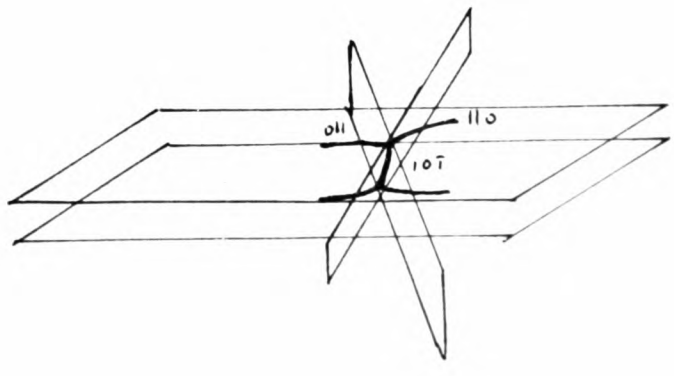


111









normal to the $\langle 110 \rangle$ direction which is parallel to its Burgers vector.

(iii) Image Contrast from Emitter Edge Dislocations

In the array previously shown in Fig. 5.5, all dislocations have a Burgers vector $\frac{1}{2}[10\bar{1}]$ and are invisible in the 111 and $\bar{1}1\bar{1}$ reflections. As may be seen in Fig. 5.13, the widths of the dislocation images are extremely narrow, up to a quarter that predicted by the simple tilt criterion, (Lang and Polcarova, 1965). This may be explained by including the misorientation produced by neighbouring dislocations.

The effective misorientation around a dislocation is given by, (Authier, 1966):

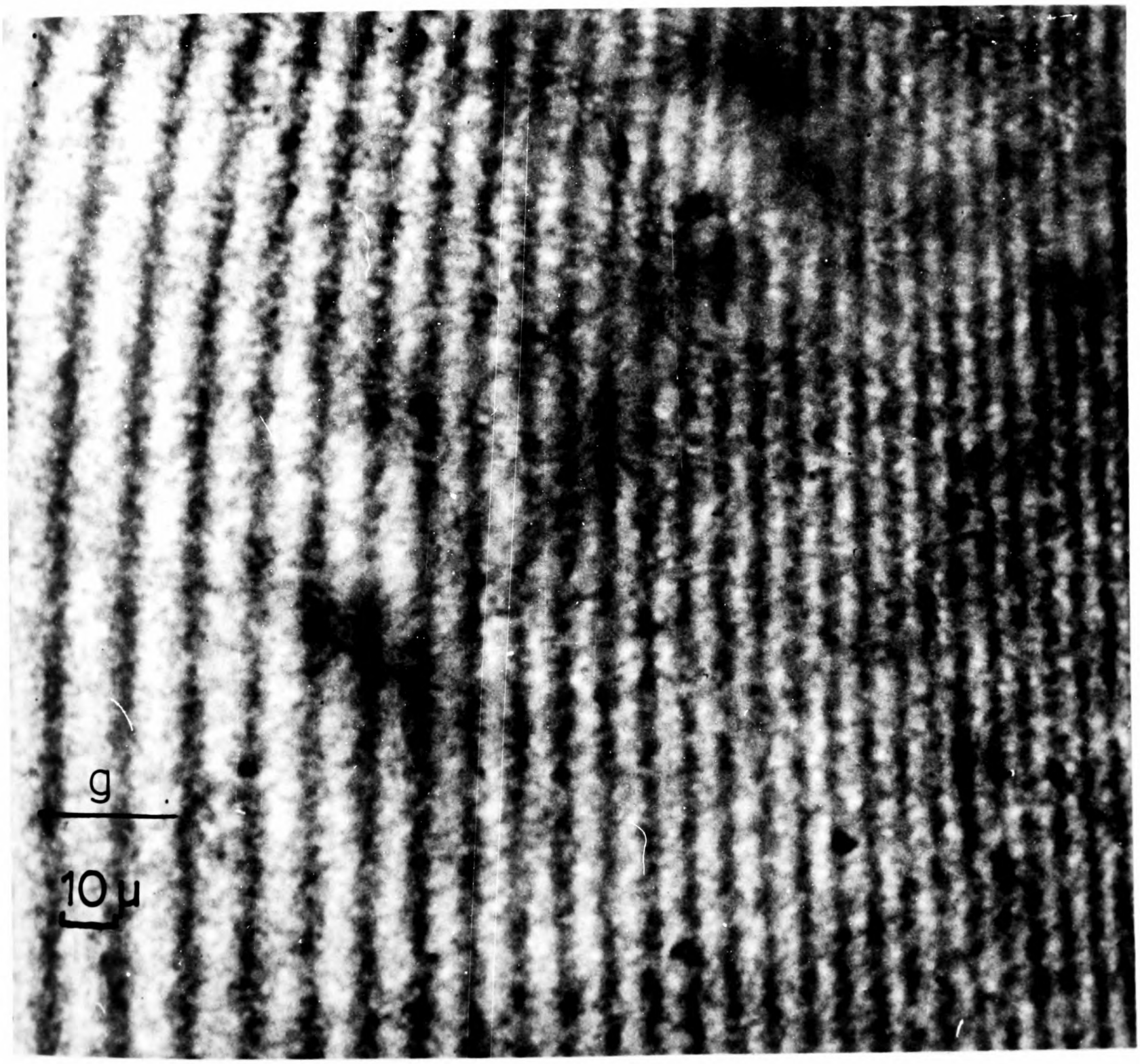
$$\delta(\theta) = \frac{-1}{K \sin 2\theta} \frac{\partial}{\partial s_g} (\underline{g} \cdot \underline{u}) \qquad (5.3)$$

where $\underline{u}$ is the atomic displacement and $\frac{\partial}{\partial s_g}$ represents the partial derivative in the diffracted beam direction, and θ is the Bragg angle. Coordinates are taken as x_1 parallel to the edge component of Burgers vector, x_3 parallel to the dislocation line and $\underline{x}_2 = \underline{x}_1 \wedge \underline{x}_3$. The $\bar{1}1\bar{1}$ reflection is treated only, as here the g vector is perpendicular to [011], the direction of the dislocation line. Then,

$$\frac{\partial}{\partial s_g} = \cos\theta \frac{\partial}{dx_2} + \sin\theta \frac{\partial}{dx_1} \qquad (5.4)$$

For a general dislocation,

FIG 5.13



$$u_1 = \frac{b_e}{2\pi}\left[\tan^{-1}\frac{x_2}{x_1} + \frac{x_1 x_2}{2(1-\nu)(x_1^2+x_2^2)}\right]$$

$$u_2 = -\frac{b_e}{8\pi(1-\nu)}\left[2(1-2\nu)\log_e\frac{\sqrt{x_1^2+x_2^2}}{r_o} + \frac{x_1^2-x_2^2}{x_1^2+x_2^2}\right] \qquad (5.5)$$

In the case considered here $g_3 = 0$ and the maximum misorientation occurs at $x_2 = 0$ so the expression reduces to:

$$\delta(\Delta\theta)_{max.} = -\frac{1}{K\sin 2\theta}\left[\frac{\cos\theta\, g_1 |b_e|}{2\pi}\left\{1 + \frac{1}{2(1-\nu)}\right\} - \frac{g_2 |b_e| \sin\theta}{8\pi(1-\nu)}\left\{2(1-2\nu) - 4\right\}\right]\frac{1}{x_1} \qquad (5.6)$$

If the width of an isolated dislocation is 2a, then the effective misorientation at which the image is formed is given by:

$$\delta(\Delta\theta_I) = \frac{A}{a} \qquad (5.7)$$

where A is the constant defined above.

Considering the strain field due to the nearest neighbour in the parallel array, at a distance r from the dislocation, gives for the total misorientation

$$\delta(\Delta\theta_T) = A\left(\frac{1}{x} - \frac{1}{r-x}\right) \qquad (5.8)$$

Thus the image half width, x, is related to the half width of an isolated dislocation by :

$$\frac{1}{a} = \frac{1}{x} - \frac{1}{r-x} \quad . \tag{5.9}$$

This relation between image width, 2x, and separation of dislocations, r, is plotted in Fig. 5.14 for 2a = 7.5 μm, together with the experimental values from the CuKα topograph. Theory and experiment lie within the error bars imposed by the variation of image width observed on the topograph, but it appears that the predicted widths are rather larger than those observed for small separations.

The relation between x and r including second nearest neighbour effects is:

$$\frac{1}{r} - \frac{1}{r-x} + \frac{1}{r+x} - \frac{1}{2r-x} = \frac{1}{a} \tag{5.10}$$

Figure 5.15 shows the predicted curves for MoKα radiation for first and second nearest neighbour interactions, together with the experimental results. It is clear that, compared with the experimental error, the correction is insignificant. However, within the error imposed, this approach does account for the narrowing of the emitter edge dislocation images.

(c) Diffusion Induced Dislocations Inside Diffused Regions

(1) Introduction

It was shown by Prussin, (1961) and Queisser,(1964),

FIG 5.14

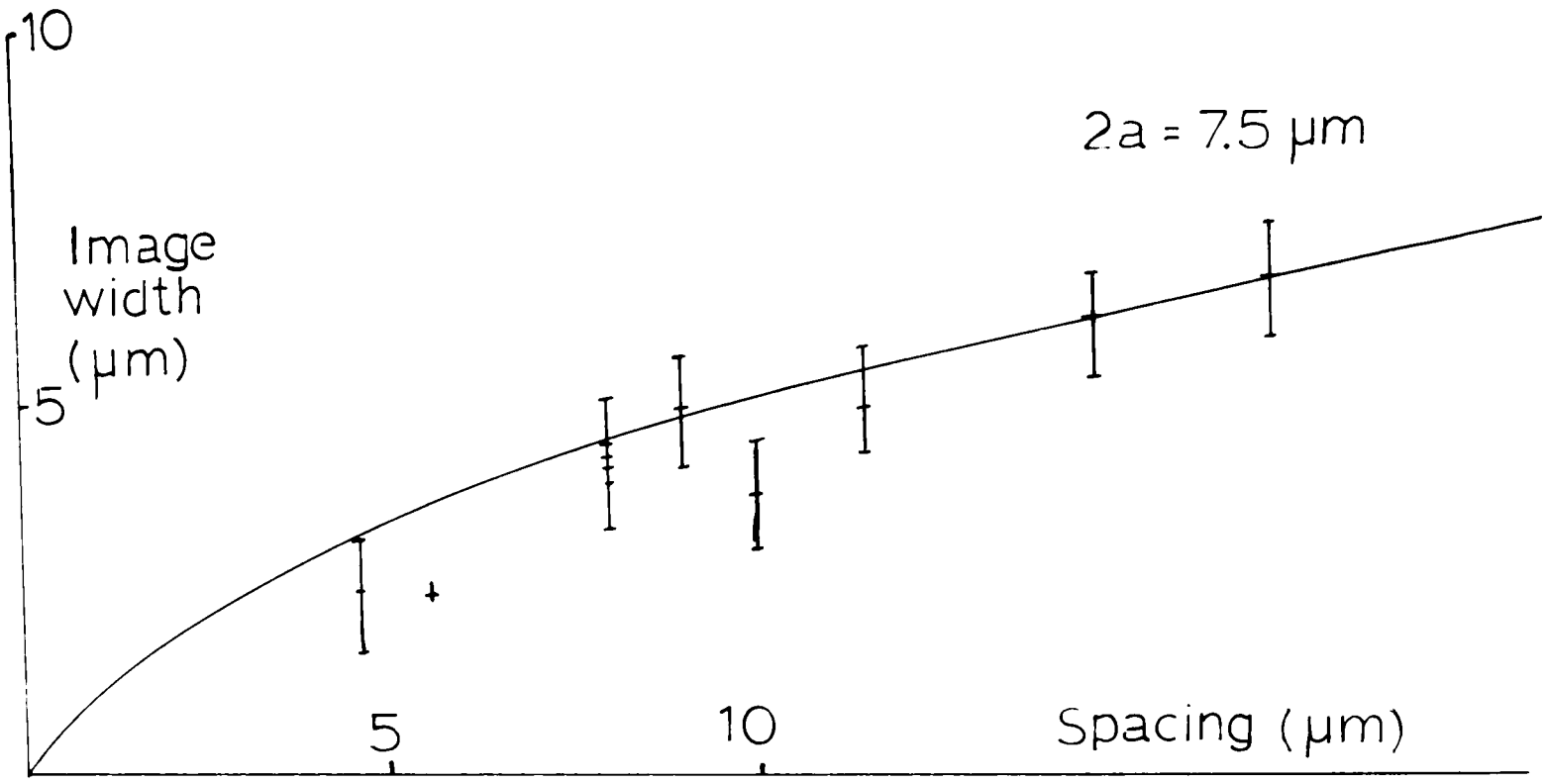
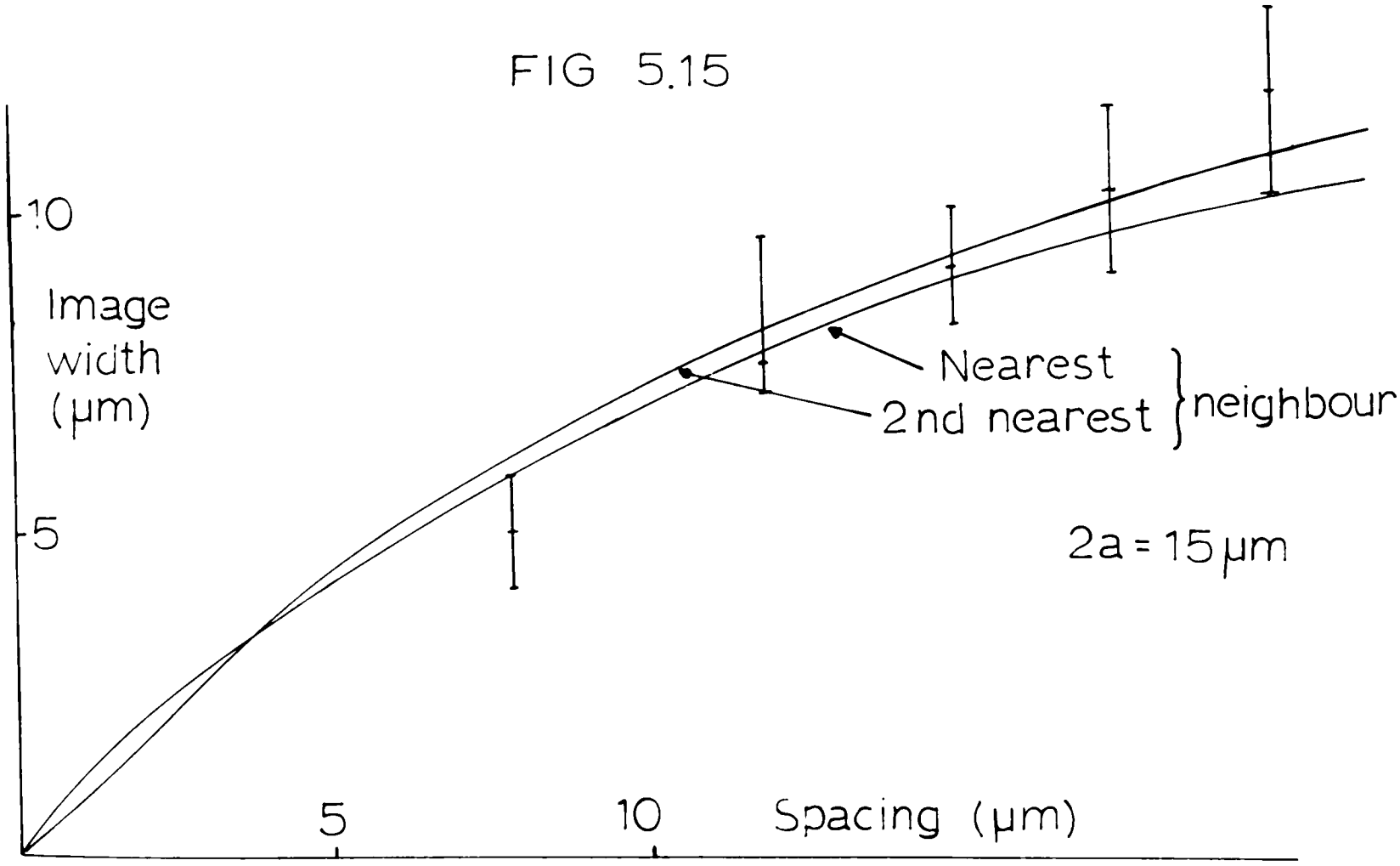


FIG 5.15

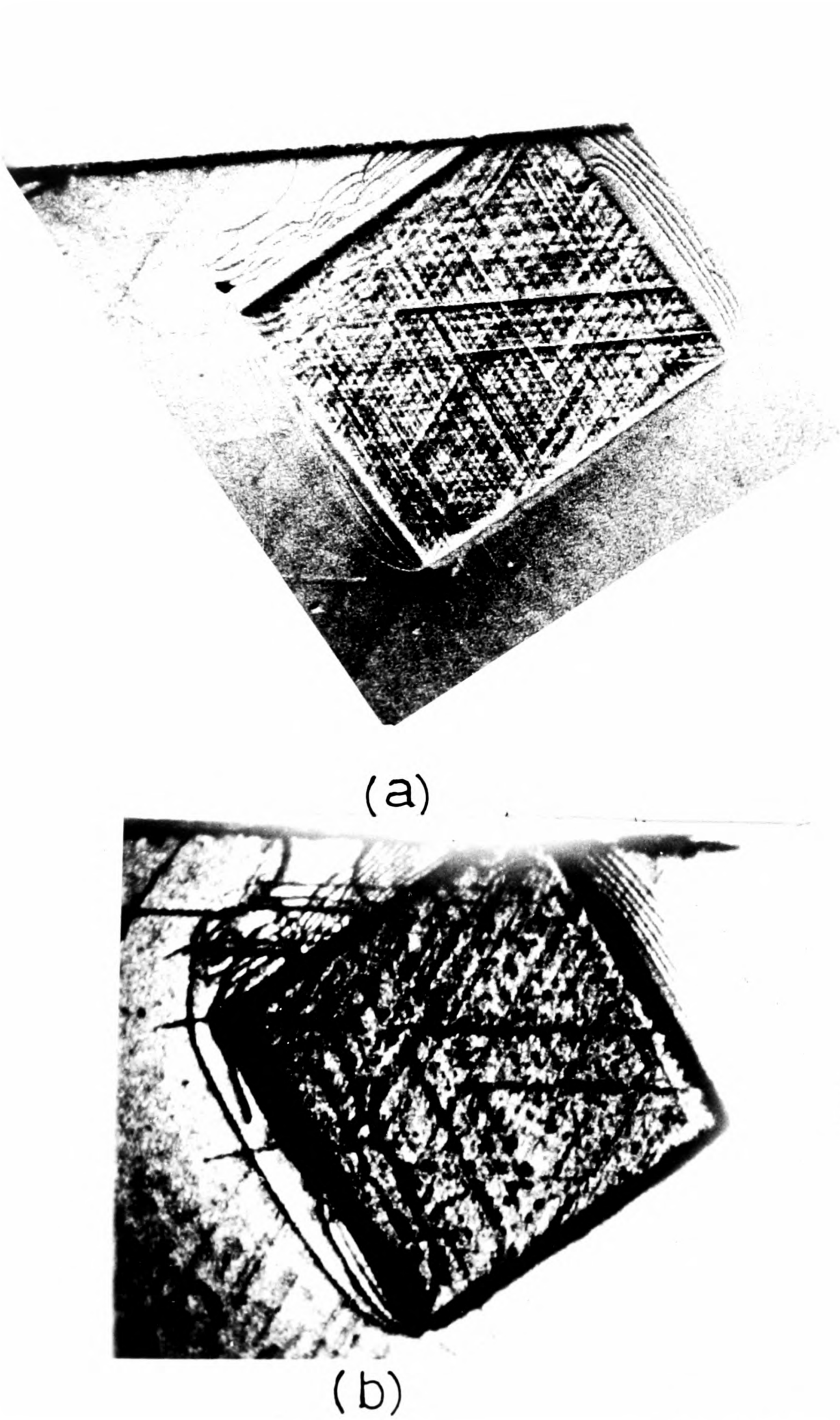


that in the diffused region, enough stress may exist from the mismatch of ionic radii to nucleate dislocations. Since then, diffusion induced dislocations have been studied by many authors using a variety of techniques, (Schwuttke and Quiesser, 1962; Rupprecht and Schwuttke, 1966; Sato and Arata, 1964; Washburn et al., 1964; Levine et al., 1967). The analysis of diffusion induced dislocations in boron doped silicon, described below is complementary to the X-ray work of Yoshida et al., (1968), on phosphorus doped silicon. It will be shown that in the high dislocation density regions, the results are very similar.

(ii) High Defect Density

Defects were observed inside all the diffused windows of Specimen A. In most windows, the contrast was mottled when using CuKα radiation, Fig. 5.16(a), there being diffuse lines running in the $\langle 110 \rangle$ directions. With MoKα, Fig. 5.16(b), no lines were visible though the net contrast was enhanced, and what appeared to be precipitates were observed. There can be little doubt that the contrast is due to dislocations. This mottled contrast has been found in specimens used by Titchmarsh, (1971) and Shaw, (1969) for T.E.M. and S.E.M. studies. Titchmarsh observed long straight dislocations lying along $\langle 110 \rangle$, frequently interrupted by by aggregates of precipitate. Shaw observed lines, spaced about 20 μm apart, lying along $\langle 110 \rangle$ in the E.I.C. mode of the S.E.M.. Dislocations previously observed in this mode showed uniform contrast, (Czaja and Wheatley, 1964;

FIG 5.16



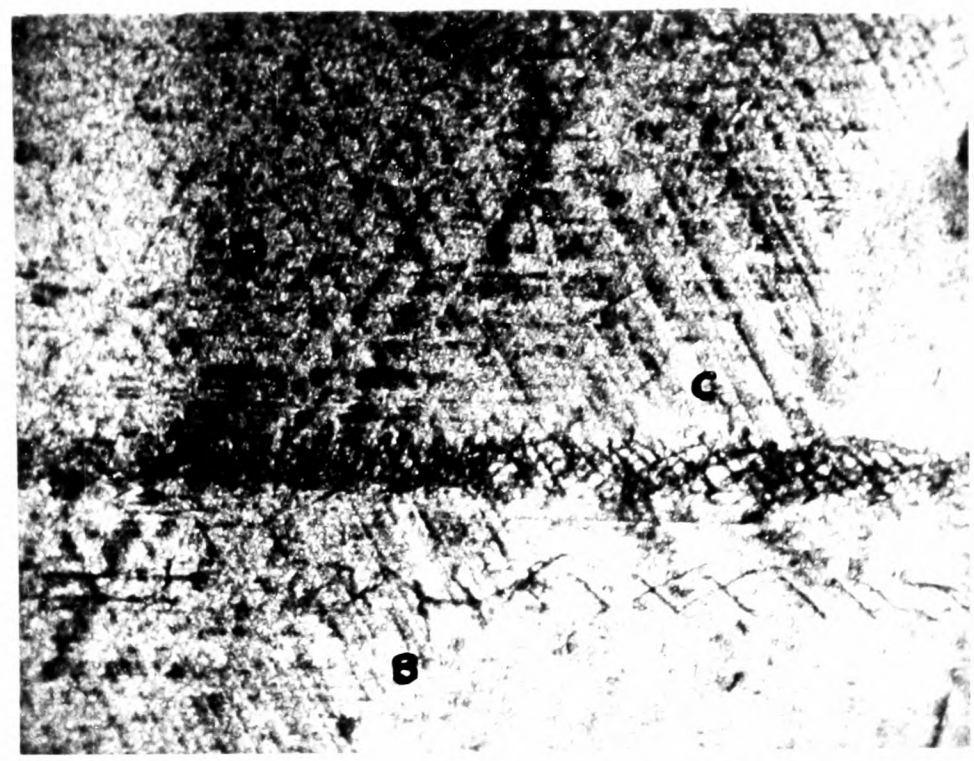
Lander et al., 1963), and to account for the discontinuous, mottled nature of the contrast, it was suggested that the dislocations might be decorated with impurity.

The loss of contrast in the MoKα topographs may be explained in terms of overlapping of dislocation images. In region B, of Fig. 5.17(a), where dislocations in one direction only are present, individual dislocation lines, about 9 μm apart are clearly discernable. In region D, where dislocations in all three $\langle 110 \rangle$ directions are present, the contrast becomes that described in Fig. 5.16(b). Reference to Figs. 5.14 and 5.15 shows that image widths of an array 9 μm apart will be 6 μm using MoKα radiation, and 4 μm with CuKα radiation. As seen from the construction of Fig. 5.17(b), in the former case the contrast is nearly uniform for such an array, while in the latter case, Fig. 5.17(c), lines in the three $\langle 110 \rangle$ directions may just be distinguished. This construction is rather crude, in that it assumes equispaced dislocations but it does indicate that at about this separation, the images become confused.

Titchmarsh, (1971), reported that some of the dislocations lying along $\langle 110 \rangle$, crossed the junction, and in his specimens, "inside" dislocations were observed to do so when examined by X-ray topography, Fig. 5.18. In the bulk specimen A, only near the edge of the specimen were appreciable numbers of dislocations found to cross the junction. In the central region, no 'inside' diffusion induced dislocations crossed the window edges into the undiffused region.

One window in this specimen contained a large number

FIG. 5.17



500 μ

(a)



MoKa

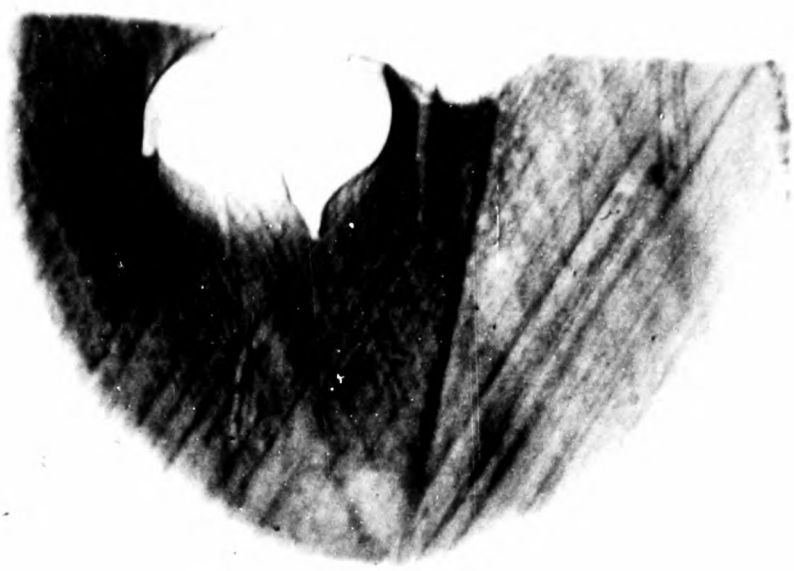
(b)



CuKa

(c)

FIG 5.18



500 μ



200μ

g

CuKβ

of dislocations, but yet of just low enough density to resolve individual dislocations. The 220 reflections of this window are shown in Fig. 5.19 and the corresponding 111 reflections in Fig. 5.20. Burgers vector determinations were made for the dislocations marked A to L in the schematic diagram in Fig. 5.21(a), and the visibility of these dislocations in all six topographs is tabulated in Table 5.3. The Burgers vectors assigned for the visibility criterion $\underline{g} \cdot \underline{b} = 0$ are also listed. All Burgers vectors identified were parallel to $\langle 110 \rangle$ and Burgers vectors both in the plane of the foil and inclined to it were found. The results are shown in Fig. 5.21(b), and one finds that both inclined and non-inclined Burgers vectors have been found for all three $\langle 110 \rangle$ directions of the dislocation lines. For the dislocation lying along [110], all 60° type Burgers vectors were observed. It is reasonable to assume that in the other directions also, all 60° type vectors could be found if enough dislocations were examined.

The results obtained, thus complement the work of Yoshida *et al.* on phosphorus diffused silicon. In both studies dislocations with inclined and planar Burgers vectors were observed and all dislocations lay along $\langle 110 \rangle$ directions. Such dislocations appear to be different from the network dislocations observed by Levine *et al.* and would seem to be similar to the crystallographic dislocations seen by Titchmarsh. No satisfactory explanation of their nucleation has been found. Suffice to say that they are formed to relax the stress caused by the diffusion.

FIG 5.19

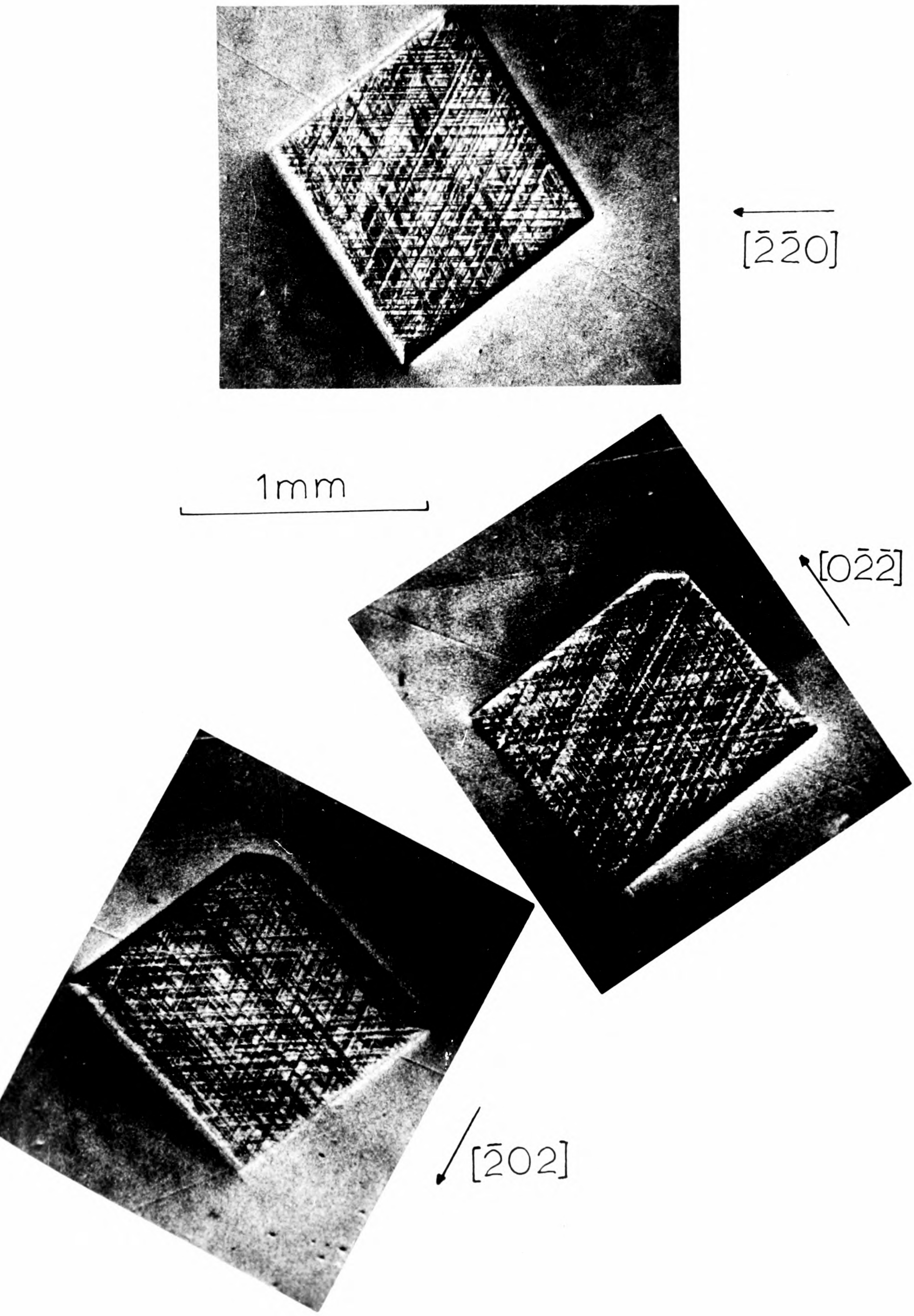


FIG 5.20

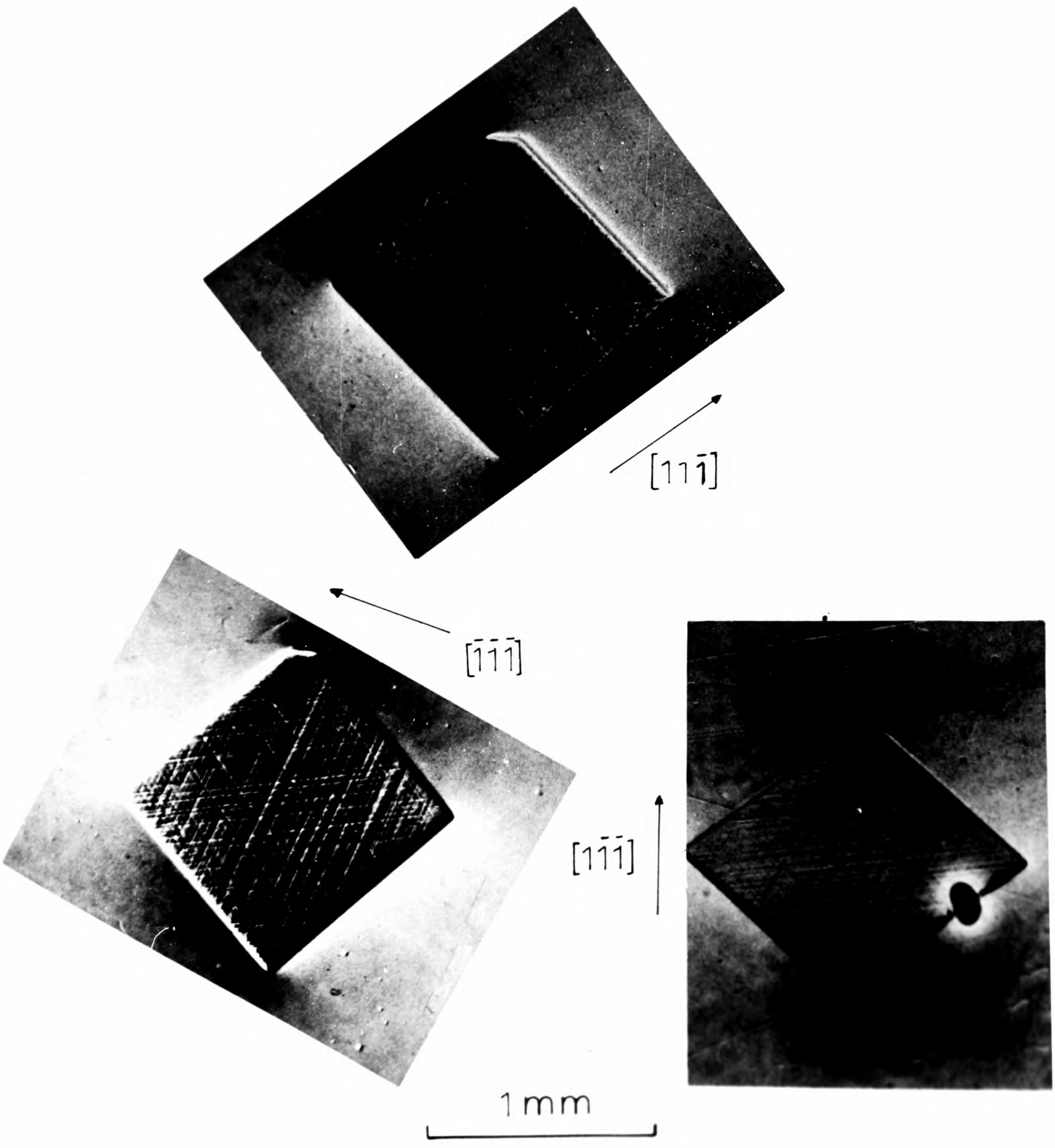
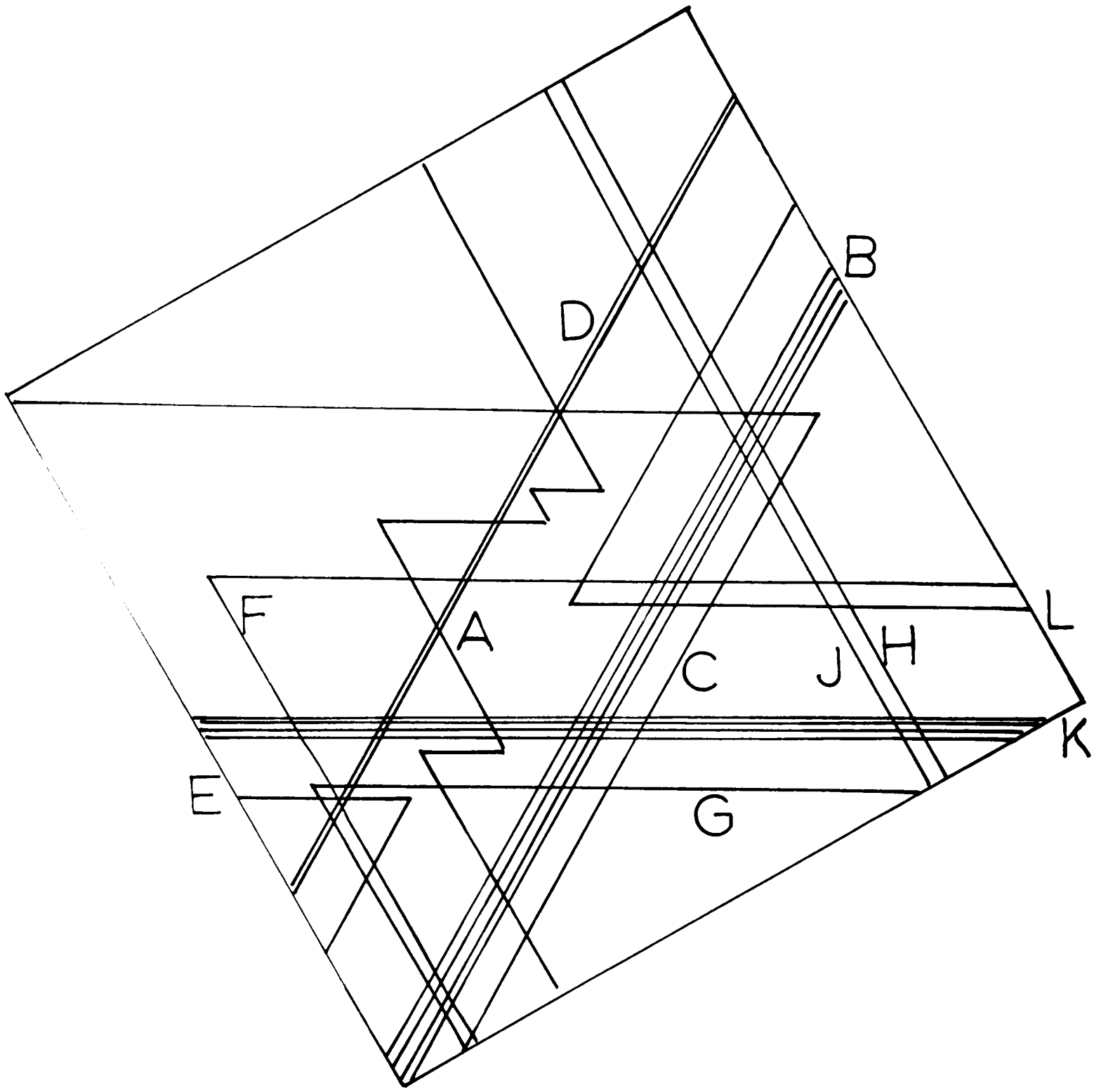
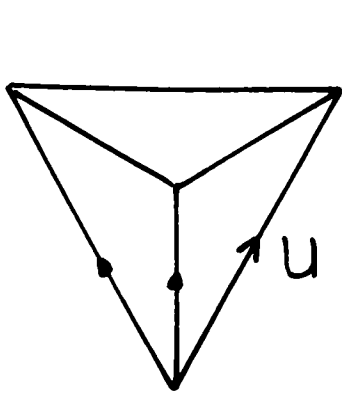
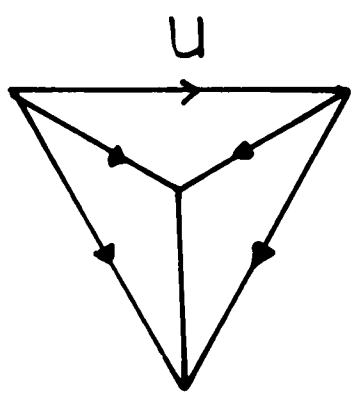


FIG 5.21







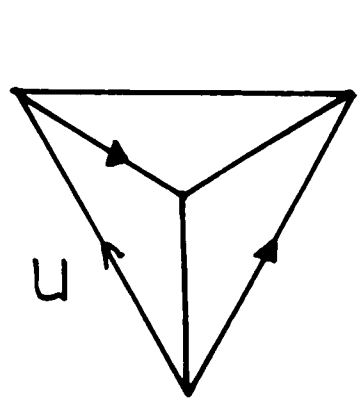


Table 5.3

Analysis of Diffused-in Dislocations

Dislocation	111	$\bar{1}\bar{1}\bar{1}$	111	220	$20\bar{2}$	022	u	b	Type
A	✓	x	x	✓	x	?	[011]	$\frac{1}{2}$[101]	60° inclined
A	✓	x	x	✓	x	?	[110]	$\frac{1}{2}$[101]	60° inclined
B	✓	x	✓	✓	✓	✓	[10$\bar{1}$]	$\frac{1}{2}$[011]	60° foil
C	x	✓	x	✓	?	?	[110]	$\frac{1}{2}$[0$\bar{1}$1]	60° inclined
C	x	✓	x	✓	?	?	[10$\bar{1}$]	$\frac{1}{2}$[0$\bar{1}$1]	60° inclined
D	✓	x	✓	✓	✓	✓	[10$\bar{1}$]	$\frac{1}{2}$[011]	60° foil
E	x	✓	x	✓	✓	?	[10$\bar{1}$]	$\frac{1}{2}$[0$\bar{1}$1]	60° inclined
E	x	✓	✓	✓	✓	?	[110]	$\frac{1}{2}$[10$\bar{1}$]	60° foil
F	✓	x	x	✓	x	✓	[011]	$\frac{1}{2}$[101]	60° inclined
F	✓	x	x	✓	x	✓	[110]	$\frac{1}{2}$[101]	60° inclined
G	✓	x	x	✓	x	?	[110]	$\frac{1}{2}$[101]	60° inclined
G	✓	x	x	✓	x	?	[011]	$\frac{1}{2}$[101]	60° inclined
H	x	✓	✓	✓	✓	✓	[011]	$\frac{1}{2}$[10$\bar{1}$]	60° foil
J	✓	x	x	✓	x	✓	[011]	$\frac{1}{2}$[101]	60° inclined
K	✓	x	✓	✓	✓	✓	[110]	$\frac{1}{2}$[011]	60° foil
L	?	✓	x	?	✓	?	[110]	$\frac{1}{2}$[0$\bar{1}$1]?	60° inclined?
L	?	✓	x	?	✓	?	[10$\bar{1}$]	$\frac{1}{2}$[0$\bar{1}$1]?	60° inclined?

(iii) Low Defect Density

(a) Dislocation interactions

Figure 5.22 shows the CuKα 111 reflections from a window containing few dislocations. Figure 5.23 shows the similar reflections using MoKα radiation. The emitter edge dislocations are invisible in 111 and have Burgers vector $\frac{1}{2}[10\bar{1}]$. The contrast from the dislocations inside the diffused region is poor, but it is clear that each set of dislocations is invisible in one reflection. The visibility is tabulated in Table 5.4.

Table 5.4

$\underline{u}$	111	$\bar{1}\bar{1}\bar{1}$	$\bar{1}11$	$\underline{b}$
[011]	x	✓	✓	$\frac{1}{2}[10\bar{1}]$
(110)	x	✓	✓	$\frac{1}{2}[10\bar{1}]$
$(10\bar{1})$	✓	x	x	$\frac{1}{2}[011]$

All appear to be 60° type dislocations with Burgers vectors in the plane of the foil. What is surprising is that what appears to be a continuous dislocation should change its Burgers vector when it changes direction. In no case does any dislocation vanish completely with CuKα radiation. Table 5.5 shows that the $\underline{g} \cdot \underline{b} \wedge \underline{u}$ contrast is strong. Similar examples of dislocations changing both direction and Burgers vector have been seen previously, (Yoshida et al., 1968), though no remark has been made about them.

FIG 5.22

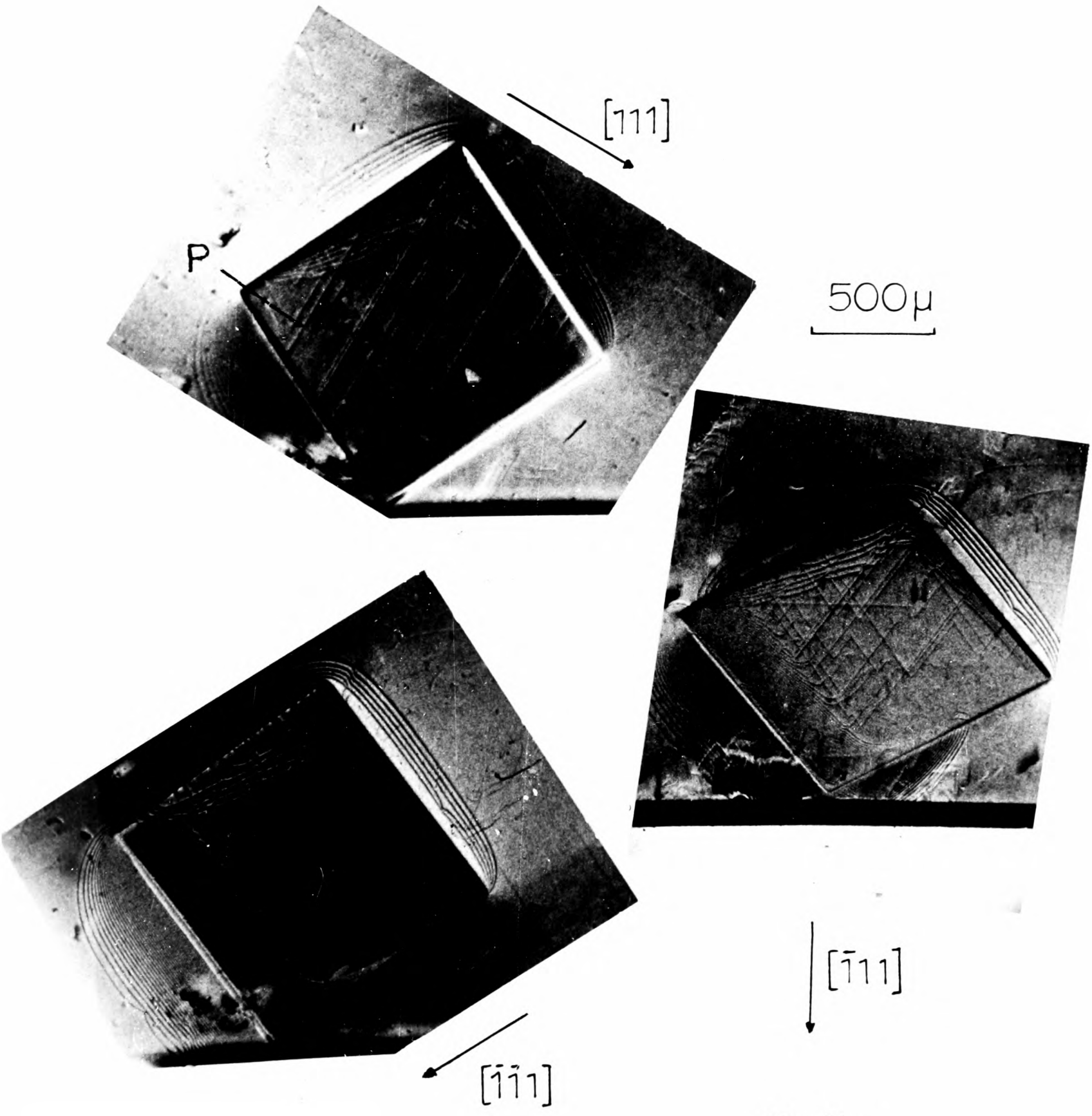


FIG 5.23

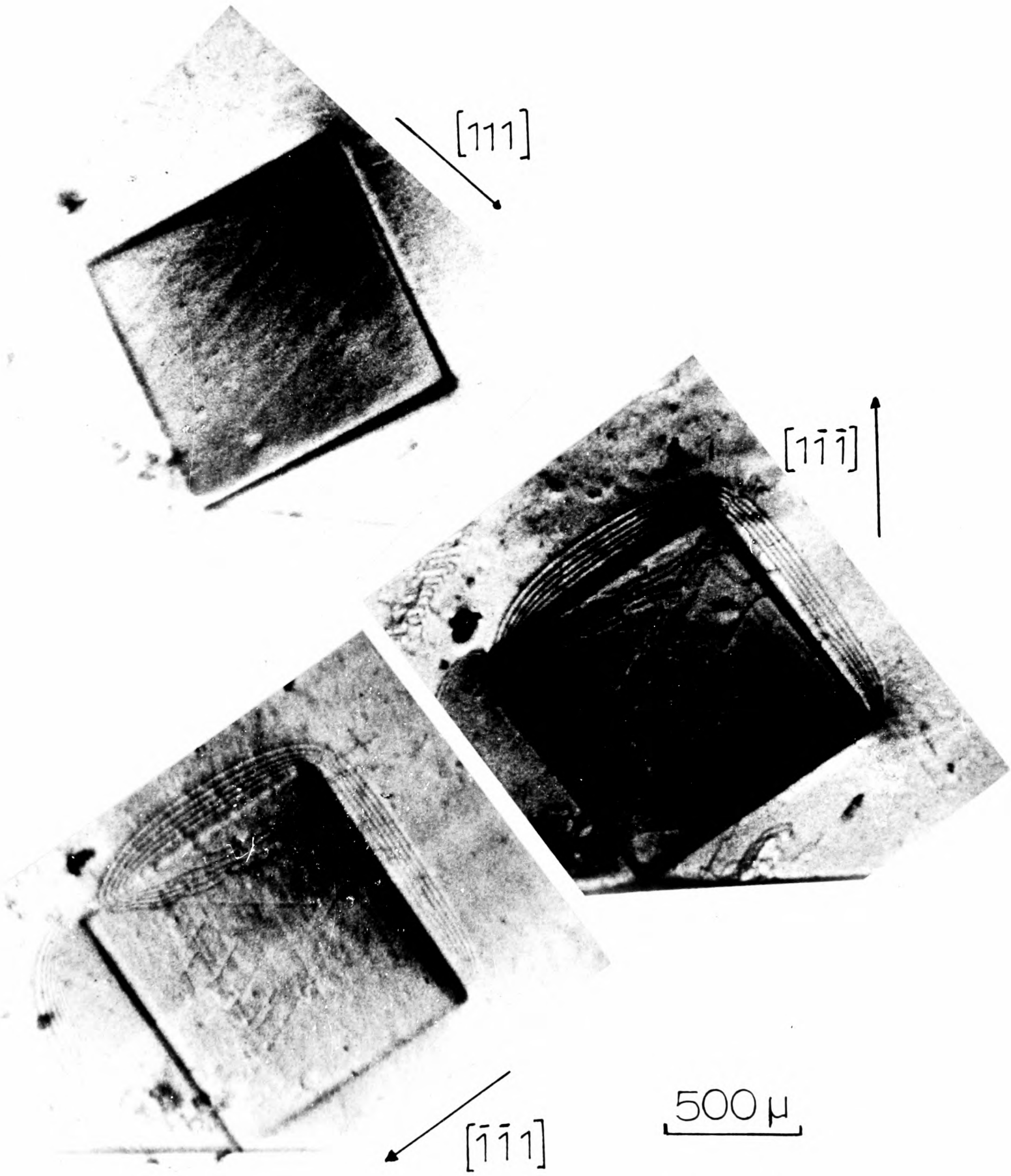


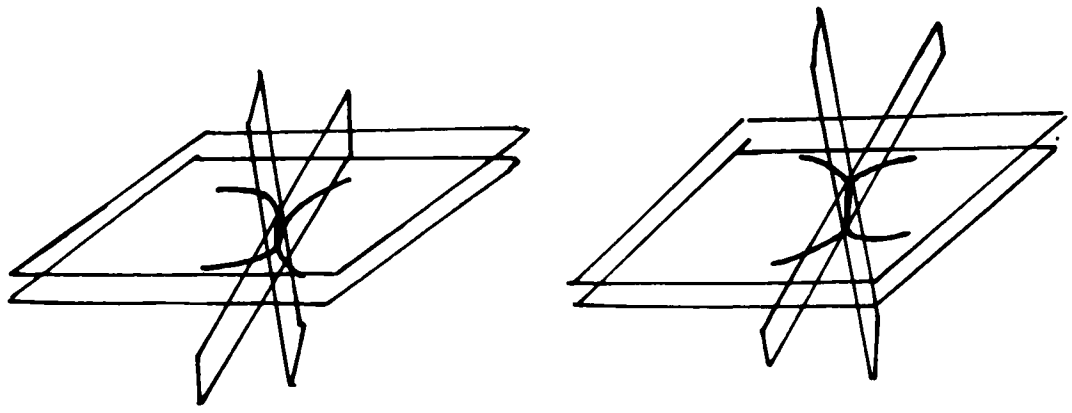
Table 5.5

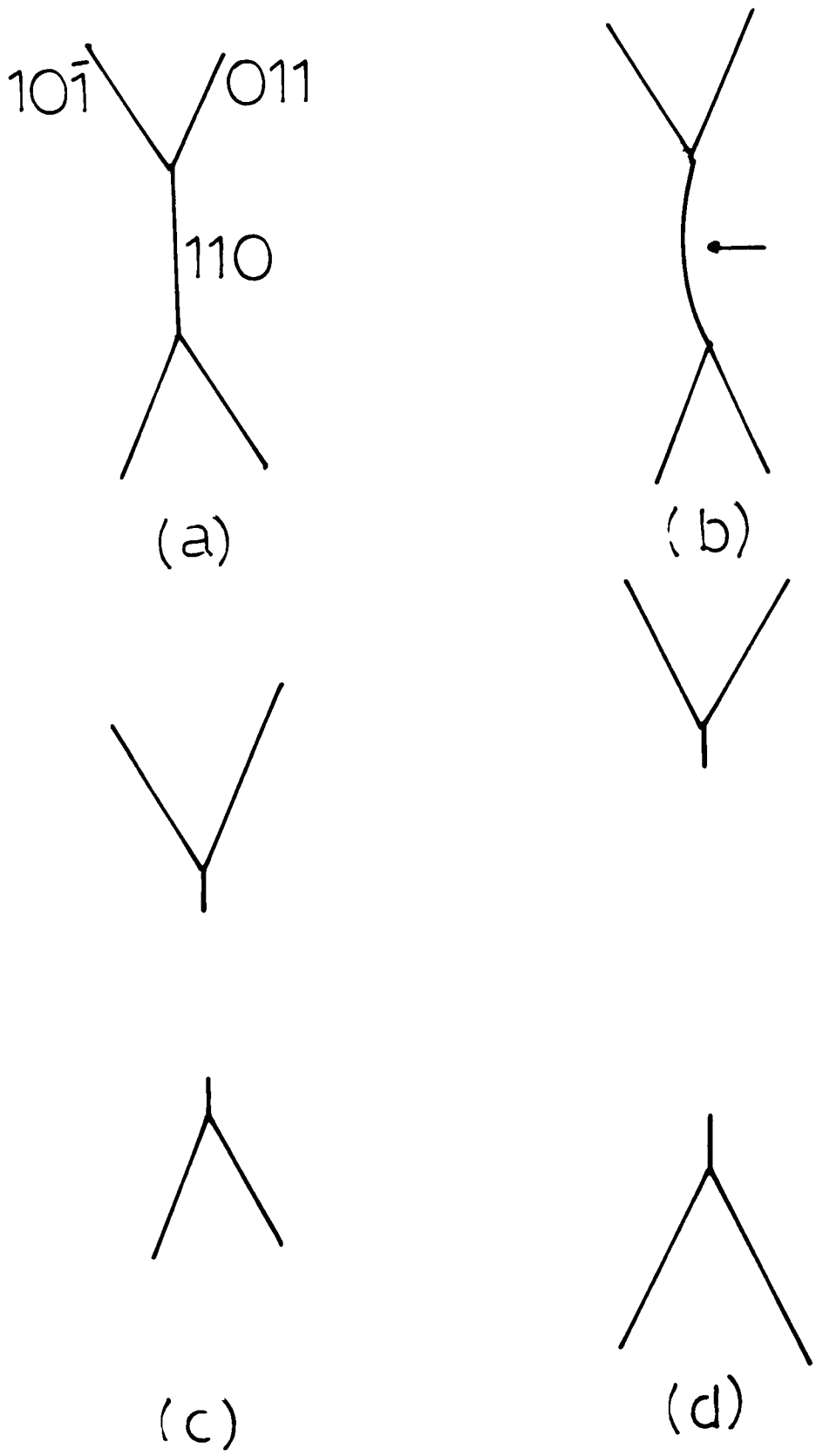
u	b	b∧u	111 g.b	111 g.b∧u	1$\bar{1}\bar{1}$ g.b	1$\bar{1}\bar{1}$ g.b∧u	$\bar{1}\bar{1}$1 g.b	$\bar{1}\bar{1}$1 g.b∧u
10$\bar{1}$	$\frac{1}{2}$[011]	$\frac{1}{2}$[1$\bar{1}$1]	1	$\frac{1}{2}$	-1	$\frac{1}{2}$	0	$\frac{1}{2}$
110	$\frac{1}{2}$[101]	$\frac{1}{2}$[$\bar{1}$1$\bar{1}$]	0	$-\frac{1}{2}$	-1	$-\frac{1}{2}$	-1	$-\frac{1}{2}$
011	$\frac{1}{2}$[$\bar{1}$0$\bar{1}$]	[$\bar{1}$1$\bar{1}$]	0	$-\frac{1}{2}$	-1	$-\frac{1}{2}$	-1	$-\frac{1}{2}$

To account for this phenomenon, a small segment of dislocation must be assumed, connecting the observed dislocations with the surface. A reasonable mechanism of formation of such 60° joints may be postulated following section 4.b.ii. Consider, as in Fig. 5.24, two 60° dislocations with Burgers vectors in the plane of the foil to be gliding on parallel slip planes. On crossing, they interact, forming a short segment, of pure edge character. This segment may glide only in the (100) plane. If a stress is applied, by thermal shock for example, it is possible for this edge segment to bow out and glide out of the surface. This leaves two short segments connecting with the surface. The two sections may now glide apart dragging the segment along the [$\bar{1}$12] direction, leaving what appears to be a zig-zag dislocation changing its Burgers vector.

These long straight dislocations are seen to interact with the emitter edge dislocations. Consider the dislocation, P, lying along [10$\bar{1}$] with Burgers vector $\frac{1}{2}$[011], Fig. 5.22. In the 111 reflection, this appears to extend right to the

FIG 5.24





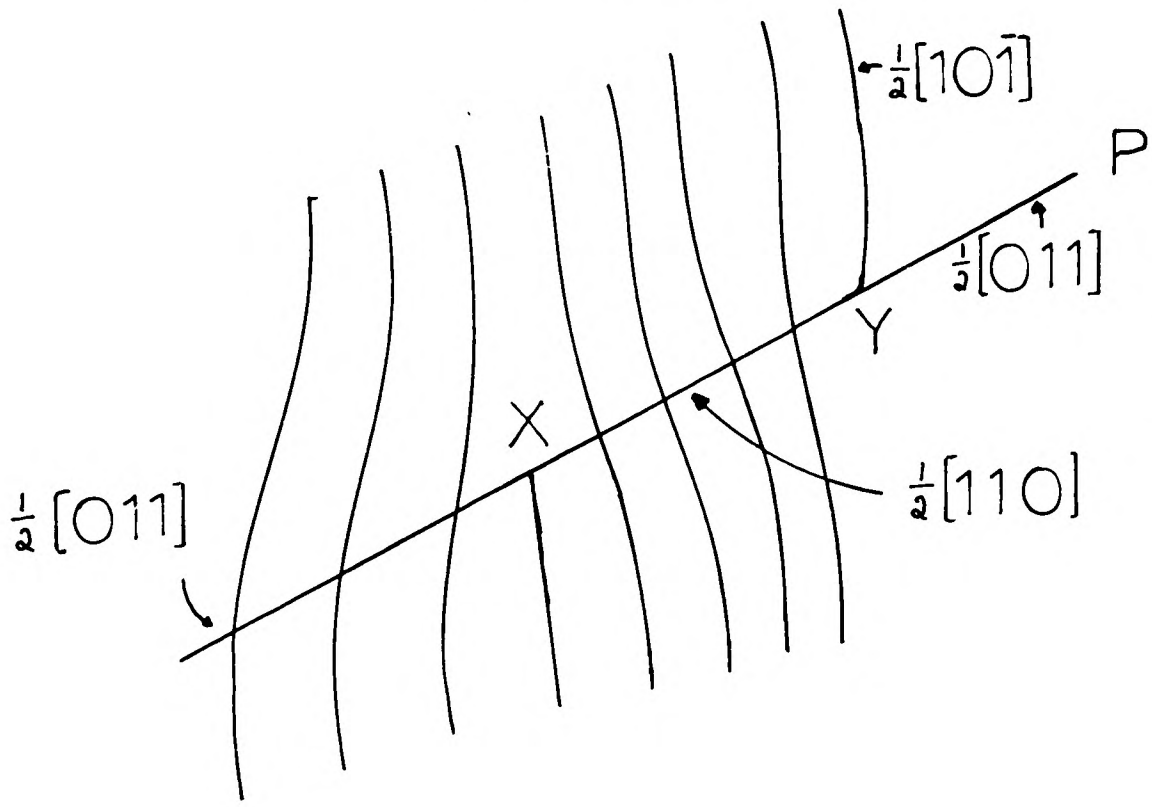
(a)

(b)

(c)

(d)

FIG 5.25



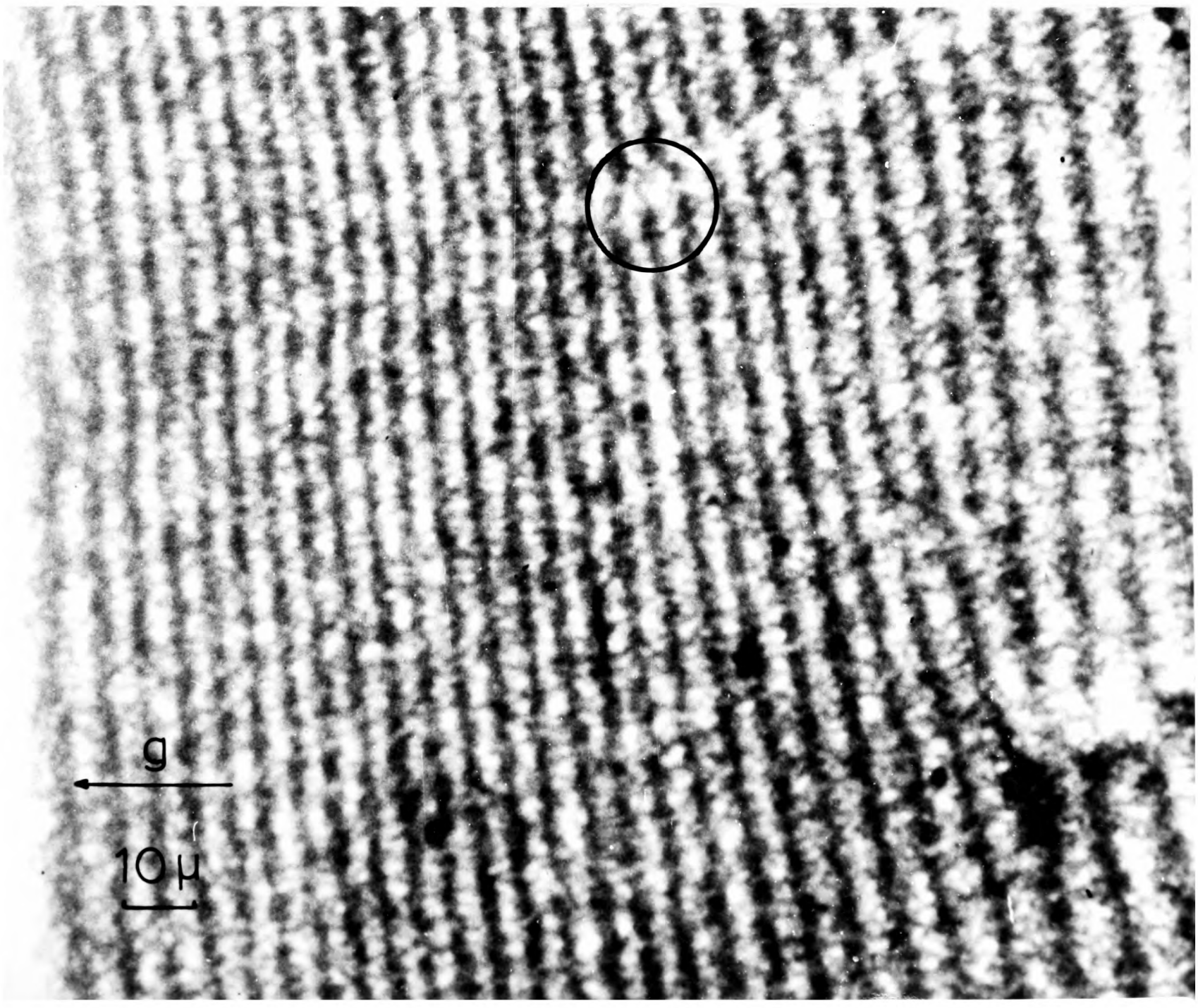
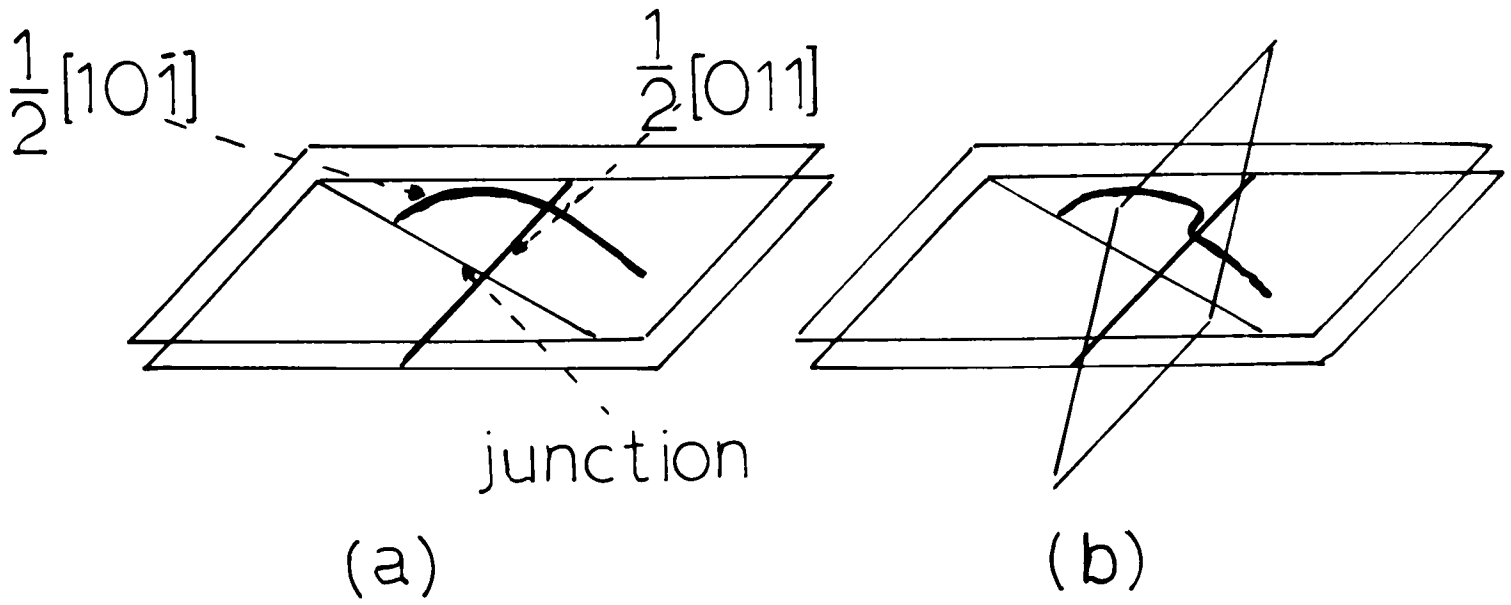
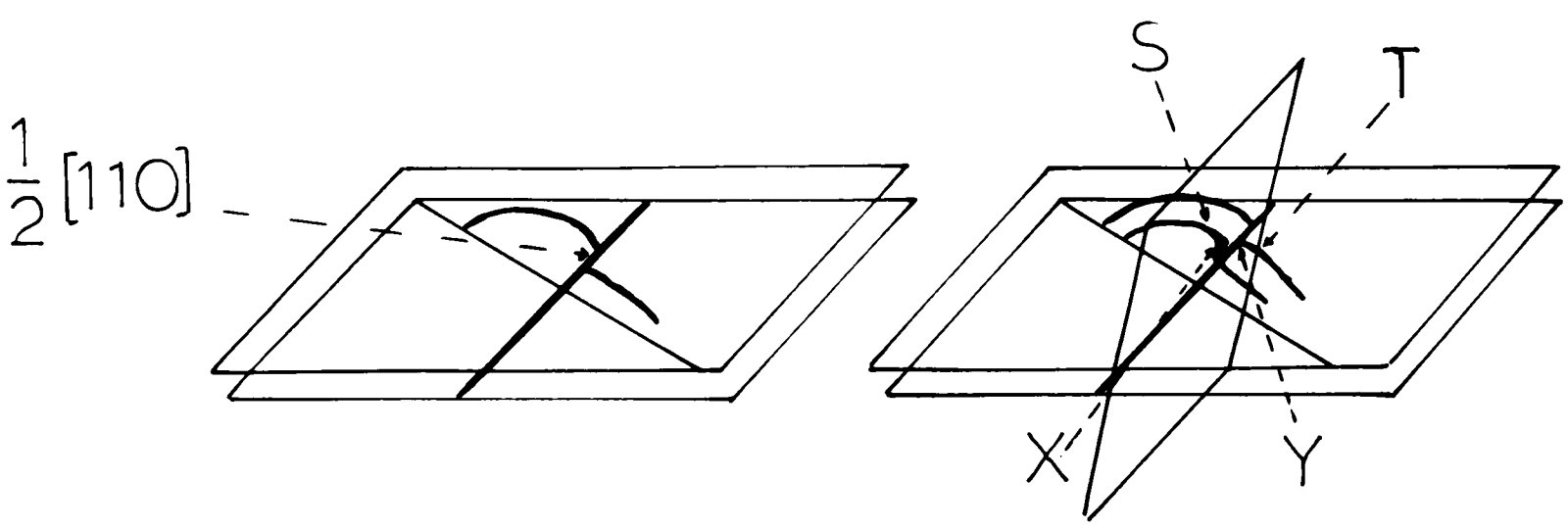


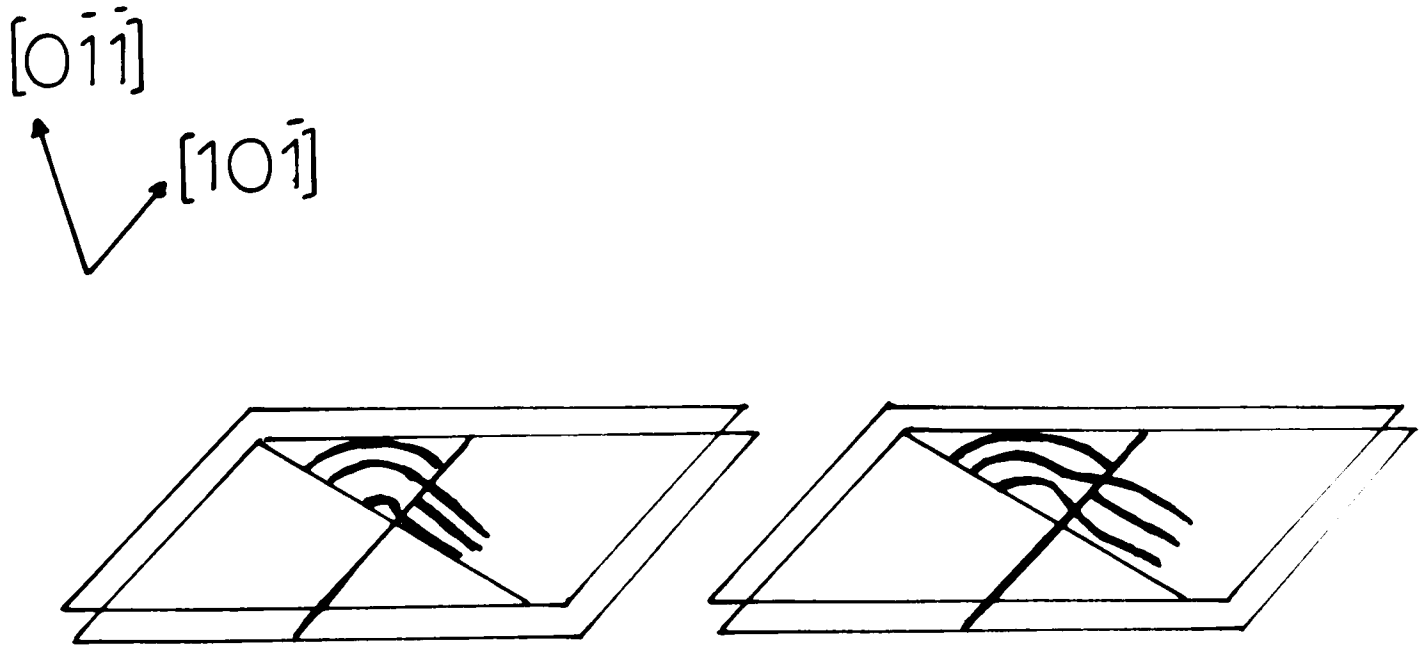
FIG 5.26



(a) (b)



(c) (d)



(e) (f)

junction, beneath the emitter edge dislocations. Two interactions take place with the emitter edge dislocations, as is shown in the schematic diagram of Fig. 5.25(a). Burgers vectors are assigned from the contrast in Fig. 5.22. The interaction, X, gives a rather spectacular "dislocation within dislocations" as shown in Fig. 5.25(b).

A suggested mechanism is given in Fig. 5.26. The emitter edge dislocation is generated and glides, Fig. 5.26(a). On crossing the straight dislocation, P, which is assumed to be immobile, it kinks, Fig. 5.26(b). The segment cross slips and a reaction occurs, Fig. 5.26(c). The next emitter edge dislocation generated will take up a kinked position, and will also cross slip, Fig. 5.26(d). Adjacent segments X and Y annihilate, and segments T and S link up, Fig. 5.26(e) and the interaction continues. After reacting, a dislocation will re-arrange its direction to minimise the elastic energy in the emitter edge array, Fig. 5.26(f). The result is the "dislocation in dislocations" observed in Fig. 5.25(b).

(b) Contrast from homogeneous strain

As was remarked previously, the contrast of dislocations in the 111 reflections is poor. In these reflections, Fig. 5.23, the contrast from the background inside the window is higher than that outside. This effect, clearly seen in the $1\bar{1}\bar{1}$ reflection of Fig. 5.23, has only been observed in the asymmetric 111 reflections. In the symmetric 220 or 224 reflections, this is not observed, Fig. 5.5.

It has recently been shown that the region below an

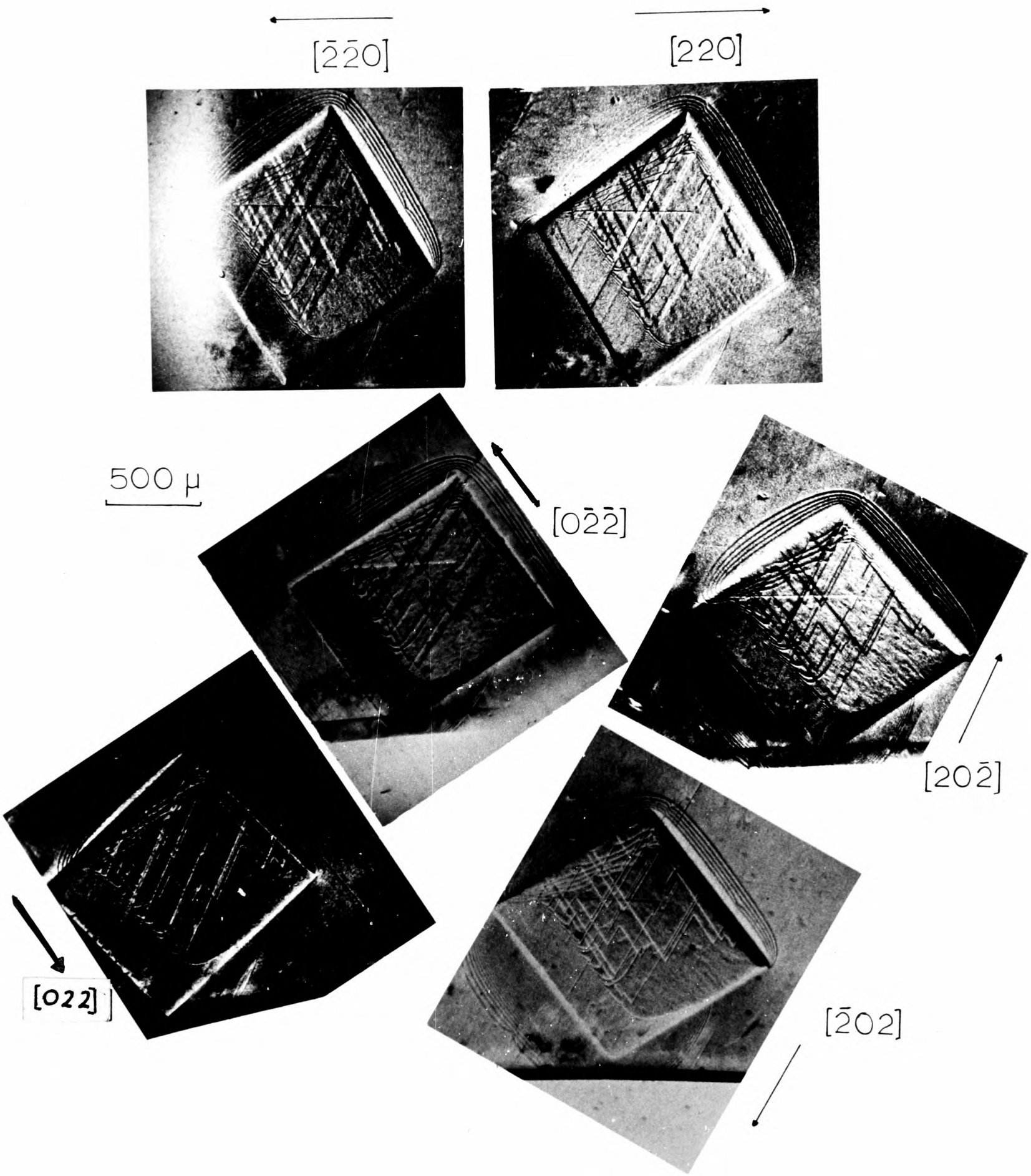
oxide or metal film which is homogeneously bent, may give enhanced diffracted intensity in the asymmetric reflections, (Saccocio, 1970,1971; Gajda, 1971; Meieran and Blech, 1971). Similar "area" contrast would be expected from strains resulting from the diffusion process, providing the concentration of impurity is large enough. It is suggested that the enhanced contrast observed here in the asymmetric reflections is a result of the distortion of the lattice planes normal to the foil surface and may be explained in a similar manner to the 'area' contrast from an evaporated film, (Saccocio, 1971).

(c) Contrast of Diffusion induced dislocations

The complete set of 220 topographs taken with CuKα radiation is shown in Fig. 5.27. Where g is parallel to u, the contrast is black and white, reversing with the g vector. Where g is not parallel to u, the contrast is either black, or white, and reverses with g. Normally, dynamical images are white in both hkl and $\bar{h}\bar{k}\bar{l}$ reflections. The contrast reversal may be explained by considering the effects of surface relaxation, and, using the method developed by Hart, (1963), based on the Penning-Polder theory, a qualitative description of the contrast may be obtained.

Provided that the distortion is small, so that inter-branch scattering does not occur, and assuming the X-ray paths lie parallel to the lattice planes, Hart, (1963), has shown that the contrast, C, is given by :

FIG 5.27



$$C = - \frac{\sin 2\theta_B}{\chi_g} \left[\frac{\partial u}{\partial x} \right]_{x=o}^{x=t} + \frac{4 \sin^2 \theta_B}{\chi_g} \left[\frac{\partial u}{\partial y} \right]_{x=o}^{x=t} \qquad (5.11)$$

where the Bragg planes are in the XZ plane, u is the component of atomic displacement normal to the Bragg planes, χ_g is the Fourier component of susceptibility and t is the crystal thickness.

In the calculations performed by Hart, only the image formed at large distances to the dislocation core was considered, as interbranch scattering occurs closer than about 10 μm from the core, (Kato, 1963a,b).

Using the expression for a surface relaxed dislocation given by Head, (1953) and Titchmarsh, (1971), calculations have been performed for the misorientation and radius of curvature of the lattice planes. At distances greater than 8 μm from the core of a 60^o dislocation, ½ μm from the crystal exit surface, the radius of curvature is not enough to cause interbranch scattering. Between 2 and 8 μm from the core, the lattice curvature does not exceed the limit set on tie point migration, except in the region very close to the surface.

Using the strain field given in Chapter 7 of Titchmarsh's thesis, (Titchmarsh, 1971), the contrast due to the tie point migration effects has been calculated. At all points the radius of curvature has been calculated and using a method similar to that of Lawn, (1968), used previously, the image of the dislocation up to 2 μm from the core has been computed. Where the radius

of curvature exceeds $g \int_g^2$, this value of the contrast has been taken as that contributing to the image.

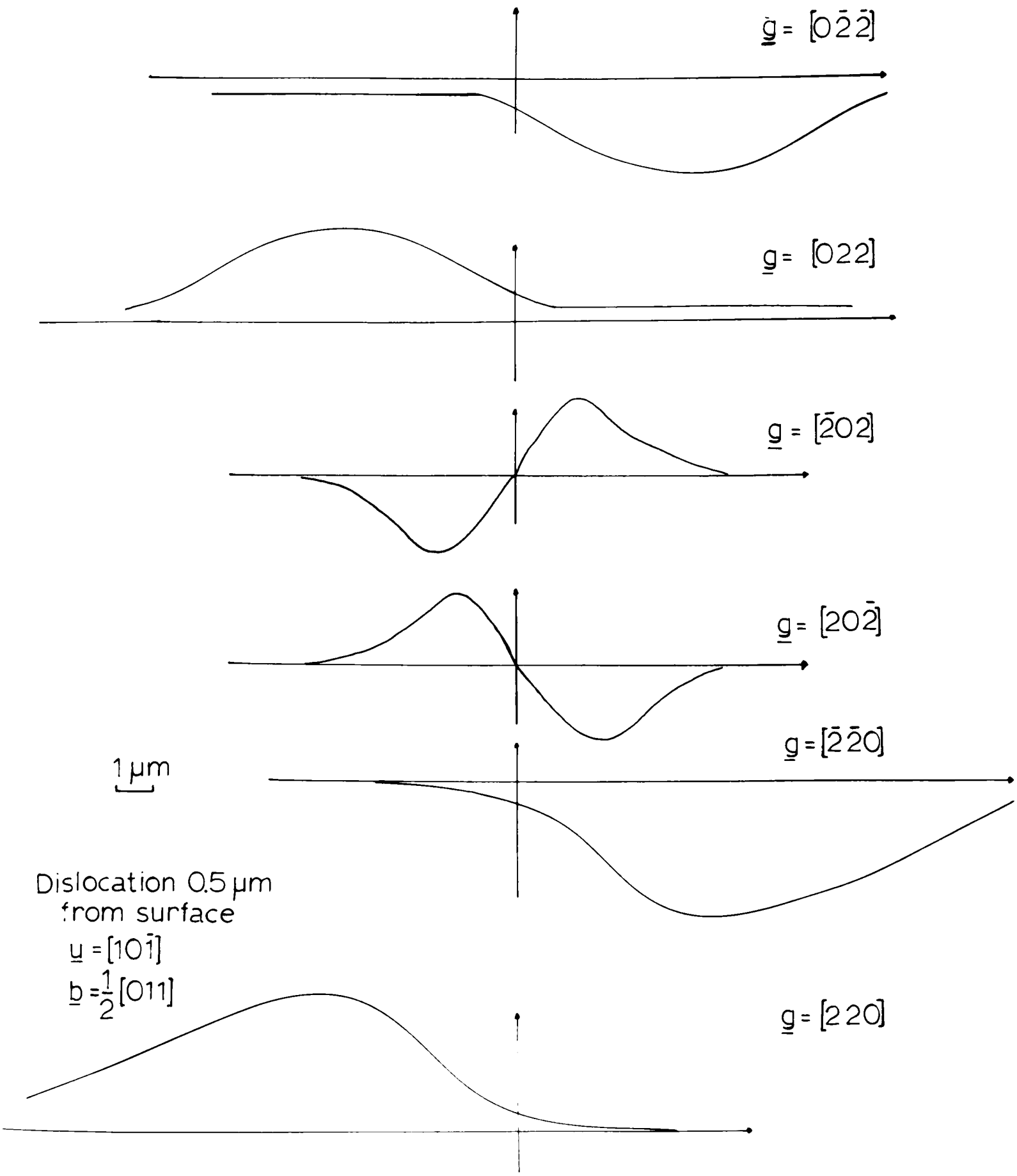
Figure 5.28 shows the computed images for the dislocation lying along $[\bar{1}01]$ with Burgers vector $\frac{1}{2}[011]$. The dislocation was assumed to lie $\frac{1}{2}$ μm below the surface. The contrast is black and white with g parallel to $\underline{u}$ and reverses sign with g. In the $\bar{2}\bar{2}0$ and $0\bar{2}\bar{2}$ reflections, the contrast is white and reverses with the g vector.

While this method of calculation makes certain assumptions which render it qualitative rather than quantitative, the asymmetry in dislocation image contrast is explained. Clearly a more quantitative simulation is desirable, in order, for example to explain the relative widths of the images. However, this column approximation approach is simple and gives an explanation of the contrast. It is clear that surface relaxation effects must be considered in topographs of diffusion induced dislocations.

Summary

Following a survey of the previous applications of X-ray topography to semi-conductor research and discussion of the types of defects observed, an attempt was made to measure the junction stress produced by mis-match of ionic radii of dopant and matrix. A value of the order of 2×10^4 dynes/cm was given for the force on unit length of junction measured using the theory developed by Lawn. In the following discussion, several obstacles to accurate measurement of the stress were pointed out. There followed a description of an

FIG 5.28


g = [0$\bar{2}\bar{2}$]
g = [022]
g = [$\bar{2}$02]
g = [20$\bar{2}$]
g = [$\bar{2}\bar{2}$0]
1 μm
Dislocation 0.5 μm from surface
u = [10$\bar{1}$]
b = $\frac{1}{2}$[011]
g = [220]

X-ray topographic and S.E.M. investigation of the origin of breakdown fingers seen in the Beam Induced Conductivity Mode at the junction edges. From analysis of contrast in X-ray topographs and in the voltage contrast mode in the S.E.M., it was concluded that they were due to scratches in the oxide mask prior to diffusion. A description of dislocations observed in a heavily boron-doped silicon slice was then given. The slip behaviour was similar to that described by Miltat in a phosphorus doped sample, supporting that author's conclusion that the deformation occurred from thermal shock and was not directly due to the diffusion process. Interactions in emitter edge dislocations were demonstrated and the very narrow images observed explained by consideration of the effects from neighbouring strain fields in the dislocation array. Reasonable agreement was found between theory and experiment.

Burgers vectors of the dislocations inside the window region were determined, and results similar to those of previous workers using phosphorus doped silicon were found. The loss of image at high density with MoKα radiation was interpreted as an effect from overlapping of images. Dislocation interactions in the low density region were discussed and interactions with emitter edge dislocations described. The intense background contrast in the asymmetric reflections was interpreted as being similar to the contrast observed from homogeneous straining by films. The distinctive contrast reversal of the dislocations when imaged with CuKα was explained in terms of surface relaxation effects using Penning-Polder theory.

C H A P T E R VI

STUDY OF DEFECTS IN NATURAL FLUORITE

1. Introduction

Calcium fluoride is found naturally in many parts of the world as fluorite or fluospar. It crystallises as three interpenetrating face centred cubic lattices with basis calcium atoms at [000] and fluorine atoms at $[\frac{1}{4},\frac{1}{4},\frac{1}{4}]$ and $[-\frac{1}{4},\frac{1}{4},\frac{1}{4}]$. The crystals vary from colourless to deep purple depending on location and its beauty and relative inexpensiveness makes it a common ornament. Industrially it is used in powdered form, as a flux for blast furnaces in steel production.

A large number of papers have been published on the electronic properties of calcium fluoride and the effects of small additions of rare earth elements, but relatively few on the defect properties. Dislocations have been observed in fluorite by decoration techniques and electron microscopy, but no Burgers vectors or glide planes have been identified. Bontinck and Dekeyser (1956) heat-treated natural fluorite with sodium at 700°C and observed dislocations in the ultramicroscope due to the decoration of impurities along the dislocation lines. Using the crystallographic construction of Jaswon and Dove (1955), they predicted the two most common Burgers vectors to be $\frac{1}{2}\langle 101\rangle$ and $\frac{1}{2}\langle 112\rangle$, though the latter would be less likely. Complex networks of dislocations were observed, the density being high.

In synthetic fluorite, treated at 1100°C in a reducing atmosphere containing excess silver, decorated dislocation helices and closed loops were observed in the ultra-microscope, (Bontinck, 1957; Bontinck and Amelinckx, 1957). Several mechanisms were suggested to account for the various configurations of helices and loops observed, the unifying feature being that large amounts of climb were required by the mixed dislocations, (Amelinckx, Bontinck, Dekeyser and Seitz, 1957).

Schuller and Amelinckx (1960) chemically polished thin cleavage flakes of natural fluorite and around holes in the flake, the crystal was sufficiently thin to allow appreciable electron transmission. Material melted in the electron beam, and dislocations were observed to move into the foil from the edges. No well-defined slip planes nor Burgers vector analysis was reported.

Several authors have discussed dislocation core arrangements in fluorite. Evans and Pratt (1969) suggest that the edge dislocation on the primary slip system, $\{100\}\langle 110\rangle$, should adopt a mixed configuration between charged and jogged nature, to minimise the electrostatic energy. It was shown that the primary screw dislocation and secondary, $\{110\}\langle 110\rangle$, edge dislocation will be electrically neutral. Recently a revised core model for the primary edge dislocation has been suggested which leaves the dislocation neutral, (Ashbee and Frank, 1970).

An interesting similarity between fluorite and diamond is indicated in some etching experiments. Using 0.2N nitric acid, Patel, Goswami and Desai (1964) produced small etch

pits on the {111} faces resembling the trigons on the octahedral faces of natural diamond, (Tolansky and Willock, 1947). Some debate existed at one time as to whether these trigons were etching or growth effects. The analogy between the etch pits on fluorite and diamond trigons indicated an etching origin. It was subsequently shown that trigons correspond to dislocation outcrops, (Lang, 1964) and trigons have also been produced by etching under suitable conditions, (Patel and Patel, 1969). A further analogy between diamond and fluorite is the phenomenon of micro-discs, first observed in dodecahedral diamond faces, (Pandeyn and Tolansky, 1961). Patel and Desai (1966) produced similar micro-discs, attributed to bubbles impeding the etchant, when natural fluorite was etched with 3:1 perchloric acid and aluminium chloride at 90°C.

Several studies have been made on the deformation behaviour of fluorite using various etches. Keig and Coble (1968) measured the dislocation velocities by etching, deformation and subsequent etching, and Patel and Desai (1969) carried out a deformation study using a micro-indenter on neutron irradiated fluorite.

In this chapter natural fluorite is examined by X-ray topography, optical birefringence microscopy and etching techniques.

2. Study by X-ray Topography

(a) General survey

The relatively low absorption coefficient of fluorite

for X-rays makes it amenable in this respect to study by X-ray topography. Reference to Table 6.1 indicates that with silver Kα radiation, direct images will be clearly visible in specimens over ½ mm thick.

Table 6.1

Absorption coefficients for calcium fluoride

Radiation	μ (cm^{-1})	Thickness for $\mu t=1$
CuKα	310	30 μm
MoKα	35	280 μm
AgKα	17.5	570 μm

Figure 6.1(a) shows an X-ray topograph of a cleaved slice of natural fluorite, 1 mm thick, and Fig. 6.1(b) the corresponding optical micrograph (unpolarised light). Figure 6.1(c) shows a magnified version of Fig. 6.1(a) and from it, several features which would seem to be common amongst the specimens studied may be pointed out.

Two distinct regions exist, one with a relatively low dislocation density, A, and the other, B, with a relatively high density and in which individual dislocations cannot be resolved by X-ray topography. In a few regions the crystal seems almost perfect, for example, in area C, thickness fringes are observed from the specimen edge. This is a dynamical diffraction phenomenon, only occurring in relatively perfect material. In general, the crystal edges corresponding

FIG 6.1

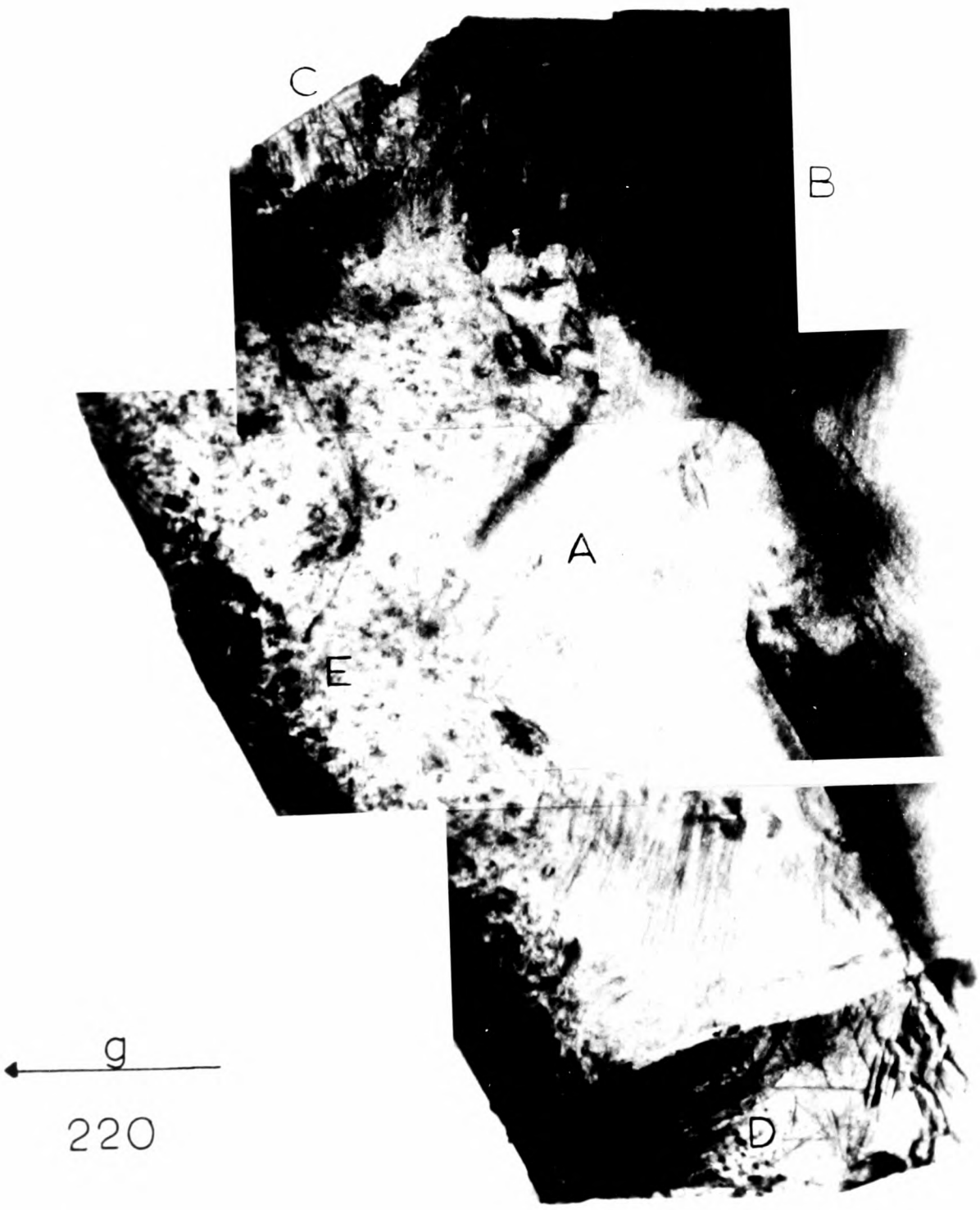


1mm

(a)



(b)



(c)

to faces in the natural, uncleaved crystal are less perfect than the central region. In region E, enhanced contrast may be observed in both optical and X-ray micrographs. A large amount of the contrast appears to arise from roughly spherical defects, visible under the optical microscope. It is not clear whether these are precipitates of impurity or bubbles of trapped gas. A study of this area in the energy dispersive mode in the scanning electron microscope might provide the answer to this question.

The dislocations marked D are examples of dislocations produced by an inclusion or artifact in the crystal during growth. Numerous examples will be seen in other crystals.

(b) Dislocations

In order to obtain good dislocation images it was necessary to thin the crystals. Chemical thinning over large areas with hot sulphuric acid proved difficult and left a dirty deposit on the surface. The (111) cleavage slices were easily ground down, but produced a poor surface. Polishing for several hours on 1 μm diamond paste left a surface which showed no signs of damage under the optical microscope. This proved adequate for most purposes. However, to obtain clearly visible fringes across the stacking faults, it was necessary to take limited projection topographs, (Lang 1963).

Figure 6.2 shows the 220 type reflections from a specimen which has one cleaved and one polished surface. Figure 6.3 shows the corresponding 111 type reflections. Once again two distinct regions are visible, one with high

FIG 6.2

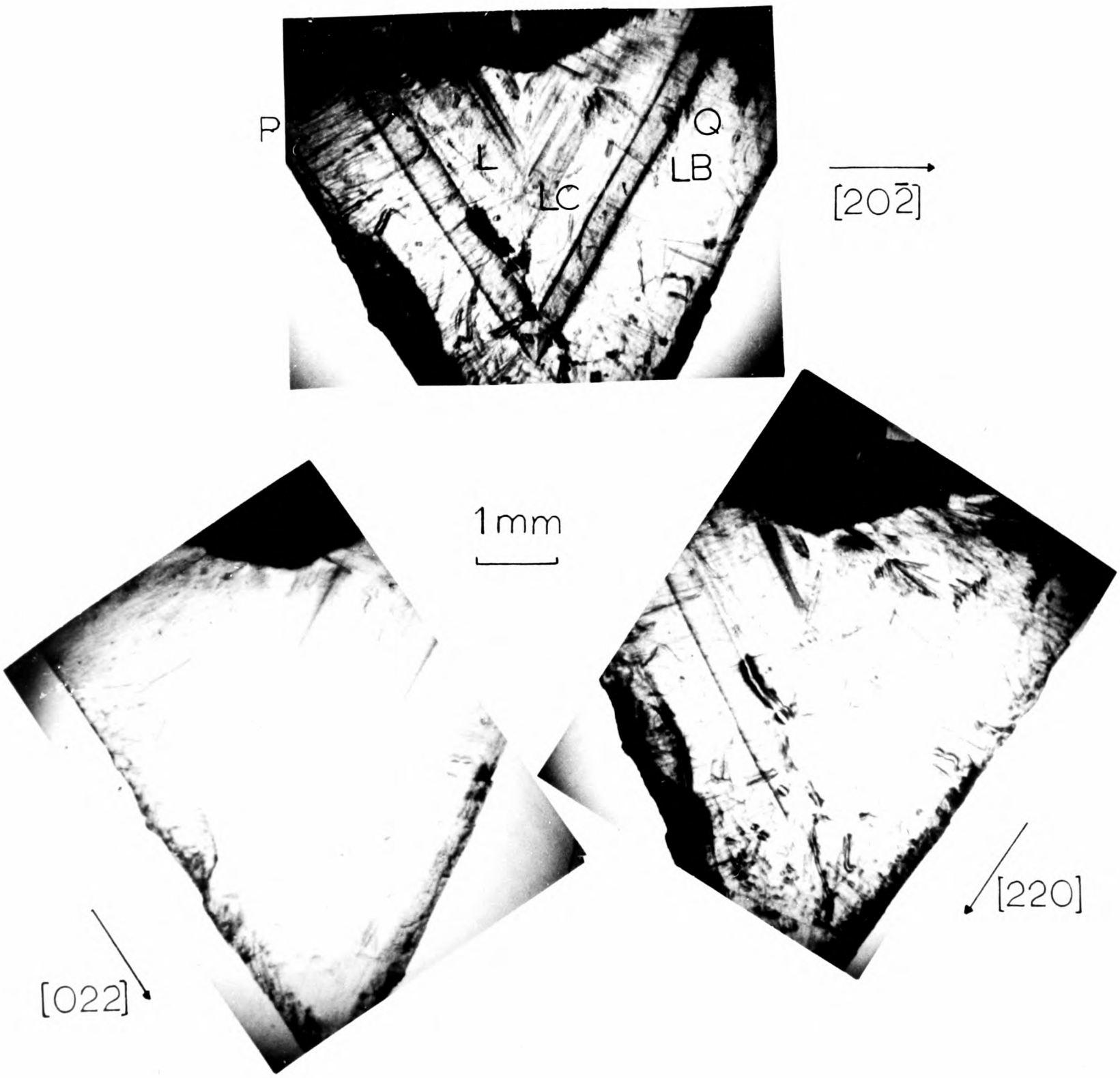
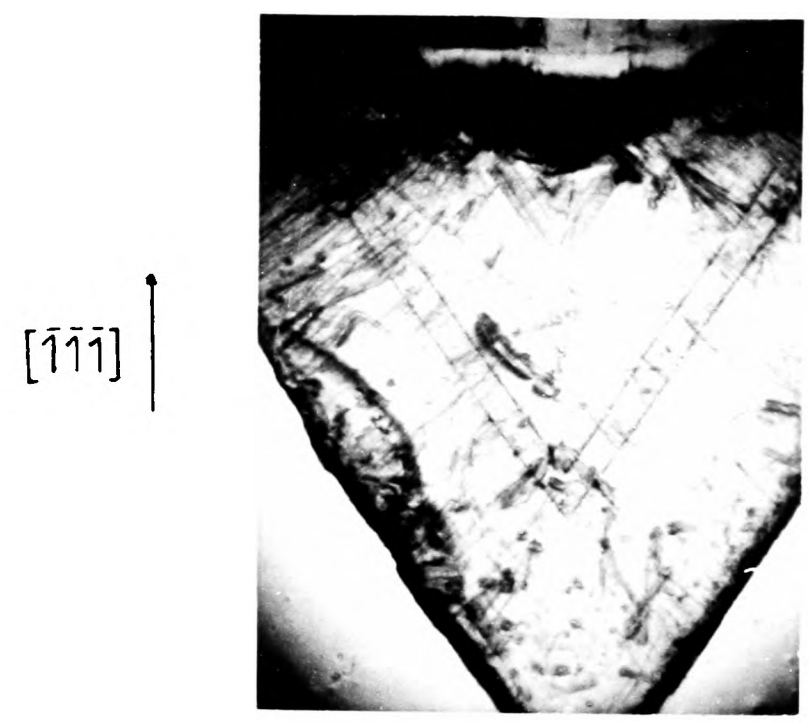
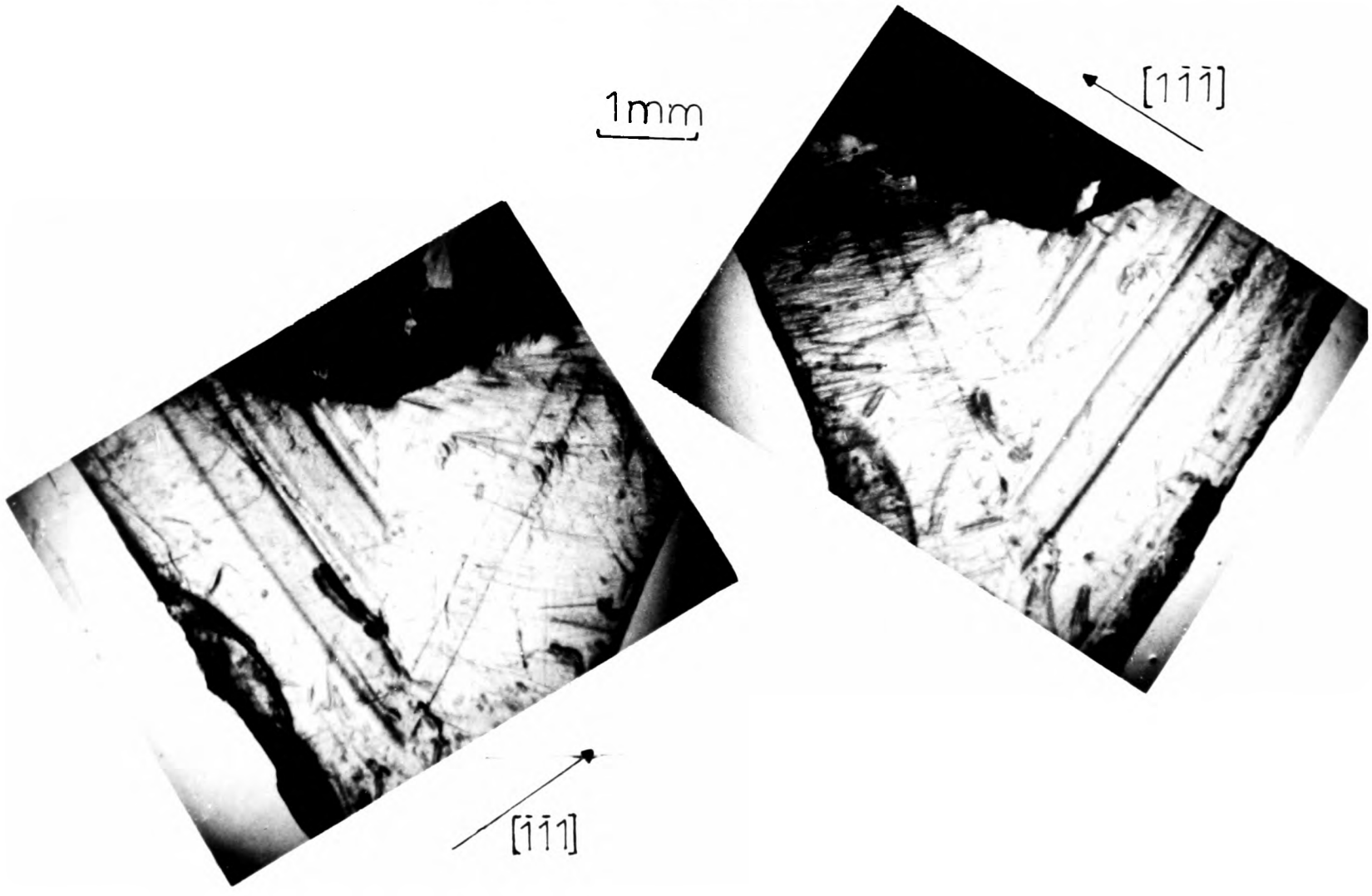


FIG 6.3



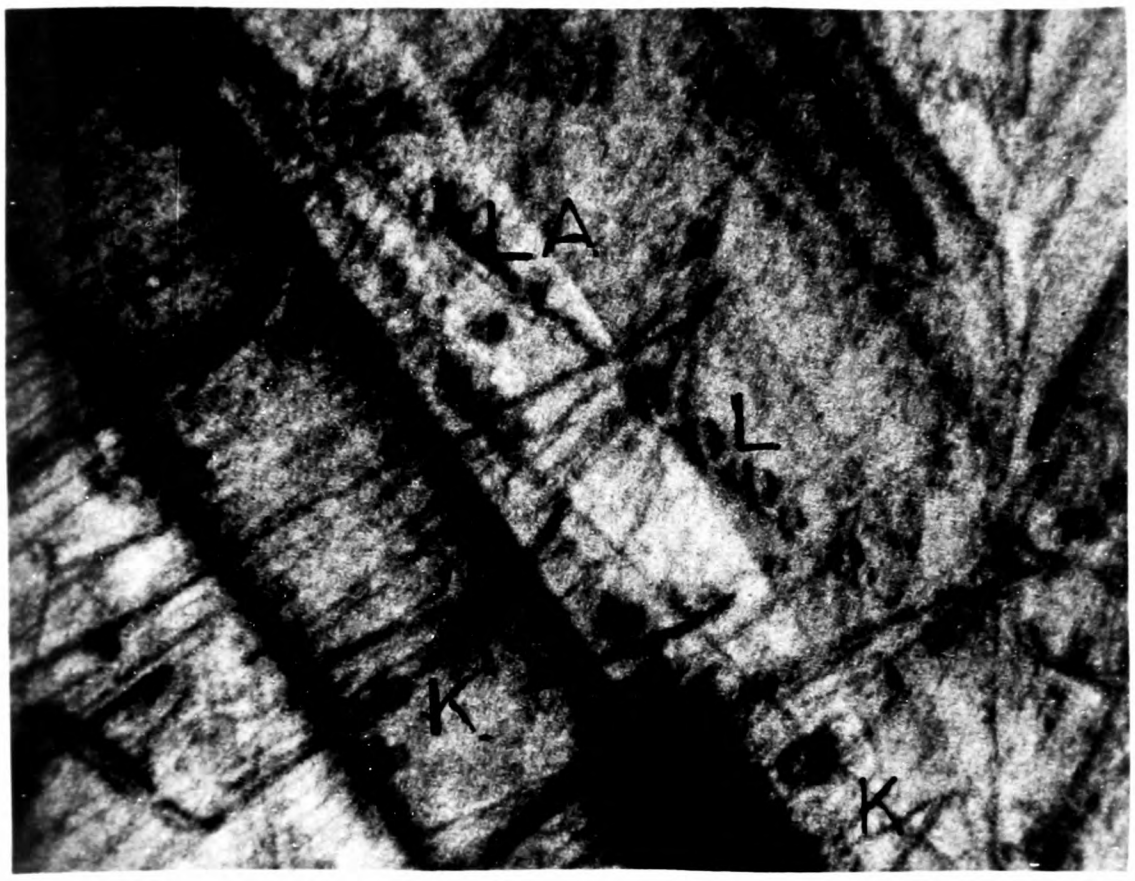


and the other with low dislocation density. The remarks in this section are confined to the low dislocation density region.

Two sets of dislocations are observed, one set, P, normal to [011] and the other, Q, normal to [110]. The dislocations are generally associated in bundles radiating from a point, and do not appear to lie along definite crystallographic directions. Crystals grown from a single seed usually exhibit a single bundle of dislocations, radiating from the nucleus outwards to the crystal surfaces (Frank and Lang, 1959; Lang, 1964; Kamiya and Lang, 1965; Emara, Lawn and Lang, 1969; Ikeno, Maruyama and Kato, 1967). In fluorite, dislocations are continuously generated during growth presumably by the inclusion of impurity particles. Similar configurations have been observed in natural quartz, (Lang, 1959, 1967; Lang and Muiscov, 1969) and synthetic magnesium aluminate spinel, (Wang and McFarlane, 1968). All dislocations are visible in the 220 type reflections. Set P are invisible in the $\bar{1}\bar{1}1$ reflection, giving a Burgers vector parallel to [011], presumably $\frac{1}{2}$[011] and set Q are invisible in the $1\bar{1}\bar{1}$ reflection, indicating a Burgers vector of $\frac{1}{2}$[110]. Both sets of dislocations are thus predominantly edge in character.

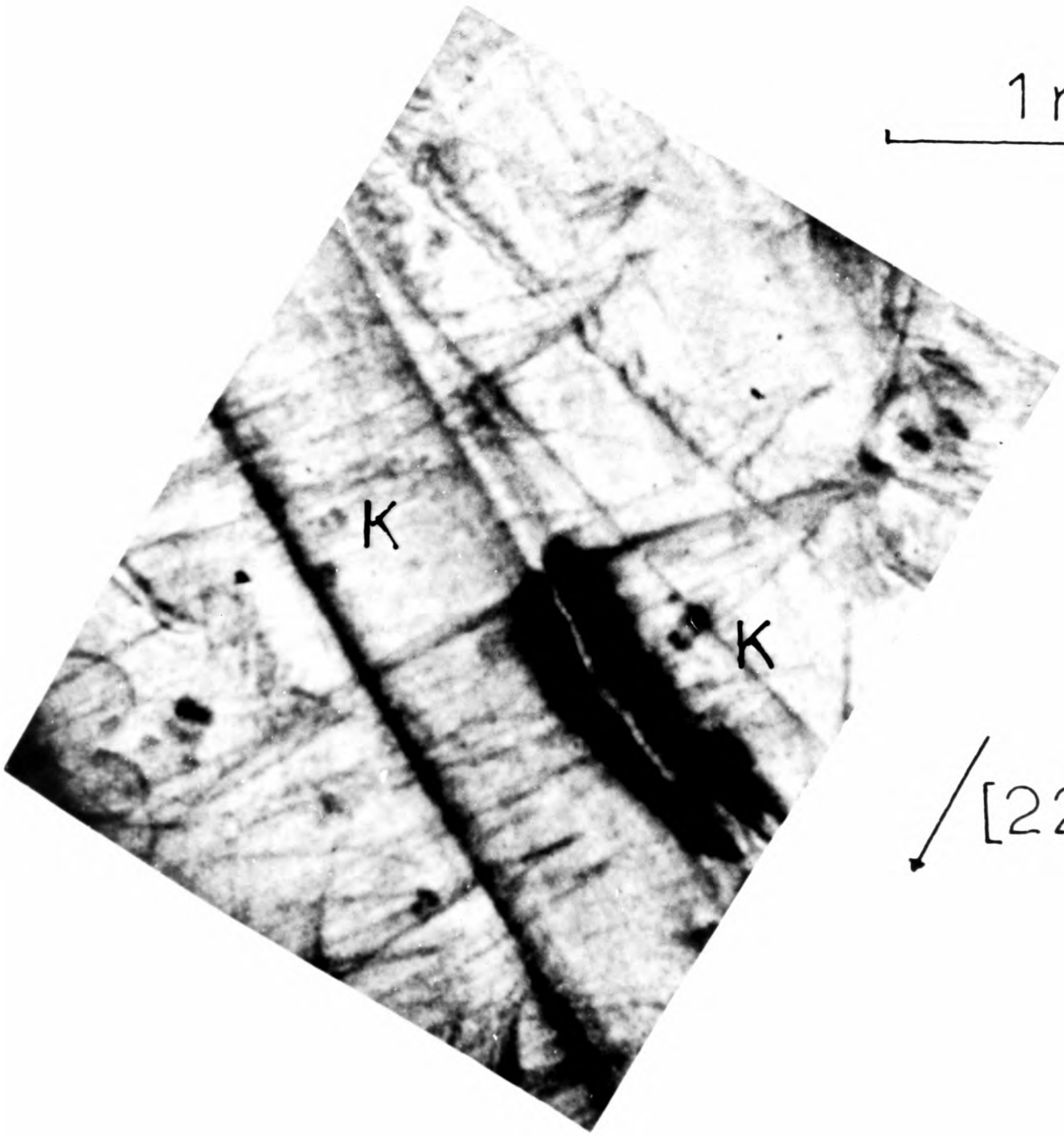
An interesting line of defects is observed at L, Fig. 6.4. The contrast on the topographs shows a line of no contrast, but this does not appear to rotate with the $\bar{g}$ vector, in the same way as the defects marked K, which are presumably inclusions of some kind. The axis of these defects is a continuation of a line defect, LA. This, and similar

FIG 6.4



[20$\bar{2}$]

1 mm



[220]

defects LB and LC do not vanish completely in any of the topographs. A possible explanation is that the defects LA, LB and LC are dislocation helices which break up into closed loops, L. Strong $\underline{g}\cdot\underline{b}_{\wedge}\underline{u}$ contrast prevents complete loss of image in any topograph seen. The mechanisms of formation of helices and closed loops are described by Bontinck and Amelinckx (1957) and involve substantial climb. This would suggest that the crystal was subjected to high temperatures following growth. Climb of the edge dislocations P and Q would occur roughly perpendicular to their glide plane, i.e., perpendicular to the specimen surface.

(c) Fault Surfaces

In Figures 6.2 and 6.3, planar defects are observed cutting the specimen surface in the [110] and [011] directions. In the limited projection topograph shown in Fig. 6.5(a) and in the image produced in another specimen, Fig. 6.5(b), fringes can be seen across these defects. In both crystals $\mu t=2$, and the fringe visibility is seen to be greater near the intersection of the defect with the surfaces than in the centre. This is exactly what is expected from an inclined planar fault. The fringes occur from interference between wave-fields of a given branch of the dispersion surface and wave-fields associated with a tie point which has jumped from one branch to another, (Whelan and Hirsch, 1957). In the thick crystal, the branch 1 wave-fields are the only ones which propagate large distances. Then, interference can only occur between the branch 1 wave-fields and wave

FIG 6.5



(a)



(b)

fields which have jumped from branch 2 to branch 1 near the entrance surface, or from branch 1 to branch 2 near the exit surface. The fringe visibility is thus appreciable only at the edges. Also, in agreement with the theoretical predictions, the fringe contrast is opposite on either side of the fault, (Hashimoto, Howie and Whelan, 1962; Authier, 1968). In the case where the phase difference between the original and new wave fields is an integral multiple of 2π, no contrast is expected from the fault. These considerations apply equally well to stacking faults, twin lamellae or thin plate-like precipitates.

To determine the nature of the defect, it is necessary to make a detailed study of several reflections. The projected width of the defect indicates that the fault surfaces are $(1\bar{1}\bar{1})$ and $(\bar{1}\bar{1}1)$, [projected width perpendicular to the fault is 185 μm, in a crystal of thickness 520 μm]. The fault along [110] on $(1\bar{1}\bar{1})$ is completely invisible only in the 220 reflection and similarly that along the [011] on $(\bar{1}\bar{1}1)$ is only invisible in the 022 reflection.

In the face-centred cubic structure, a stacking fault along $(1\bar{1}\bar{1})$ will have one of the fault vectors,

$$\pm \tfrac{1}{3}[1\bar{1}\bar{1}], \quad \pm \tfrac{1}{6}[211], \quad \pm\tfrac{1}{6}[\bar{1}1\bar{2}], \quad \pm \tfrac{1}{6}[\bar{1}\bar{2}1] .$$

This fault is caused either by glide of a $\frac{1}{6}\langle 112\rangle$ partial dislocation or addition or removal of a $(1\bar{1}\bar{1})$ plane of atoms, e.g., by interstitial or vacancy condensation. This fault will have δ, which is given by

$$\delta = -2\pi (\underline{g} \cdot \underline{R})$$

equal to zero or 2π for the 220 and $1\bar{1}\bar{1}$ reflections. Thus, this does not correspond to the faults observed here in fluorite as it brings anions and cations on adjacent {100} planes into juxtaposition, (Evans and Pratt, 1969).

Fringes are also observed across twin lamellae, (Sauvage and Authier, 1965; Authier and Sauvage, 1966; Authier, Milne and Sauvage, 1968). However, the displacement vector of such a lamella parallel to $(1\bar{1}\bar{1})$ would be a vector in this plane. The defect would thus be invisible in the $1\bar{1}\bar{1}$ reflection, which is not in agreement with the experimental contrast.

From the observed contrast it may be concluded that the defects have fault vectors $\frac{n}{3}[1\bar{1}\bar{1}]$ and $\frac{n}{3}[\bar{1}\bar{1}1]$ respectively, where n is non integral. As the $(1\bar{1}\bar{1})$ fault is visible in the $4\bar{4}\bar{4}$ and $6\bar{6}\bar{6}$ reflections, fault vectors $\pm \frac{1}{2} \cdot \frac{1}{3}[1\bar{1}\bar{1}]$, $\frac{1}{4} \cdot \frac{1}{3}[1\bar{1}\bar{1}]$ and $\frac{1}{6} \cdot \frac{1}{3}[1\bar{1}\bar{1}]$ are eliminated.

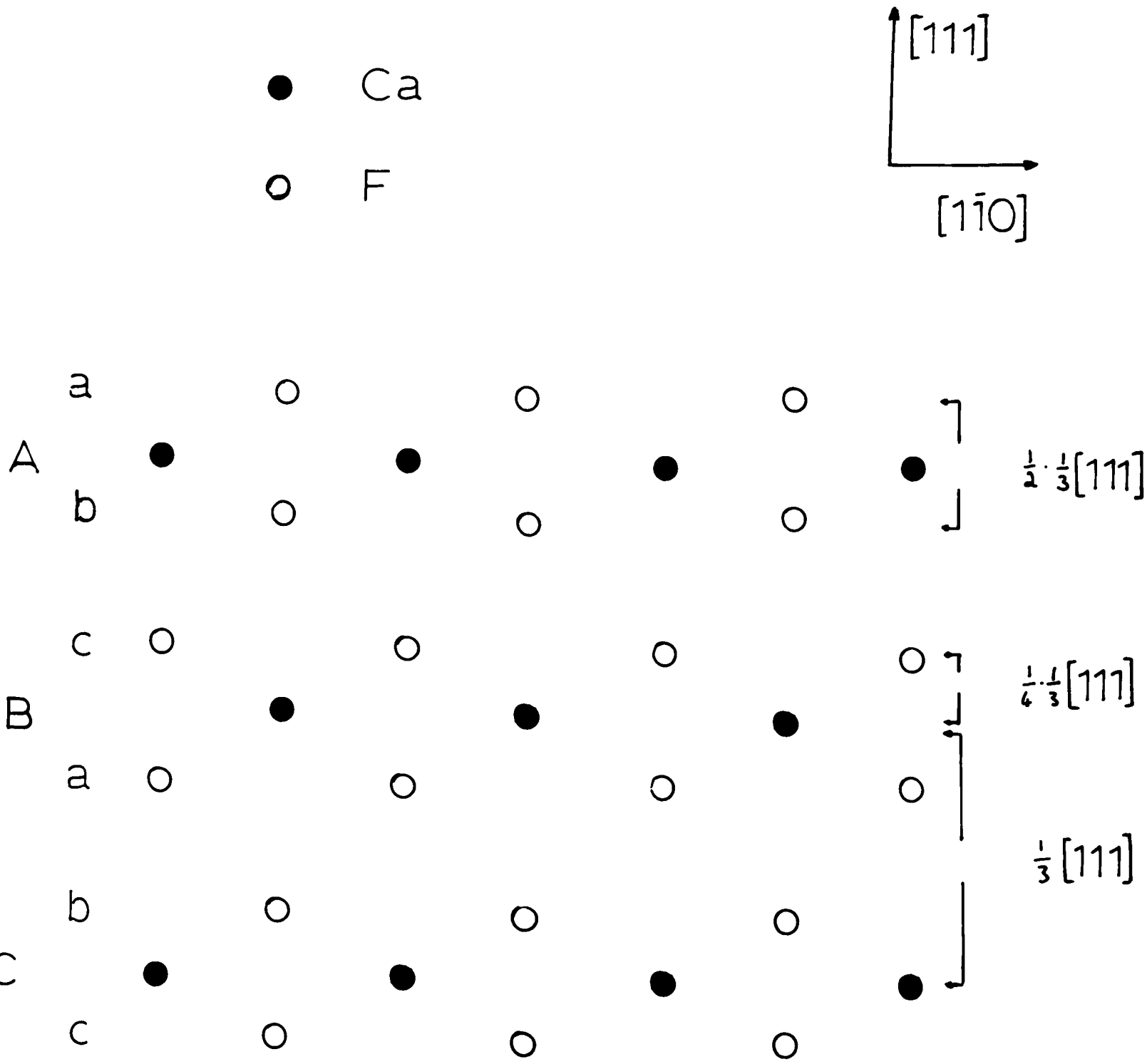
Reference to the stacking sequence on the (111) plane of fluorite, shown in Fig. 6.6 projected onto $[11\bar{2}]$, suggests that removal of a layer of fluorine atoms might produce such a fault. It is known that it is easy to remove fluorine from fluorite, for example by electron bombardment. However, to produce an uncharged fault, electrons must replace the fluorine ions. The whole concept is rather unattractive. Interpretation in terms of a planar growth boundary is much more plausible, as is shown below.

3. Study of Birefringe in Natural Fluorite

(a) Origin of Birefringence or Double Diffraction

In a non-isotropic crystal, the polarisation $\underline{P}$ may be

FIG 6.6


Ca
F
[111]
[1$\bar{1}$0]
a
A
b
c
B
a
b
C
c
$\frac{1}{2}\cdot\frac{1}{3}$[111]
$\frac{1}{4}\cdot\frac{1}{3}$[111]
$\frac{1}{3}$[111]

expressed as a tensor relation in terms of the electric field, $\underline{E}$, and the susceptibility tensor, $\underline{\chi}$.

$$\begin{bmatrix} P_x \\ P_y \\ P_z \end{bmatrix} = t_o \begin{bmatrix} \chi_{11} & \chi_{12} & \chi_{13} \\ \chi_{21} & \chi_{22} & \chi_{23} \\ \chi_{31} & \chi_{32} & \chi_{33} \end{bmatrix} \begin{bmatrix} E_x \\ E_y \\ E_z \end{bmatrix} \qquad (6.1)$$

The general wave equation is given by :-

$$\nabla \wedge (\nabla \wedge \underline{E}) + \frac{1}{c^2} \frac{\partial^2 \underline{E}}{\partial t^2} = - \frac{1}{c^2} \underline{\chi} \frac{\partial^2 \underline{E}}{\partial t^2} \qquad (6.2)$$

For monochromatic plane waves of wave vector $\underline{k}$ this reduces to :

$$\underline{k} \wedge (\underline{k} \wedge \underline{E}) + \frac{\omega^2}{c^2} \underline{E} = - \frac{\omega^2}{c^2} \underline{\chi} \underline{E} \qquad (6.3)$$

In non-absorbing crystals, there always exists a set of principal axes such that the tensor $\underline{\chi}$ is diagonal :

$$\underline{\chi} = \begin{bmatrix} \chi_{11} & 0 & 0 \\ 0 & \chi_{22} & 0 \\ 0 & 0 & \chi_{33} \end{bmatrix} \qquad (6.4)$$

In order to have non-trivial solutions of equation (6.3),

the determinant of the coefficients of the three component equations must vanish.

Defining refractive indices :

$$n_i = \sqrt{1 + \chi_{ii}}$$

one obtains :

$$\begin{vmatrix} \frac{n_1 \omega^2}{c^2} - k_y^2 - k_z^2 & k_x k_y & k_x k_z \\ k_y k_z & \frac{n_2 \omega^2}{c^2} - k_x^2 - k_z^2 & k_y k_z \\ k_z k_x & k_z k_y & \frac{n_3 \omega^2}{c^2} - k_x^2 - k_y^2 \end{vmatrix} = 0$$

(6.5)

This is the equation of the ray wave vector surface in $\underline{k}$ space. It may be shown, (Born and Wolf, 1964) that for any direction of the wave vector there are two propagation velocities corresponding to two mutually orthogonal polarisations. (For an excellent exposition of the subject of double diffraction, see Fowles, 1968.)

In an isotropic solid, there is only one value of the wave velocity and between crossed polarisers no light will be transmitted. If now a uniaxial crystal is substituted, for a given direction of incident wave vector, two directions of propagation exist inside the crystal. These two directions have mutually orthogonal polarisations. The two rays propagate independently through the crystal with different wave velocities. On re-emergence, a phase change will have

been introduced during the passage through the crystal. The resultant state of polarisation of the emergent wave will then be changed with respect to the incident polarisation. One then obtains appreciable transmitted light through the analyser.

In an isotropic crystal, birefringence may be used to reveal stresses. Application of a stress distorts the chemical bonds and the susceptibility then becomes a function of direction. In the correct orientation with respect to the polariser, it is possible to obtain appreciable transmission through the stressed region. The stress field around an individual dislocation may be detected by infra-red birefringence, (Bond and Andrus, 1956). Between crossed polarisers, the infra-red image produced of an edge dislocation in silicon was the same as that of the stress field calculated from isotropic elasticity theory. Optical birefringence has been used to study slip in sodium chloride and to determine the sense of the average Burgers vector, (Mendelson, 1961, 1962). The correlation between optical birefringence and dislocation bundles in natural diamond was reported by Lang (1967). Using both X-ray topography and birefringence topography, it was shown that the latter technique could reveal bundles of dislocations of between 3 and 4 unit Burgers vectors.

Birefringence in fluorite, another isotropic material, has been known for a long time, (Mallard, 1876; Pockels, 1889). A considerable number of papers were produced about this time concerning this unexpected phenomenon, for which no

satisfactory explanation could be given, (Hintze, 1913). Figure 6.7 shows a comparison between optical birefringence and dislocation configurations revealed by X-ray topography. The dislocation bundles are clearly distinguishable in the birefringence topograph. The area of high dislocation density, D, exhibits strong birefringence as would be expected. Examination of fluorite between crossed polarisers is thus a useful indicator of crystal perfection.

Surprisingly, however, the crystal matrix itself was found to transmit a little in one orientation. The transmission was small compared with that from region D, but comparable with that produced by the dislocation bundles. In Fig. 6.7, the dislocation bundles are observed as regions of less transmission against the background, due to this effect. The perfect crystal transmission is shown more clearly in Fig. 6.8(a). This shows a birefringence topograph of a small cleavage fragment in which the birefringence from the perfect crystal is clearly seen. Three distinct areas exist, A, B and C, which have positions of total extinction at 120^{o} to each other and between which distinct boundaries exist along the $\langle 112 \rangle$ directions. Inspection of Fig. 6.8(b) indicates that apart from stress associated with the cleavage cracks, the crystal is relatively perfect. No contrast due to the boundaries revealed in the birefringence topograph was observed in this topograph, nor in any of the 111 topographs.

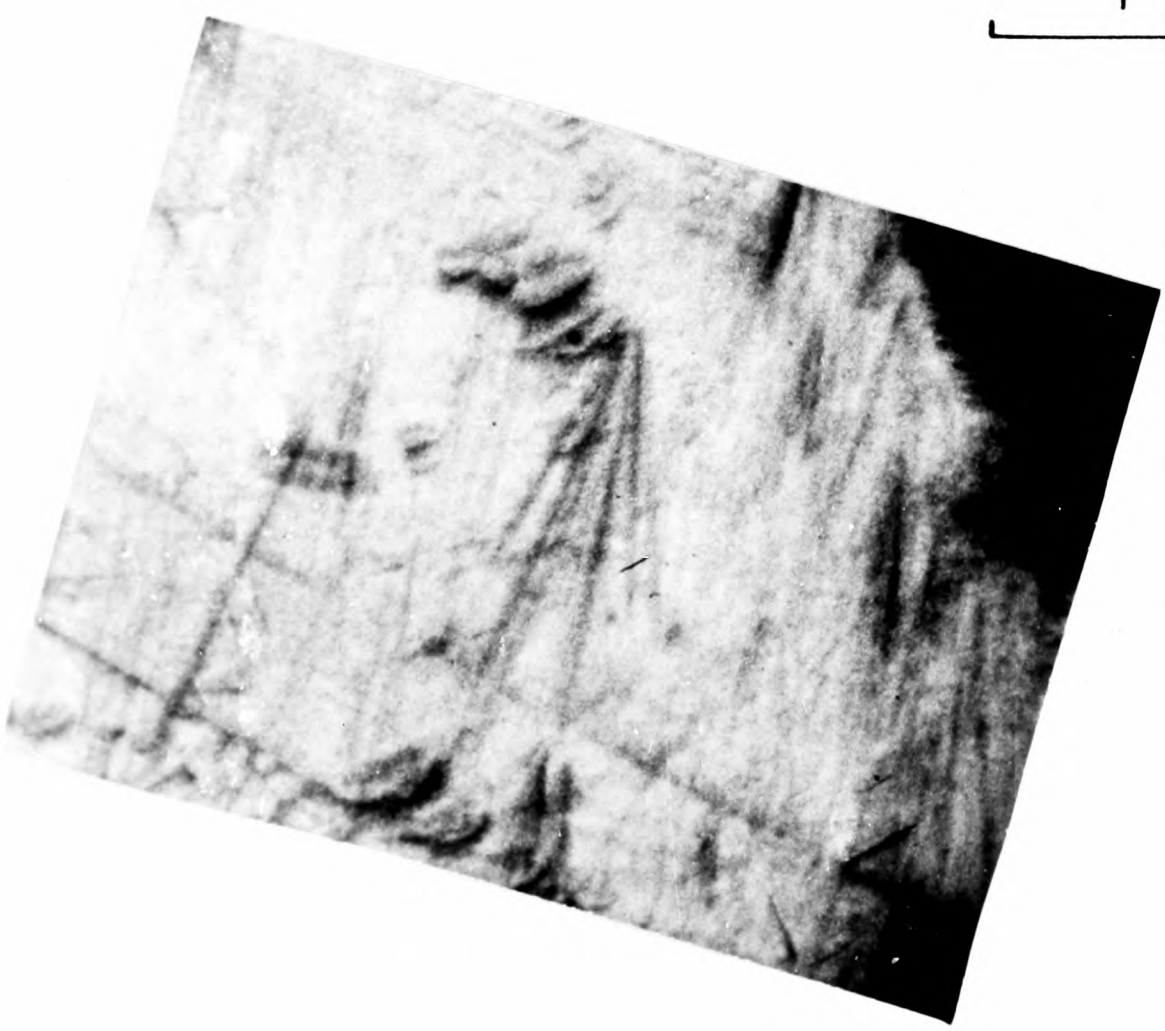
Birefringence in isotropic materials may be caused by impurities. Free fluorine is known to exist in some calcium fluoride samples, such crystals give a characteristic smell

FIG 6.7



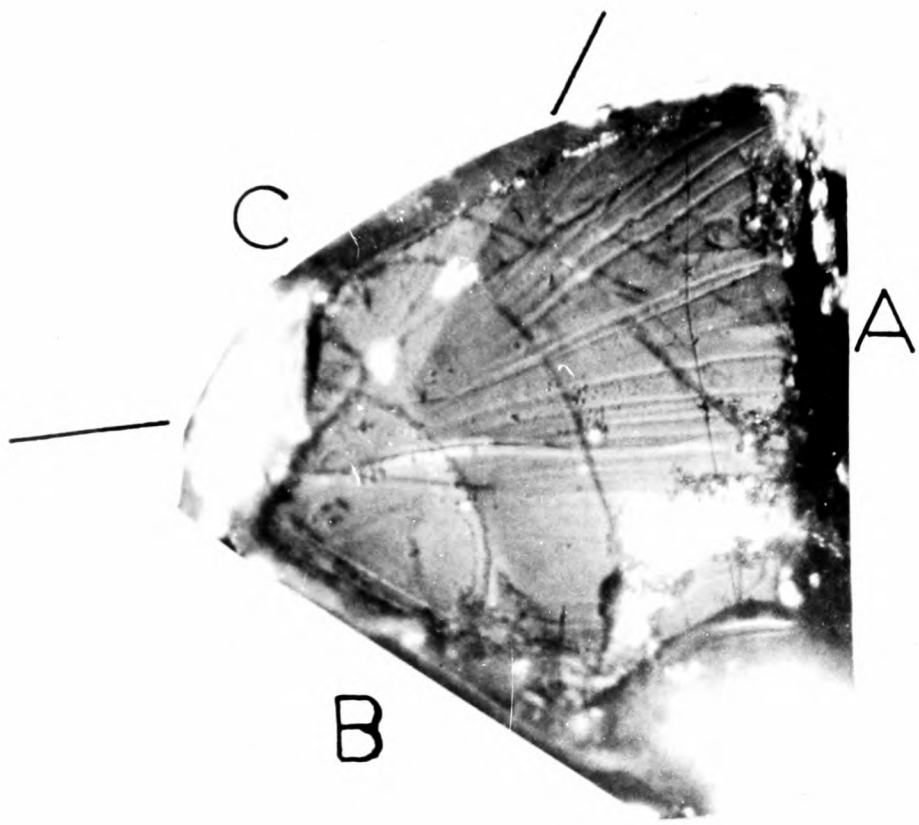
Birefringence

1 mm



X ray

FIG 6.8



Birefringence

1mm

(a)



X ray

(b)

of ozone and hydrogen fluoride when ground with water. Furthermore, this free fluorine is thought to be sited between {111} planes. An explanation for the birefringence and the planar faults is suggested in terms of this impurity fluorine.

During growth on the {111} faces, free fluorine is included between these {111} planes. This produces a small lattice distortion normal to the {111} planes. The crystal then becomes birefringent and the areas associated with growth on each {111} face have positions of extinction at 120° to each other. The boundaries between regions of different impurity atom siting lie along the inclined <110> directions, as observed experimentally. Provided the impurity concentration in each of the three regions is the same, and as growth presumably occurred on the three faces simultaneously, the lattice distortions at the boundaries will match. Here, one has what might be called an "impurity twin" and as no strain is associated with the boundary, no strain contrast is observed in the X-ray topographs. Provided the impurity concentration is small, the change in lattice parameter may be assumed to be too small to cause inter-branch scattering and thus no dynamical contrast is observed. It is thus possible to account for the visibility of the boundaries in the birefringence micrographs and their invisibility in the X-ray topographs.

The fault surfaces observed in the X-ray topographs may be explained as lamellae of greatly differing impurity concentration. During the growth process, the impurity

concentration changed rapidly, probably to a high level, and remained there for some time. At a later stage in the growth process, the impurity concentration reverted to near its original level. Provided the concentration change was large enough, the lattice will have been expanded, (or contracted), in this lamella and will not diffract the X-rays which are diffracted by the matrix. The problem then becomes that of the non-diffracting lamella treated by Authier, Milne and Sauvage, (1968). Interbranch scattering occurs, producing fringes across the defect. In order that the lamella be non-diffracting, the lattice spacing must change such that the change in Bragg angle, $\Delta\theta$, is given by :-

$$\Delta\theta > \frac{1}{g\,\xi_g} \qquad (6.6)$$

where ξ_g = the extinction distance and g the reciprocal lattice vector. For a dilation :

$$0 = 2 \cdot \Delta d \sin\theta + 2 d \cos\theta \; \Delta\theta \qquad (6.7)$$

Then :

$$\Delta\theta = - \frac{\Delta d}{d} \tan\theta \qquad (6.8)$$

where d is the lattice spacing.

Then for interbranch scattering to occur :

$$\frac{\Delta d}{d} = \frac{d}{\tan\theta}\, \xi_g \qquad (6.9)$$

By measuring the fringe spacing on the topographs, the 111 extinction distance is found to be approximately 60 μm.

As $\theta \simeq 5^{o}$ and $d \simeq 2$ Å, one obtains :

$$\frac{\Delta d}{d} \simeq 3 \times 10^{-5} .$$

An interplanar spacing change of one part in 30,000 suffices.

Measurements of the lattice parameters of fluorite have been made by the Back Reflection Laue technique, (Adàms 1952). Unit cell parameter, a, of various specimens ranged between :

5.46277 Å and 5.46342 Å

a variation of one part in 10,000. The above suggestion does not, then, contradict this evidence.

This explanation accounts for the effective displacement normal to the defect being a non-integral value of the lattice spacing. It also accounts for the fact that the two sets of faults are roughly of equal length and equidistant from the crystal edges, as would be expected if they were formed at the same time. A birefringence boundary is noted along the [121] direction, supporting these ideas.

The faults are not visible in the birefringence micrographs, as the intensity reflected from this thin area is small compared with that reflected from the bulk. A single growth boundary between areas of differing levels should:

a) be visible in the birefringence micrographs, and
b) display Moiré fringes across the defect, lying perpendicular to the g vector.

Neither are observed and thus a lamella is required to explain these observations.

4. Etching experiments

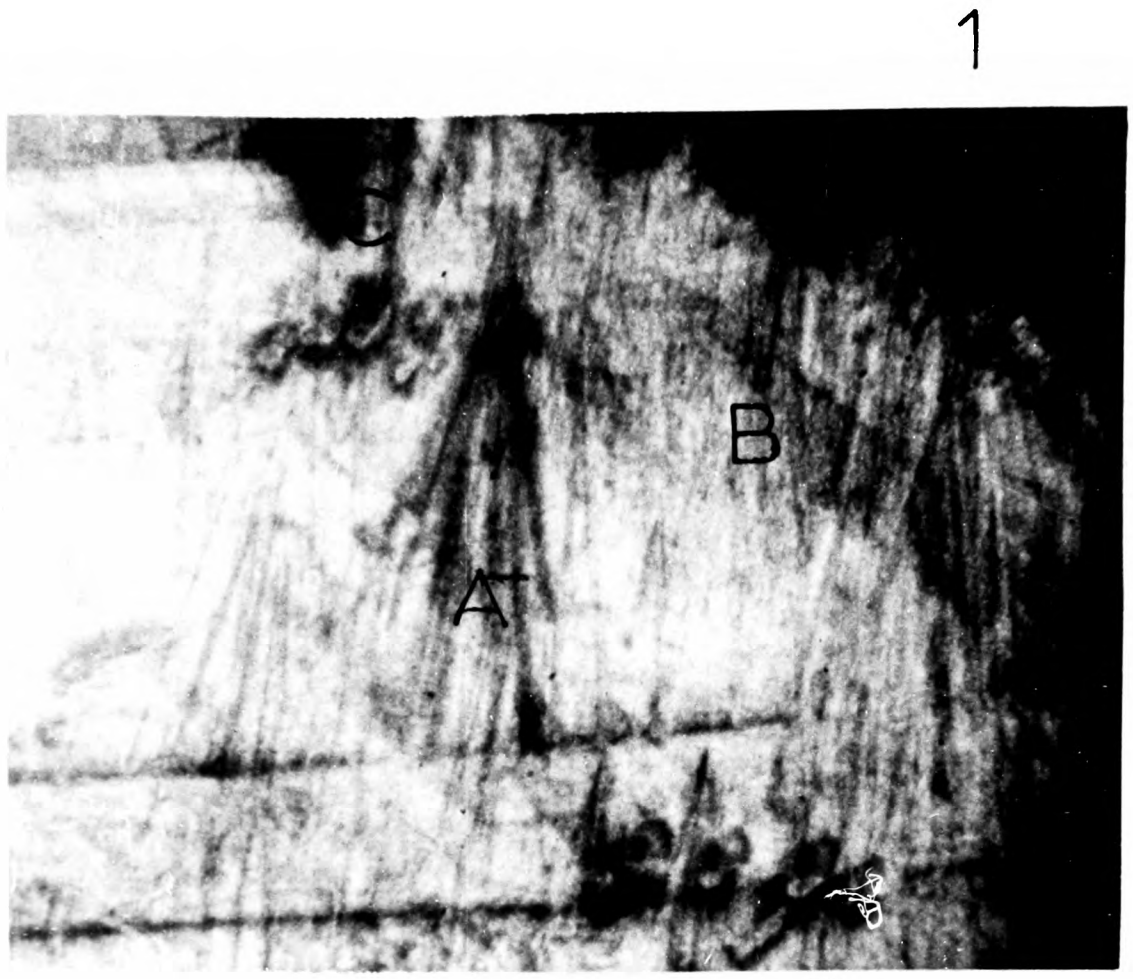
A one to one correspondence between etch pits and dislocation outcrops on the X-ray topographs was not possible owing to the high dislocation density. However, as seen in Fig. 6.9, the density of etch pits produced by 1:6 HCl in water was much greater in the high dislocation density region, 1, than in the low density region, 2. In the region, 3, both dislocation and etch pit density were intermediary between the two extremes. Further, clusters of etch pits are observed at the base of the dislocation fans, A, B and C. As stated previously, a direct correlation proved impossible.

Conclusions and Summary

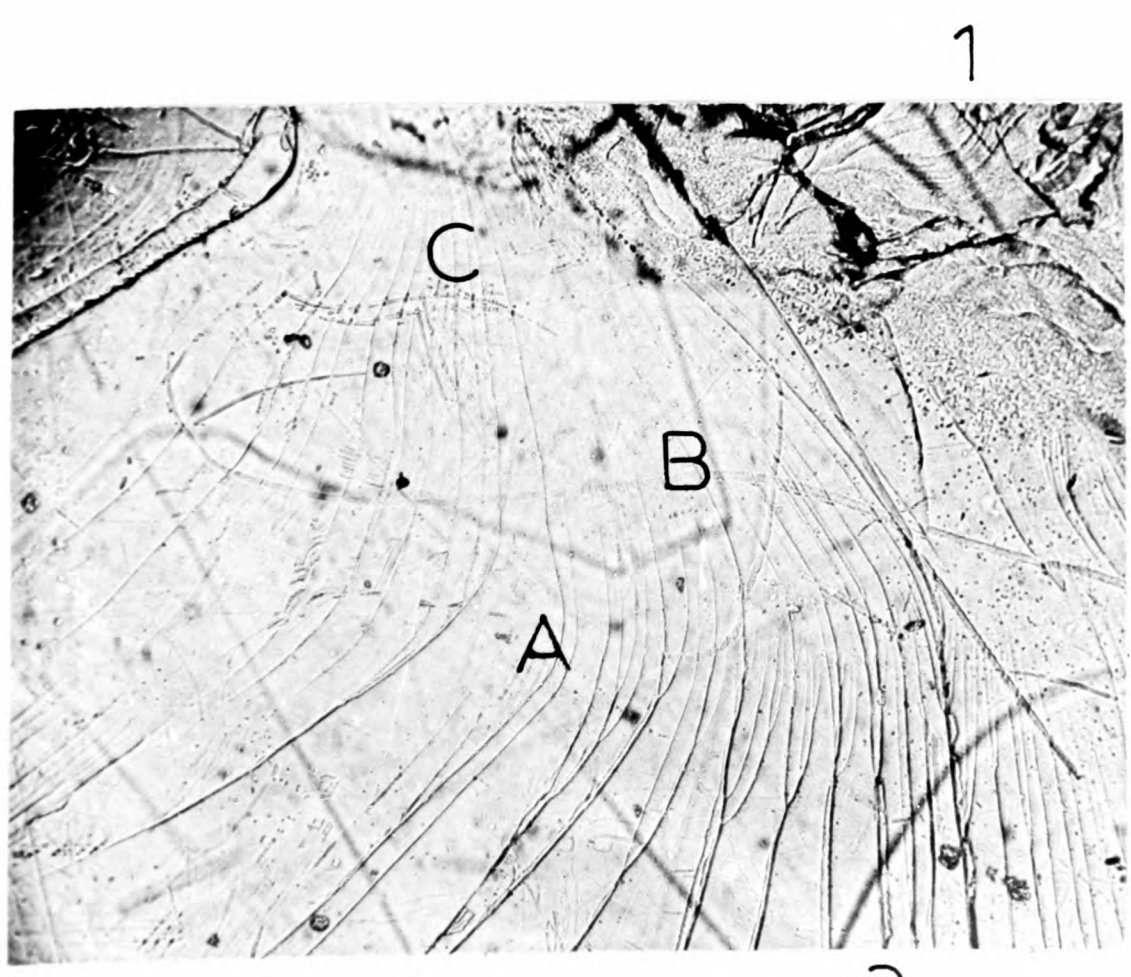
Dislocations, nearly pure edge in character, have been observed in natural fluorite by X-ray topography. Burgers vectors parallel to $\langle 101 \rangle$ have been identified.

An explanation of the origin of birefringence in fluorite has been given in terms of the stress produced by dislocations and also the effect of impurity atoms. In terms of impurities sited between the $\{111\}$ planes during growth and distorting the lattice normal to these faces, the birefringence boundaries not visible in the X-ray topographs may be accounted for. The planar defects, with an effective fault vector normal to the defect and a non-integral value of the lattice spacing, are postulated to be thin lamellae of material with a markedly different impurity concentration.

FIG 6.9



(a)



(b)

C H A P T E R VII

STUDY OF VAPOUR GROWN LAYER COMPOUNDS BY X-RAY TOPOGRAPHY

1. Introduction

The di-sulphides, di-selenides and di-tellurides of tin, titanium, zirconium and hafnium are isomorphous members of a group of layer-compounds crystallising with the cadmium iodide structure. This structure is formed by superposition of composite layers, each consisting of a sheet of metal atoms sandwiched between two sheets of calcogenide atoms. Each metal atom is surrounded symmetrically by six calcogenide atoms at the corners of an octahedron and the entire structure is built up by the superposition of layers in identical orientation. It may be described in terms of the simple hexagonal unit cell.

The stacking sequence then, is : BAB:BAB where B is the sulphur, selenium or tellurium atom and A is the metal atom. Adjacent layers are held together only by weak van der Waal's forces, as primary valency is satisfied within the :BAB: sandwich. One then finds that the crystals grow in thin plates, with extended growth perpendicular to the C axis. Marked cleavage occurs parallel to the growth plane of these crystals.

2. Crystal Growth

The crystals studied were grown by Mr. H.P.B. Rimmington and Dr. A.A. Balchin of Brighton Polytechnic. While the author

had no part in the crystal growth, it is felt pertinent to include here a brief description of the growth procedure.

The technique used was that of vapour transport, (Scheffer, 1964), using iodine as the transporting agent. Stoichiometric quantities of the pure elements were placed in quartz ampoules, together with a small quantity of iodine. (The iodine concentration was arranged to be about 5 gram ρ^{-1} of the ampoule volume.) Volatile impurities were removed from the ampoules by heating before the reagents were introduced, and the ampoules were sealed at a pressure of 10^{-5} Torr at liquid nitrogen temperature.

Crystal growth took place in a two zone furnace. The temperature of each zone could be controlled separately and was maintained constant to within 1^{o} C. The temperature gradient between the two zones was found to be almost linear. Ampoules were placed in the centre of the furnace with the charged end nearer the high temperature zone. Growth conditions corresponding to the compounds studied by X-ray topography are given in Table 7.1. [Some lattice parameters are taken from Rimmington and Balchin (1971).] When removed from the furnace, the ampoule was cooled by a jet of water directed towards the empty region of the ampoule, in order to condense the iodine away from the crystals. Care was taken not to tilt the ampoule, thus not subjecting the crystal to thermal or mechanical shock. The ampoule, when cool, was opened and the crystals washed in alcohol.

Table 7.1

Growth Conditions

Material	Lattice Parameter Å	Colour	Growth Temp. °C	Growth Time (hours)
SnS_2	a = 3.645 c = 5.889	Transparent yellow	680 - 620	8
$SnSe_2$	a = 3.807 c = 6.130	Metallic black	650 - 610	12
ZrS_2	a = 3.667 c = 5.818	Deep red to metallic black	900 - 820	500
TiS_2	a = 3.410 c = 5.690	Metallic gold	800 - 720	500
$TiSe_2$	a = 3.535 c = 6.004	Metallic bronze	780 - 740	500
HfS_2	a = 3.623 c = 5.842	Transparent, red	1010 - 1000	1000

3. Electrical Properties

While little work has been done on the electrical properties of the metal di-calcogenides, what has been done has revealed some extremely interesting features. The crystals are highly anisotropic with respect to optical and electrical properties

and while carrying out experiments to investigate the conduction mechanism parallel to the C axis, it was discovered that SnS_2 and ZrS_2, at least, exhibited distinct negative resistance, and current controlled switching behaviour, (Lee, Said and Davis, 1969). The material shows an ohmic region at low current, becoming non-linear up to a maximum voltage, V_{max}. Above this, increase in current results in a region of negative resistance. Application of a voltage pulse above V_{max} results in an irreversible reduction of resistance by up to six orders of magnitude. The low resistance state is restored by applying a further pulse which is considerably less than V_{max}.

Several mechanisms have been suggested to explain switching phenomena. In the amorphous glass devices, (Ovshinsky, 1968), it has been suggested that rapid heating and slow cooling of a filament is responsible. A different explanation has been given for the switching observed in ZnS and amorphous SiO films, (Simmons and Verdeber, 1967). It is assumed that the electrode material diffuses into the switching material and remains unionised in the high resistance state. At high fields, due to impact ionisation, the conduction band is effectively moved below the Fermi level and providing the specimen is thin, current flow takes place by tunnelling.

Neither of these theories explains the behaviour of the layer compounds, as the first should not enable the low resistance state to be maintained at zero current, and the second predicts that the resistance in the low resistance state shall be temperature independent, contrary to observation. The most attractive theory is that of Mott, (1969). In the

discussion of conduction in amorphous materials, he shows that movement of electrons between localised states may lead to a hopping mechanism, with a mobility of the form:

$$\mu = \mu_0 e^{-E/kT} \quad . \tag{7.1}$$

Measured mobilities along the C axis of SnS_2, (Gowers, 1968) are observed to obey this relation. Further measurements of the a.c. conductivity also support this theory.

However, no satisfactory explanation for the phenomena has been given and it was felt to be important that the crystal perfection be investigated. While it may seem improbable that crystal defects should play a major part in the switching phenomena, this possibility must be considered. Etch pit studies indicated that the dislocation density was certainly below 10^4 lines/cm^2, and as the crystals grow in plates typically a few tens of microns thick and several millimetres square, X-ray topography seemed an ideal method of study.

4. Experimental Details

Topographs were taken using CuKα and CuKβ radiation in the thinner specimens and MoKα in the thicker ones. Table 7.2 shows the absorption coefficients for the compounds studied and the maximum thickness in which good direct images would be expected. In general, CuKα radiation was preferable as the narrower image widths enabled individual dislocations to be resolved at higher dislocation densities than with MoKα radiation.

As exposure times were only of the order of 20 minutes

Table 7.2

Absorption Coefficients

Material	μ (cm^{-1})		Thickness μm $\mu t = 1$	
	CuKα	MoKα	CuKα	MoKα
SnS_2	900	111	11	90
$SnSe_2$	950	340	10	30
ZrS_2 *	600	70	16	140
TiS_2 *	570	64	18	160
$TiSe_2$ *	640	250	15	40
HfS_2 *	580	300	17	33

* Densities not readily available. Estimate, circa 4g/cc.

when using Nuclear L 4 plates, and the Elliott GX6 generator, vacuum 'L' grease was found to be suitable for mounting specimens. In the few instances where the Elliott GX6 generator was not used, and long exposure times were required, Araldite was used as an adhesive. The effect of mounting on the crystals is discussed later.

Some of the crystals examined contained a considerable amount of elastic strain, and in several cases, the Lang technique proved to be too sensitive to orientation. For example, in HfS_2, only very small areas exactly satisfying the reflecting position gave appreciable intensity. Attempts to use the wide beam method of Dionne, described in Chapter II, also proved

unsuccessful. A feature of this technique not often stressed is that while it is extremely easy to set the crystal in the horizontal plane, it is very difficult to orient the reciprocal lattice vector in the vertical plane. In a bent specimen containing several subgrains, each of which has the reciprocal lattice vector making a slight angle to the horizontal, it is difficult to obtain good contrast for any one grain. The wide beam samples intensity from all subgrains and the position of maximum intensity is often not the position for good defect contrast from any one grain. Though one is obtaining the largest average X-ray flux reaching the counter, it is often the case that all the g vectors are slightly inclined, no one being exactly set horizontal. One way to avoid this is to set up the wide beam method using a very narrow slit. This then still has the advantage of a wide rocking curve, but as the beam can then sample only one grain, the sensitivity in the vertical direction is greatly improved. The other way is to modify the wide beam technique to use a small focus and scan the crystal and film as in the Lang technique.

Figure 7.1 shows a diagram of the arrangement using a divergent beam. It is useful in that the only modification between this technique and Lang's technique is use of a wide slit. The two techniques may be used in conjunction with one another simply by interchanging slits and without disturbing the crystal, which will remain oriented at the exact Bragg angle for either technique. To avoid double reflections, one must use the Kβ radiation and to view the entire crystal the crystal and film must be scanned across the entire crystal.

FIG 7.1

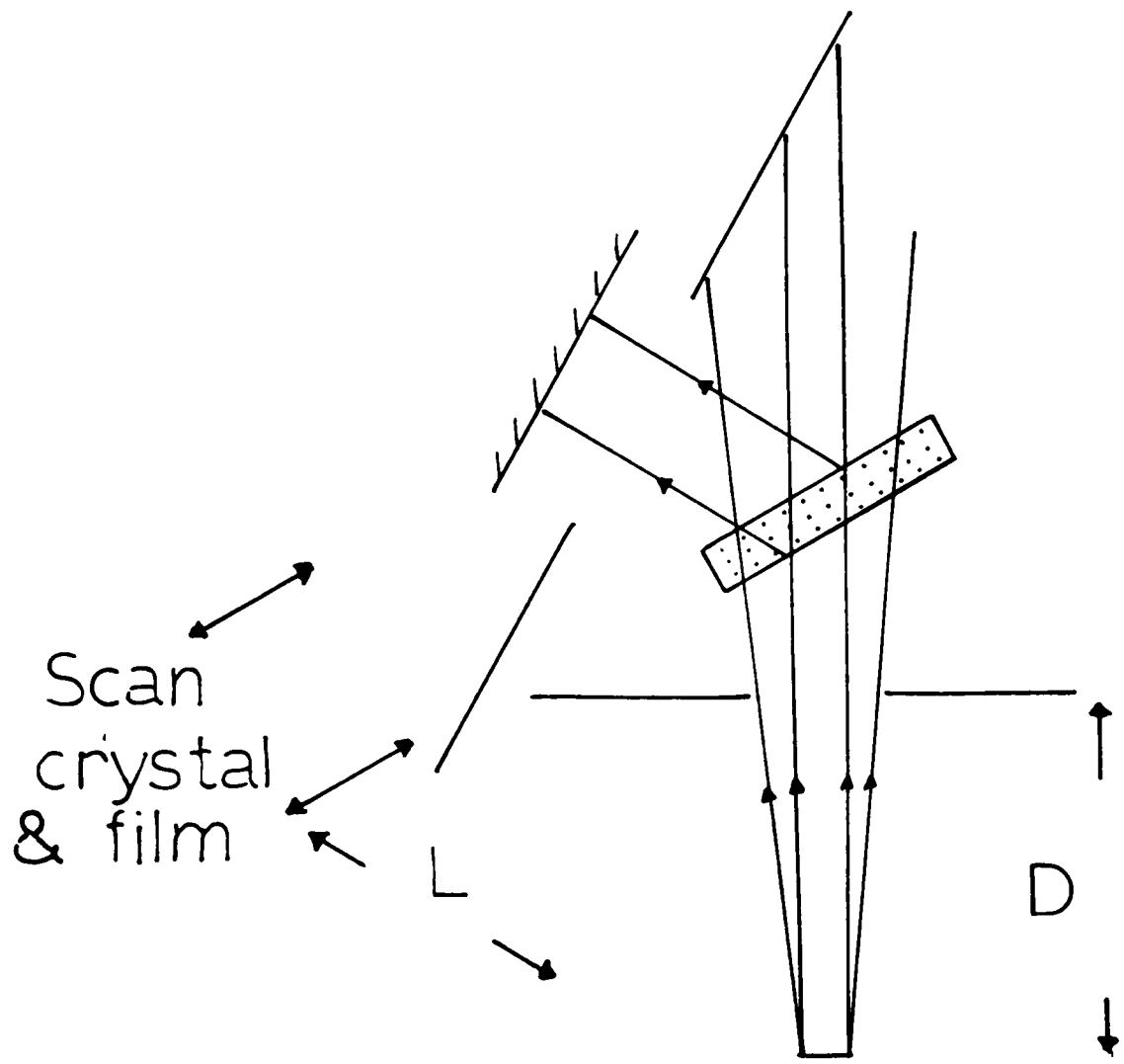


FIG 7.3

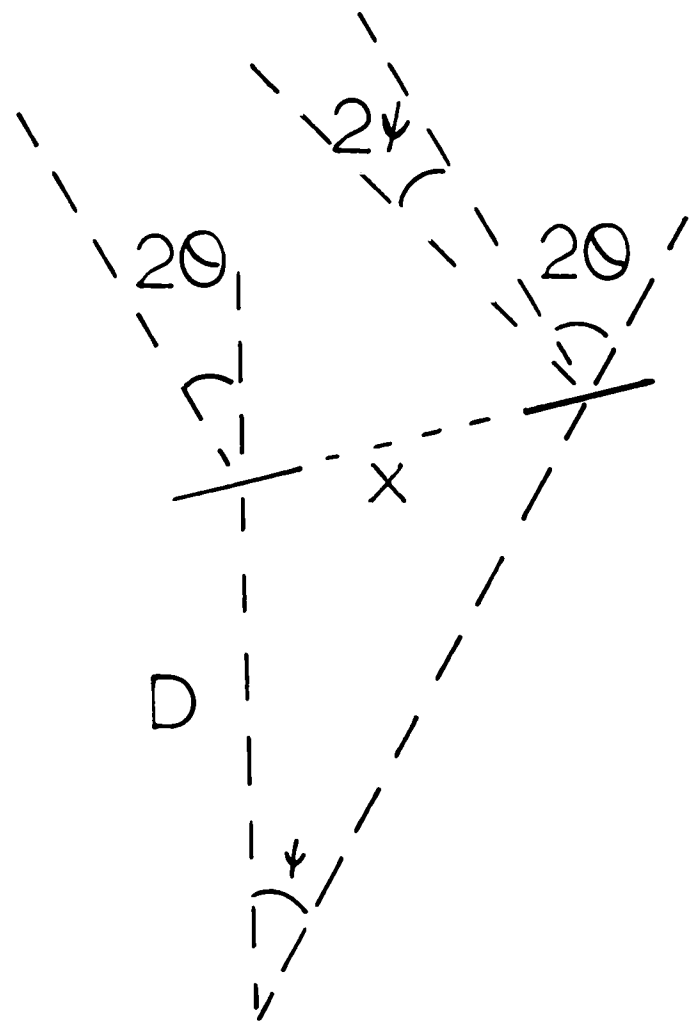
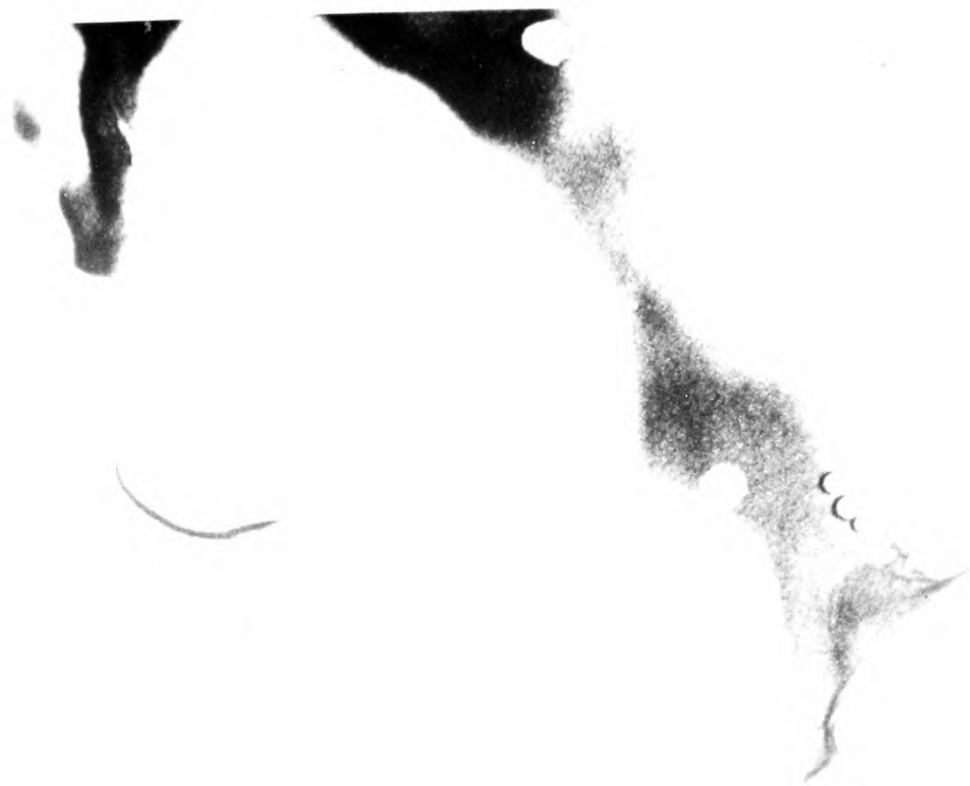


FIG 7.2



(a)

[11$\bar{2}$0]



(b)

1 mm

HfS_2

Exposure times are 5 times that of the Lang technique due to the low intensity of the Kβ line, but this is offset, when using the Elliott GX6 generator, by the fact that if only one camera is being used, no rearranging of the apparatus is necessary except for the trivial procedure of interchanging slits. Following the conclusions of Chapter II, the images observed are almost identical to those of Lang's technique, except for the loss of visibility due to scatter. It was found that using a point source and scanning, rather than a stationary wide source, the scatter from the collimator and slit received on the film was reduced to negligible proportions. Figure 7.2(a) shows a topograph of HfS_2 taken using Lang's technique, and Fig. 7.2(b) the same specimen using the scanning divergent beam method. While with Lang's technique the area viewed was too small to be useful, the divergent beam method produces contrast from an area large enough for a general impression of the crystal perfection to be obtained. The minimum necessary width of the diffracted beam slits is related to the divergence of the beam and the angle the crystal is bent through. As shown in Fig. 7.3, if two regions of the crystal are mis-oriented by an angle ψ , the mis-oriented region will give a strong reflection at a position such that the rays coming from the source satisfy the exact Bragg condition. This position is displaced D sin ψ from the position of reflection in the non-misoriented region. The diffracted beam will also make an angle 2ψ with the diffracted beam from the unbent region.

Thus, the net shift in image position will be:

$$y = D \sin \psi \cos\theta_B + L \sin 2\psi \qquad (7.2)$$

Now ψ will not be greater than $\frac{1}{2}^{o}$ or so, then $\sin\psi \approx 0.01$ and we can neglect the second term. Taking D = 50 cm, we find that the diffracted beam slits are required to be about 5 mm wide to enable diffracted images from this sort of angular bending in the crystal to be recorded. It should be noted that some distortion of the images in the horizontal direction will occur.

It is not suggested that this technique has any new advantages for general applicability. It has proved useful in particular circumstances, and in cases such as this, when setting up times are of the same order as exposure times, there are definite advantages in not having to change cameras. The difficulty of setting up the distorted crystal in the wide beam technique is eliminated and a further advantage is that the background scatter is much less than with a line source. Reduction of the specimen to source length is not practical, as in most cases this would lead to an intolerable vertical resolution.

5. Defect Configurations in Layer Compounds

(a) Tin di-sulphide

Figure 7.4 shows a set of topographs taken using the Lang technique, of a specimen of SnS_2. A large area, of approximately 1 mm square, exists completely free from defects. At the edge of the grain, the defect density is very high and individual dislocations cannot be resolved. Between the perfect and

FIG 7.4

imperfect regions, several dislocations are clearly resolved. The dislocations, A, may be seen to vanish in the $10\bar{1}0$ reflection and, as may be seen in Fig. 7.5, also vanish in the $10\bar{1}1$ reflection. The Burgers vector of these dislocations with reference to the stereographic projection of Fig. 7.6, is seen to be along $[1\bar{2}10]$. The length of the vector is presumed to be an atomic spacing in this direction. Such considerations applied to the other dislocations yield similar results. These dislocations, varying from screw to edge orientation along their length would appear to be similar to the undissociated dislocations observed using the transmission electron microscope in MoS_2, (Amelinckx and Delavignette, 1962).

It is important to make clear that it is not possible to determine whether these are perfect or dissociated dislocations. The contrast on the X-ray topographs is due to the net strain field, as is shown in Chapter V. For small splittings (that is, less than about a micron) perfect and dissociated dislocations would give similar contrast in the topographs.

The dislocations whose slip plane is the crystal plane, (0001), appear to have started at the grain boundary and glided inwards towards the centre. It was not clear at this stage whether the dislocations were produced during growth or from subsequent handling. As will be shown later, the indications are that they were generated in handling.

The radius of curvature of the dislocations marked 'A' is nearly 500 μm. Now the stress acting on a bowed out dislocation is given by :-

$$\sigma \approx \frac{\mu b}{R} \qquad (7.3)$$

FIG 7.5

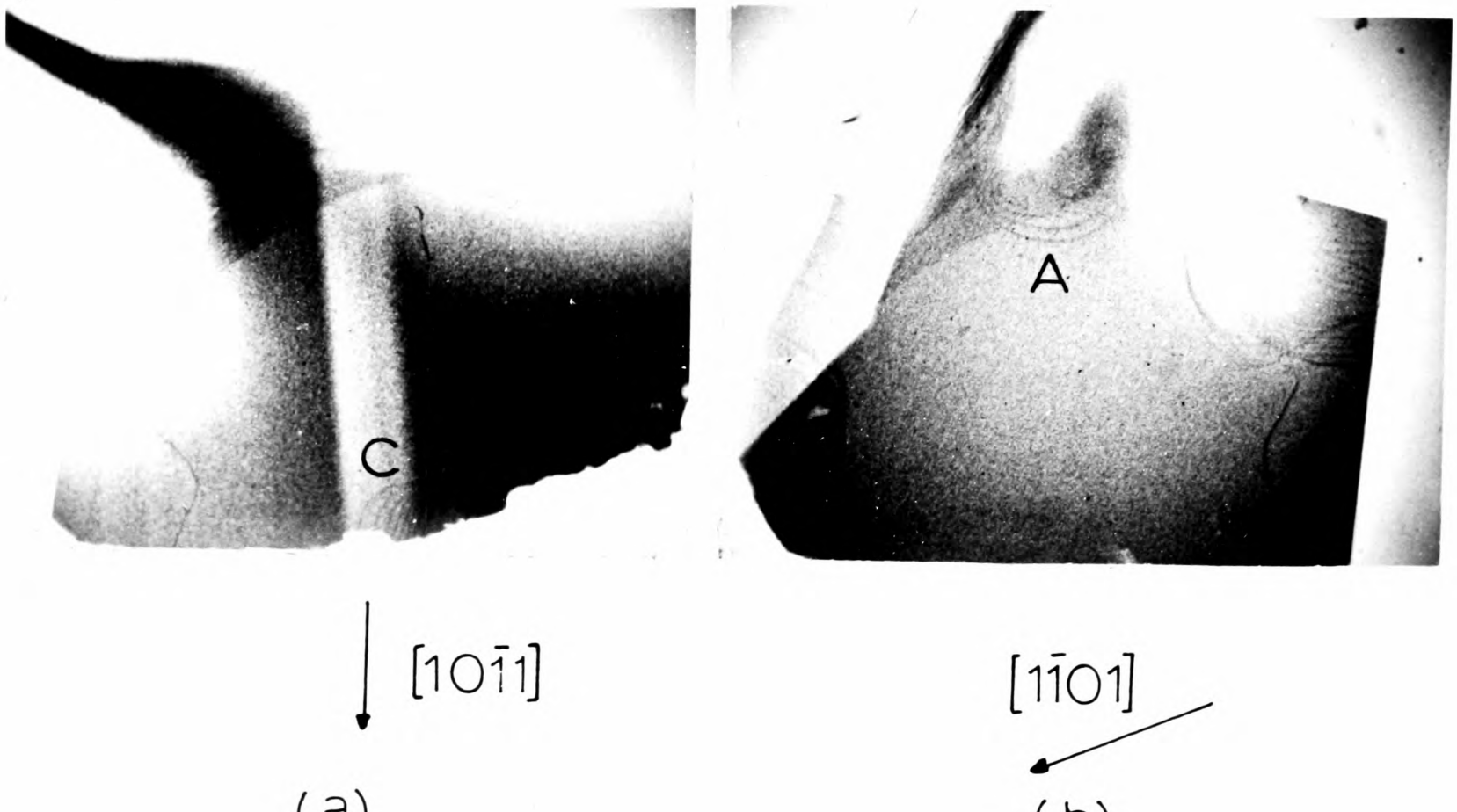
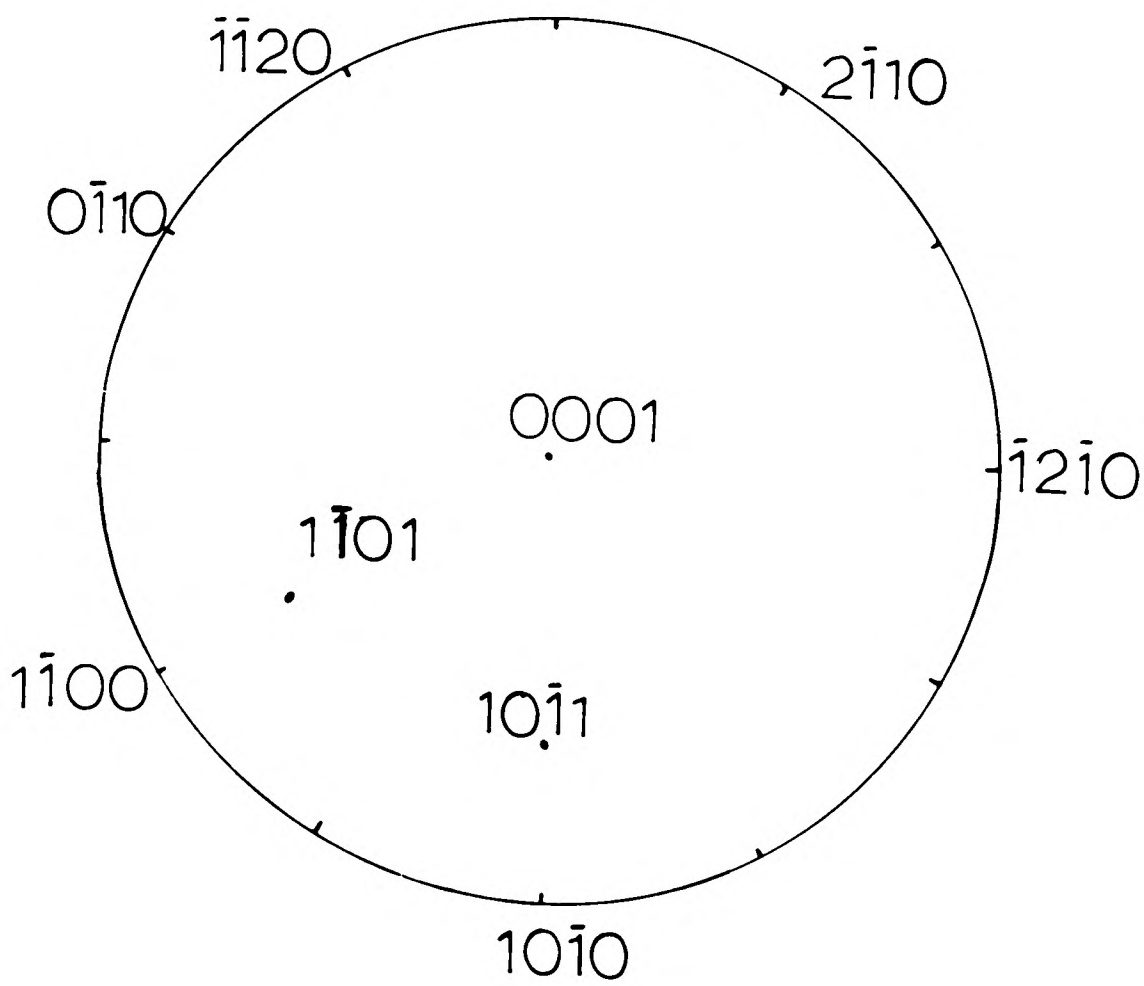

C
A
[10$\bar{1}\bar{1}$]
[1$\bar{1}$01]
(a)
(b)

FIG 7.6


$\bar{1}\bar{1}$20
2$\bar{1}$10
0$\bar{1}$10
0001
$\bar{1}$2$\bar{1}$0
1$\bar{1}$01
1$\bar{1}$00
10$\bar{1}$1
10$\bar{1}$0

where μ is the shear modulus, b, the magnitude of the Burgers vector and R is the radius of curvature, (Friedel, 1964).

Values of μ are not readily available, but may be assumed to be of the order of 10^{11} dynes/cm^2. Then :-

$$\sigma \approx \mu \times 10^{-6} \approx 10^{5} \text{ dynes/cm}^2.$$

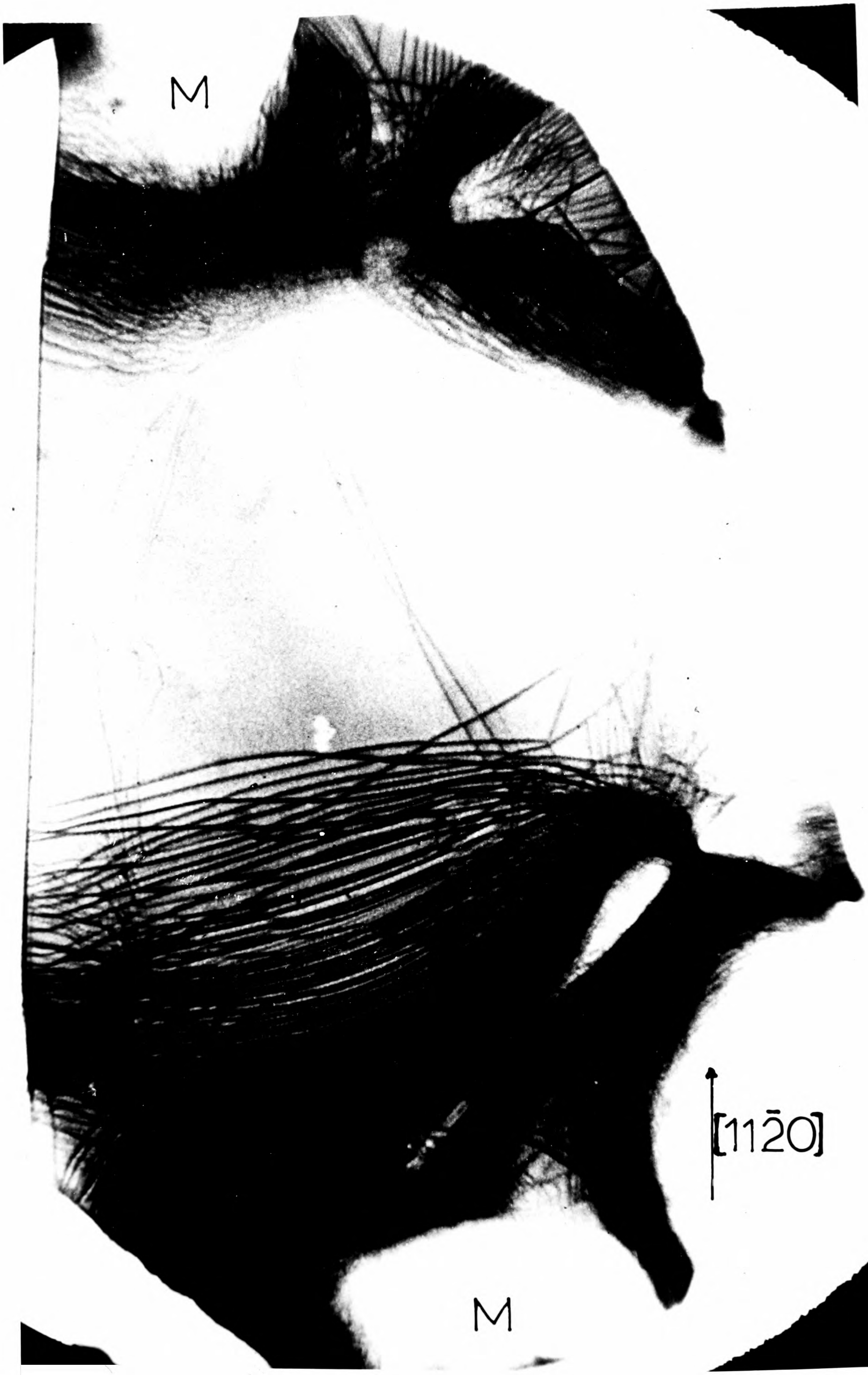
For a simple cantilever of cross section, A, loaded with weight, W,

$$\sigma = \frac{W}{A} \qquad (7.4)$$

To an order of magnitude this may be taken as the lower limit of the yield stress. Thus, for a specimen 20 μm thick and 2 mm broad, one finds that loads greater than about 40 mg applied to one end might be expected to cause plastic deformation. Evidence for this extreme fragility is presented in Fig. 7.5. The array of dislocations marked C in Fig. 7.5(a) was nucleated between the time of taking the topographs of Fig. 7.4 and those of Fig. 7.5. In the $1\bar{1}01$ reflection, this array is absent, indicating that the Burgers vector is along $[11\bar{2}0]$. It is believed that these dislocations arose through the specimen being accidently knocked by the diffracted beam slits while the experiment was being set up.

Further evidence to support the explanation that these defects arose from handling is given in Fig. 7.7. This $11\bar{2}0$ topograph of an SnS_2 specimen mounted with vacuum grease at each end, M. The central region is nearly perfect, but large arrays are seen to originate near the mounted edges. No

FIG 7.7



dislocation interactions could be observed in the arrays. The specimen shown in Fig. 7.8 would seem to provide more conclusive evidence. This specimen was carefully mounted with vacuum grease at the top right-hand corner only. Surrounding the grease is an area of considerable bending, which shows up white in the topographs, as no X-rays are diffracted from this region, and an array of dislocations extending into the crystal. This array contains two families of dislocations, one set with Burgers vector along $[\bar{2}110]$ which vanish in the $01\bar{1}0$ reflection, and the other set with Burgers vector along $[11\bar{2}0]$, which vanish in the $1\bar{1}00$ reflection. There seems little doubt that these dislocations were produced by bending when mounted. It seems most probable that all the $\langle 11\bar{2}0 \rangle$ type dislocations were produced after growth.

The other type of dislocation seen is of considerable interest. These are the long, straight dislocations, lying in many cases along crystallographic directions. They do not appear to have been generated in handling. As seen in Fig. 7.8, they are either invisible or exhibit only residual contrast in one of the $11\bar{2}0$ reflections, indicating that these are partial dislocations with Burgers vector along $\langle 1\bar{1}00 \rangle$. In the $1\bar{1}00$ type reflection, Fig. 7.9, stacking faults are observed bounded by these dislocations. No stacking fault is visible in any of the $11\bar{2}0$ reflections and all faults are visible in the $1\bar{1}00$ reflections. The fault vector is then consistent with $\frac{1}{3}\langle 1\bar{1}00 \rangle$. This is exactly what one would expect from such faults bounded by $\frac{1}{3}\langle 1\bar{1}00 \rangle$ partials. Reference to Fig. 7.10 indicates that the stacking fault arises from glide

FIG 7.8



FIG 7.9

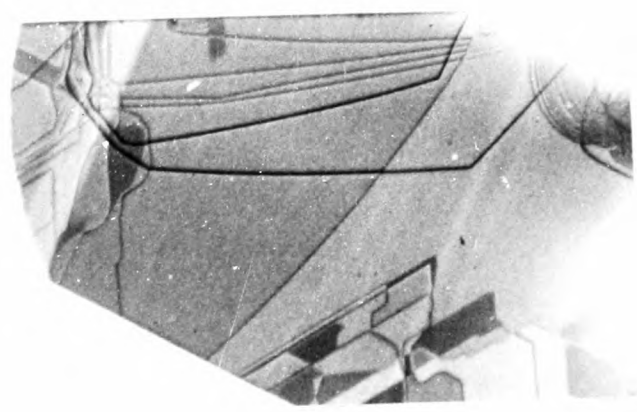
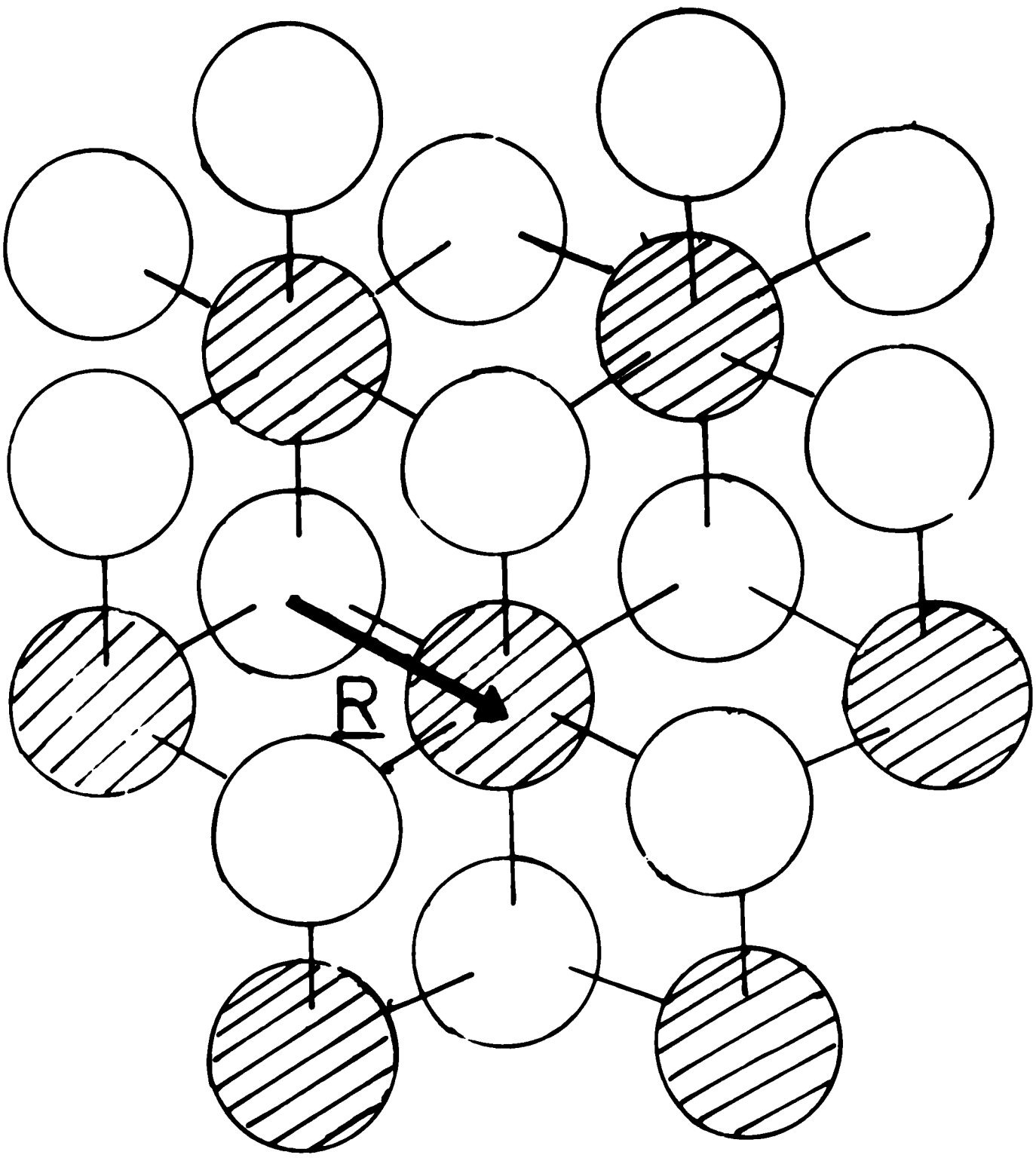


FIG 7.10



Stacking : BA'B" : BA'B" :

Faulted : BA'B" : B'A"B :

of the weakly bound S - Sn - S sandwich layers over one another. Normal stacking is a direct superposition of layers B'Aβ:B'Aβ. If in stacking, the sulphur atom is sited above the tin atom, the stacking sequence becomes B'Aβ: BαB':BαB': and a fault with vector $\frac{1}{3}\langle 1\bar{1}00\rangle$ is produced. Due to the weak bonding between layers, the fault is expected to have a low energy.

Amelinckx and Delavignette (1962) reported two types of $\frac{1}{3}\langle 1\bar{1}00\rangle$ stacking fault in molybdenum sulphide. One fault with low energy was assigned the stacking sequence similar to that described here, i.e., glide of two layers over one another, but to account for the extremely low energy faults, it was necessary to postulate that more than two layers were involved in the fault. However, the cadmium iodide structure and molybdenum sulphide structure, though similar, have an important difference. In MoS_2, the metal atom is surrounded by six sulphur atoms arranged at the corner of a trigonal prism and the stacking is such that two layers are required in the unit cell, (Evans, 1966). Thus, in MoS_2, a number of stacking sequences can be devised for the fault if several layers are considered, but this is not the case with the cadmium iodide structure. Because of the very simple stacking, i.e., direct superposition, only one fault is permissible.

The origin of these faults is not immediately clear. Even though the stacking fault energy is low, these faults are several hundred microns square and thus considerable energy will be associated with them. They are certainly associated with the growth process. Except where interactions have taken

place, the faults lie near the crystal edges, and are bounded by a loop of dislocation, the Burgers vector of which is necessarily the same all round, (vide: fault marked 'X' in Figs. 7.8 and 7.9). This eliminates the possibility that the faults arose from a dissociation of a perfect dislocation. Dissociation is favourable, but the perfect dislocation will not dissociate into two partials of opposite sign. Two possibilities remain; either that the faults are formed by the partials sweeping them out as they glide in the crystal, or that the faults are formed during growth, as growth islands. The former suggestion is a little unattractive, as in this case some kind of stress is required to expand the loops. This could conceivably occur from the crystal edge during growth, but it is then surprising that mobile partials should lie along crystallographic directions over such large distances. In contrast, the dislocations nucleated by stresses when handling do not have any crystallographic orientation.

A much more attractive explanation would seem to be that the faults occurred during growth from several points. The energy required during growth to misplace, for some reason, a SnS_2 molecule on a completed layer will not be extremely high. As the primary valency in this completed layer is satisfied, the stacking of further molecules will be influenced by the misplaced molecule rather than by the original substrate. Islands of stacking fault, bounded by partial dislocations will then be formed when growth islands have enlarged enough to meet. This mechanism which is analogous to the formation of faults in epitaxial silicon layers, would also account for

the crystallographic nature of the partials.

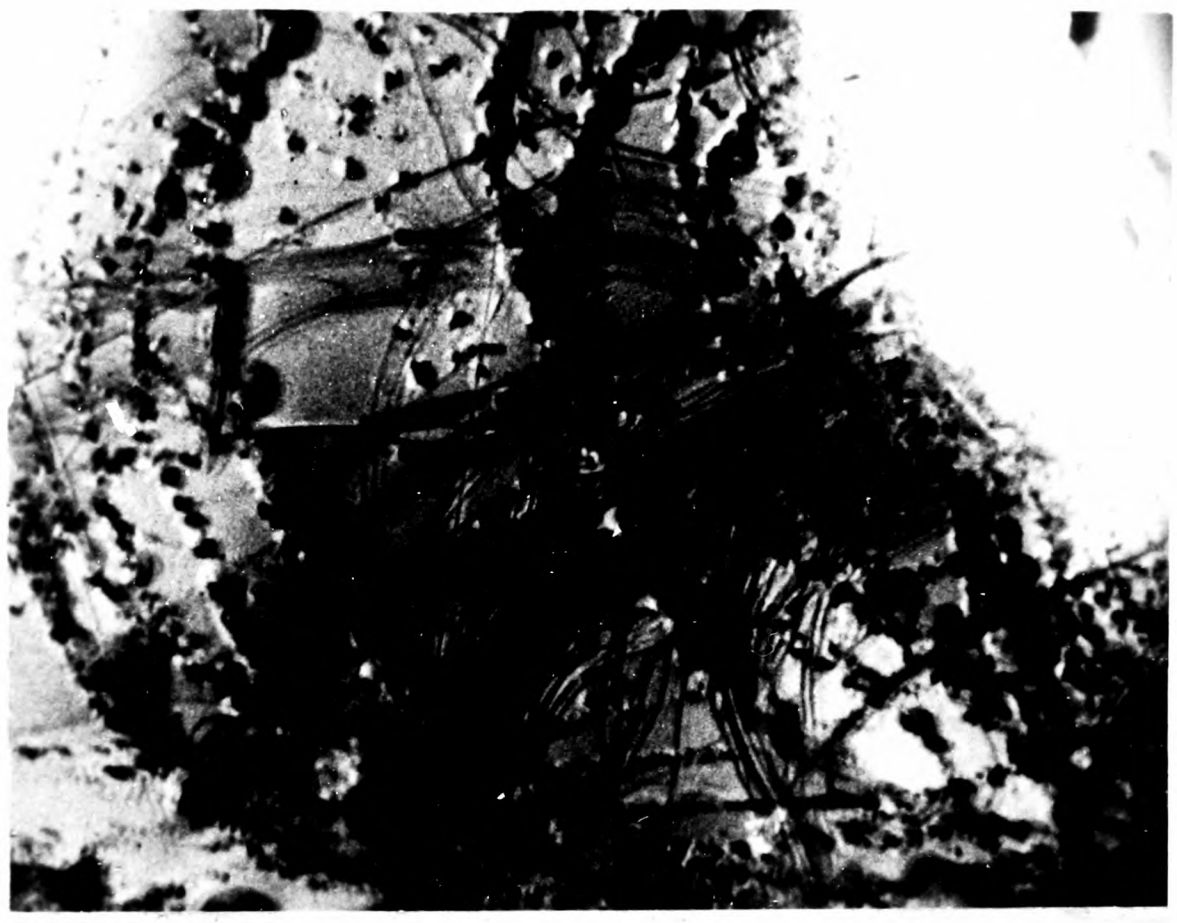
(b) Tin Di-Selenide

Figure 7.11(a) shows a typical area of the $SnSe_2$ samples studied. Large areas free from dislocations are observed, but the specimens are full of precipitates, typically 20-50 μm across, which may be seen on the surface of the specimen under the optical microscope, Fig. 7.11(b). These precipitates are seen to interact with the dislocations in the specimens, in some places dislocations can be seen to bow right round the precipitates.

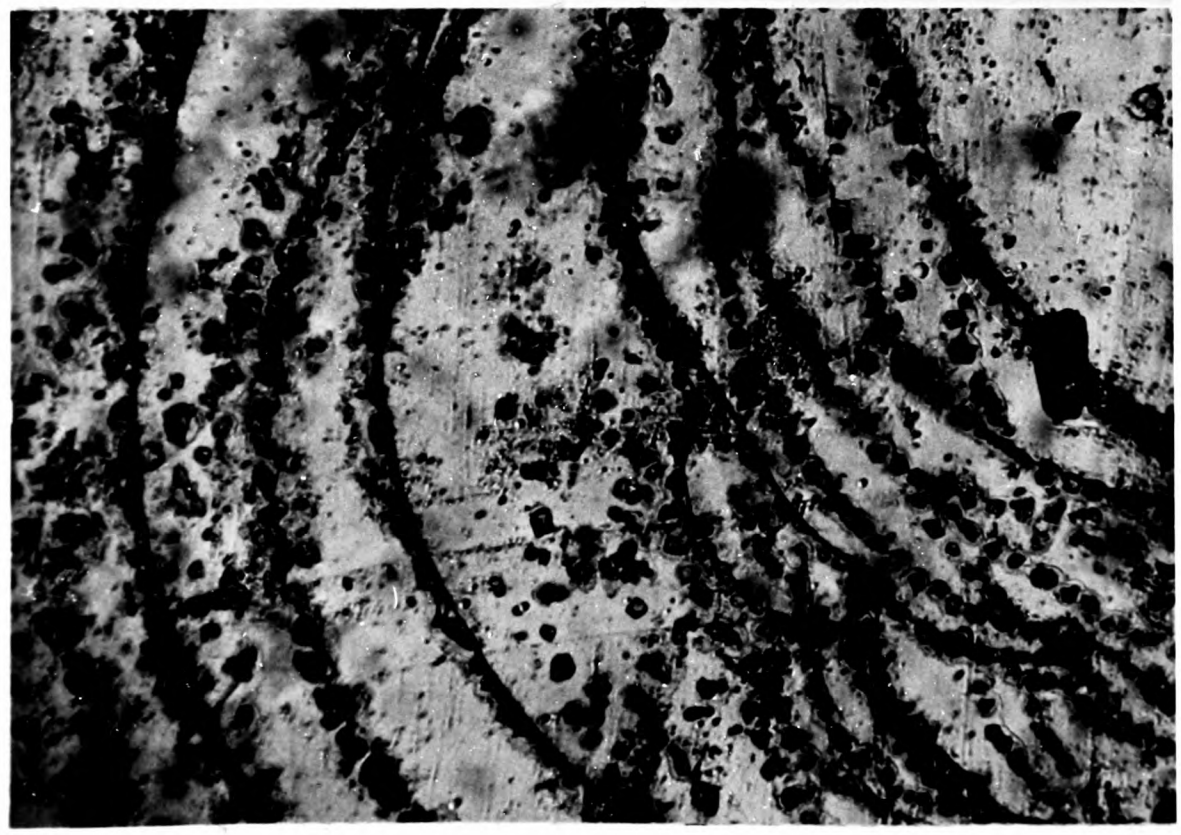
In an attempt to determine the nature of these precipitates, use was made of the Cameca Electron Microprobe analyser. It was thought that the precipitates might be SnI_2 and consequently the flux of fluorescent X-rays with wavelengths corresponding to the Kα lines of these elements was monitored. Results of the analysis for tin are shown in Table 7.3 and those for iodine in Table 7.4. It is clear that while the precipitates are richer in iodine than the surrounding matrix, the concentration is too low by an order of magnitude for the precipitates to be SnI_2.

Considerable drift occurred in the microprobe analyser and also the concentrations of elements varied in different parts of the specimen. However, as readings were taken in pairs, one from the matrix and one from a precipitate, a significant difference in concentration was detected. This was also well outside the statistical error.

FIG 7.11



(a)



(b)

500 μ

$[11\bar{2}0]$

Table 7.3

Tin Analysis

Standard 92820 cps

Matrix	Precipitate	Ratio
30730 ± 180 cps	48650 ± 250 cps	1.6 ± 1 %
33210 ± 180 cps	48460 ± 250 cps	1.5
37720 ± 200 cps	50220 ± 250 cps	1.35
39520 ± 200 cps	48460 ± 250 cps	1.25

Table 7.4

Iodine Analysis

Standard 23900 cps

Matrix	Precipitate	Ratio
1495 cps ± 40	2031 cps ± 40	1.35 ± 4 %
1486 cps ± 40	2330 cps ± 50	1.55
1161 cps ± 30	1437 cps	1.25

The nature of these precipitates is still undetermined but it is seen from the electron probe microanalysis that the precipitates are richer in iodine and tin than the surrounding matrix. It is possible that the precipitates are of SnSe with a nucleus of SnI_2. Use of the energy dispersive system in the scanning electron microscope and possibly removal of a

single precipitate granule for transmission electron microscope analysis might help to provide more information about these defects.

(c) Titanium Sulphide

These crystals were much less perfect, Fig. 7.12, showing a typical example. The dislocation density was estimated to be about 10^3 lines/cm^2, but because of the widths of the dislocation lines, this was near the resolution limit of the X-ray technique. The specimens were so imperfect that it was very difficult to produce good dislocation images with the more strain sensitive MoKα radiation. The strain gradients were such that interbranch scattering took place in the matrix, completely obscuring detail. Much more detailed micrographs were obtainable using CuKα radiation.

(d) Zirconium and Hafnium Sulphides

These crystals, though containing large areas free from dislocations were rather distorted and due to this elastic strain it was necessary to use the divergent beam technique previously described. A micrograph of HfS_2 has already been shown, Fig. 7.2, and it may be seen from Fig. 7.13 that zirconium sulphide has quite a similar configuration of dislocations. Titanium selenide was even more distorted than the HfS_2 and ZrS_2 crystals, amd although dislocations were resolved, little could be determined about their distribution.

FIG 7.12



TiS_2

$[11\bar{2}0]$

FIG 7.13



1 mm

ZrS_2

6. Conclusion

Using X-ray topography, it has been demonstrated that very nearly perfect crystals of layer compounds may be grown by the iodine vapour transport technique. In particular, tin sulphide, which is easy and quick to grow, and in which switching effects have been observed may have large areas free from dislocations. These crystals are extremely fragile, and it has been shown that dislocations are easily introduced in handling. There are two types of dislocations observed, undissociated dislocations of Burgers vector along $\langle 11\bar{2}0 \rangle$ produced in handling and partial dislocations of Burgers vector $\frac{1}{3} \langle 1\bar{1}00 \rangle$ which would seem to be associated with the growth process. These latter are associated with large area stacking faults. It will be of considerable interest to make a detailed study of switching behaviour as a function of defect concentration and distribution. With refined technique, using X-ray topography as a monitoring routine, it is thought that the perfection of the other layer compounds may also be considerably improved.

Summary

Using X-ray topography, individual dislocations have been observed in the layer compounds, tin and titanium selenide and tin, titanium, zirconium and hafnium sulphides grown by iodine vapour transport. The Burgers vectors of the dislocations in tin sulphide were determined and the nature of these defects discussed. Speculations were also made on the origin of the

faulted partial dislocation loops observed. The dislocation configuration in the other layer compounds were described and a modified divergent beam method for taking X-ray topographs of bent crystals was demonstrated.

C H A P T E R VIII

PRELIMINARY X-RAY STUDIES OF IRON SINGLE CRYSTALS GROWN BY THE STRAIN-ANNEAL METHOD

1. Introduction

While few X-ray topographic studies have been reported on metal crystals, even fewer have been concerned with body centred cubic materials. The work of Pegel and Becker on molybdenum stands out as the only good deformation work on b.c.c. metals. In their experiments they observed dislocation helices which collapsed on deformation, (Pegel and Becker, 1969; Becker and Pegel, 1969). Similar experiments on niobium were unsuccessful owing to a high dislocation density in the as-grown crystal, (Miltat, 1971). Several studies have been made on iron-silicon alloys. Lang and Polcarova (1965) described the dislocation configuration of strain-anneal grown iron 1.5% silicon alloy. However, most of the work in this material has been in the study of the ferromagnetic domains, (Polcarova and Lang, 1962; Roessler et al.,1965; Roessler 1967; Kuriyama and McManus, 1968; Wu and Roessler, 1971; Schlenker and Kleman, 1971).

It has proved extremely difficult to prepare crystals of iron with low dislocation density. Spark-cutting introduced damage which penetrated through large regions of the crystal and a satisfactory method of acid-sawing has not yet been developed, (Polcarova, 1970). The crystals used here were 99.9% pure iron grown by the strain-anneal method in a flat

sheet about 10 thousandths to an inch thick. They were then chemically thinned to about 30 μm and this arrangement avoided introducing mechanical damage in the thinning procedure. Futagami (1971) has recently published a note reporting X-ray topographic contrast in crystals grown by a similar method, that of secondary re-crystallisation in a thin sheet.

The crystals described here were grown at the Birmingham University Metallurgy Department for Dr. D.E. Crutchley. Table 8.1 lists the impurity content. Material was rolled to between 11 and 14 thou.. The pre-anneal took place at 830°C for ½ hour and the crystals were then strained to 4%. Annealing was performed in a slow moving temperature gradient with the furnace at 830°C. The temperature gradient moved at a rate of 1 cm in 2 hours.

Table 8.1

Impurity content of Iron Crystals

Impurity	Concentration (weight %)
C	0.044
Mn	0.006
P	0.003
Cu	0.01
Ni	0.01
Al	0.001
O	0.004

The thinning was performed using a polishing solution containing:

8' grms oxalic acid
100 grms distilled water
5c.c. conc. H_2SO_4
1:1 with 100 vol H_2O_2

Dilute HCl to stop passivation.

2. Experimental results

No magnetic contrast could be identified in any of the specimens studied, and in several of the specimens it proved impossible to obtain an untarnished surface. Such tarnished crystals exhibited intense "blotchy" contrast, which may be ascribed to the surface damage. The two crystals on which a good surface was obtained, retained this surface for several months, and remain, at the time of writing, untarnished. All topographs shown were taken from these two crystals.

Dislocation images in iron taken using a 110 reflection and MoKα radiation are expected to be about 3 to 4 μm wide. Consequently, care was taken to ensure that the specimen-plate distance was small, in order that a good vertical resolution might be obtained. The contrast observed in the two specimens was rather different and will be discussed separately.

(a) Crystal 1

This specimen had been accidentally deformed in one region and was also considerably bent. It proved impossible to take repeat topographs with different reflections of the same area as a result of this bending. In this work, a Bragg angle controller of the type described by van Mellaert and Schwuttke (1970) or Hart (1971) would be invaluable. Wide beam topography was not attempted because of the large amount of fluorescent scatter from the iron when MoKα radiation is used.

As a result of this distortion it proved difficult to set up the crystal exactly on the $K\alpha_1$ peak. It is suggested

that the wide images seen in Fig. 8.1 arise from overlapping of the $MoK\alpha_1\alpha_2$ doublet. If this is true, it is reasonable to assume the contrast to be due to dislocations. What appear to be rows of loops and dislocation helices are observed, which are reminiscent of the dislocation configurations seen by Pegel and Becker with molybdenum. The intensity reflected from these defects is of the same order as that from the dislocations seen in crystal 2. Furthermore, near the deformed regions wide bands of enhanced contrast are observed, not lying along crystallographic directions and those may be the result of collapsing of the helices. It would be of great interest to study the deformation, to check if the mechanism of deformation in molybdenum also occurs in iron. At present, however, the contrast from what appears to be rows of loops and helices can only be tentatively ascribed to dislocations. Further experiments are in progress using $MoK\beta$ radiation in an attempt to sharpen up the images.

(b) Crystal 2

In this specimen, which was not deformed or bent, no contrast similar to that described above was observed. The specimen showed a 'Black Death' type contrast, intense black dots distributed throughout the specimen. These dots were typically 10 μm in diameter and are presumed to be produced by the strain associated with the production of oxide at localised spots. Alternatively, they could be small crystal defects. The density of these spots did not increase appreciably with time, which might support the second hypothesis. However, no positive identification has been

FIG 8.1



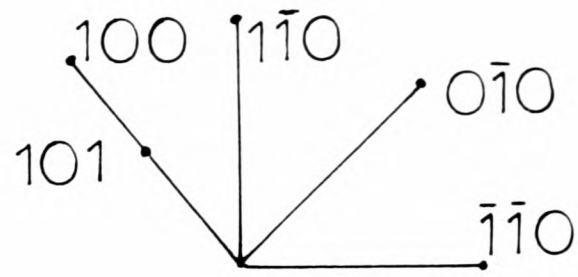
made. Two interesting arrays of defects are indicated at A and B in Fig. 8.2. These lines are roughly parallel to [100] and in array A, the image width is consistent with that expected from a dislocation line. The contrast of array B in the 110 reflection appears to be double, each broad line consisting of two lines of width similar to that in array A. The defects are absent in both 200 and 101 reflections and visible in $1\bar{1}0$ and 110, this contrast being consistent with that expected from a pure edge dislocation, with Burgers vector parallel to [010].

Since these topographs were taken, Futagami (1971) has published a note reporting similar arrays of defects in iron, grown in a flat sheet by the method of secondary recrystallisation, (Foster, Kramer and Wiener, 1963). While Futagami does not mention the point, the images in his micrograph are too wide to be ascribed to dislocations. They are, however, consistent with the width of the array B shown in the present topographs. No exact determination of the Burgers vectors was given in his paper but the arrays were ascribed to low angle boundaries containing pure edge dislocations on a {110} plane with ⟨100⟩ Burgers vector. Futagami showed that after annealing for a week, the arrays disappeared. This, added to the fact that the value of the magnetostration in the ⟨100⟩ directions is small, indicated that the contrast was not due to magnetic domains.

In the experiments carried out by the author and his colleague, the Burgers vector was unambiguously determined as parallel to [010] with the dislocation lying along [100].

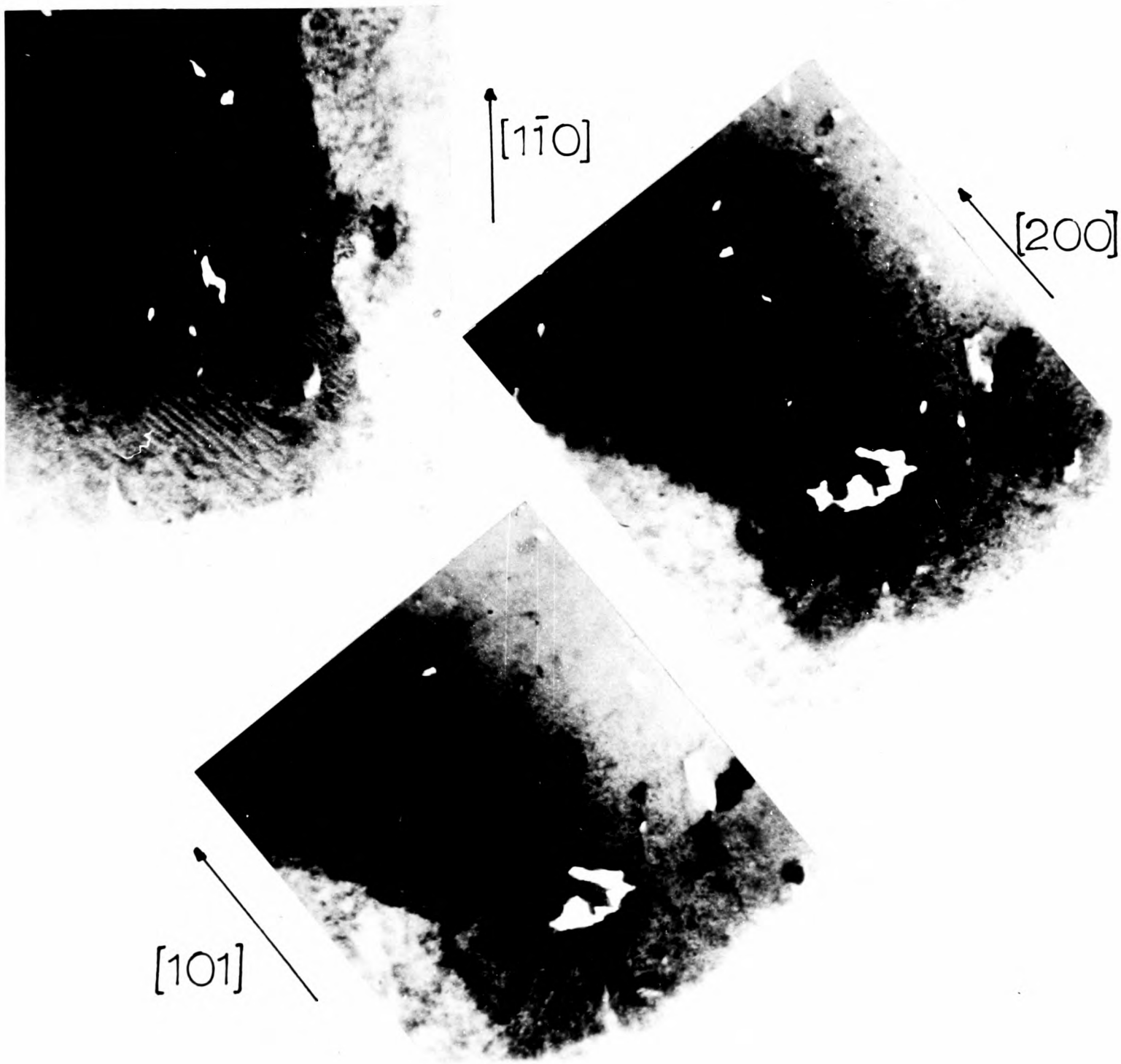
FIG 8.2





[110]

500 μm



This is consistent with the explanation of Futagami. Two perfect $\frac{a}{2}\langle 111\rangle$ Burgers vector dislocations react during the recrystalissation to form a low angle boundary, (Carrington, Hale and McLean, 1960).

$$\frac{a}{2}[\bar{1}11] + \frac{a}{2}[11\bar{1}] = a[010]$$

The dislocations lie along the [100] direction, this being the intersection of the (011) and $(01\bar{1})$ planes. The projected widths of the boundaries is consistent with this explanation.

According to the simple model of a low angle grain boundary, the dislocation spacing is constant, (Shockley and Read, 1949, 1950; Read, 1953), and the tilt angle across the boundary is given by :-

$$\phi \approx \frac{b}{\ell}$$

where b is the Burgers vector and ℓ is the spacing of the dislocations. The dislocations in array A are equi-spaced and are about 15 μm apart. This yields a tilt angle of 4 seconds, similar to that in Futagami's specimen.

The array B, which appears to contain pairs of dislocations is curious. Energy considerations show that the minimum energy configuration in a low angle boundary is when the dislocations are equally spaced. It must be concluded that the array B consists of two low angle boundaries on parallel and displaced planes. The tilt angle for each boundary is then between 2 and 3 seconds of arc.

3. Conclusions and Summary

Crystals of 99.9% pure iron, grown in a flat sheet by the strain-anneal method and chemically thinned may have a dislocation density low enough to resolve individual dislocations by X-ray topography. Evidence for the presence of dislocation helices and loops is presented and arrays of dislocations forming low angle boundaries are identified. The tilt angle of these is between 2 and 4 seconds of arc and the dislocations making up the boundary lie along [100] with a Burgers vector along [010]. This identification of Burgers vector confirms the previous work of Futagami in which the nature of the dislocations was not determined unambiguously.

C H A P T E R IX

SUGGESTIONS FOR FURTHER WORK

The diversity of subject matter presented in this thesis is such that a whole range of possibilities for further study is left open. It is the belief of the author that the most fruitful X-ray topographic studies in the next few years will be those which combine the strain sensitivity of topography with another technique measuring a totally unrelated parameter. A good example of this is shown in the X-ray and S.E.M. experiments described in Chapter V. In this work, the cause of breakdown in a particular case was determined. However, it is not necessarily a general rule that such breakdown is caused by oxide mask scratches. To formulate a more general statement a systematic study of many such junctions must be undertaken.

Similarly, combined electrical and X-ray work on the compounds discussed in Chapter VII would make an extremely interesting project. It is not clear what effect the addition of an extra half plane of atoms would have on the electron transport characteristics of such materials. The conduction parallel to the C axis is tentatively explained in terms of a hopping mechanism and whether this is sensitive to crystal perfection is unknown. It would be useful at least to determine whether the electrical properties of perfect and dislocated crystals differ. Furthermore, there are several layer compounds, the crystals of which are at present still rather

imperfect, e.g., $TiTe_2$. Use of X-ray topography as a monitoring routine should enable the best conditions for growth of perfect layer compound crystals to be determined. Such studies will be carried out at Brighton Polytechnic under the supervision of Dr. A.A. Balchin.

Two projects on which the author intends to work arise in Chapter IV. Firstly, it has been shown that the lower limit of crystal thickness for good dislocation contrast is about 0.4 of an extinction distance in low order reflections. Using the 220 reflection with CrKα radiation, the maximum thickness of silicon in which good images may be formed is about 3½ μm. This is within the range of penetration of 1 MeV electrons and it should be possible to study the same dislocation in the high voltage electron microscope and X-ray topographic camera. It will be of considerable value to make such a comparison in order to help relate micro- and macro-scale defects, which often at present look confusingly different.

Secondly, the computer programs developed by Sworn and Howie enable relatively rapid simulations of dislocation images in X-ray topographs. Using the programs developed in Cambridge, it would be of interest to simulate image contrast in some specific cases. A case in point is the contrast of dislocations near a free surface. While the column approximation calculations using Penning-Polder theory have given a qualitative description of the contrast, using the dynamical theory without taking a column approximation, a quantitative comparison should be possible. In the electron microscope studies, Titchmarsh, (1971), found that the contrast observed

could only be simulated if, in addition to the surface relaxation, a sheath of precipitate was included around the dislocation. It is important to check whether precipitation needs to be included in order that the X-ray contrast should be matched. If appreciable precipitation is present, this will modify the electrical characteristics of the dislocation and presumably its effect on junction characteristics. There are other contrast problems encountered during this study which have yet to be solved. Several examples of double loop contrast, from what appear to be precipitates, have been observed. Attempts will be made to simulate these images using the dynamical theory programs.

It is, however, the intention of the author to devote considerable time to the study of nearly perfect metal crystals. Only recently have large-scale studies taken place on metal crystals, mainly due to the problems of growing crystals perfect enough for X-ray study. Now that nearly perfect crystals of a variety of metals may be prepared by several techniques, X-ray topography in conjunction with high voltage electron microscopy should give useful information about the deformation in the early stages. At Oxford, it is hoped to contrast the deformation behaviour of several copper alloys with pure copper and relate this to the macroscopic yield phenomena. Crystals will be grown by the method described by Sworn, (1971), and deformed in a straining jig similar to that used by Young and Sherrill, (1971). Similarly, the time is ripe for a deformation study of pure iron single

crystals. An X-ray topographic study of deformation of a b.c.c. metal is long awaited.

APPENDIX A

A.1. Consider a screw dislocation lying in the plane of the crystal surface and along the z direction. The y axis is along the normal to the crystal surface and the x axis is at right angles to the dislocation and in the plane of the surface.

The effective misorientation around a defect $\delta(\Delta\theta)$ is given by

$$\delta(\Delta\theta) = -\frac{1}{K \sin 2\theta} \frac{\partial}{\partial s_g} (\underline{g} \cdot \underline{u}) \qquad (A.1)$$

where $\underline{s}_g$ is the diffracted beam direction.

Approximating the direction $\underline{s}_g$ by the y direction will introduce little error for small Bragg angles. Then with this approximation,

$$\delta(\Delta\theta) = \frac{-\lambda}{\sin 2\theta} \frac{\partial}{\partial y} (\underline{g} \cdot \underline{u}) \qquad (A.2)$$

For a screw dislocation

$$u_x = u_y = 0$$

$$u_z = \frac{b}{2\pi} \tan^{-1} \left(\frac{y}{x}\right) \qquad (A.3)$$

Now if g is parallel to the dislocation line

$$\underline{g} \cdot \underline{u} = |g| u_z \qquad (A.4)$$

Then:

$$\delta(\Delta\theta) = -\frac{\lambda}{2\sin\theta\cos\theta} g \frac{\partial}{\partial y}(u_z)$$

$$= -\frac{1}{\cos\theta} \frac{\partial}{\partial y}\left(\frac{b}{2\pi} \tan^{-1}\frac{y}{x}\right)$$

$$= -\frac{1}{\cos\theta} \cdot \frac{b}{2\pi}\left(\frac{x}{x^2+y^2}\right) \qquad (A.5)$$

For constant x this has a maximum value in the plane of the dislocation, i.e., when y = 0.

Then:

$$\delta(\Delta\theta)_{max} = -\frac{b}{2\pi\cos\theta} \cdot \frac{1}{x_1} \qquad (A.6)$$

which justifies the approximation for the misorientation used in Chapters II and IV, provided the Bragg angles does not become so large that $\underline{s}_g$ cannot be approximated to y.

A.2. The volume enclosed, per unit length of dislocation line, by a contour of equal misorientation $\delta(\Delta\theta)$ is given by:

$$V = \int_0^{x_1} y\, dx \qquad (A.7)$$

where y is related to x by equation (A.5) and x_1, the maximum value of x, for misorientation $\delta(\Delta\theta)$. They are given by :

$$x_1 = \frac{b}{2\pi \cos\theta \; \delta(\Delta\theta)} = \frac{1}{M} \qquad (A.8)$$

$$y = \sqrt{\frac{x}{M} - x^2}$$

Then $$V = \int_0^{1/M} \sqrt{\frac{x}{M} - x^2} \; dx \qquad (A.9)$$

writing $z^2 = x$, $a^2 = \frac{1}{M}$ and $t = (a^2 - x^2)^{\frac{1}{2}}$

one obtains

$$V = \int_0^a 2z^2 t \, dz$$

$$= 2 \left[-\frac{zt^3}{4} + \frac{a^2 zt}{8} + \frac{a^4}{8} \sin^{-1} \frac{z}{a} \right]_0^a$$

$$= 2 \cdot \frac{a^4}{8} \cdot \frac{\pi}{2} \; . \qquad (A.10)$$

In other words, volume enclosed by contour of equal misorientation is proportional to $\left[\frac{b}{\delta(\Delta\theta)} \right]^2$ or x_1^2 .

Thus the approximation that the volume enclosed by a contour of equal misorientation is proportional to the square of the image width is satisfactory for a screw dislocation, provided again that the Bragg angle is not too large that $\frac{\partial}{\partial y}$ becomes markedly different from $\frac{\partial}{\partial s_g}$.

A.3. For Takagi's theory to be valid, $\underline{D}_g$ and $\underline{g} \cdot \underline{u}$ must remain nearly constant over a range, ℓ, where

$$\ell = \frac{}{\sqrt{\lambda \xi_g}} \tag{A.11}$$

The condition on $\underline{g} \cdot \underline{u}$ requires, (Takagi, 1969)

$$\left|\nabla^2 (\underline{g} \cdot \underline{u})\right| \ll \frac{1}{\lambda \xi_g} \tag{A.12}$$

For a pure edge dislocation with $\underline{g} \;//^{\ell}\; \underline{b}$, one has :

$$u_x = \frac{b}{2\pi} \tan^{-1}\left(\frac{y}{x}\right) + \frac{xy}{2(1-\nu)(x^2+y^2)} \tag{A.13}$$

Then:

$$\frac{\partial^2}{\partial x^2}(gu_x) + \frac{\partial^2}{\partial y^2}(gu_x)$$

$$= \frac{gb}{2\pi(1-\nu)} \frac{3x^3y - xy^3 + 3y^3x - x^3y}{(x^2+y^2)^3}$$

$$= \frac{gb}{\pi(1-\nu)} \frac{x^3y + y^3x}{(x^2+y^2)^3} \tag{A.14}$$

This has a maximum value where

$$y = \pm \sqrt{3}\, x \,.$$

Then, substituting approximate values one finds for $x \gtrsim 0.03$ μm, this condition on Takagi's theory holds. Except within regions closer than 0.03 μm from the dislocation core, the requirement that $\nabla^2 |\underline{g} \cdot \underline{u}| \ll {}^{1}/_{\lambda \xi_g}$ is satisfied. The misorientation corresponding to regions closer than this to the core is greater than 2×10^{-3} radians.

APPENDIX B

To obtain high quality topographs, the specimen to plate distance must be as small as possible to give good vertical resolution (see Chapter II). Vibration was minimised by placing a latex foam mat beneath the camera. [It was found that mounting the Lang camera directly on the Elliott GX6 did not introduce any detrimental movement.]

Ilford L4 and G5 Nuclear Emulsions were used, the former for high resolution work, the latter for speed. Emulsions were stored refrigerated but not frozen. Processing was performed at about $0^{o}C$ in a refrigerator to slow the development rate to a value comparable with the diffusion rate. Details are given in Table B.1.

Table B.1

Processing of Ilford Nuclear Emulsions

Radiation	CoKα CrKα CuKα	MoKα AgKα
Thickness Emulsion	25 μm	50 μm
Soak (Deionised Water)	10 min	15 min
Develop. - $0^{o}C$ (1:3 D 19b with Deionised Water	12-30 min	15-45 min
Stop. - (1% Acetic Acid)	5 min	10 min
Fix - 300g. Hypo 30 g Sodium bisulphite per litre H_2O.	30 min	60 min
Wash	2 hours	2 hours

The plates were carefully wiped with cotton wool under running water to remove any particles of dirt. [This did not lead to damage of the emulsion and is recommended.] Plates were dried in a desiccator at room temperature and protected from damage by placing a drop of emulsion oil on the emulsion and covering with a microscope cover slip. This was secured at the edges with "collodion" or similar adhesive.

Photomicrography was performed on a Reichert Microscope and enlargements were made either directly on Polaroid film or using Ilford "Lantern contrast" plates.

REFERENCES

Adams, J., Advances in Electronics and Electron Physics, 22A (1966) 139.

Adams, J. and Manley, B., Electronic Engineering, 37 (1965) 180.

Adams, J. and Manley, B., I.E.E.E. Trans. Nuc. Sci., NS 13 (1966) 88.

Adams, J. and Manley, B., Philips Tech. Rev. 28 (1967) 156.

Allen, R.D., American Mineralogist, 37 (1952) 910.

Amelinckx, S., Bontinck, W., Dekeyser, W. and Seitz, F., Phil. Mag. 2 (1957) 355.

Amelinckx, S. and Delavignette, P., Direct Observations of Imperfections in Crystals, Interscience (1962) 295.

Anderson, A. Lindegaard, Rev. Sci. Inst. 36 (1965) 1888.

Anderson, A. Lindegaard, Rev. Sci. Inst. 39 (1968) 775.

Ando, M. and Hosoya, S., J. App. Cryst. 4 (1971) 146.

Ando, Y. and Kato, N., Acta. Cryst. 21 (1966) 284.

Ashbee, K.H.G. and Frank, F.C., Phil. Mag. 21 (1970) 211.

Authier, A., Adv. X-Ray Anal. Plenum 10 (1967) 9.

Authier, A., Phys. Stat. Sol. 27 (1968) 77.

Authier, A., Modern Diffraction and Imaging Techniques in Material Science. N. Holland (1970a) 481.

Authier, A., Advances in Structure Research by Diffraction Methods, Pergamon (1970b) 1.

Authier, A. Balibar, F. and Epelboin, Y., Phys. Stat. Sol. 41 (1970) 225.

Authier, A. and Lang, A.R., J. App. Phys. 35 (1964) 1956.

Authier, A., Malgrange, C. and Tournarie, M., Acta Cryst. A24 (1968) 126.

Authier, A., Milne, D. and Sauvage, M., Phys. Stat. Sol. 26 (1968) 469.

Authier, A. and Rimski, A., J. de Physique 24 (1963) 132A.

Authier, A., Rodgers, C.B. and Lang, A.R., Phil. Mag. 12 (1965) 547.

Authier, A. and Sauvage, M., J. de Physique c.27 supp. 7-8 (1966) 3.

Badrick, A. and Puttick, K., Phil. Mag. 23 (1971) 585.

Barrett, C.S., Trans. AIME 161 (1945) 15.

Barth, H. and Hoseman, R., Z. Naturforsch. 13a (1958) 792.

Batterman, B.W. and Cole, H., Rev. Mod. Phys. 36 (1964) 681.

Becker, C. and Pegel, B., Phys. Stat. Sol. 35 (1969) 157.

Berg, W.F., Naturwissenschaften 19 (1931) 391.

Bertocci, U., Bertocci, C. and Young, F.W., J. App. Phys. 40 (1969) 674.

Blech, I.A., Meieran, E.S. and Sello, H., App. Phys. Lett. 7 (1965) 176.

Blech, I.A. and Meieran, E.S., App. Phys. Lett. 9 (1966) 245.

Blech, I.A. and Meieran, E.S., J. App. Phys. 38 (1967) 2913.

Bond, W.L. and Andrus, J., Phys. Rev. 101 (1956) 1211.

Bonse, U., Direct Observations of Dislocations (1962) 431.

Bonse, U., Z. Physik 184 (1965) 71.

Bonse, U. and Hart, M., App. Phys. Lett. 6 (1965) 155.

Bonse, U. and Hart, M., App. Phys. Lett. 7 (1965) 99.

Bonse, U. and Hart, M., Z. Physik 188 (1965) 154.

Bonse, U. and Hart, M., Z. Physik 190 (1966) 455.

Bonse, U. and Hart, M., Z. Physik 194 (1966) 1.

Bonse, U. and Hart, M., Acta Cryst. A24 (1968) 290.

Bonse, U. and Hart, M., Phys. Stat. Sol. 33 (1969) 351.

Bonse, U., Hart, M. and Newkirk, J.B., Adv. X-Ray Anal. Plenum 10 (1967) 1.

Bonse, U., Hart, M. and Schwuttke, G.H., Phys. Stat. Sol. 33 (1969) 361.

Bontinck, W., Phil. Mag. 2 (1957) 561.

Bontinck, W. and Amelinckx, S., Phil. Mag. 2 (1957) 94.

Bontinck, W. and Dekeyser, W., Physica 22 (1956) 595.

Born, M. and Wolf, E., Principles of Optics (Pergamon) (1964).

Borrmann, G., Z. Physik 42 (1941) 157.

Borrmann, G., Z. Physik 127 (1950) 297.

Brädler, J. and Lang, A.R., Acta Cryst. A24 (1968) 246.

Brümmer, D. and Alex, V., Phys. Stat. Sol. (a) 3 (1970) 193.

Bullough, R., Maher, D.M. and Perrin, R.C., Nature 224 (1969) 364.

Burcham, W.E., Nuclear Physics, Longmans (1963).

Carlson, H.A. and Wegener, H.A., J. App. Phys. 32 (1961) 125.

Carrington, W., Hale, K.E. and McLean, D., Proc. Roy. Soc. 259 (1960) 203.

Carron, G.J., App. Phys. Lett. 9 (1966) 355.

Carron, G.J. and Walford, L.K., J. App. Phys. 38 (1967) 3949.

Carron, G.J. and Walford, L.K., J. App. Phys. 39 (1968) 3813,5802.

Caslavsky, J., Rev. Sci. Inst. 41 (1970) 517.

Caslavsky, J. and Suri, S.K., J. Cryst. Growth 6 (1970) 213.

Caslavsky, J. and Vedam, K., Phil. Mag. 22 (1970) 255.

Chaudhuri, A.R., Patel, J.R. and Rubin, L.G., J. App. Phys. 33 (1962) 2736.

Chikawa, J-I., App. Phys. Lett. 4 (1964) 159.

Chikawa, J-I., App. Phys. Lett. 5 (1964) 31.

Chikawa, J-I., App. Phys. Lett. 7 (1965) 193.

Chikawa, J-I., J. App. Phys. 36 (1965) 3496.

Chikawa, J-I., J. Phys. Chem. Solids, supp. 1 (1967) 817.

Chikawa, J-I., App. Phys. Lett. 13 (1968) 387.

Chikawa, J-I. and Austerman, S.B., J. App. Cryst. 1 (1968) 165.

Chikawa, J-I. and Austerman, S.B., Adv. X-Ray Anal. Plenum 11 (1968) 394.

Chikawa, J-I. and Fujimoto, J., App. Phys. Lett. 13 (1968) 387.

Clareborough, L.M., Michell, D. and Smith, A., Phys. Stat. Sol. 21 (1967) 369.

Cockayne, D., Ray, I.L.F. and Whelan, M.J., Phil. Mag. 20 (1969) 1265.

Coslett, V.E. and Thomas, R.N., Brit. J. App. Phys. 15 (1964) 1283.

Czaja, W. and Wheatley, G.H., J. App. Phys. 35 (1964) 2782.

Czaja, W. and Patel, J.R., J. App. Phys. 36 (1965) 1476.

Compton, A.H. and Allison, S.K. X rays in Theory and Experiment (N.Y. van Nostrand) (1935).

Dale, R. and Hamilton, M., C.V.D. Co-Ord. Meeting, University of Southampton (1971).

Davies, I.G., Hughes, K.A., Solway, D.V. and Thornton, P.R., Solid State Electronics 9 (1966) 275.

Dionne, G., J. App. Phys. 38 (1967) 4094.

Emara, S.H., Lawn, B.R. and Lang, A.R., Phil. Mag. 19 (1969) 7.

Evans, R.C., Introduction to Crystal Chemistry, Cambridge U.P. (1966).

Evans, A.G. and Pratt, P.L., Phil. Mag. 20 (1969) 1213.

Fairfield, J.M. and Schwuttke, G.H., J. Electrochem. Soc. 115 (1968) 415.

Fehmer, H. and Uelhoff, W., J. Sci. Inst. 2 (1969) 767.

Fiermans, L., Phys. Stat. Sol. 6 (1964) 169.

Filby, J., Private Communication (1971).

Foot, J., Thesis, University of Nancy (1968).

Foster, K., Kramer, J.J. and Wiener, G.W., Trans. AIME 227 (1963) 185.

Fowles, G.R., Introduction to Modern Optics, Holt, Rinehart and Winston (1968).

Frank, F.C. and Lang, A.R., Phil. Mag. 4 (1959) 383.

Frank, F.C., Lawn, B.R., Lang, A.R. and Wilks, E.M., Proc. Roy. Soc. A 301 (1967) 239.

Fremiot, M., Baudelet, B. and Champier, G., J. Cryst. Growth 34 (1968) 711.

Friedel, J., Dislocations, Pergamon (1964).

Fujiwara, T., Dohi, S. and Sunada, J., Jap. J. App. Phys. 3 (1964) 129.

Futagami, K., Jap. J. App. Phys. 10 (1971) 814.

Gajda, W.J. Jr., Phys. Stat. Sol. (a) 5 (1971) K143.

Gerold, V. and Meier, F., Z. Physik 155 (1959) 387.

Gerward, L., Phys. Stat. Sol.(a) 2 (1970) 143.

Glaenzer, R.H. and Jordan, A.G., Phil. Mag. 18 (1968) 717.

Guest, A., Private Communication (1970).

Guest, A., Holmshaw, R. and Manley, B., Adv. Electronics and Electron Physics 28A (1969) 471.

Hart, M., Ph.D. Thesis, University of Bristol (1963).

Hart, M., Science Progress, (Oxford) 56 (1968) 429.

Hart, M., X-Ray Topography Symposium, University of Bristol (1971).

Hart, M. and Lang, A.R., Acta Cryst. 16 (1963) A 102.

Hashimoto, H., Howie, A. and Whelan, M.J., Proc. Roy. Soc. A 269 (1962) 80.

Hashizume, H., Kohra, K., Yamaguchi, T. and Kinoshata, K., App. Phys. Lett. 18 (1971) 213.

Head, A.K., Proc. Phys. Soc. (Lond.) (1953) 66 793.

Heroux, L., Manson, J.E., Hinteregger, H.E. and McMahon, W.J., J. Optic. Soc. Am. 55 (1965) 103.

Hintze, H., Mineralogie 1 (1915) 2401.

Hirsch, P.B., Howie, A., Nicholson, R.B., Pashley, D.W. and Whelan, M.J., Electron Microscopy of Thin Crystals, Butterworth (1965).

Horn, F.H., Phys. Rev. 97 (1954) 1521.

Hosoya, S., Jap. J. App. Phys. 7 (1968) 1.

Hosoya, S. and Ando, M., Phys. Rev. Lett. 6 (1971) 321.

Howie, A., Modern Diffraction and Imaging Techniques in Material Science, N. Holland (1970).

Howie, A. and Basinsky, Z., Phil. Mag. 17 (1968) 1039.

Howie, A. and Sworn, C.H., Phil. Mag. 22 (1970) 871.

Humble, P., Modern Diffraction and Imaging Techniques in Material Science, N. Holland (1970).

Humphreys, C.J., Ph.D. Thesis, University of Cambridge (1967).

Ikeno, S., Maruyama, H. and Kato, N., J. Cryst. Growth 3,4 (1968) 683.

Itagaki, K., Adv. X-Ray Anal. Plenum 13 (1970) 526.

Jaswon, M.A. and Dove, D.B., Acta Cryst. 8 (1955) 88, 806.

Jenkinson, A.E. and Lang, A.R., Direct Observations Of Imperfections (1962) 471.

Jouffrey, B. and Taupin, D., Phil. Mag. 16 (1967) 703.

Jourdan, C. and Sauvage, M., Phys. Stat. Sol.(a) 3 (1970) 343.

Joy, D.C. and Titchmarsh, J.M., 7th Int. Cong. Microsc. Electronique, Grenoble (1970) 221.

Kamiya, Y. and Lang, A.R., J. App. Phys. 36 (1965) 579.

Kannan, V.C. and Washburn, J., J. App. Phys. 41 (1970) 3589.

Kato, N., Acta Cryst. 13 (1960) 349.

Kato, N., Acta Cryst. 14 (1961,a,b) 526,627.

Kato, N., Acta Cryst. 16 (1963,a,b) 276,282.

Kato, N., Crystallog. and Crystal Perfection. Academic Press (1963) 153.

Kato, N., J. Phys. Soc. Jap. 18 (1964) 1875.

Kato, N., J. Phys. Soc. Jap. 19 (1964) 67, 971.

Kato, N. and Ando, Y., J. Phys. Soc. Jap. 21 (1966) 964.

Kato, N. and Lang, A.R., Acta Cryst. 12 (1959) 787.

Kato, N. and Patel, J.R., App. Phys. Lett. 13 (1968) 42.

Kato, N., Usami, K., and Katagawa, T., Adv. X-Ray Anal. 13 (1967) 46.

Keig, G.A. and Coble, R.L., J. App. Phys. 39 (1968) 6090.

Kohra, K., Hashizume, H. and Yoshimura, J-I., Jap. J. App. Phys. 9 (1970) 1029.

Kohra, K. and Takano, Y., Jap. J. App. Phys. 7 (1968) 982.

Kohra, K. and Yoshimatsu, M., J. Phys. Soc. Jap. 17 (1962) 1041.

Kranje, K., J. App. Cryst. 1 (1968) 227.

Kranje, K., J. App. Cryst. 2 (1969) 262.

Kuriyama, M. and McManus, G.M., Phys. Stat. Sol. 25 (1968) 667.

Lander, J.J., Schreiber, H. Jr., Buck, T.M. and Mathews, J.B., App. Phys. Lett. 3 (1963) 206.

Lang, A.R., Acta Met. 5 (1957)(a) 358.

Lang, A.R., Acta Cryst. 10 (1957)(b) 837.

Lang, A.R., J. App. Phys. 29 (1958) 597.

Lang, A.R., J. App. Phys. 30 (1959) 1748.

Lang, A.R., Acta Cryst. 12 (1959) 249.

Lang, A.R., Brit. J. App. Phys. 14 (1963) 904.

Lang, A.R., Proc. Roy. Soc. A 278 (1964) 238.

Lang, A.R., Disc. Fardday Soc. 38 (1964) 292.

Lang, A.R., Z. Naturforsch. 20 A (1965) 636.

Lang, A.R., J. Phys. Chem. Solids Supp. (1967) 833.

Lang, A.R., Nature 213 (1967) 248.

Lang, A.R., Nature 226 (1968) 652.

Lang, A.R., Modern Diffraction and Imaging Techniques In Material Science. N. Holland (1970) 407.

Lang, A.R. and Miles, G.D., J. App. Phys. 36 (1965) 1863.

Lang, A.R. and Muiscov, V.F., Phil. Mag. 10 (1964) 263.

Lang, A.R. and Muiscov, V.F., App. Phys. Lett. 7 (1965) 214.

Lang, A.R. and Muiscov, V.F., J. App. Phys. 38 (1967) 2477.

Lang, A.R. and Polcarova, M., Proc. Roy. Soc. A 285 (1965) 297.

Lang, A.R. and Reifsneider, K., App. Phys. Lett. 15 (1969) 258.

von Laue, M., Acta Cryst. 2 (1949) 106.

Lawn, B.R., Adv. X-Ray Anal. Plenum 11 (1967) 385.

Lawn, B.R., Kamiya, Y. and Lang, A.R., Phil. Mag. 12 (1965) 177.

Lawrence, J.E., J. Electrochem.Soc. 113 (1966) 819.

Lawrence, J.E., J. Electrochem. Soc. 115 (1968) 860.

Lee, P.A., Said, G. and Davis, R., Sol. State Comm. 7 (1969) 1359.

Lefeld-Sosnowska, M., Phys. Stat. Sol. 7 (1964) 449.

Levine, E., Washburn, S. and Thomas, G., J. App. Phys. 38 (1967) 81.

Mallard,-., Ann. Mines, 10 (1876) 115.

Meieran, E.S., Siemens Review, 4th special issue: X-Ray and E.M. News 37 (1970) 1.

Meieran, E.S. and Bleeh, I.A., J. App. Phys. 36 (1965) 3162.

Meieran, E.S. and Bleeh, I.A., J. App. Phys. 38 (1967) 3495.

Meieran, E.S. and Bleeh, I.A., Phys. Stat. Sol. 29 (1968) 653.

Meieran, E.S. and Bleeh, I.A., Fairchild R and D Report 525 (J. App. Phys., in press) (1971).

van Mellaert, L.J. and Schwuttke, G.H., Phys. Stat.Sol. (a) 3 (1970) 687.

Mendelson, S., J. App. Phys. 32 (1961) 1999.

Mendelson, S., Direct Observations of Dislocations (1962).

Merlini, A. and Guinier, A., Bull. Soc. Franç. Min. Cryst. 80 (1957) 147.

Michell, D., Morton, A. and Smith, A., Phys. Stat. Sol.(a) 5 (1971) 341.

Michell, D. and Ogilvie, G.J., Phys. Stat.Sol. 15 (1966) 83.

Michell, D. and Smith, A., Phys. Stat. Sol. 27 (1968) 291.

Michell, D., Smith, A. and Sabine, T.M., Acta Cryst. B 25 (1969) 2458.

Miltat, J.E.A., D.Phil. Thesis, University of Oxford (1971).

Miltat, J.E.A. and Bowen, K., Phys. Stat. Sol.(a) 3 (1970) 431.

Mott, N.F., Contmp. Physics 10 (1969) 125.

Mouser, D.P., Ruggles, P.C. and Slark, N.A., T.V. Soc. J. 11 (1967) 261.

Nagakura, S. and Chikaura, Y., J. Phys. Soc. Jap. 30 (1971) 495.

Nes, E. and Nøst, B., Phil. Mag. 13 (1966) 124.

Newkirk, J.B., Phys. Rev. 110 (1958) 1465.

Newkirk, J.B., Trans AIME 215 (1959) 483.

Nimura, H., Ito, N., Nakau, T. and Nakahara, O., Jap. J. App. Phys. 7 (1968) 43.

Nittono, O., Jap. J. App. Phys. 10 (1971) 188.

Nittono, O, and Nagakura, S., Jap. J. App. Phys. 8 (1969) 1180.

Nittono, O., Onodera, N, and Nagakura, S., Jap. J. App. Phys. 9 (1970) 328.

Nøst, B., Phil. Mag. 11 (1965) 109.

Nøst, B, and Nes, E., Acta Met. 17 (1969) 13.

Nøst, B. and Sorensen, G., Phil. Mag. 13 (1966) 125.

Nøst, B., Sorensen, G. and Nes, E., J. Cryst. Growth 1 (1967) 149.

Oatley, C.W. and Everhart, T.E., J. Electronics 2 (1957) 568.

O'Hara, S. and Schwuttke, G.H., J. App. Phys. 36 (1965) 2475.

Oki, S. and Futagami, K., Jap. J. App. Phys. 8 (1969) 1574.

Ovshinsky, S.R., Phys. Rev. Lett. 21 (1968) 1450.

Pandeyn, D.C. and Tolansky, S., Proc. Phys. Soc. Lond. 78 (1961) 12.

Parkes, W., Gott, R. and Pounds, K., Trans. IEEE Nuclear Sci. 17 (1970) 360.

Parpia, D.Y. and Tanner, B.K., Phys. Stat. Sol.(a) 6 (1971) 689.

Patel, A.R. and Desai, C.C., India J. Pure and App. Phys. 4 (1966) 124.

Patel, A.R., Goswami, K.N. and Desai, C.C., Phil. Mag. 10 (1964) 931.

Patel, A.R. and Patel, S.M., India J. Pure and App. Phys. 7 (1969) 690.

Patel, J.R. and Freland, V., J. App. Phys. 41 (1970) 2814.

Patel, J.R., Jackson, K.A. and Dillon, J.F. Jr., Journal App. Phys., 39 (1968) 3763.

Patel, J.R. and Kato, N., App. Phys. Lett. 13 (1968) 40.

Pegel, B. and Becker, C., Phys. Stat. Sol. 32 (1969) 443.

Penning, P., Thesis, Tech. University of Delft. (1966).

Penning, P. and Goemans, A.H., Phil. Mag. 18 (1968) 297.

Penning, P. and Polder, D., Philips Res. Repts. 16 (1961) 419.

Phakey, P.P., Phys. Stat. Sol. 34 (1969) 105.

Phakey, P.P. and Aly, A.M., Phil. Mag. 22 (1970) 1217.

Phakey, P.P. and Leonard, J., J. App. Cryst. 3 (1970) 38.

Pockels, F., Ann. Phys. 37 (1889) 144,372.

Polcarova, M. and Gemperlova, J., Phys. Stat. Sol. 32 (1969) 769.

Polcarova, M. and Lang, A.R., App. Phys. Lett. 1 (1962) 13.

Polcarova, M. and Lang, A.R., Bull. Soc. Franc. Min. Cryst. 91 (1968) 645.

Prussin, S., J. App. Phys. 32 (1961) 1876

Ramachandran, G.N., Proc. Indian Acad. Sci. A19 (1944) 280.

Randall, R.P., Adv. Electronics and Electron Physics. 22A (1966) 87.

Read, W.T., Dislocations in Crystals. McGraw Hill (1953).

Rimmington, H.P.B. and Balchin, A.A., Phys. Stat. Sol. (a) 6 (1971) K 47.

Roessler, B., Phys. Stat. Sol. 20 (1967) 713.

Roessler, B., Kramer, J. and Kuriyama, M., Phys. Stat. Sol. 11 (1965) 713.

Rozgonyi, G., Haszco, S. and Statile, J., App. Phys. Lett. 16 (1970) 443.

Rumsh, M.A., Lukirskii, A.P. and Shchemelev, V.N., Soviet Phys. Doklady 135 (1960) 1231.

Rupprecht, H. and Schwuttke, G.H., J. App. Phys. 37 (1966) 2862.

Rustad, O. and Lohne, O., Phys. Stat. Sol.(a) 6 (1971) 153.

Saccocio, E.J., App. Phys. Lett 17 (1970) 149.

Saccocio, E.J., J. App. Phys. 42 (1971) 3619.

Sato, Y. and Arata, H., Jap.J. App. Phys. 3 (1964) 511.

Sauvage, M., Phys. Stat. Sol. 29 (1968) 725.

Sauvage, M., Phys. Stat. Sol. 34 (1969) 105.

Sauvage, M. and Authier, A., Phys. Stat. Sol. 12 (1965) K73.

Sauvage, M. and Simon, D., Phys. Stat. Sol. 35 (1969) 173.

Schaffer, H., Chemical Transport Reactions, Academic Press (1964).

Schlenker, M, and Kleman, M., J. de Physique 32, c.1 (1971) 256.

Schuller, E. and Amelinckx, S., Naturwissenschaft 47 (1960) 491.

Schulz, L.G., Trans AIME 200 (1954) 1082.

Schwuttke, G.H., J. App. Phys. 36 (1965) 2712.

Schwuttke, G.H., Proc. Trans. 3rd Int. Vacuum Cong. 2 (1966) 301.

Schwuttke, G.H., I.B.M. Scientific Report AFCRL/67/0564 (1967).

Schwuttke, G.H., I.B.M. Scientific Report AFCRL/70/0110 (1970).

Schwuttke, G.H. and Fairfield, J.M., J. App. Phys. 37 (1966) 4394.

Schwuttke, G.H. and Howard, J.K., J. App. Phys. 39 (1968) 1581.

Schwuttke, G.H. and Queisser, H.J., J. App. Phys. 33 (1962) 1540.

Segmuller, A., I.B.M. J. Res. and Dev. 12 (1968) 448.

Segmuller, A. and Light, T.B., J. App. Phys. 40 (1969) 1972.

Shaw, A.M.B., Ph.D. Thesis, University of Cambridge (1969).

Shetty, M.N., Taylor, J.B. and Calvert, L.D., Adv. X-Ray Anal. Plenum 12 (1969) 151.

Shockley, W. and Read, W.T., Phys. Rev. 75 (1949) 692.

Shockley, W. and Read, W.T., Phys. Rev. 78 (1950) 275.

Simmons, J.G. and Verdeber, R.R., Proc. Roy. Soc. A 301 (1967) 77.

Smith, D.G. and Pounds, K.A., Trans IEEE Nuclear Sci. 15 (1968) 541.

Stanford, J.L., Hamm, R.N. and Arakawa, E.T., J. Optic. Soc. Am. 55 (1965) 103.

Suzuki, T. and Kojima, H., Acta Met. 14 (1966) 913.

Sworn, C.H., Ph.D. Thesis, University of Cambridge (1971).

Takagi, S., Acta Cryst. 15 (1962) 1311.

Takagi, S., J. Phys. Soc. Jap. 26 (1969) 1239.

Taupin, D., Acta Cryst. 23 (1967) 25.

Timoshenko, S., Theory of Elasticity (2nd Ed.) McGraw-Hill (1964).

Titchmarsh, J.M., D.Phil. Thesis, University of Oxford (1971).

Tolansky, S. and Wilcock, W.L., Proc. Roy. Soc. A. 191 (1947) 182.

Tucker, T.N. and Schwuttke, G.H., App. Phys. Lett. 9 (1966) 919.

Turner, P.J., Cartwright, P., Southern, M.J., van Oomstrum, A. and Manley, B., J. Sci. Inst. 2. (1969) 731.

Wagatsuma, R., Sumino K., Uchida, W. and Yamamoto, S., J. App. Phys. 42 (1971) 222.

Wang, C.C. and McFarlane, S.H., J. Cryst. Growth 4 (1968) 485.

Washburn, J., Thomas, G. and Quesser, H.J., J. App. Phys. 35 (1964) 1906.

Webb, W.W. and Hayes, C.E., Phil. Mag. 16 (1967) 909.

Whelan, M.J., Unpublished work (1969).

Whelan, M.J., Modern Diffraction and Imaging Techniques in Material Science. N. Holland (1970) 35.

Whelan, M.J. and Hirsch, P.B., Phil. Mag. 2 (1957) 1121,1303.

Wooster, N. and Wooster, W.A., Nature 155 (1945) 786.

Wu, C.C.M. and Roessler, B., J. App. Phys. 42 (1971) 1814.

Yoshida, M., Arata, H. and Terunuma, Y., Jap.J. App. Phys. 7 (1968) 209.

Yoshimatsu, M., J. Phys. Soc. Jap. 18 (1963) 335.

Yoshimatsu, M., Jap. J. App. Phys. 3 (1964) 94.

Yoshimatsu, M., Jap. J. App. Phys. 4 (1965) 619.

Yoshimatsu, M., Suzuki, T., Kobayashi, A. and Kohra, K., J. Phys. Soc. Jap. 17 (1962) 583.

Young, F.W., Int. Conf. Electron Diff. and Crystal Defects. Melbourne (1965).

Young, F.W. and Savage, J.R., J. App. Phys. 35 (1964) 1917.

Young, F.W. and Sherrill, F.A., Canad. J. Phys. 45 (1967).

Young, F.W. and Sherrill, F.A., J. App. Phys. 42 (1971) 230.

Yukimoto, Y., Jap. J. App. Phys. 7 (1968) 348.

Yukimoto, Y., Hirano, A. and Sugioka, Y., Jap. J. App. Phys. 6 (1967) 420.

Zachariasen, W.H., Theory of X-Ray Diffraction in Crystals. John Wiley (1945).

Zarka, A., Bull. Soc. Franc. Min. Cryst. 92 (1969) 160.